

33rd conference with international participation



BOOK OF EXTENDED ABSTRACTS

November 6 - 8, 2017

HOTEL HORIZONT, ŠPIČÁK
CZECH REPUBLIC



BOOK OF EXTENDED ABSTRACTS

33rd conference with international participation **Computational Mechanics 2017**

ISBN 978-80-261-0748-4

Published by

University of West Bohemia, Univerzitní 8, 301 00 Plzeň, Czech Republic, IC 49777513

Edited by

Vítězslav Adámek

Alena Jonášová

Stanislav Plánička

Martin Zajíček

Conference secretariat

Monika Nocarová

Department of Mechanics

Faculty of Applied Sciences

University of West Bohemia

Univerzitní 8

301 00 Plzeň

Czech Republic

phone: +420 377 632 301

e-mail: vm@kme.zcu.cz

Copyright © 2017 University of West Bohemia, Plzeň, Czech Republic

PREFACE

The Book of Extended Abstracts contains 80 two-page abstracts presented at the 33rd conference **Computational Mechanics 2017**, which was held at the Hotel Horizont in Špičák, Czech Republic, on November 6 – 8, 2017. This annual conference, which was attended by over one hundred participants from the Czech Republic, Slovakia and from abroad, was organised by the Department of Mechanics, Faculty of Applied Sciences of the University of West Bohemia under the auspices of

- Vlasta Radová, the Dean of the Faculty of Applied Sciences,
- Ivana Bartošová, the Vice-President of the Pilsen Region for Education and Tourism,
- Czech Society for Mechanics,
- Czech National Committee of IFToMM,
- Central European Association for Computational Mechanics.

The main objective of this traditional conference is to bring together academicians, researchers and industrial partners interested in relevant disciplines of mechanics including

- solid mechanics,
- dynamics of mechanical systems,
- mechatronics and vibrations,
- reliability and durability of structures,
- fracture mechanics,
- mechanics in civil engineering,
- fluid mechanics and fluid-structure interaction,
- thermodynamics,
- biomechanics,
- heterogeneous media and multiscale problems,
- experimental methods in mechanics,

to create an opportunity for meeting, discussion and collaboration among the participants. As in the previous years, the three best papers presented at this conference were awarded the Czech Society for Mechanics Award for young researchers under 35 years of age.

To all conference participants, we offer the possibility to publish their peer-reviewed full papers in the international journal **Applied and Computational Mechanics** indexed by Scopus. This journal has been published by the University of West Bohemia since 2007 (see <http://www.kme.zcu.cz/acm/>).

We would like to express our gratitude to all the invited speakers for their significant contribution to the conference and the time and effort they put. Considerable acknowledgement belongs also to the members of the Organising Committee for their important work.

We strongly believe that all participants of the CM2017 enjoyed their stay in the beautiful nature of the Šumava region in a meaningful way. Finally, we would like to invite you all to come to the next conference CM2018.

Jan Vimmr
University of West Bohemia
Chairman of the Scientific
Committee

Vítězslav Adámek
University of West Bohemia
Chairman of the Organising
Committee

SCIENTIFIC COMMITTEE

Chairman:

Jan Vimmr

University of West Bohemia, Faculty of Applied Sciences, Czech Republic

Members:

Miroslav Balda

Research and Testing Institute Plzeň, Czech Republic

Jiří Burša

Brno University of Technology, Faculty of Mechanical Engineering, Czech Republic

Jan Dupal

University of West Bohemia, Faculty of Applied Sciences, Czech Republic

Václav Dvořák

Technical University of Liberec, Faculty of Mechanical Engineering, Czech Republic

Jiří Fůrst

Czech Technical University in Prague, Faculty of Mechanical Engineering, Czech Republic

Miroslav Holeček

University of West Bohemia, Czech Republic

Jaromír Horáček

Institute of Thermomechanics, Czech Academy of Sciences, Czech Republic

Michal Kotoul

Brno University of Technology, Faculty of Mechanical Engineering, Czech Republic

Jiří Křen

University of West Bohemia, Faculty of Applied Sciences, Czech Republic

Vladislav Laš

University of West Bohemia, Faculty of Applied Sciences, Czech Republic

Justín Murín

Slovak University of Technology in Bratislava, Faculty of Mechanical Engineering, Slovak Republic

Milan Naď

Slovak University of Technology in Bratislava, Faculty of Materials Science and Technology in Trnava, Slovak Republic

Jiří Náprstek

Institute of Theoretical and Applied Mechanics, Czech Academy of Sciences, Czech Republic

Miloslav Okrouhlík

Institute of Thermomechanics, Czech Academy of Sciences, Czech Republic

Luděk Pešek

Institute of Thermomechanics, Czech Academy of Sciences, Czech Republic

Jindřich Petruška

Brno University of Technology, Faculty of Mechanical Engineering, Czech Republic

Jiří Plešek

Institute of Thermomechanics, Czech Academy of Sciences, Czech Republic

František Pochylý

Brno University of Technology, Faculty of Mechanical Engineering, Czech Republic

Pavel Polach

Research and Testing Institute Plzeň, Czech Republic

Eduard Rohan

University of West Bohemia, Faculty of Applied Sciences, Czech Republic

Josef Rosenberg

University of West Bohemia, Faculty of Applied Sciences, Czech Republic

Milan Růžička

Czech Technical University in Prague, Faculty of Mechanical Engineering, Czech Republic

Milan Sága

University of Žilina, Faculty of Mechanical Engineering, Slovak Republic

Petr Sváček

Czech Technical University in Prague, Faculty of Mechanical Engineering, Czech Republic

Zbyněk Šika

Czech Technical University in Prague, Faculty of Mechanical Engineering, Czech Republic

Michael Valášek

Czech Technical University in Prague, Faculty of Mechanical Engineering, Czech Republic

Jaroslav Zapoměl

VŠB – Technical University of Ostrava, Faculty of Mechanical Engineering, Czech Republic

Vladimír Zeman

University of West Bohemia, Faculty of Applied Sciences, Czech Republic

Table of Contents

Baniari V., Vaško M., Kopas P.: <i>Design and computation of the crane attachment</i>	1
Bartošák M., Jurenka J., Kulíšek V., Růžička M., Doubrava K.: <i>Structural-acoustic analysis of air duct using FEM</i>	3
Bartošák M., Španiel M.: <i>FEM implementation of unified viscoplastic Chaboche model</i>	5
Beneš P., Krejza R., Hromčík M., Šika Z., Zavřel J.: <i>Control of flexible 2D mechanical structure by multiple planar piezoelectric patches</i>	7
Boušková V., Vychytil J.: <i>A virtual musculoskeletal model of hand and its application for PC-mouse development</i>	9
Brůha J., Zeman V.: <i>Modelling of turbine blades with tie-boss contacts</i>	11
Bublík O., Pecka A., Vimmr J.: <i>FlowPro – multipurpose CFD software written in Java</i>	13
Čečrdle J.: <i>Some special techniques for preparation of aeroelastic stick models</i>	15
Čekan M., Hučko B., Horvat F., Bachratý M., Čambal M.: <i>Measurement and optimization of the abdominal retractor end effectors</i>	17
Denk P., Šika Z., Steinbauer P., Macek J., Morkus J.: <i>Mathematical model of the Hybrid Electric Vehicle for driving consumption optimization</i>	19
Dlhý P., Novák P.: <i>Analysis of contact force along spherical roller bearing element</i>	21
Fischer C., Náprstek J.: <i>Numerical assessment of stability of the ball vibration absorber</i>	23
Fumfera J., Halama R., Kuželka J., Španiel M.: <i>Strain-range dependent cyclic plasticity material model calibration for the 08Ch18N10T steel</i>	25
Fürst J.: <i>Numerical simulation of flows over oscillating airfoil</i>	27
Fürst J., Musil J.: <i>Development of non-reflective boundary condition for free-surface flows</i>	29
Heczko J., Kottner R.: <i>Modelling of ageing and fatigue under large strains</i>	31
Hora P.: <i>The guided waves modelling: A spectral method approach</i>	33
Horák Z., Tichý P., Goldmann T., Vilímek M.: <i>FE analyses and experimental validation of heat distribution during hole drilling</i>	35
Hrouda A., Paur L.: <i>Experimental and numerical research of the structure made of geopolymer composite</i>	37
Hučko B., Bényi M., Jančo R., Musil M.: <i>Akaike information criterion and cartilage models</i>	39
Hynčík L., Bońkowski T., Vychytil J., Špička J.: <i>Motorcyclist barrier impact: A comparative study</i>	41
Jančo R., Élesztös P., Écsi L.: <i>Experimental and numerical solution of friction stir welding</i>	43
Janouchová E., Lepš M.: <i>Sensitivity analysis of laser drawing process of Mg tubes</i>	45

Karlíček J., Šika Z., Volech J.: <i>Active vibration suppression using collocated pair of piezo-patches</i>	47
Kašpárek M., Nováková L., Adamec J.: <i>Pressure relationship in the area of hemodialysis access when determining the blood flow rate through the vein using the dilution method</i>	49
Klesa J., Piksa Š.: <i>Method for the preliminary design of the fan propulsion system</i>	51
Kocáb J., Kottner R., Krystek J.: <i>Identification of material parameters of cork-rubber composite based on uniaxial and biaxial experiments</i>	53
Kottner R., Hrdlička V., Krystek J., Kaňáková S.: <i>Computational model of plastic shoulder protector</i>	55
Kouba J., Radnic T., Novotný J.: <i>Numerical simulation of thermomechanical phenomena and fluid flow inside a small chamber</i>	57
Kratochvíl A., Sommer T., Slavík S.: <i>Flutter analysis of 28m wingspan sailplane</i>	59
Kraus K., Hlaváček V., Beneš P., Šika Z.: <i>Optimization of a dynamic vibration absorber with multiple degrees of freedom</i>	61
Krejčová M., Holeček M.: <i>Myosin motor movement controlled by a potential barrier</i>	63
Kruisová A., Kolman R., Mračko M.: <i>Full dispersion analysis of the Newmark family in finite element method in elastodynamics</i>	65
Křen J., Lobovský L., Jansová M., Hartlová J., Salášek M.: <i>Biomechanics in clinical practice</i>	67
Kutiš V., Paulech J., Gálik G., Murín J.: <i>Thermohydraulic and structural analyses of VVER 440 components</i>	69
Kůrečka J., Habán V., Himr D.: <i>Acoustic modal analysis of water filled pipe</i>	71
Machovská I., Novotný J.: <i>Corrected Signal to noise ratio and Mutual information for accuracy determination in PIV</i>	73
Machů T., Pochylý F., Šulc J.: <i>Computational study of novel valveless piston pump for macro scale</i>	75
Medúna O., Hisem P.: <i>Stiffness analysis of the helmet</i>	77
Michálek T., Haupt L., Zelenka J., Kohout M., Liberová S.: <i>Modelling of effects of a locomotive three-axle bogie on track</i>	79
Mochar D., Trnka J., Valeš F., Chlada M., Červ J., Masák J., Gabriel D., Vtípil J.: <i>Experimental and finite element analysis of composite gun barrels</i>	81
Moravcová F., Lukeš V., Rohan E.: <i>Shape optimization of obstacles in incompressible viscous flow using OpenFOAM</i>	83
Mračko M., Tkachuk A., Kolman R., Plešek J., Gabriel D.: <i>Critical time step estimators in explicit dynamics</i>	85

Murín J., Aminbaghai M., Hrabovský J., Kutíš V.: <i>Non-uniform torsional modal analysis of thin walled FGM beams</i>	87
Náhlík L., Majer Z., Štegnarová K., Pokorný P., Bermejo R.: <i>Lifetime assessment of particulate ceramic composite with residual stresses</i>	89
Náprstek J., Fischer C.: <i>Stochastic stability of the generalized van der Pol system under random additive excitation</i>	91
Padovec Z., Sedláček R., Růžička P., Růžička M.: <i>Static and fatigue testing of composite external fixator</i>	93
Pecka A., Bublík O., Vimmr J.: <i>Validation of a fluid-structure interaction code based on the discontinuous Galerkin method</i>	95
Pečínka L., Svoboda J.: <i>Experimental verification of the friction and fretting wear coefficients for strong adhesion of two unlubricated surfaces</i>	97
Petríková I., Marvalová B.: <i>Experimental research and modelling of the response of magnetorheological elastomers to cyclic loading</i>	99
Poduška J., Hutař P., Kučera J., Arbeiter F., Frank A., Náhlík L.: <i>Asymmetry in CRB specimen and its influence on test results</i>	101
Polach P., Smolík L., Hartl M., Omasta M., Šperka P., Hajžman M.: <i>Computational and experimental investigation of rotor dynamics with fluid film instabilities</i>	103
Půst L., Pešek L., Byrtus M.: <i>Aero-elastic vibration of bladed turbine wheel</i>	105
Rendl J., Hajžman M., Menclová E.: <i>Suspension design and tire modelling of Formula SAE</i>	107
Repka M., Sládek V., Sládek J.: <i>The numerical studies of symmetric and non-symmetric strain gradient theory of elasticity</i>	109
Rohan E., Lukeš V.: <i>The computational homogenization for modelling of large deforming fluid saturated porous media</i>	111
Rohan E., Lukeš V.: <i>Towards smart porous piezoelectric materials</i>	113
Rosenberg J., Byrtus M.: <i>Time-reversibly thermostatic oscillators in the modelling of dynein</i>	115
Sátor L., Sládek V., Sládek J.: <i>Transient analysis of thin FGM plates with multi-gradation coupling effects</i>	117
Slávik O., Majer Z.: <i>Mutual interaction of multiple cracks growing in the particulate composite with brittle matrix under conditions of sub-critical crack growth</i>	119
Steinbauer P., Němec J.: <i>Modal testing as a tool for composite damage detection?</i>	121
Stojan R., Šika Z., Steinbauer P.: <i>Advanced control systems in vehicle flow simulations</i> .	123
Sváček P.: <i>On boundary conditions in problem of flow induced vibrations of human vocal folds model</i>	125
Šedlbauer D.: <i>Random heterogeneous materials: Wang tile size vs circular particle packing</i>	127

Šika Z., Bulín R., Zavřel J., Beneš P., Miletín J.: <i>Design and optimization of additional piezo-actuated platform of cable mechanism</i>	129
Špička J., Kander L.: <i>Application of the neural networks for evaluation of structural steel material properties based on small punch test results</i>	131
Špirk S.: <i>Simulations of explosions for improvements of passive safety</i>	133
Štorkán J., Vampola T.: <i>Numerical simulation of the human vocal fold vibration – reconstruction of videokymography records</i>	135
Šulka P., Sapietová A., Sapieta M.: <i>Analysis of processing vibration signal</i>	137
Tinoco H. A., Cardona C., Peña F., Gomez J., Roldan-Restrepo S.: <i>Identification of vibration modes in high frequency of a piezo-device with electromechanical impedance technique</i>	139
Tran Xuan T., Cirkl D.: <i>FEM model of pneumatic spring supported by a steel plate</i>	141
Turjanicová J., Rohan E., Lukeš V.: <i>Quasi-static model of ionic transport through deformable porous media</i>	143
Urban O., Rudolf P.: <i>Reduced order model of laminar Kármán vortex street</i>	145
Volech J., Šika Z., Kraus K., Beneš P.: <i>H-inf control of additional piezo-actuated platform of cable mechanism</i>	147
Voltr O., Jilek P.: <i>Influence of initial imperfections of changing amplitude on the laterally loaded cylindrical shell</i>	149
Winter O., Sváček P.: <i>Interaction of incompressible fluid flow and a vibrating airfoil</i>	151
Zapoměl J., Ferfecki P., Kozánek J., Jirsa M.: <i>Reducing energy losses in the supports of rotating machines by application of smart materials</i>	153
Zavřel J., Vampola T., Dušková-Smrčková M., Pawlik V.: <i>Modelling of the ball gel</i>	155
Zeman V., Hlaváč Z., Dyk Š.: <i>Modelling of the nuclear fuel assembly with impact interactions</i>	157
Zrůbek L., Kučerová A., Doškář M.: <i>Micromechanical quantities based on Wang tiles with local tilings</i>	159

Design and computation of the crane attachment

V. Baniari ^a, M. Vaško ^a, P. Kopas ^a

^a University of Žilina, Faculty of Mechanical Engineering, Department of Applied Mechanics,
 Univerzitná 1, 010 26 Žilina, Slovak Republic, vladislav.baniari@fstroj.uniza.sk

Technical solution refers to changeable crane attachment which is set first of all for crane works, e.g. raising, starting, giving the material on the given place and its transportation. It can be done in these kinds of works mainly in the constructions, but occasionally as well in the case when the activity of the crane attachment is required only just as the assistant activity. The crane works were, are and will be needed to be performed by the special constructed machines, so-called cranes. The second offered alternative is to use trucks with the crane superstructure, in other words “the knuckle boom cranes”. But using of these kinds of machines is expensive and difficult for the time and logistics. In addition, we cannot use the services of the cranes because of the boundaries of the place where they should operate.

The start of the modern construction machines helped to open up the alternative of their multifunctional putting and then we can use the simplified cranes machines for loaders, excavators and backhoeloaders by the form of additional machine. The simplified cranes additional machines offer the alternative of the boom extension and so they gain more attractive parameters which can the construction equipment during the craning work.

The authors are thinking about the new concept of construction with more alternatives of work but all with the same principle [2]. According to the introduced technical solution [3] the cranes additional machine consists of the coupler, the frame construction and moveable holder whose movement is secured by the hydraulic actuator.

The coupler is designed regardless on the shape and parameters because of the difference of the construction machines where should be connected and will be adapted by the parameters and shapes for the certain construction machine.

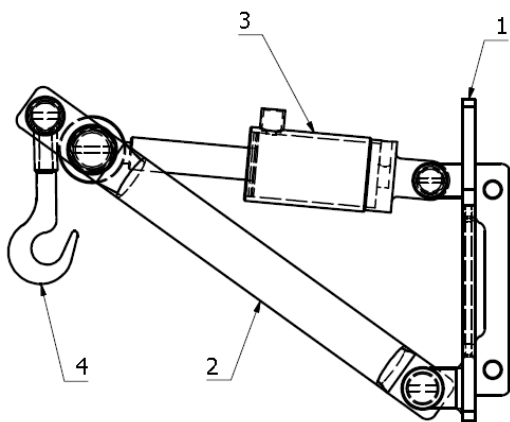


Fig. 1. Crane attachment, 1st variant

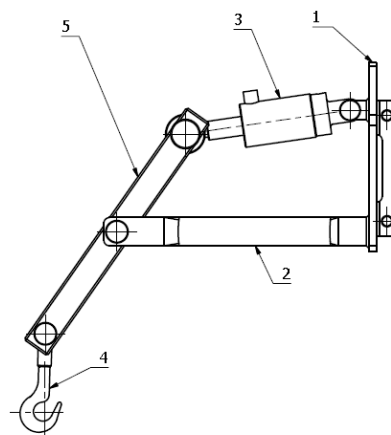


Fig. 2. Crane attachment, 2nd variant

On Fig. 1: The additional crane machine which consists of coupler (1) where in the down part through the pin joined connected two booms (2). In the purpose of movement through the pin joined the second ends of these booms (2) connected by the linear hydraulic actuator (3) and other pin joined joint with the upper part of the coupler (1). At the same time are the ends of the booms (2) connected with the pin joints with the hook (4).

On Fig. 2: The additional crane machine which consists of coupler (1), where in the down part through permanent joint by the fixed two booms (2). The second ends of these booms (2) are connected by the pin joints with the moveable lever (5) in its middle for the purpose of its movement. The moving lever (5) is on the one end also connected through linear hydraulic actuator (3) with another pin joint with the upper part of the coupler (1). At the same time is the second end of the moveable boom (5) connected with the pin joint and the hook (4).

The simulation of stress with FEM [1] helped to determine the first parameters of the construction. The boundary conditions contained the freight with weight multiplied by the measure of security. Consequently, there were chosen materials and profiles for the construction, modeled in CAD software and added by the normalized parts, like the pins, hydraulic actuator and hook.

Thanks to knowledge from the research of several projects and some practical experiences as well from one of the originator was this type of construction chosen the material with high Yield stress, the construction steal DOMEX. The whole additional crane holds the modern philosophy, so-called scalable construction. In this case there are imagined two variants, but during the research there was caused more alternative variants of additional crane which is working on the same principal.

Figs. 3 and 4 show simulations of the both variants for the 9 tons wheeled excavator with applied weight of 10 tons after multiplying by the safety factor.

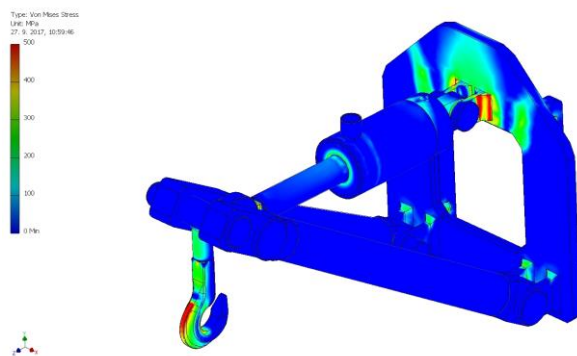


Fig. 3. FEM simulation of 1st variant

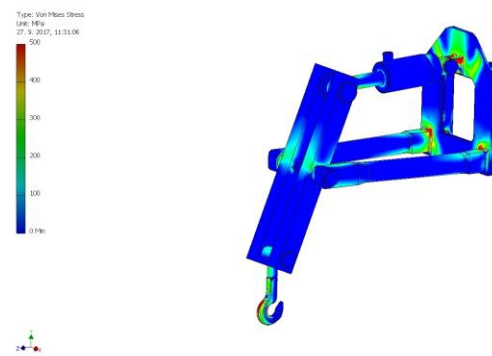


Fig. 4. FEM simulation of 2nd variant

Acknowledgement

This work was supported by the Slovak Research and Development Agency under the contract No. K-17-001-00.

References

- [1] Bathe, K. J., Finite element procedures, Prentice Hall, 1996.
- [2] Sága, M., Kopas, P., Vaško, M., Some computational aspects of vehicle shell frames optimization subjected to fatigue life, Communications 12 (4) (2010) 73-79.
- [3] Utility Model 7786, [online] <https://wbr.indprop.gov.sk/WebRegistre/UzitkovyVzor/Detail/50070-2016>

Structural-acoustic analysis of air duct using FEM

M. Bartošák, J. Jurenka, V. Kulíšek, M. Růžička, K. Doubrava

Faculty of Mechanical Engineering, CTU in Prague, Technická 4, 166 07, Czech Republic

Tone noise radiated through the inlet of a turbofan is generated mainly by rotor and stator interactions at subsonic regimes and by the shock waves generation at transonic fan tip speeds. The generated noise may reach very high sound pressure level and ultimately it can lead to a fatigue failure of air inlet duct.

In this study structural-acoustic analysis of the aircraft duct is presented. The acoustic pressure field of the ducted air is determined by finite element method using the boundary condition of acoustic pressure in the rotor cross-section [2], which is determined on the basis of the analytical equations [4, 3] and [5]. A structural-acoustic analysis of the composite air duct is solved as fully coupled and also as sequentially coupled. On the basis of the structural-acoustic finite element analysis, stress and strains histories of the duct walls are determined.

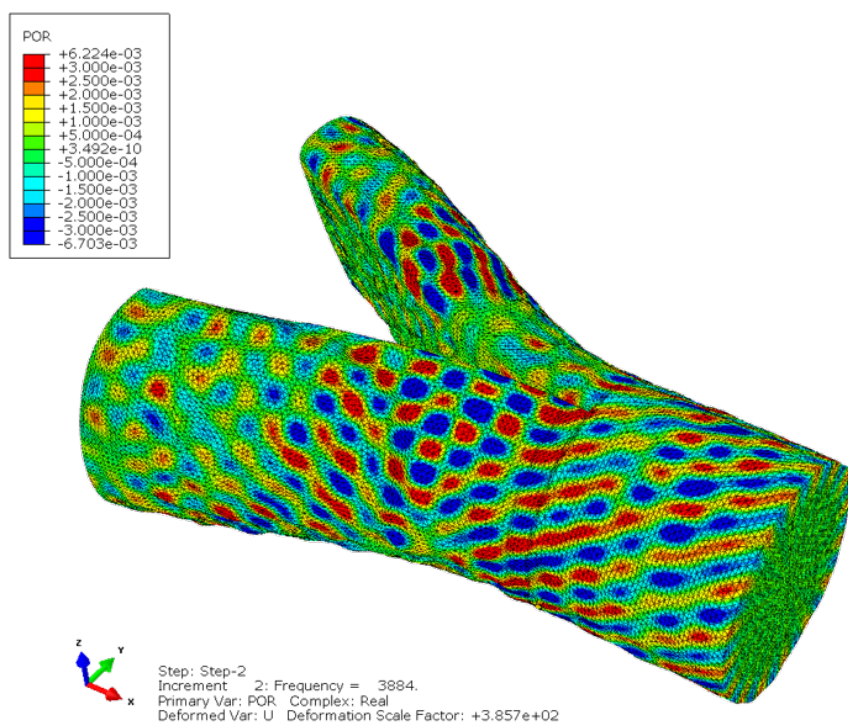


Fig. 1. Steady-state response at the first blade passing frequency – pressure (real) field for the acoustic part of model

The FE analysis are solved in the frequency and time domains. Direct, steady-state dynamics procedure [1] is used for determining frequency dependent response of the numerical

model. In the time domain, response is evaluated by an implicit method. Selected results for the fully-coupled analysis are presented in Figs. 1 and 2.

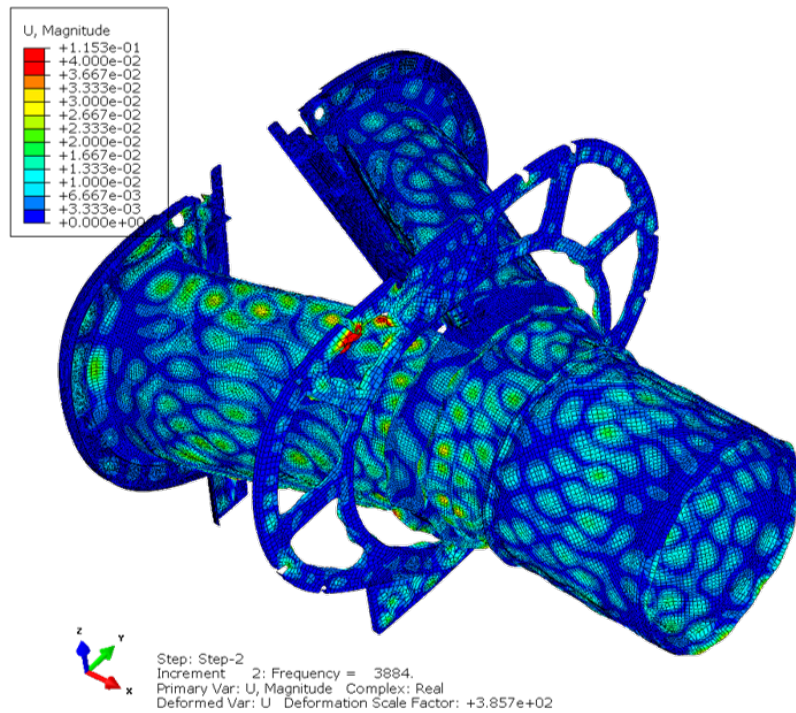


Fig. 2. Steady-state response at the first blade passing frequency – displacement (real) field for the mechanical part of model

Future plans are as follows. On the basis of the experiment, damping will be added for the both parts of the model, i.e. acoustic and mechanical. Finally, damage will be assessed for the composite air duct and design changes will be proposed.

Acknowledgements

The authors would like to acknowledge the support from the Technology Agency of the Czech Republic, grant No. TE02000032.

References

- [1] Abaqus Users Manual, Abaqus Version 6.14 Documentation, Dassault Systems Simulia Corporation, 2011.
- [2] Bartošák, M., Jurenka, J., Růžička, M., Doubrava, K., Calculation of the sound power in the inlet of the aero-engine based on the analytical prediction, Proceedings of the 32nd conference with international participation Computational Mechanics 2016 – Book of Extended Abstracts, Pilsen, University of West Bohemia, 2016.
- [3] Kurosaka, M., A note on multiple pure tone noise, Journal of Sound and Vibration 19 (4) (1971) 453–462.
- [4] Lewy, S., Polacsek, C., Barrier, R., Analytical and numerical prediction of harmonic sound power in the inlet of aero-engines with emphasis on transonic rotation speeds, Journal of Sound and Vibration 333 (26) (2014) 7165–7182.
- [5] Rienstra, S. W., Hirschberg, A., An introduction to acoustics, Eindhoven University of Technology, 2004.

FEM implementation of unified viscoplastic Chaboche model

M. Bartošák, M. Španiel

Faculty of Mechanical Engineering, CTU in Prague, Technická 4, 166 07, Czech Republic

A whole range of industrial components (internal combustion engines, turbochargers, turbines, turbine discs etc.) is subjected to a thermo-mechanical loading cycles. Inhomogeneous temperature distribution and boundary conditions of a component usually constrain thermal expansion, resulting in restricted inelastic strains. Together with additional mechanical loads leading to a component failure. This is termed as a thermo-mechanical fatigue. A cyclic viscoplastic material behaviour is characteristic for these components. An accurate damage assessment of components subjected to a thermo-mechanical fatigue depends on the selected constitutive model used for the numerical modelling of stress-strain response during a cyclic thermo-mechanical loading.

The implementation of a viscoplastic Chaboche type material model in the framework of the finite element method (FEM) is presented in this paper. The multiaxial version of unified temperature-dependent viscoplastic Chaboche model [3] is implemented as a user-defined material subroutine for commercial finite element software Abaqus [1]. Only one inelastic strain is presented in the model, Fig. 1, creep and plasticity are coupled together, resulting in a better description of cyclic stress-strain behaviour for metals compared to uncoupled material models. Unified viscoplastic Chaboche model is widely accepted and commonly used for a deformation modelling, e.g. [5] and [2], but it is not implemented in FE commercial software packages like Abaqus and Ansys, only its rate-independent (elastic-plastic) form is available.

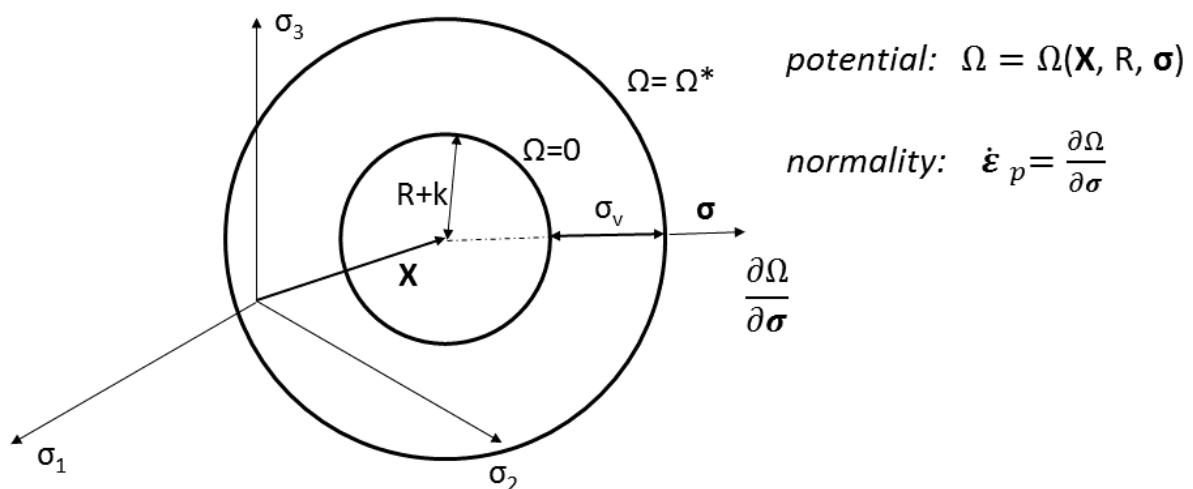


Fig. 1. Viscoplasticity equations and normality rule

Based on the implicit (backward) Euler method, the elastic predictor and viscoplastic corrector methodology is used, constitutive equations are solved in the local Newton iterative method [4]. The material model is implemented together with the consistent tangent operator, which is derived completely for the first time, ensuring quadratic convergence of the global Newton scheme.

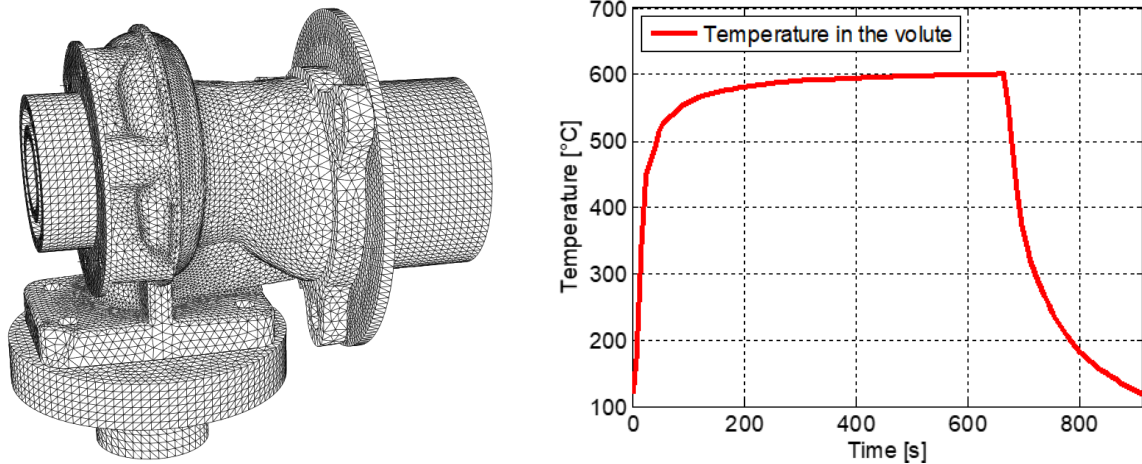


Fig. 2. Finite element model of the turbocharger turbine housing assembly (left); temperature history in the volute of turbocharger turbine housing (right)

The implemented material model is used for a deformation modelling of the thermo-mechanically loaded turbocharger turbine housing, Fig. 2. Consequently, based on the simulated material response, a thermo-mechanical fatigue damage is predicted for the component.

Acknowledgement

This publication is under the Center of Advanced Aerospace Technologies, reg. No. CZ.02.1.01 / 0.0 / 0.0 / 16_019 / 0000826, which is co-financed by the European Regional Development Fund through the Operational Programme Research, Development and Education.

References

- [1] Abaqus Users Manual, Abaqus Version 6.14 Documentation, Dassault Systems Simulia Corporation, 2011.
- [2] Barrett, R. A., ODonoghue, P. E., Leen, S. B., An improved unified viscoplastic constitutive model for strain-rate sensitivity in high temperature fatigue, *International Journal of Fatigue* 48 (2013) 192–204.
- [3] Chaboche, J. L., A review of some plasticity and viscoplasticity constitutive theories, *International Journal of Plasticity* 24 (10) (2008) 1642–1693.
- [4] Dunne, F., Petrinic, N., *Introduction to computational plasticity*, Oxford University Press, 2005.
- [5] Kullig, E., Wippler, S., Numerical integration and FEM-implementation of a viscoplastic Chaboche-model with static recovery, *Computational Mechanics* 38 (6) (2006) 1–13.

Control of flexible 2D mechanical structure by multiple planar piezoelectric patches

P. Beneš^a, R. Krejza^a, M. Hromčík^b, Z. Šika^a, J. Zavřel^a

^a Faculty of Mechanical Engineering, CTU in Prague, Technická 4, 166 07 Praha 6, Czech Republic

^b Faculty of Electrical Engineering, CTU in Prague, Technická 2, 166 27 Praha 6, Czech Republic

One of goals in new and upcoming hi-tech projects e.g. in automotive or aerospace industry is usually the weight reduction, very often based on usage of new lightweight materials. The problem of this approach is usually low mechanical damping of components resulting in unwanted vibration and acoustic discomfort. The traditional passive mechanic solution in the form of additional masses is not applicable as it is in conflict with the mentioned primary goal. On the other hand, the usage of active elements incorporated in the structure should be considered because they could be lighter than the passive ones and achieve significantly better results. The aim of this paper is to investigate the concept of modeling and control of 2D mechanical structure with multiple planar piezoelectric patches. Patches are used for both actuating and sensing. The efficiency of the global controller is compared with the strategy of many local controllers.

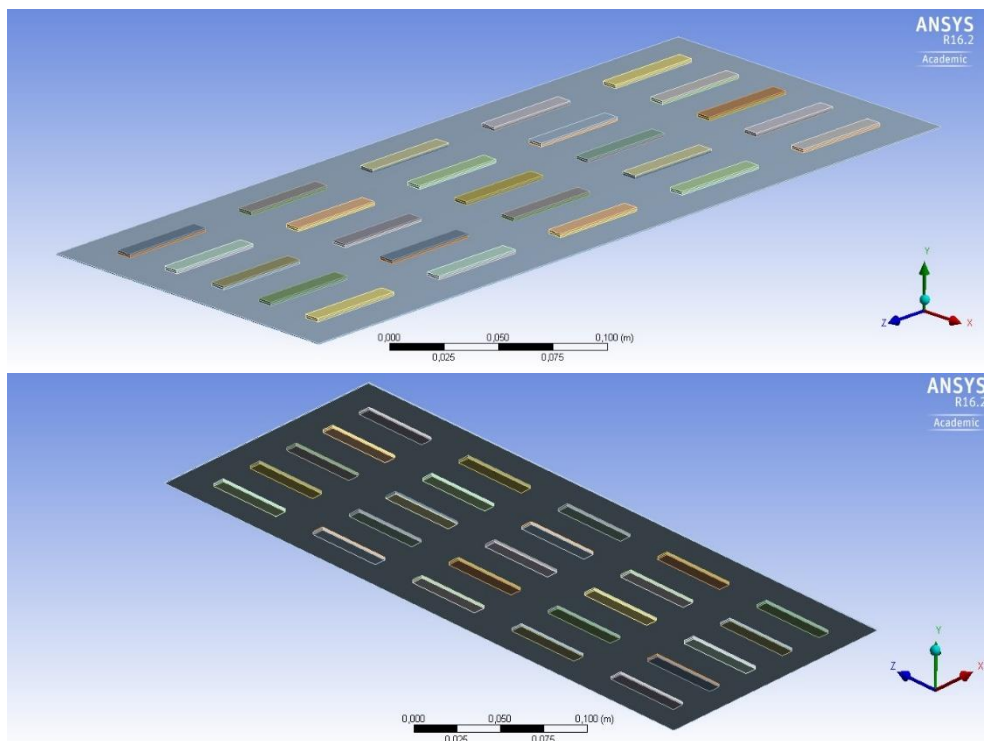


Fig. 1. Plate with piezoelectric patches – top/bottom view

The simulation model (Fig. 1) is a rectangular metal plate with 25 uniformly distributed pairs of collocated piezoelectric patches [4], [2]. Patches on the top of the plate are actuators,

patches on the bottom side act as sensors. The finite element model was prepared in the program ANSYS. The coupled piezoelectric FE formulation is described in terms of nodal quantities

$$\begin{bmatrix} \mathbf{M}_{UU} & \mathbf{0} \\ \mathbf{0} & \mathbf{0} \end{bmatrix} \begin{bmatrix} \ddot{\mathbf{U}} \\ \ddot{\mathbf{V}} \end{bmatrix} + \begin{bmatrix} \mathbf{C}_{UU} & \mathbf{0} \\ \mathbf{0} & \mathbf{0} \end{bmatrix} \begin{bmatrix} \dot{\mathbf{U}} \\ \dot{\mathbf{V}} \end{bmatrix} + \begin{bmatrix} \mathbf{K}_{UU} & \mathbf{K}_{UV} \\ \mathbf{K}_{UV}^T & -\mathbf{K}_{VV} \end{bmatrix} \begin{bmatrix} \mathbf{U} \\ \mathbf{V} \end{bmatrix} = \begin{bmatrix} \mathbf{F} \\ \mathbf{L} \end{bmatrix}, \quad (1)$$

where \mathbf{M}_{UU} is the mass matrix, \mathbf{C}_{UU} is the structural damping matrix, \mathbf{K}_{UU} is the mechanical stiffness matrix, \mathbf{K}_{UV} is the piezoelectric stiffness matrix, \mathbf{K}_{VV} is the dielectric stiffness matrix, \mathbf{U} is the vector of nodal displacements, \mathbf{V} is the vector of electrical potentials, \mathbf{F} and \mathbf{L} are vectors of mechanical forces and charges.

The matrices were exported from ANSYS in the form of sparse matrices in Harwel-Boeing format and processed in MATLAB. The modal reduction was performed with respect to the first 20 eigenmodes.

Two control strategies were used for simulations. The first one is the strategy of one global controller and the second one is the strategy of many local controllers. Based on previous experiments [3] the different numbers and combinations of active elements were tested.

Generally, experiments have confirmed that the higher number of active elements means better control of damping properties and increasing power consumption. In case that active elements are not distributed or tuned uniformly and therefore some areas are more influenced than the others, the system can be tuned specifically for considered excitation. The performance and the stability could be further increased using the optimization of pole placement [1].

There is still large area for ongoing research focused on optimization of the placing of active elements. Our model is more or less capable to simulate optimized position of active elements by defining which of them are really activated, however they are still part of the regular grid and we can only switch between them and not continuously tune their position.

It has been proven that the described procedure is capable to significantly increase damping properties of the mechanical structure. The strategy of modeling structures with piezoelectric elements in ANSYS and their export in matrix form to MATLAB for further processing has been proven as well.

Acknowledgements

The work has been supported by the Czech Science Foundation project GA16-21961S - Mechatronic structures with heavily distributed actuators and sensors.

References

- [1] Beneš, P., Šika, Z., Hromčík, M., Krejza, R., Cloth-like Structures with Distributed Active Damping, Proceedings of the 8th ECCOMAS Thematic Conference on Multibody Dynamics, Prague, 2017.
- [2] Gawronski, W.K., Advanced Structural Dynamics and Active Control of Structures, Springer-Verlag New York, Inc., 2004.
- [3] Hromčík, M., Šika, Z., Beneš, P., Zavřel, J., Volech, J., Hušek, P., Low-complexity control laws for active damping of smart structures with heavily distributed actuators and sensors, Bulletin of Applied Mechanics, 12 (38) (2016) 1-6.
- [4] Preumont, A., Vibration Control of Active Structures An Introduction, 2nd Edition, Solid Mechanics and its Application, Volume 96, Kluwer Academic Publishers, 2002.

A virtual musculoskeletal model of hand and its application for PC-mouse development

V. Boušková^a, J. Vychytil^a

^a*New Technologies – Research centre, Univerziti 8, 306 14 Plzeň, Czech Republic*

Due to the long-term everyday work with a PC-mouse, pain in hand is a medical problem. Therefore this research is focused on this problem of population. For this work a virtual model of hand was developed.

The model of hand is created in Anybody Modeling System. It is based on real mass distribution of bones, on muscles and real shapes and sizes of bones obtained from measurements of The Visible Human Project (VHP) [1]. There are 26 bones, which means 19 bones for fingers and 7 bones of wrist. They are connected with joints, main muscles, tendons and ligaments, where places of their insertions and positions are based on real anatomy [2].

In our approach, a correct position of muscles, tendons and ligaments is kept by obstacles. These are artificial objects with a smooth surface such as balls and ellipsoids that are connected to bones. In the model, muscles are crossing over these obstacles. In contrast to the so-called via-point method, the obstacle approach ensures smooth shape of muscles that are not penetrating other objects. That is, more realistic representation of musculoskeletal system is obtained.

A research of PC- mice was made and focused on their consequences on our health. From lots of publications it was clear, that the main problem is in carpal tunnel, muscles, tendons and ligaments [3].

At first, two mice were made from clay. The aim was to design the mice as ergonomic and comfortable as possible. One of them was designed with supination angle 0° and the second with 25° [4]. Then they were created in designer program Rhinoceros and cut from polystyrene. Models made from polystyrene had to be varnished to avoid crumbling. All these kinds of models are depicted in Fig. 1.

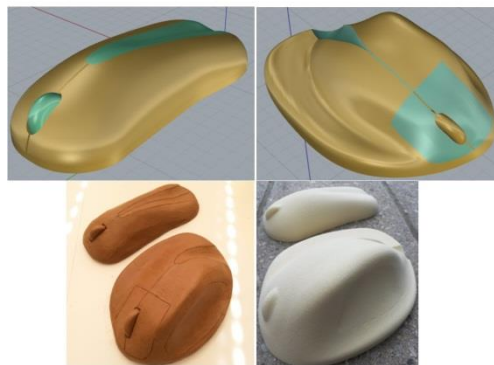


Fig. 1. Kinds of mice models – top – model in Rhinoceros designer program
 – bottom left – models from clay
 – bottom right – models from polystyrene.

Model of mice from polystyrene were ideal for measurement of real movements during work with PC, because this material is very light. Data of real movements, such as left-clicking, right-clicking, move with wheel etc., were measured by Vicon system.

After that one of these movements was imported to model of hand. Conditions, kinematic and inverse dynamic were solved after the optimization process that is necessary to run the model.

Now, the simulation of this model reconstructs the real motion data measured by Vicon system during a work with computer. This model with real data is in Fig. 2.

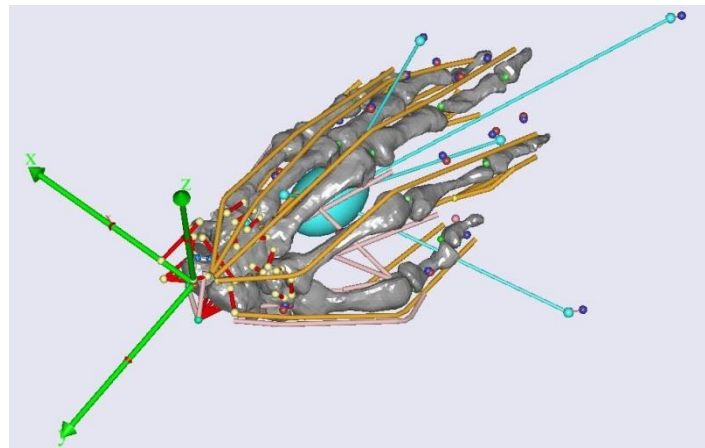


Fig. 2. Whole model of hand with imported data from Vicon System

Using this model it is possible to compare maximal force and tension in every muscle, tendon or ligament and maximal reaction forces in joints and come to the conclusion which of these prototypes of mice is better.

Currently, the model of hand in Anybody Modeling repository is only one rigid body without fingers. Therefore, our model of hand could be connected with the whole musculoskeletal model of human body that is implemented in Anybody Modeling System.

Acknowledgements

The work has been supported by the project SGS-2016-059.

References

- [1] Boušková, V., Virtual musculoskeletal model of hand, Bachelor thesis, University of West Bohemia, Pilsen, 2016. (in Czech)
- [2] Čihák, R., Anatomy 1, 3rd editon, M. Grim, O. Fejfar (eds.), Grada, Praha, 2011.
- [3] Schmid, A. B., Kubler, P. A., Johnston, V., Coppieters, M. W., A vertical mouse and ergonomic mouse pads alter wrist position but do not reduce carpal tunnel pressure in patients with carpal tunnel syndrome, *Applied Ergonomics* 47 (2015) 151-156.
- [4] HandShoe Mouse [online]. [cit. 2017-06-16]. Available at: <http://handshoemouse.com/>

Modelling of turbine blades with tie-boss contacts

J. Brůha ^a, V. Zeman ^a

^a *European Centre of Excellence NTIS – New Technologies for the Information Society, Faculty of Applied Sciences, University of West Bohemia, Univerzitní 8, 306 14 Plzeň, Czech Republic*

Vibration of the blades as a side effect of running steam turbines can be very dangerous. If a blade receives an excitation, usually from an aerodynamic source, at a frequency close to one of the natural frequencies, large amplitudes and high vibratory stresses can result [5, 9]. Failure, as a consequence of high-frequency fatigue, can then be rapid. Thus, various friction effects in blade couplings can be advantageously used as a source of passive damping [5-8]. The contribution is concerned with computational modelling of turbine blades with inter-blade couplings realised by tie-boss contact parts working as vibration damping mechanisms.

The blades, which are considered to be clamped into a rotating rigid disk, are modelled by means of the finite element method using Rayleigh beam elements with six degrees of freedom in each of nodes (see Fig. 1) [1-3]. The tie bosses, also known as integral snubbers, are partially considered to be rigid. The modelling of interactions at the contact surfaces is carried out using a frictional contact model with constant normal contact stiffness [2, 4]. The considered dry friction characteristic is smooth and includes the micro- and macro-slip phases [2].

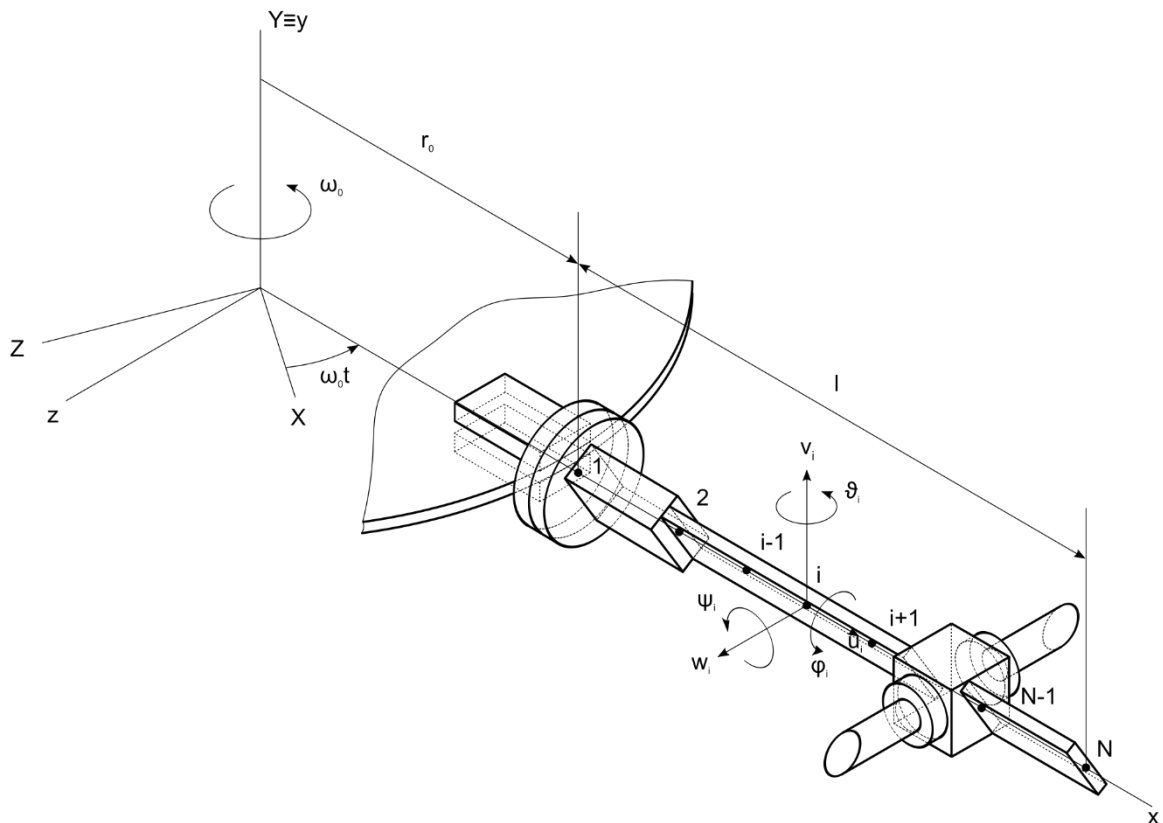


Fig. 1. Rotating turbine blade with a tie boss

The developed in-house code in MATLAB computing environment is capable to analyse modal properties, including visualizing corresponding mode shapes, as well as forced response of the blades.

Acknowledgements

This work was supported by the project GACR 16-04546S “Aero-elastic couplings and dynamic behaviour of rotational periodic bodies” of the Czech Science Foundation.

References

- [1] Brůha, J., Rycheký, D., Modelling of rotating twisted blades as 1D continuum, *Applied Mechanics and Materials* 821 (2016) 183-190.
- [2] Brůha, J., Zeman, V., Dynamic properties of a turbine blade couple: Analysis of the contact force effects, *Proceedings of the 32nd conference with international participation Computational Mechanics 2016*, Špičák, University of West Bohemia, 2016.
- [3] Brůha, J., Zeman, V., Numerical analysis of the modal properties of a shrouded turbine blading, *Proceedings of the 22nd international conference Engineering Mechanics 2016*, Svatka, Institute of Thermomechanics AS CR, Prague, 2016, pp. 94-97.
- [4] Hajžman, M., Byrtus, M., Zeman, V., Solution of the mutual contact in the finite element analysis of twisted blades, *Proceedings of the Colloquium Dynamics of Machines 2012*, Prague, 2012, pp. 51-58.
- [5] Pešek, L., Hajžman, M., Půst, L., Zeman, V., Byrtus, M., Brůha, J., Experimental and numerical investigation of friction element dissipative effects in blade shrouding, *Nonlinear Dynamics* 79 (3) (2015) 1711-1726.
- [6] Pešek, L., Půst, L., Bula, V., Cibulka, J., Numerical analysis of dry friction damping effects of tie-boss couplings on three blade bundle, *Proceedings of the ASME 2017 International Design Engineering Technical Conferences and Computers and Information in Engineering Conference*, Cleveland, 2017.
- [7] Petrov, E. P., Analysis of sensitivity and robustness of forced response for nonlinear dynamic structures, *Mechanical Systems and Signal Processing* 23 (2009) 68-86.
- [8] Sextro, W., *Dynamic contact problems with friction*, Springer, Berlin, Heidelberg, 2007.
- [9] Wilson, D. G., Korakianitis, T., *The design of high-efficiency turbomachinery and gas turbines*, Prentice-Hall, New Jersey, 1998.

FlowPro - multipurpose CFD software written in Java

O. Bublík^a, A. Pecka^b, J. Vimmr^a

^aNTIS, Faculty of Applied Sciences, University of West Bohemia, Univerzitní 8, 306 14 Plzeň, Czech Republic

^bDepartment of Mechanics, Faculty of Applied Sciences, University of West Bohemia, Univerzitní 8, 306 14 Plzeň, Czech Republic

This contribution introduces FlowPro - a multipurpose numerical software developed by the authors of this paper. FlowPro was initially designed for complex fluid flow simulations, such as fluid-structure interaction or aerofoil optimisation and for complicated geometries such as vibrating blades in a steam turbine. The current version of the numerical software is capable of solving a wide range of hyperbolic-parabolic non-linear systems of partial differential equations in one, two or three spatial dimensions, for example the system of Euler equations, Navier-Stokes equations, shallow water equations or equations of ideal magnetohydrodynamics. Fig. 1 illustrates the computational capability of FlowPro on a couple of simple examples. The examples are namely the 3D air flow around the MIG15 aircraft, Karman vortex street, magnetohydrodynamic rotor and acoustic wave in solid excited by a vibrating boundary, which are respectively described by the Euler equations, Navier-Stokes equations, equations of ideal magnetohydrodynamics and acoustic wave equation. FlowPro has been validated on various fluid flow benchmark, see for instance the validation of fluid-structure interaction [2].

The programming code has been and is still being developed in the Java programming language. This makes the product portable among computers with various hardware setups and operating system. The numerical software is equipped with the MATLAB/Python interface, which contains scripts necessary for pre- and post-processing. During pre-processing a user defines the geometry for the problem in graphical interface, the mesh is then generated automatically, finally the user sets the physical and numerical parameters. The physical parameters include the initial and boundary conditions and parameters for the mathematical model and the numerical parameters include the terminal condition, order of accuracy, artificial damping parameter, etc. Post-processing is just the data processing and visualisation.

A very attractive feature available for users of FlowPro is the possibility to create a mathematical model which was not yet implemented in FlowPro using the FlowPro API. This way a user of FlowPro can quickly develop new or modify existing mathematical models. Another advantage of FlowPro is an easy automatisation of computations in the MATLAB/Python interface. It is extremely useful for problems where many similar computations are desired, for instance, for a study of influence of one or several parameters on a variable of interest.

The FlowPro uses the discontinuous Galerkin method [3, 5] for spatial discretization, which was derived in our previous works [1, 4, 6]. The discontinuous Galerkin method leads to an algorithm which is capable of solving problems with a high order of spatial accuracy. For the temporal discretisation the BDF scheme is used [1], which is a family of unconditionally stable implicit methods of various order of accuracy. This choice allows to select relatively large time steps, which may drastically decrease the time of computation. FlowPro is capable of parallel computing and so it can exploit all CPUs and cores of the computer. Moreover, it has a regime in which the computation is distributed onto computers which are either connected in a local area network or to the internet [6].

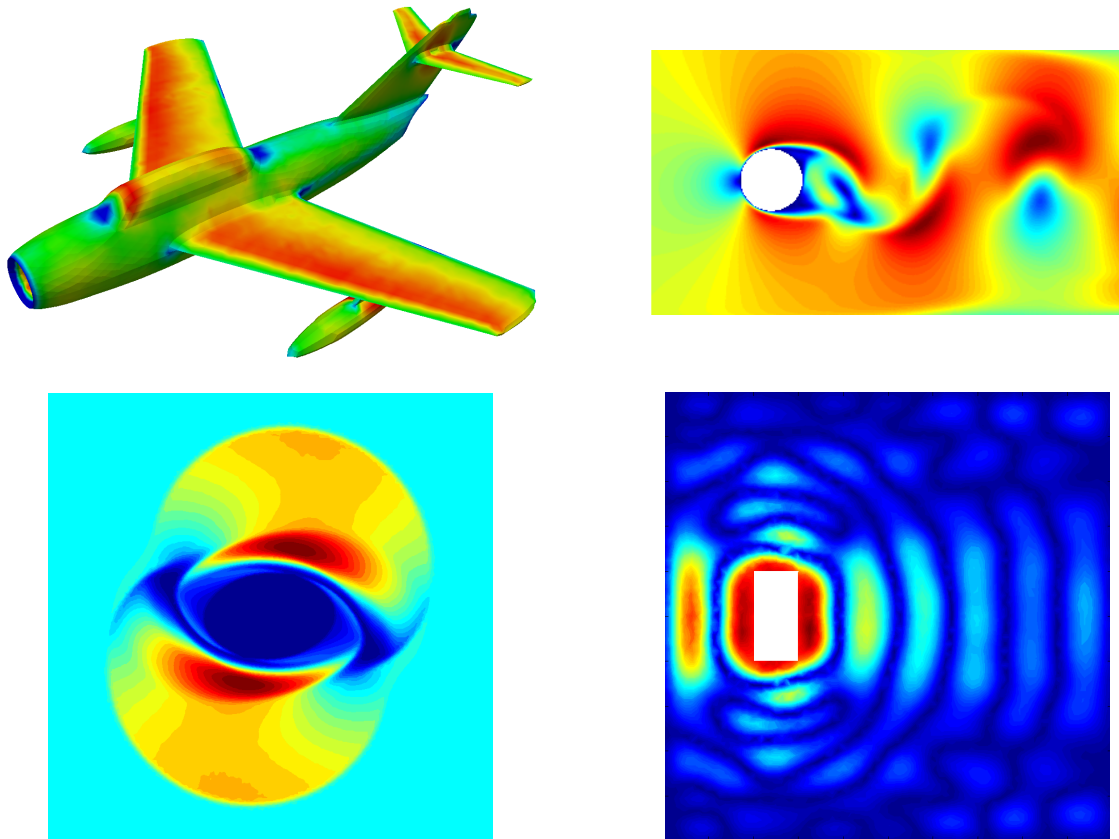


Fig. 1. Example simulations performed by FlowPro - the Mach number on the surface of the MIG15 aircraft (*top left*), the Mach number distribution of Karman vortex street (*top right*), magnetic pressure of magnetohydrodynamic rotor (*bottom left*) and acoustic displacement in solid (*bottom right*)

Acknowledgements

The authors appreciate the kind support by the project LO1506 of the Czech Ministry of Education, Youth and Sports and by the internal student grant projects SGS-2016-038 of the University of West Bohemia.

References

- [1] Bublík, O., Vimmr, J., Jonášová, A., Comparison of discontinuous Galerkin time integration schemes for the solution of flow problems with deformable domains, *Applied Mathematics and Computation* 267 (2015) 329–340.
- [2] Bublík, O., Vimmr, J., Pecka, A., Validation of a fluid-structure interaction code based on the discontinuous Galerkin method, *Proceedings of the 33th conference with international participation Computational Mechanics 2017*, University of West Bohemia, Plzeň, 2017.
- [3] Cockburn, B., Shu, C.-W., Runge-Kutta discontinuous Galerkin methods for convection-dominated problems, *Journal of Scientific Computing* 16 (3) (2001) 173–261.
- [4] Prausová, H., Bublík, O., Vimmr, J., Luxa, M., Hála, J., Clearance gap flow: Simulations by discontinuous Galerkin method and experiments, *EJP Web of Conferences* 92 (2015) No. 02073.
- [5] Reed, W. H., Hill, T. R., *Triangular mesh methods for the neutron transport equation*, Los Alamos Scientific Laboratory Report LA-UR-73-479, 1973.
- [6] Vimmr, J., Bublík, O., Pecka, A., A parallel implementation of an implicit discontinuous Galerkin finite element scheme for fluid flow problems, *Advances in Engineering Software* 113 (2017) 108–119.

Some special techniques for preparation of aeroelastic stick models

J. Čečrdle^a

^a VZLU – Czech Aerospace Research Centre, Beranových 130, 199 05 Praha - Letňany, Czech Republic

Aeroelastic analyses of aircraft structures are usually performed using simple dynamic structural models (stick models). Stiffness characteristics of aircraft structural parts are modelled by means of massless beam elements, and inertial characteristics are modelled by concentrated mass elements with appropriate moments of inertia. Models also include spring elements, various conditions, multi-point constraints and auxiliary elements (controls suspension, visualization, etc.). Stick models are simple, effectively usable and suitable for variation of parameters or for updating according experimental results. Considering the conventional aircraft structure with high or middle aspect ratio wing, stick model schematisation is sufficiently accurate; and therefore, is ordinarily used. However, in some specific cases, special elements or modelling patterns must be used. This paper is focused on the description of the following modelling techniques:

Model of Control Surface or Tab without Stiffness Parameters. Control surfaces and tabs are usually modelled with the stiffness parameters allowing simulating a control surface or tab deformation modes. However, provided no stiffness data of control surface or tab structure are available, modelling without stiffness must be applied. In this case, control surface (tab) is, in fact, rigid body with a single degree-of-freedom (flapping mode) and it does not add any stiffness to the system and its deformation follows the deformation of a main surface.

Control surface suspension points at the rotation axis are connected to the main surface using multi-point constrains. Control surface is divided into the spanwise segments in order to obtain a smooth deformation. Nodes on the rotation axis are connected using a rigid body element for the rotational degree-of-freedom around the rotation axis with the actuation point. In addition, each node is connected to the neighbouring suspension points using an interpolation constraint element. The dependent degrees-of-freedom are represented by the remaining five degrees-of-freedom while the independent degrees-of-freedom are represented by all six ones. The coefficients of interpolation are proportional to the distance of a node and a particular suspension point.

Common symmetric and antisymmetric model for control surface and tab flapping modes. In the most cases, half-span models with either symmetric or antisymmetric boundary condition are used for aeroelastic calculations. Half-span models can cover also the cases of a small unsymmetries using the specifications of both port and starboard side. However, the noticeably unsymmetrical cases as well as some specific issues must be analysed using a full-span model. In this case, both symmetric and antisymmetric vibrations of control surface and tab flapping must be modelled. The following paragraphs describe the technique for ailerons and elevator. Note, that modelling of conventional rudder flapping shows no difference compare to half-span models.

Ailerons with a single side tab. Considering the fixed stick condition, ailerons are vibrating antisymmetrically with the lower frequency as the complete control system is

involved in this mode and symmetrically with the higher frequency, because only a part of the control system is involved in this mode. Tab is considered at a single side only as is typical for smaller aircraft. Actuation system is modelled using a single grounded spring element and a pair of rod elements oriented according the rotation axis. Rods connect the actuation points of both left and right aileron. Grounded spring is connected to the middle node at the plane of symmetry. The system includes only a single degree-of-freedom; remaining ones are omitted from the analysis or constrained by rigid body elements. In order to obtain the antisymmetric vibrations at the lower frequency, a multi-point constrain changing the sign of rotational deformation is included on a single side. Spring constant of the grounded spring element (K_{δ}) and the torsional stiffness of rod elements (GI_k) determine natural frequencies of both modes. Spring constant is decisive for the antisymmetric one while rod torsional stiffness is decisive for the symmetric one. Note, that there is also cross-influence; and therefore, both parameters must be used as a pair to set both frequencies. Tab is included on a single side only and the actuation is realised using a rotational spring element and the frequency is determined by the spring constant ($K_{\delta 2}$) as usual for half-span models. The system includes three degrees-of-freedom in total.

Elevator with a tab on both sides. Considering the fixed stick condition, elevator vibrates symmetrically with the lower frequency as the complete control system is involved in this mode and antisymmetrically with the higher frequency, because only a connection of both sides of elevator is involved in this mode. Tab is considered on both sides of elevator. Actuation of both elevator and tab is realised in the same manner as described for ailerons (excluding the multi-point constrain changing the sign of rotational deformation). The system includes four degrees-of-freedom in total.

Common symmetric and antisymmetric model for twin-engine aircraft engine vibration modes. Considering a twin wing-mounted engine aircraft, symmetric and antisymmetric vibrations of engines must also be modelled on a full-span model [1, 2]. Described pattern allows modelling of pitch and yaw, symmetric and antisymmetric engine vibrations. Modes have diverse frequencies and diverse node point stations. The typical mode order by frequency is: 1) Symmetric pitch, 2) Antisymmetric pitch, 3) Symmetric yaw and, 4) Antisymmetric yaw. The node points are typically stationed from the rear to the front in the order: 1) Symmetric pitch, 2) Symmetric yaw, 3) Antisymmetric pitch and, 4) Antisymmetric yaw. Each engine vibration mode is modelled using a pair of grid points placed at the node station. The appropriate degree-of-freedom, i.e. pitch or yaw rotation, of a symmetric mode is connected to a grounded spring element, while the one of antisymmetric mode is connected to a system of two rod elements, which are oriented in the appropriate direction. These elements are placed at the station of the node point of the appropriate mode. Also, grounded spring is connected to the middle point of rod elements. The remaining degrees-of-freedom are constrained using rigid body elements. Systems for pitch and for yaw modes of two degrees-of-freedom each are separate.

References

- [1] Čečrdle, J., Application of whirl flutter optimization-based solution to full-span model of twin turboprop aircraft, Proceedings of the 7th European Congress on Computational Methods in Applied Sciences and Engineering, Crete, Greece, 2016, Vol II, pp. 3293-3309.
- [2] Čečrdle, J., Updating of finite element model of aircraft structure according results of ground vibration test, Proceedings of the Institution of Mechanical Engineers, Part G: Journal of Aerospace Engineering, 230 (7) (2016) 1348-1356.

Measurement and optimization of the abdominal retractor end effectors

M. Čekan ^a, B. Hučko ^a, F. Horvat ^a, M. Bachraty ^a, M. Čambal ^b

^a Faculty of Mechanical Engineering, Slovak University of Technology in Bratislava, Nam. Slobody 17, 812 31 Bratislava, Slovakia

^b 1st Surgery Clinic, Faculty of Medicine, Comenius University, Špitálska 24, 813 72 Bratislava, Slovakia

Retractors are used worldwide to assist in open cavity surgeries. They are employed to improve access during surgical intervention being particularly useful to reliably hold/move soft tissues or organs. The retractor end effector is typically within the operating envelope of a surgeon, making it particularly obtrusive if overdesigned (bulky). This work investigates the Mikulicz deep surgery retractor [1]. The model of this effector along with its parametric definitions can be observed in Fig. 1. The effector material is defined as CSN 17 024 (EN X38Cr13 or AISI 420 equivalent) with a surface hardness, ultimate, and yield strength of 42HRC, $R_m = 1305$ MPa, and $R_e = 1095$ MPa respectively.

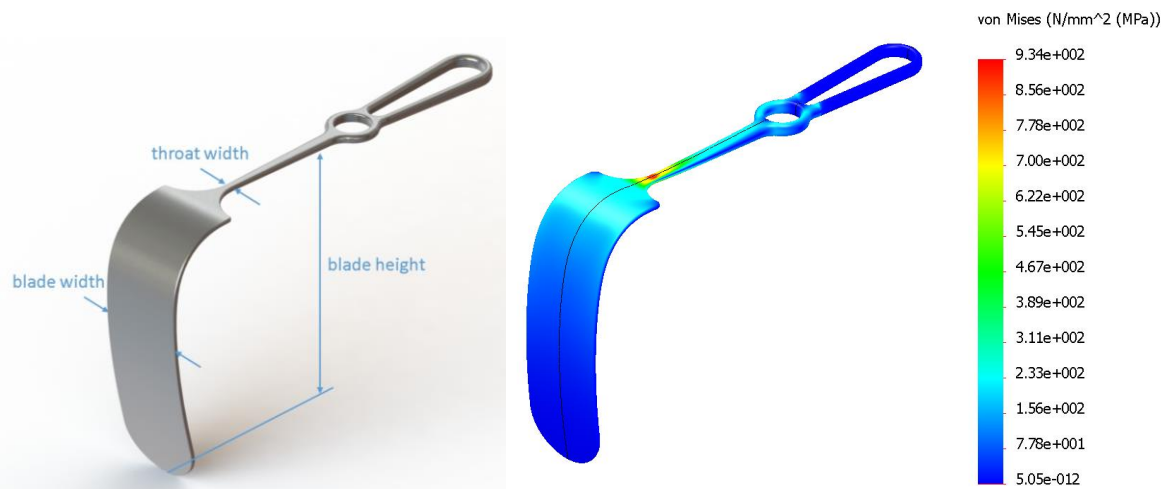


Fig. 1. Model of retractor end effector (*left*), stress distribution in loaded model (*right*)

Load definitions were obtained during simulated open cavity surgery on a torso trainer model. The retractor is pulled on at the bell end by an experienced surgeon. To measure the force generated by the surgeon in different manoeuvres, a force transducer was placed between the surgeon's hand and the bell end (handle) of the retractor. The design criterion was based upon a max measured value of 90 N applied on the lower half of the retractor blade.

The effector is modelled with three variable parameters: blade width, blade depth, and throat width. Geometric modelling and analysis were performed in Solidworks 3D CAD/simulation utilizing the design study toolbox [2]. This tool box allows for a parametric model to be solved with user defined parameters, constraints and design goals. The design goal of the analysis was to reduce/vary the three parametric variables of the model in order to minimize peak stresses in the design to investigate areas of interest. The interface between the

Complete 10 node quadratic tetrahedral solid elements were used to discretise the model for FEA [3]. Meshing of the model ensured adequate through element thickness of at least 3 elements. Areas of high stress were refined to ensure convergence. It was reasonable to assume that the problem be solved as a symmetric case, greatly reducing solution, as well as, optimization iteration time. The bell end of the retractor was fixed, while the blade was loaded on its lower half. The resulting design iteration results can be observed in Fig. 2, while the general stress distribution can be observed in Fig. 1 (right).

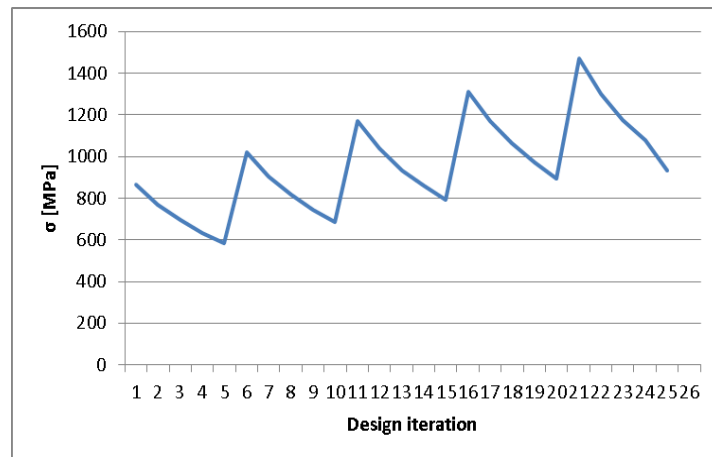


Fig. 2. Peak von Mises stress of the design study (design iteration no. 5 most suitable, with blade height = 120 mm and throat width = 6 mm)

It is no surprise that the resulting high stress region was at the interface between handle and blade (throat). It was also expected that blade width would have very little effect on the resulting stresses since the load resultant did not move with a change in this parameter. The blade depth had a significant impact on resulting stresses mainly due to the bending effects that the loading induces at the throat of the retractor. Neck diameter (thickness) also significantly contributed to the resulting stresses.

From the initial pass, the Mikulicz deep surgery retractor is well designed for its intended purpose given the loading from measurements. However, the results of the design study show that significantly reducing blade width could improve access within the cavity, however it would be necessary to investigate the effects of a thinner blade on soft tissues (pinching, pressure, haemorrhaging, etc...). Blade depth also represents a significant contribution on the resulting stresses in the throat of the retractor however reducing its dimension would possible defeat the purpose of a “deep” retractor. Finally, the neck diameter represents a good place for strength optimization without significantly obstructing surgeon’s access.

Acknowledgements

The work presented herein was financially supported by the APVV-15-0757 grant.

References

- [1] <http://www.surgicalinstruments.net.au/standard-surgical-instruments/Retractors/standard-retractors/Mikulicz-retractor-for-deep-surgery-straight-55x85mm-25-5cm>
- [2] Solidworks 3D CAD/simulation.
- [3] Thomas J. R. Hughes, The Finite Element Method, Linear Static and Dynamic Finite Element Analysis, Dover Publication, New York, 2000.

Mathematical model of the Hybrid Electric Vehicle for driving consumption optimization

P. Denk^a, Z. Šika^a, P. Steinbauer^a, J. Macek^b, J. Morkus^b

^a Faculty of Mechanical Engineering, Czech Technical University, Department of Mechanics, Biomechanics and Mechatronics, Technická 4, 166 07 Praha, Czech Republic

^b Faculty of Mechanical Engineering, Czech Technical University, Department of Automotive, Combustion Engine and Railway Engineering, Technická 4, 166 07 Praha, Czech Republic

The basic and general definition of the hybrid Electric Vehicle (HEV) taken from encyclopedia is [1]: “A type of hybrid vehicle and electric vehicle that combines a conventional internal combustion engine (ICE) system with an electric propulsion system (hybrid vehicle drivetrain)“. And when we are reading some following sentences we can read that the HEV is vehicle designed with respect towards to the idea to reduced vehicle energy consumption based on the possibilities of the recuperation energy (recuperated energy saved to the electric battery) and based on the optimal control of implemented drive units. The idea and this goal are restricted by using a particular design of the drive unit at all, but for chosen specific design of the HEV is just important the control of the drives unit in cooperation with other vehicle auxiliary units (like heating and air conditioning units etc.). The successful controlling have to be based on the well knowledge of the vehicle physical model with respect to the specific properties given by vehicle unit design. The following contribution is focused on the design of the HEV mathematical model, which will be used for optimization of the drive unit control strategy, based on the route trajectory knowledge and which can be used for identification of HEV basic parameters (especially battery and charger unit).

The HEV mathematical model at all describes very complex technical units with complicated physical structure. The main input to considered mathematical model is velocity profile in dependence on the route trajectory (or equivalent dependence on the time) and the main input from considered mathematical model is total energy consumption in specific vehicle units (for example on the battery terminals, charger terminals or generators output). The value of the total energy consumption is just function of the vehicle unit control and in general and with respect to the vehicle design is possible divided the mathematical model to the two separated parts. The first part describes a mechanical energy consumption way and the second part describes a thermal energy consumption way, but both of the introduced parts are not strictly independent. One of the possible diagram of the HEV mathematical model is shown in Fig. 1, where are marked both of these introduced ways. The first – mechanical – energy way is consist of separately blocks, which in the first is defined driving resistances, in the second is defined chosen type of the gearbox and clutch which is represented appropriate mathematical models and in the last third block are describes mechanical efficiencies with respect to chosen goal units (like the battery terminals etc. – see above).

The second – thermal – energy way is consist of two separately blocks, where the first is represents the whole thermal management (heat pump unit, air conditioning unit and motor cooling system) and the second block represents the thermal efficiencies which are fixed on the chosen thermal power unit.

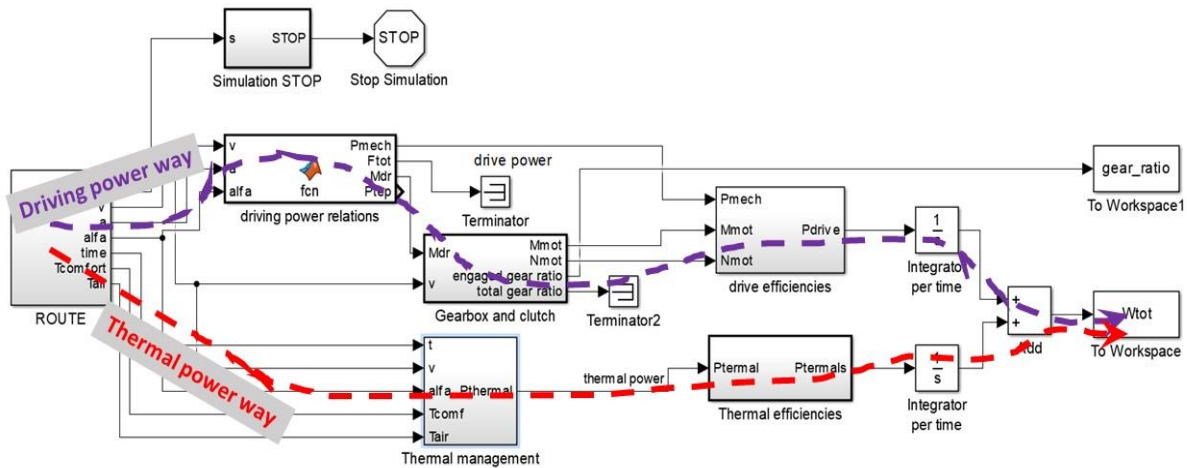


Fig. 1. HEV mathematical model diagram

Generally speaking, this introduced mathematical model is based on the power relations for the both ways. The first (driving) way is obtained from the power relations between a driving resistances power and engine power to the output shaft with respect to the adhesion limit on the vehicle tires and with respect to the engine power characteristics. This power relation also respects the transmissions efficiencies along the whole drive chain (efficiencies on the gearbox and other transmissions units). The following efficiencies block reduces/increases the previous obtained driving power to the chosen power unit or to the value of the fuel consumption (which is consisted from external electric fuel consumption and petrol fuel consumption).

The second (thermal) way is obtained from the power relations between processes on the motor cooling, vehicle cabin heating and external thermal loss caused by thermal losses on the vehicle windscreen and thermal losses from the vehicle bodywork. The following efficiencies block represents again reduce or increase the previous obtained thermal power to the chosen thermal unit or to the fuel consumption as the previous described driving power way. The total energy consumption is obtained from sum of the both reduced powers using the integrator per time.

The shown approach to the design of the HEV mathematical model allows create the mathematical model from the basic separate blocks, which can represent many various vehicle designs and it is easily possible to build the vehicle mathematical model with more of the one driving units. This mathematical model can be following used for control of these driving units.

Acknowledgements

The work has been supported by the grant EU project “ADVANCE” (ADVancing user acceptance of general purpose hybridized Vehicles by Improved Cost and Efficiency) number 724095 and the word of thanks belongs also to Technology Agency of the Czech Republic in program “Josef Božek – Competence Centre of Automotive Industry”.

References

- [1] Wikipedia the free encyclopedia, URL: https://en.wikipedia.org/wiki/Hybrid_electric_vehicle, (25. 9. 2017)

Analysis of contact force along spherical roller bearing element

P. Dlhý ^{a,b}, P. Novák ^c

^a Institute of Physics of Materials, Academy of Sciences of Czech Republic, Žižkova 22, 616 62 Brno, Czech Republic
^b Central European Institute of Technology, Brno University of Technology, Technická 10, 616 00 Brno, Czech Republic
^c Department of Applied Mechanics, Faculty of Mechanical Engineering, University of Žilina, 010 26 Žilina, Slovak Republic

This contribution is dealing with static contact analysis of roller bearing elements. Roller bearings are frequently used machinery parts. Typically, mutual rubbing of the roller bearing parts causes friction, which generates wear and energy losses. To prevent early failure of the bearing, friction and wear must be minimized by appropriately designing the bearing elements [2, 3]. The basic step in designing the roller bearing elements is static analysis carried out by FEM that provides distribution of contact pressure and allows to assess the overall loading capacity [4].

This contribution is aimed at describing a particular case of static analysis of a spherical roller bearing elements that was carried out for a roller bearing manufacturer. The objective was to find out the distribution of contact pressure and also to determine the influence of the shape correction of the roller bearing element.

For static analysis, software Ansys was used. Parametrical FEM model of spherical roller bearing (see Fig. 1) was created. Model included some simplifications that are common for this type of simulations and enable better parametrization. The whole model was created in several steps. At first, geometry of one segment of bearing was created. This segment looked like quarter of part corresponding to one roller bearing element. Then, the contact pair was defined and meshed with contact elements. For contact of roller element and rings we used pair based contact because of big number of needed contacts and faster initialization at the beginning of simulation. Springs were needed to be applied between the bearing element and rings for better convergence. After that, the volume mesh was created. At last, the created mesh with the contact pair was copied to set up the whole model of the roller bearing using

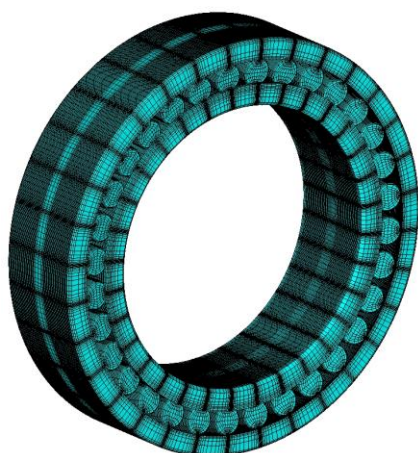


Fig. 1. FEM model of spherical roller bearing

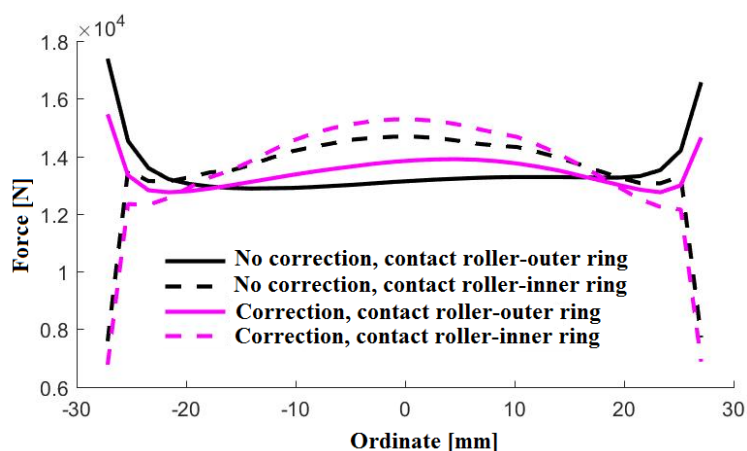


Fig. 2. Trend of contact forces along chosen roller bearing element before and after correction

symmetry. After copying, pair based contact settings were fixed.

The Hertzian contact was used, which implies some assumptions. Maximum compressive stress occurs at the point of contact. Maximum tensile stress takes place just beyond the edge of the contact area on the surface [1].

Coordinate system for every rolling element was created to find out normal stress at contact areas as the result of simulation. Birth of edge stresses concentration was found at bearing elements. Large stress concentration at edge of bearing element has negative influence on lifetime of the whole bearing. The common way to lower the high edge stress is the correction of shape of rolling element. To monitor the influence of correction, forces along roller bearing element were compared, as we can see in Fig. 2. More analyses then showed the importance of correction at bearing elements to removing stress concentration.

Simple bearing cage with shaft was used as outer construction for testing simulation. However, bearing model includes semi-automatic localization for importing bearing model to a specified place at some external (supplied by customer) construction.

For the whole bearing FEM model, linear elements were used. FEM model of one spherical roller bearing has about 10^6 nodes. If we want to simulate two bearings with some model of real external construction we get more than $2 \cdot 10^6$ nodes. However, for a better approximation of contact surfaces quadratic elements are a better choice. For high hardware difficulty, we can't use them in the whole model. We decided to use combination of linear elements at majority of solid model, while quadratic elements were used only at contact surfaces. With this combination, better approximation of contact surfaces was obtained and lower simulation times were preserved.

FEM simulations were used to find influence of correction of roller bearing elements shape. Results show that correction has significant influence on layout and magnitude of contact pressure. Main change occurs in the stress at the edge of the bearing elements. With the right correction, the adverse edge stress can be removed completely.

Acknowledgements

The research work has been partially supported by the Project of the Structural Funds of the EU, Operational Program Research and Development, Measure 2.2 Transfer of knowledge and technology from research and development into practice: Title of the project: Development of optimal technology for the analysis of the limit states of structural elements in contact, ITMS code: 26220220118, and by the Slovak Research and Development Agency under the contract No. APVV-0736-12.

References

- [1] Danyluk, M., Dhingra, A., Rolling contact fatigue in ultra high vacuum, In: Performance evaluation of bearings, Dr. Rakesh Sehgal (ed.), InTech, 2012, pp. 93-114.
- [2] Harnoy, A., Bearing design in machinery: Engineering tribology and lubrication, Marcel Dekker, Inc., New York, 2002.
- [3] Harris, A. T., Rolling bearing analysis, 4th edition, John Wiley & Sons, Inc., New York, 2000.
- [4] Šooš, L., Radial ball bearings with angular contact in machine tools, In: Performance evaluation of bearings, Dr. Rakesh Sehgal (ed.), InTech, 2012, pp. 27-48.

Numerical assessment of stability of the ball vibration absorber

C. Fischer^a, J. Náprstek^a

^a*Institute of Theoretical and Applied Mechanics, CAS v.v.i., Prosecká 76, CZ-190 00 Praha, Czech Republic*

Passive vibration absorbers or tuned mass dampers (TMD) are widely used in the construction industry. These devices are designed to mitigate unwanted vibrations of structures, which are induced by the wind or earthquake excitation. High popularity of the passive damping devices follows from their simple design, reliability and long service life, cheap realization and low maintenance requirements. From the mechanical point of view, such devices can be easily represented by a simple linearized model, whose parameters can be easily derived according to needs of the structural engineer.

It appears, that the linear model is not able to describe complex behaviour of the device in case close to resonance. This could be a serious drawback of the linear design, because the devices are tuned up to exploit their maximal sensitivity (i.e. resonance) to fight against the resonance effect of the supporting structure. Thus, non-linear models have to be adopted in the TMD description and design.

The ball vibration absorber (BVA) is in principle a heavy ball rolling inside a semi-spherical cavity. It is a convenient alternative to the usual pendulum-based dampers, mostly in cases where the limited vertical space prevents installation of a pendulum-type device. The dynamics of the real ball absorber is significantly more complicated in comparison to the pendulum one. For a short discussion on differences in models of pendulum and ball based dampers see [3]. However, the numerical examination of the non-linear model of the BVA indicates that its resonance behaviour is similar to the spherical pendulum, which was thoroughly described from theoretical and experimental perspectives in, e.g., [4]. Despite the theoretical differences, the resonance curves in both cases form similar patterns, i.e. stable and unstable branches, type of bifurcation points, etc. It seems that detailed study of both separate cases can provide complementary results, whose parallels appear in the other model.

This contribution aims at presenting some results of the numerical assessment of stability of the BVA, together with results of a new analysis of older experimental data and numerical and experimental results regarding spherical pendulum.

The mathematical model of the BVA is derived using the Appell-Gibbs approach (cf. [1]):

$$\begin{aligned}
 \dot{u}_{Cx} &= \omega_y(u_{Cz} - R) - \omega_z u_{Cy}, \\
 \dot{u}_{Cy} &= \omega_z u_{Cx} - \omega_x(u_{Cz} - R), \\
 \dot{u}_{Cz} &= \omega_x u_{Cy} - \omega_y u_{Cx},
 \end{aligned} \tag{1}$$

$$\begin{aligned}
 J_s \rho \dot{\omega}_x &= (\ddot{u}_{Ay} + \rho(\omega_z \dot{u}_{Cx} - \omega_x \dot{u}_{Cz}))(u_{Cz} - R) - u_{Cy} (g + \rho(\omega_x \dot{u}_{Cy} - \omega_y \dot{u}_{Cx})), \\
 J_s \rho \dot{\omega}_y &= (-(\ddot{u}_{Ax} + \rho(\omega_y \dot{u}_{Cz} - \omega_z \dot{u}_{Cy})))(u_{Cz} - R) + u_{Cx} (g + \rho(\omega_x \dot{u}_{Cy} - \omega_y \dot{u}_{Cx})), \\
 J_s \rho \dot{\omega}_z &= (\ddot{u}_{Ax} + \rho(\omega_y \dot{u}_{Cz} - \omega_z \dot{u}_{Cy}))u_{Cy} - (\ddot{u}_{Ay} + \rho(\omega_z \dot{u}_{Cx} - \omega_x \dot{u}_{Cz}))u_{Cx},
 \end{aligned} \tag{2}$$

where g is the gravitational acceleration, M - mass of the ball, J - central inertia moment of the ball with respect to centre of the ball (for homogeneous ball $J = 2/5Mr^2$), ω_\bullet - angular

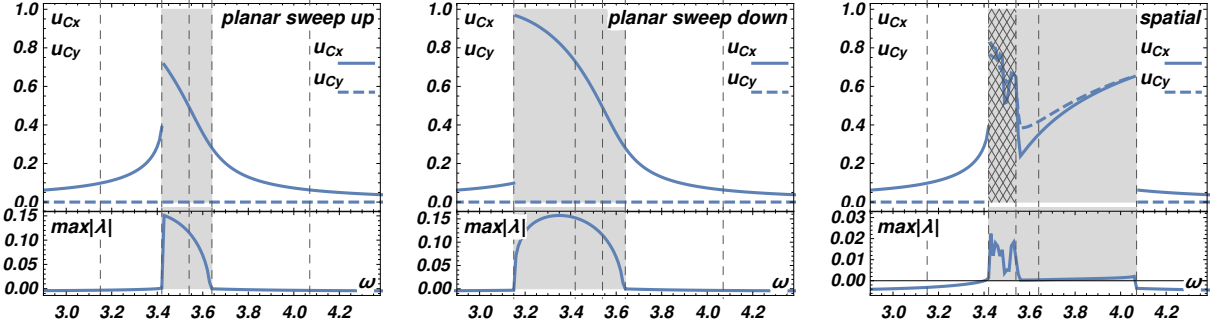


Fig. 1. Instability regions of three different branches of the resonance curves of the mathematical model of BVA. In each plot: upper part — the resonance curve, lower part — maximal Lyapunov exponent of the corresponding branch. The areas where the maximal Lyapunov exponent is positive are shaded

velocities of the ball with respect to its centre, u_C , - displacement of the contact point with respect to the absolute origin O , u_A , are components of (prescribed) movement of the cavity and $J_s = (J + M\rho^2 R^2)/(M\rho^2)$, $\rho = 1 - r/R$. The formula does not consider damping.

The model presented in Eqs. (1,2) comprises six variables, although the problem contains only three independent degrees of freedom, i.e. lateral and transversal movement and spin of the ball. This corresponds to the reduced first order base system.

For the numerical evaluation, the more advanced equations are used, i.e. those including damping terms [2]. The numerical study of the stabilised response, i.e. after the transient effects subside, shows the multiple solution branches. These branches describe substantially different states of the movement of the ball. Stability of the corresponding solutions is checked using values of the Lyapunov exponents, which are computed along the respective branches. Fig. 1 shows three different branches of the general resonance curve of the BVA model, supplemented by the values of the corresponding maximal Lyapunov coefficient λ . The shaded areas in plots correspond to $\lambda > 0$, which can be interpreted as the such part of the response, where the stability of motion is limited. The hatched part of the spatial response in the rightmost plot corresponds to the case, where the response has an apparent chaotic character. Its detailed analysis certainly deserve the additional study.

Acknowledgements

The kind support of the Czech Scientific Foundation No. 15-01035S and of the RVO 68378297 institutional support are gratefully acknowledged.

References

- [1] Náprstek, J., Fischer, C., Dynamic behavior and stability of a ball rolling inside a spherical surface under external excitation, In: A. Zingoni (ed.), Insights and innovations in structural engineering, mechanics and computation, Taylor & Francis, London, 2016, pp. 214–219.
- [2] Náprstek, J., Fischer, C., Non-holonomic dynamics of a ball moving inside a spherical cavity, Procedia Engineering 199 (2017) 613–618.
- [3] Náprstek, J., Fischer, C., Non-holonomic planar and spatial model of a ball-type tuned mass damping device, Proceedings of the conference Engineering Mechanics 2017, Svatka, VUT Brno, 2017, pp. 698–701.
- [4] Pospíšil, S., Fischer, C., Náprstek, J., Experimental analysis of the influence of damping on the resonance behavior of a spherical pendulum, Nonlinear Dynamics 78 (1) (2012) 371–390.

Strain-range dependent cyclic plasticity material model calibration for the 08Ch18N10T steel

J. Fumfera ^a, R. Halama ^b, J. Kuželka ^a, M. Španiel ^a

^a Czech Technical University in Prague, Faculty of Mechanical Engineering, Department of Mechanics, Biomechanics and Mechatronics,
Technická 4, 166 07 Praha 6, Czech Republic

^b VŠB – Technical University of Ostrava, Faculty of Mechanical Engineering, Department of Applied Mechanics,
17.listopadu 15, 708 33 Ostrava-Poruba, Czech Republic

Cyclic uniaxial tests of 08Ch18N10T austenitic stainless steel shows no cyclic hardening under $\epsilon_a \leq 0.75\%$ loading but significant and strain-range dependent cyclic hardening above this limit. This phenomenon must be included in the material model for accurate cyclic response modeling.

Material model by R. Halama [3] based on Chaboche's cyclic plasticity model with stress-based memory surface was slightly modified for optimal capture of 08Ch18N10T response. Complete set of equations and variable descriptions can be found in [2], but the most important equations should be mentioned for better understanding the model and calibration process.

Plasticity function $f = \sqrt{\left(\frac{3}{2}(\boldsymbol{\sigma}' - \boldsymbol{x}') : (\boldsymbol{\sigma}' - \boldsymbol{x}')\right)} - \sigma_y$, where σ_y is actual yield stress, $\boldsymbol{\sigma}'$ is deviatoric stress tensor, \boldsymbol{x}' is deviatoric backstress tensor given as $d\boldsymbol{x} = \sum_{i=1}^3 \frac{2}{3} c_i d\boldsymbol{\epsilon}^p - \phi \gamma_{\infty}^i \boldsymbol{x}_i dp$, where c_i and γ_{∞}^i are material parameters, $\boldsymbol{\epsilon}^p$ is plastic strain tensor and dp is increment of equivalent plastic strain. ϕ is a cyclic hardening function that changes the kinematic hardening part of the plasticity function.

Virtual backstress (defining the memory surface) is given as $\sum_{i=1}^3 \frac{2}{3} c_i d\boldsymbol{\epsilon}^p - \gamma_{\infty}^i \boldsymbol{x}_i dp$, auxiliary function $g = \|\boldsymbol{x}_{stab}\| - R_M \leq 0$, $dR_M = H(g) \left\langle \frac{\boldsymbol{x}_{stab}}{\|\boldsymbol{x}_{stab}\|} : d\boldsymbol{x}_{stab} \right\rangle$ and finally the memory surface is $R_M = \|\boldsymbol{x}_{stab}\|_{max}$. Memory surface used in following R_M dependent functions is bounded by material parameters R_M^{min} , R_M^{max} as $R_M^{min} \leq R_M^{used} \leq R_M^{max}$.

Now memory surface dependent functions can be defined. $\phi = \phi_0 - \phi_{cyc}$, where ϕ_0 is material parameter (value of ϕ at the first cycle) and $d\phi_{cyc} = \omega(\phi_{\infty} - \phi)p$. $\phi_{\infty} = A_{\infty}(R_M^{used})^4 + B_{\infty}(R_M^{used})^3 + C_{\infty}(R_M^{used})^2 + D_{\infty}(R_M^{used}) + E_{\infty}$ is value of ϕ function after the saturations of cyclic response (or in the end of fatigue life if no saturation occurs), here A_{∞} , B_{∞} , C_{∞} , D_{∞} , E_{∞} are material parameters. $\omega = A_{\omega} \exp(B_{\omega} R_M^{used}) + C_{\omega}$ is transition function to determine ϕ between ϕ_0 and ϕ_{∞} , where A_{ω} , B_{ω} , C_{ω} are material parameters. Finally the isotropic hardening part of the plasticity function can be defined as $\sigma_y = \sigma_{y0} + R$, where $R = C_R \cdot \exp(E_R \cdot R_M^{used}) \cdot p^{B_R}$, material parameters are σ_{y0} (initial yield stress), B_R , C_R and E_R .

12 specimens from the uniaxial low cycle fatigue tests described in [1] were chosen as an input data source for the calibration process in range from approximately $\epsilon_a = 0.5\%$ to $\epsilon_a = 2.5\%$. Input data are in form of stress-strain hysteresis loops in each cycle measured during the fatigue life of each specimen. Young modulus E , Poisson's ratio ν and σ_{y0} are determined from the tensile test. Fig. 1 shows scheme of the calibration process.

Calibrated material parameters in Table 1 were verified by FEA simulation using another set of uniaxial experimental data (not the one used for the calibration). FE model of the real specimen was created with boundary conditions (displacements) similar to experimental ones. The stress field was close to the plane stress in substantial part of the specimen. The match parameter was the reaction force of FEA vs the force measured during the experiment. Good agreement was achieved with average error under 5%.

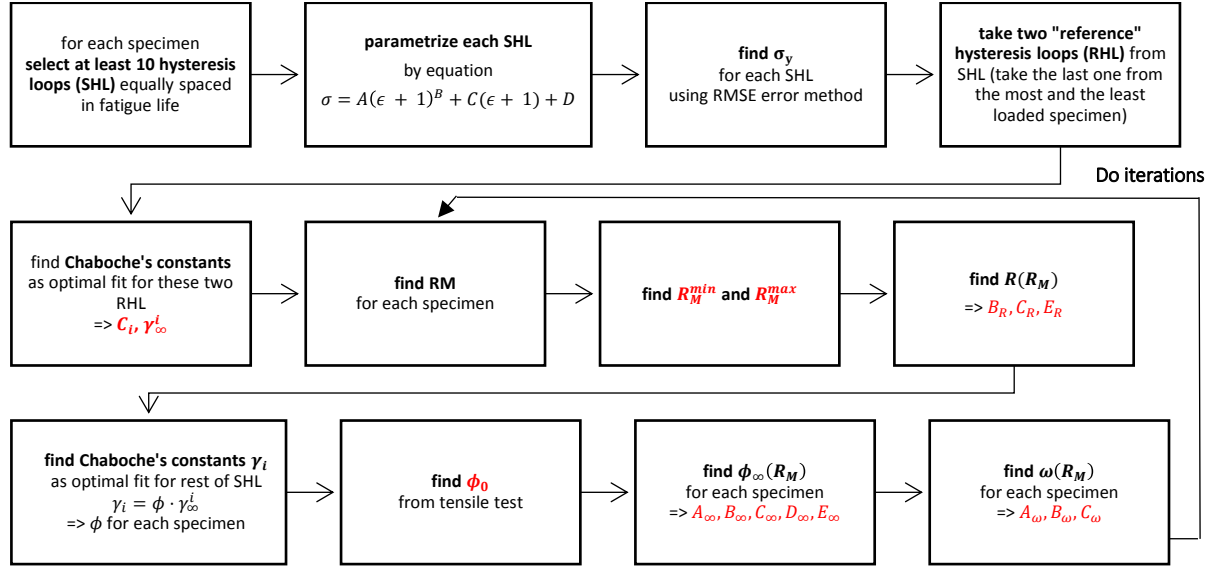


Fig. 1. Scheme of the calibration process

Table 1. Material constants of 08Ch18N10T

E [MPa]	ν	c_1 [MPa]	γ_∞^1 [-]	c_2 [MPa]	γ_∞^2 [-]	c_3 [MPa]	γ_∞^3 [-]	ϕ_0 [-]
190	0.3	68020	161.8518	9987,2	577.379	2000	0	2.3136
A_∞ [MPa ⁻⁴]		B_∞ [MPa ⁻³]		C_∞ [MPa ⁻²]		D_∞ [MPa ⁻²]	E_∞ [MPa ⁻²]	E_R [-]
$-1.5811 \cdot 10^{-9}$		$2.0128 \cdot 10^{-6}$		$-9.0398 \cdot 10^{-4}$		0.1634	-10.0057	0.0173
A_ω [-]		B_ω [MPa ⁻¹]	C_ω [-]	R_M^{min} [MPa]	R_M^{max} [MPa]	B_R [-]	C_R [MPa]	
$5.4034 \cdot 10^{-4}$		0.0179	0.7806	121	490	0.3950	0.0104	

In this paper, material model with strain-range dependent plasticity has been presented for 08Ch18N10T steel. Calibration process was described including final material parameters. The verification process using FEA simulation under the plane stress conditions was described.

Acknowledgements

The authors would like to acknowledge support from the Technology Agency of the Czech Republic, grant No. TA04020806, support from the Grant Agency of the Czech Technical University in Prague, grant No. SGS15/187/OHK2/3T/12 and by the Czech Science Foundation (GA15-18274S).

References

- [1] Fumfera, J., Kuželka, J., Španiel, M., Evaluation of strain fields from DIC measurement, Report ČVUT FS 12105/17/09, 2017. (in Czech)
- [2] Fumfera, J., Kuželka, J., Španiel, M., Material model of cyklické plasticity with strain range dependent cyclic hardening, Report ČVUT FS 12105/17/10, 2017. (in Czech)
- [3] Halama, R. et al., New material model of cyclic plasticity with cyclic hardening dependency effect on the stress amplitude, Proceedings of the conference Výpočty konstrukcí metodou konečných prvků, Brno, 2016. (in Czech)

Numerical simulation of flows over oscillating airfoil

J. Fürst^a

^a*Faculty of Mechanical Engineering, CTU in Prague, Karlovo nám. 13, 121 35 Praha, Czech Republic*

The contribution deals with the development of implicit LU-SGS solver for compressible flows using an arbitrary Lagrangian-Eulerian (ALE) formulation. The solver is built on the top of the OpenFOAM package [5] and is an extension of the steady-state solver presented at the Computational Mechanics conference in 2017 [2] or in [3].

The ALE formulation of Navier-Stokes equations for compressible flows can be written in integral form for either moving or stationary control volume $V(t)$ as

$$\frac{d}{dt} \int_{V(t)} \mathbf{W} dV + \oint_{\partial V(t)} (\vec{\mathbf{F}}^* - \vec{\mathbf{F}}^v) \cdot \vec{n} dS = 0, \quad (1)$$

where $W = [\rho, \rho\vec{u}, \rho E]$ represents the vector of conservative variables, $\vec{\mathbf{F}}^* = \vec{\mathbf{F}} - \mathbf{W}\vec{g}$ is the convective flux tensor (here \vec{g} represents the velocity of ∂V) and $\vec{\mathbf{F}}^v$ is the viscous flux tensor, see e.g. [1].

The numerical approximation is achieved with the help of finite volume method using approximate Riemann solvers for convective fluxes, central approximation for viscous fluxes and a second order backward differencing in time resulting in the unsteady residual

$$\mathbf{R}^*(\mathbf{W}^{n+1})_i = -\frac{3|V_i^{n+1}|\mathbf{W}_i^{n+1} - 4|V_i^n|\mathbf{W}_i^n + |V_i^{n-1}|\mathbf{W}_i^{n-1}}{2\Delta t} - \sum_j (\vec{\mathbf{F}}_{ij}^* - \vec{\mathbf{F}}_{ij}^v) \cdot \vec{S}_{ij}^{n+1}. \quad (2)$$

The first term at the right hand side represents the first term in eq. (1) and the second term corresponds to surface integral approximation. The numerical method for unsteady problems then drives \mathbf{R}^* to zero using several LU-SGS iterations.

In order to assess the performance of the LU-SGS solver for simulations with moving meshes the inviscid transonic flow over oscillating NACA-0012 profile was calculated. The case was experimentally studied by Landon, see [4], case 5. The free-stream Mach number is $M_\infty = 0.755$ and the profile performs a harmonic oscillatory motion with mean incidence $\alpha_m = 0.016^\circ$, pith amplitude $\alpha_o = 2.51^\circ$ and reduced frequency $k = \omega c / 2U_\infty = 0.0814$ (here c is the profile chord) given as

$$\alpha(t) = \alpha_m + \alpha_o \sin(\omega t). \quad (3)$$

The simulation has been performed using a C-type mesh with 168×40 quadrilateral cells with 120 cells at the profile and with the free-stream boundary at a distance approximately $10c$ from the profile. Fixed (physical) time step was chosen as $\delta t = T/100$, where T is the period of the oscillation. Fig. 1 shows the isolines of Mach number for four different phases of the oscillatory motion. One can see the hysteresis of the solution (compare the figures for phases

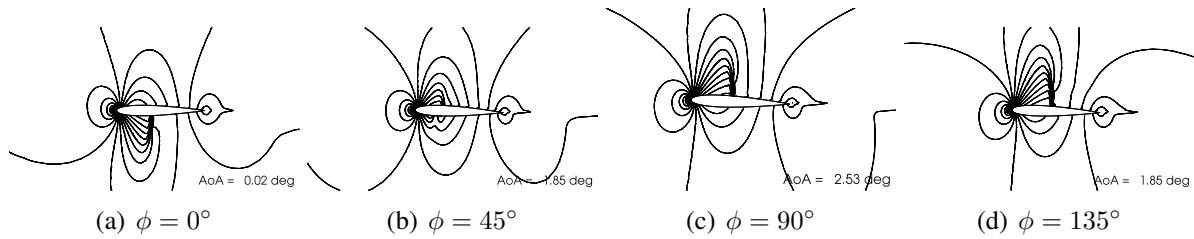


Fig. 1. Isolines of Mach number for different phases of the oscillative motion of NACA-0012 profile

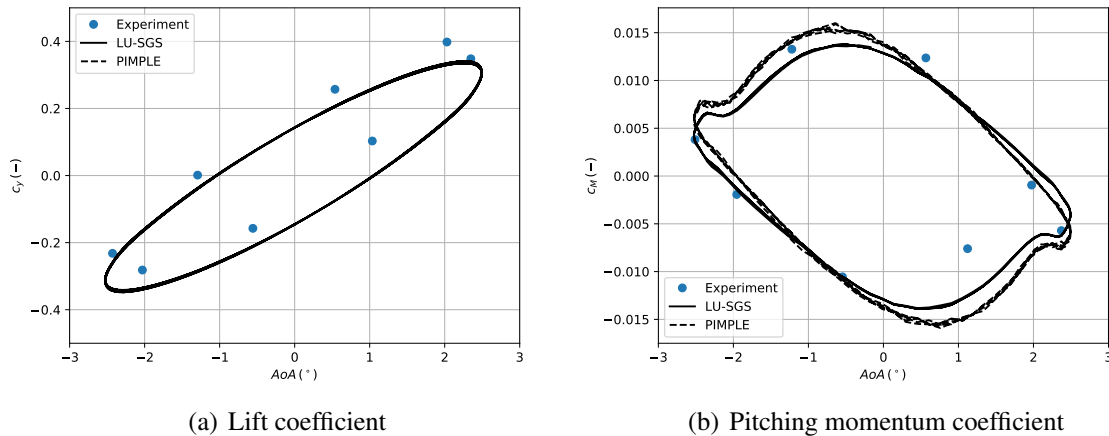


Fig. 2. Lift and pitching momentum coefficient for oscillating NACA-0012 profile

$\phi = 45^\circ$ and 135°). The comparison of lift and pitching momentum coefficients (see Fig. 2) with experimental data shows that the method provides qualitatively correct results. Moreover, the comparison shows that the results obtained with the LU-SGS method are very close to the results obtained with segregated PIMPLE solver from OpenFOAM package.

Acknowledgements

This publication was created within the framework of the Center of Advanced Aerospace Technology project, Reg. No CZ.02.1.01/0.0/0.0/16_019/0000826.

References

- [1] Blazek, J., Computational fluid dynamics: Principles and applications, B.m.: Butterworth-Heinemann, 2015.
- [2] Fürst, J., On the application of LU-SGS scheme for turbomachinery flows, Proceedings of the conference Computational Mechanics, Špičák, University of West Bohemia, Plzeň, Czech Republic, 2016.
- [3] Fürst, J., On the implicit density based OpenFOAM solver for turbulent compressible flows, EPJ Web of Conferences 143 (2017) 1–7, doi: 10.1051/epjconf/201714302027.
- [4] Landon, R. H., NACA 0012. Oscillating and transient pitching, Compendium of Unsteady Aerodynamic Measurements, AGARD-R-702, 1982.
- [5] Weller, H. G., Tabor, G., Jasak, H., Fureby, C., A tensorial approach to computational continuum mechanics using object-oriented techniques, Computers in Physics 12 (6) (1998) 620–631.

Development of non-reflective boundary condition for free-surface flows

J. Fürst^a, J. Musil^a

^aFaculty of Mechanical Engineering, CTU in Prague, Karlovo nám. 13, 121 35 Praha, Czech Republic

The main goal of this contribution is the development of non-reflective boundary condition for free-surface flows motivated by the simulation of vertical water pump situated in semi-open basin (Fig. 1). However the problem is usually described by the system of Navier-Stokes equations in the volume of fluid formulation, the development starts with simplified model of 1D shallow water equations.

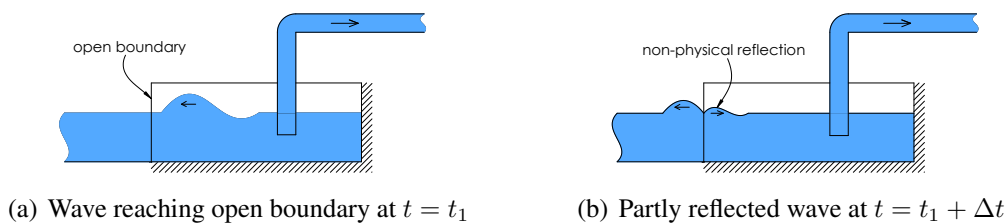


Fig. 1. Shallow water simulation of dam break problem

The original idea behind deriving well-posed non-reflective boundary conditions for 1D shallow water equations $(1)_1$ and $(1)_2$ comes from method of characteristics, which allows to obtain analytical solution as superposition of two (Riemann) variables propagating by characteristic speeds of opposite directions. Values of original variables on boundary face are then computed as: $u_B = \frac{1}{2}(R_L^+ + R_R^-)$, $h_B = \frac{1}{16g}(R_L^+ + R_R^-)^2$ with first order spatial accuracy, where $R_L^+ = u_{in} + 2\sqrt{gh_{in}}$ and $R_R^- = u_1 - 2\sqrt{gh_1}$ [2]. Here $u_{in} = 0$ and h_{in} is set as water height in infinity. Values with subscript 1 are taken from first boundary cell.

$$\frac{\partial h}{\partial t} + \frac{\partial(uh)}{\partial x} = 0, \quad \frac{\partial(uh)}{\partial t} + \frac{\partial(u^2h + \frac{1}{2}gh^2)}{\partial x} = 0. \quad (1)$$

The following figures show testing non-reflective boundary condition in MATLAB on dam-break problem. In Figs. 2b) and c), it can be seen that initial wave passed out without reflection.

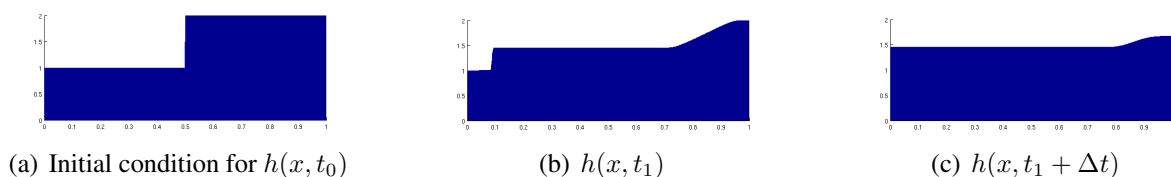


Fig. 2. Shallow water simulation of dam break problem with non-reflective boundary condition

The main goal of the contribution is the development of the non-reflecting inlet boundary condition for free-surface flows described by the system of Navier-Stokes equations in the so called volume of fluid formulation (VOF) [1]. The problem is described by the following system of equations

$$\frac{\partial u_j}{\partial x_j} = 0, \quad (2)$$

$$\frac{\partial \rho u_i}{\partial t} + \frac{\partial(\rho u_i u_j)}{\partial x_j} + \frac{\partial p}{\partial x_i} = \frac{\partial \tau_{ij}}{\partial x_j} + \rho g_i, \quad (3)$$

$$\frac{\partial \alpha}{\partial t} + \frac{\partial(\alpha u_j)}{\partial x_j} = 0. \quad (4)$$

Here $0 \leq \alpha \leq 1$ is the liquid fraction in the mixture ($\alpha = 0$ corresponds to air, $\alpha = 1$ corresponds to water) and the density of the mixture is $\rho = \alpha \rho^{water} + (1 - \alpha) \rho^{air}$. The symmetric tensor τ_{ij} expresses tangential stresses and g_i is the acceleration due to gravity.

The system is solved in two-dimensional domain with initial condition set to $\vec{u} = \vec{0}$ and α according to Fig. 3a). At the upper, right, and lower boundary the non-slip boundary condition is used for \vec{u} and homogeneous Neumann condition for α . Two variants of boundary conditions were tested at the artificial left boundary condition, the standard OpenFOAM condition allowing variable water level and the new non-reflecting boundary condition developed for shallow water problem.

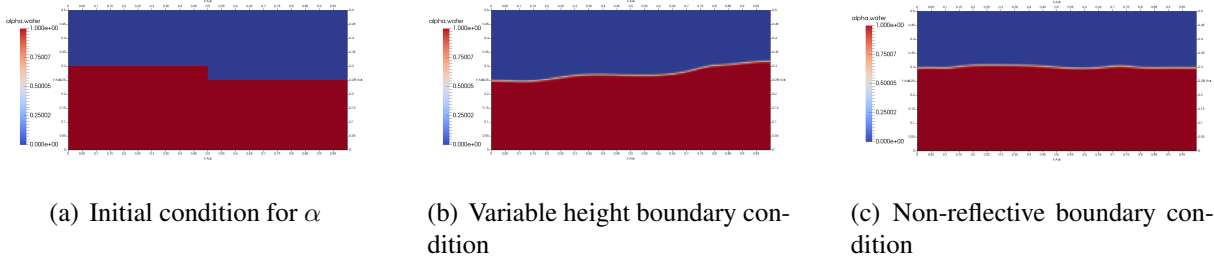


Fig. 3. VOF simulation of dam break problem

Figs. 3b) and c) show the water fraction in time $t = 2s$ obtained with the OpenFOAM solver using two above mentioned boundary conditions. One can see that the solution obtained with the first boundary condition is spoiled by false reflexion from the boundary. On the other hand the non-reflective boundary condition is transparent to incoming waves. Note that the solution in Fig. 3c) corresponds very closely to a solution obtained on an elongated domain.

The contribution proves that the non-reflective characteristic based boundary condition for shallow water equation can be effectively used also in the framework of VOF method.

Acknowledgements

This work was supported by the Grant Agency of the Czech Technical University in Prague, grant No. SGS16/206/OHK2/3T/12.

References

- [1] Blazek, J., Computational fluid dynamics: Principles and applications, 2nd edition, New York: Elsevier, 2005.
- [2] Sanders, B. F., Non-reflecting boundary flux function for finite volume shallow-water models, Advances in Water Resources 25 (2) (2002) 195–202.

Modelling of ageing and fatigue under large strains

J. Heczko^a, R. Kottner^a

^aFaculty of Applied Sciences, University of West Bohemia, Technická 8, 301 00 Plzeň, Czech Republic

Both ageing and fatigue are up-to-date topics in constitutive modelling of rubbers. Chemical reactions together with various physical phenomena cause complex behavior of such materials. This contribution deals with both increase and decrease of stiffness due to chemical reactions and the evolution of microcracks due to mechanical loading. As opposed to most works in this area, the aim is not to describe the fatigue life in terms of number of cycles to failure, but in terms of changes of mechanical properties during the whole service life.

The dynamic network model [2] was used to represent chemical ageing. The *continuum damage mechanics* framework was used to treat fatigue damage, namely the model by Ayoub et al. [1] was used.

The crucial notion of the dynamic network model is the stress-free configuration, which may change in time due to creation of new chemical bonds in the deformed state. The isochoric part of the deformation gradient $\bar{\mathbf{F}} = \mathbf{F}_2 \mathbf{F}_1$ is split multiplicatively into the part \mathbf{F}_1 from the undeformed into the stress-free configuration, and \mathbf{F}_2 from the stress-free to the actual configuration. The Helmholtz free energy per unit reference volume is chosen in the form

$$\psi = C_{10} \mu \nu (1 - D) (\mathbf{C}_2 : \mathbf{I} - 3) = C_{10} \mu \nu (1 - D) (\mathbf{C}_1^{-1} : \bar{\mathbf{C}} - 3) , \quad (1)$$

where C_{10} is a material parameter, μ and ν are stiffness coefficients that represent ageing, D is the damage variable, and $\mathbf{C}_2 = \mathbf{F}_2^T \mathbf{F}_2$. The second Piola-Kirchhoff stress tensor is then

$$\mathbf{S} = 2 C_{10} (1 - D) \mu \nu \operatorname{dev} [\mathbf{C}_1^{-1} \cdot \bar{\mathbf{C}}] \cdot \mathbf{C}^{-1} - J p \mathbf{C}^{-1} , \quad (2)$$

where $J = \det \mathbf{F}$ and p is the hydrostatic pressure (determined from boundary conditions in the case of an incompressible material). Evolution of the ageing-related stiffness parameters is driven by the concentration of peroxy-radicals $\xi_{\text{ROO}\bullet}$ and under isothermal conditions can be expressed as

$$\nu(t) = \exp \left(-k_s \int_0^t \xi_{\text{ROO}\bullet} d\tau \right) , \quad \mu(t) = \exp \left(k_a \int_0^t \xi_{\text{ROO}\bullet} d\tau \right) , \quad (3)$$

k_s and k_a being material parameters. The concentration of peroxy-radicals is considered constant in the steady state of oxygen diffusion. Diffusion equation with a reaction term would be used to calculate $\xi_{\text{ROO}\bullet}$, should the concentration vary significantly in time.

The change of the stress-free configuration is determined by the following evolution equation (D/Dt being the material derivative):

$$\frac{D\mathbf{C}_1^{-1}}{Dt} = \frac{\dot{\mu}}{\mu} (\bar{\mathbf{C}}^{-1} - \mathbf{C}_1^{-1}) . \quad (4)$$

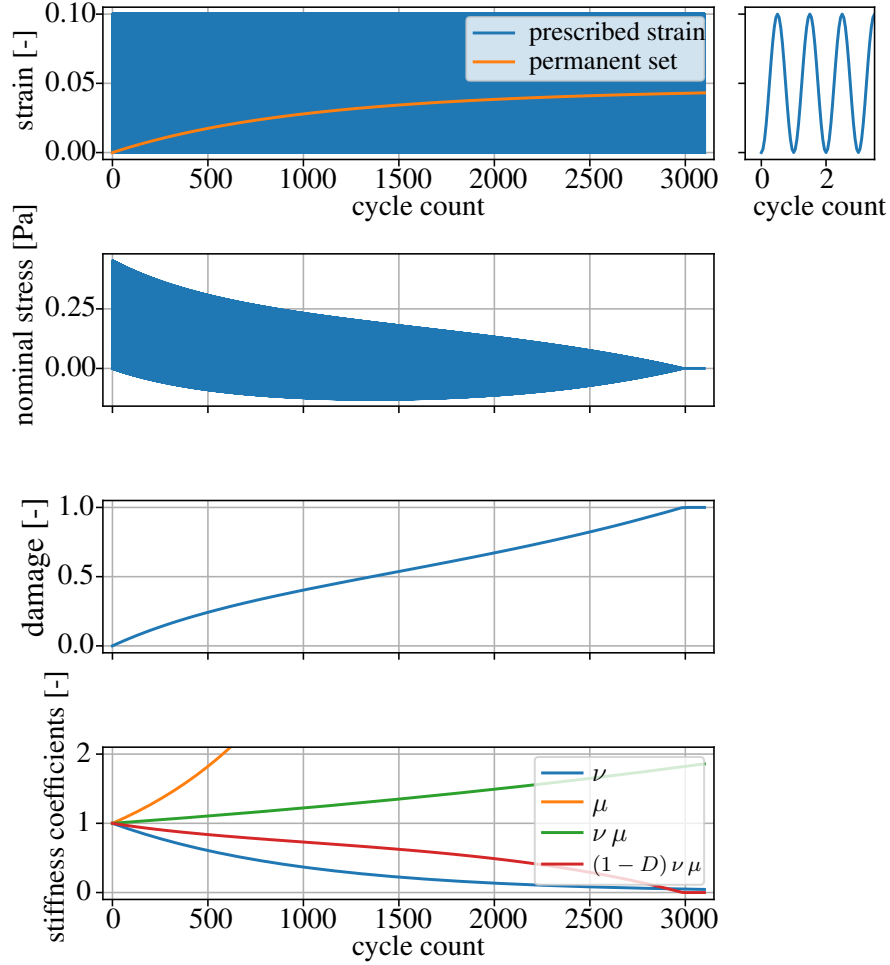


Fig. 1. Uniaxial tension

Fatigue damage is represented by the variable D , whose evolution is given by

$$\dot{D} = (-AY)^a, \quad Y = \frac{\partial \psi}{\partial D} = C_{10} \mu \nu (\bar{\mathbf{C}} : \mathbf{C}_1^{-1} - 3), \quad (5)$$

where A and a are material parameters.

In order to illustrate the working of the model, an example of homogeneous uniaxial tension is presented. Nominal strain in the form $\varepsilon(t) = 0.1 \sin^2(2\pi t)$ is prescribed in the direction of loading, while zero true stress is assumed in the other directions. Fig. 1 shows the resulting nominal stress, damage variable, permanent set, and stiffness parameters.

Acknowledgement

This work was supported by the students grant system SGS-2016-038.

References

- [1] Ayoub, G., Naït-abdelaziz, M., Zaïri, F., Gloaguen, J. M., Multiaxial fatigue life prediction of rubber-like materials using the continuum damage mechanics approach, *Procedia Engineering* 2 (2010) 985–993.
- [2] Naumann, C., Chemically-mechanically coupled modelling and simulation of oxidative aging processes in rubber components, Ph.D. Thesis, Technische Universität Chemnitz, 2016. (in German)

The guided waves modelling: A spectral method approach

P. Hora^a

^a*Institute of Thermomechanics, Czech Academy of Sciences, Veleslavínova 11, 301 14 Plzeň, Czech Republic*

Guided elastic waves are used extensively in the nondestructive evaluation (NDE) of various structures. An important step in the development of inspection techniques is the accurate and efficient calculation of dispersion curves [2].

Traditionally, mode dispersion was studied by finding roots of analytical dispersion equations. For example, the thick cylindrical bar dispersion relation $f(x, \gamma a)$ for axisymmetric motion is defined as

$$(2 - x^2)^2 J_0(\gamma a A) J_1(\gamma a B) + 4AB J_1(\gamma a A) J_0(\gamma a B) - \frac{2x^2}{\gamma a} A J_1(\gamma a A) J_1(\gamma a B) = 0,$$

where a is radius of the semi-infinite bar, γ is wavenumber, x is the ratio of the phase velocity and the shear wave velocity, κ means the ratio of the squares of the phase velocities for the bar's material, $A = \sqrt{\kappa x^2 - 1}$, $B = \sqrt{x^2 - 1}$ and J is the Bessel function of the first kind.

The resulting dispersion curves are shown (for Poisson's number 0.3) in the Fig. 1 using solid gray lines.

An alternative approach to model two-dimensional circular structures was recently introduced by Adamou and Craster [1] based on spectral methods. The idea of this method is to solve the underlying differential equations by numerical interpolation using orthogonal polynomials and spectral differentiation matrices.

The spectral method approach for a free solid cylinder consists of the following steps:

1. The formulation of the underlying equations in cylindrical coordinates.
2. The formulation of the eigenvalue problem.
3. The solution of the eigenvalue problem for an elastic cylinder by means of the spectral method.

We will show the results of this approach in the form of dispersion curves. In Fig. 1 – black dots, the dispersion curves for a free solid cylindrical bar are computed for Poisson's number $\mu = 0.3$ and number of discretization points $N = 60$. These curves (dots) are in excellent agreement with the dispersion curves, which were calculated analytically using *root-finding* techniques. The only defect in beauty is low frequency behaviour that is caused by the singularity in cylindrical coordinates ($1/r$). In the cylinder, you need to drill a small hole.

Traditional techniques require finding complex roots of nonlinear equations that involve special functions. In contrast, spectral method demands only solving generalized eigenvalue problem without involving special functions.

For numerical experiments were used MATLAB's toolbox CHEBFUN [3] and Julia's package ApproxFun [4].

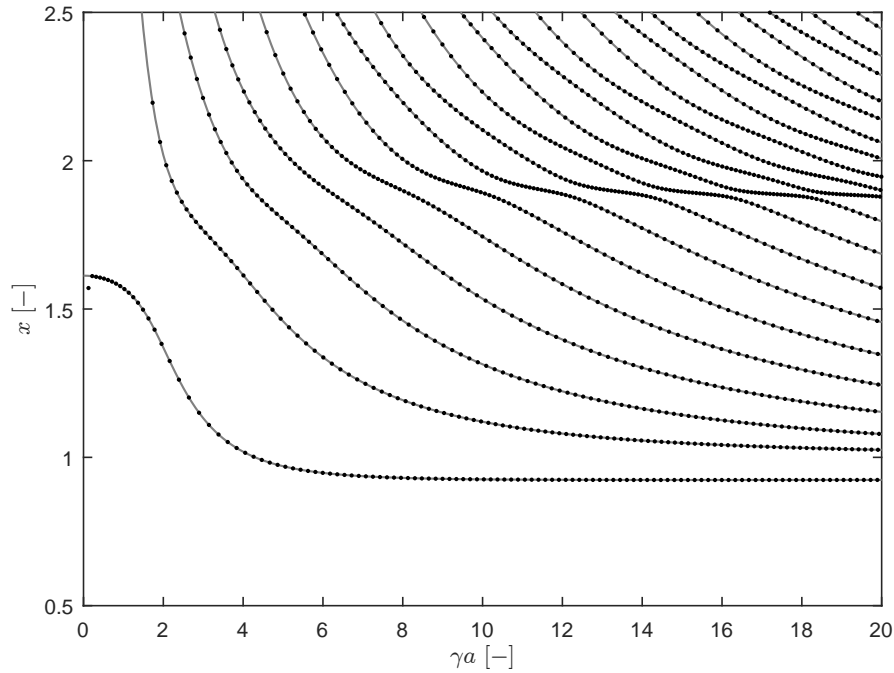


Fig. 1. Dispersion curves: analytical method (gray solid) and spectral method (black dots)

Acknowledgement

The work was supported from European Regional Development Fund-Project CeNDYNMAT, CZ.02.1.01/0.0/0.0/15_003/0000493.

References

- [1] Adamou, A. T. I., Craster, R. V., Spectral methods for modelling guided waves in elastic media, *Journal of the Acoustical Society of America* 116 (2004) 1524–1535.
- [2] Chimenti, D. E., Guided waves in plates and their use in materials characterization, *Applied Mechanics Review* 50 (1997) 247–284.
- [3] Driscoll, T. A., Hale, N., Trefethen, L. N. (editors), *Chebfun Guide*, Pafnuty Publications, Oxford, 2014.
- [4] URL: github.com/ApproxFun/ApproxFun.jl.git

FE analyses and experimental validation of heat distribution during hole drilling

Z. Horak^a, P. Tichy^b, T. Goldmann^b, M. Vilimek^b

^aDepartment of Technical Studies, College of Polytechnics Jihlava, Tolsteho 16, 586 01 Jihlava, Czech Republic

^bDepartment of Mechanics, Biomechanics and Mechatronics, Czech Technical University in Prague, Technicka 4, 166 07 Prague, Czech Republic

The aim of created numerical FE simulations were heat production analysis of drill during hole drilling into the polyurethane (PUR) foam cylinder. Heating was produced by the friction of the alloy drill on the PUR foam.

Simulations were modelled as the nonlinear contact task, where contact was defined among hole surface and outer drill surfaces. Heating was produced by the friction of the alloy drill on the PUR foam. All analyses were defined as the static, coupled thermal-displacement simulations with nonlinear contact definition. Geometry of the PUR sample was designed as solid cylinder dimensions $\varnothing 10 - 8$ mm with blind hole (see Fig. 1b).

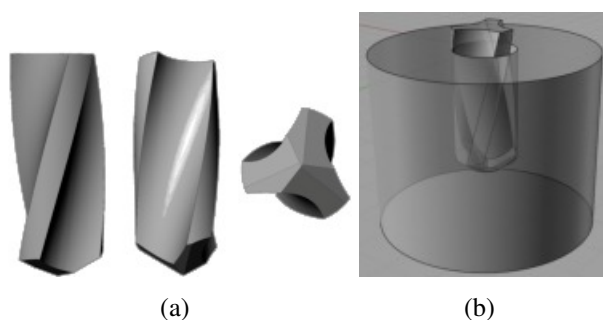


Fig. 1. a) Analyzed drill design, b) assembly of the drill and PUR sample for FE analyses

In FE analyses were used homogeneous and isotropic materials models (see Table 1). Friction coefficients for PUR foam were used 0.7 (20°), 0.3 (50°), 0.2 (100°). Analysed model was loaded by displacement and rotational boundary conditions. FE analyses were set so that correspond closely with the experiments carried out [2]. Drill was loaded by the axis displacement U_z and rotation angle UR_z . Size of the displacement U_z correspond with the drill axial movement during drill rotation about 90°. Contact formulation was normal hard contact, with friction coefficient dependent on temperature.

Temperature and stress distribution on the drill are shown on Fig. 2. Maximal temperature is placed on outer side of cutting edge. On Fig. 2b is shown that heating on PUR foam is produced on the cutting face together with cutting edge on cylinder surface. Maximal temperature is $T = 90.6^\circ\text{C}$ on drill and $T = 90.4^\circ\text{C}$ on PUR foam. Reduced stress distribution on drill is uniform and maximal magnitude was $\sigma_{red} = 290.8$ MPa.

Realised FE analyses were focused only to friction problem and drill geometry optimization towards to heat reduction. Generally drilling is more complicated process, were are acted more

Table 1. Material properties for stainless alloy 1.4112 and PUR foam

Material	Density [kg.m ⁻³]	Thermal conductivity [W.m ⁻¹ .K ⁻¹]	Thermal expansion [10 ⁻⁶ .K ⁻¹]	Specific heat [J.kg ⁻¹ .K ⁻¹]	Young's modulus [MPa]	Poisson's ratio [-]
PUR foam	640	0.02216	63	1 500	759	0.3
alloy 1.4112	7 700	24	10	460	200 000	0.3

factors [1]. Nevertheless results obtained from FE analyses have very good correlation with data obtained from experimental measurements. Maximal temperature obtained from FEA is higher by 5.3% then maximal temperature obtained from experiments. Therefore we can conclude, that realised numerical simulations are close to the real situation.

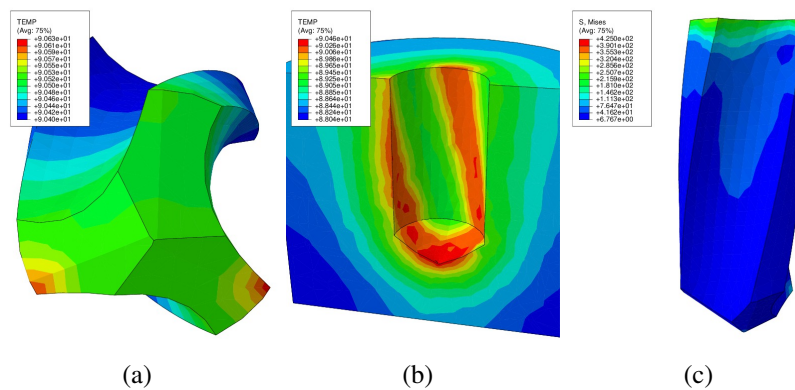


Fig. 2. a) Temperature T [°C] distribution on the drill, b) temperature distribution PUR sample, and c) reduced stress σ_{red} [MPa] distribution on the drill

Acknowledgement

This work was supported by The Czech Science Foundation project: "Evaluation and modelling of thermal field during machining of non-metallic materials", No. GA17-25821S.

References

- [1] Abukhshim, N. A., Mativenga, P. T., Sheikh, M. A., Heat generation and temperature prediction in metal cutting: A review and implications for high speed machining, *International Journal of Machine Tools and Manufacture* 46 (7-8) (2006) 782–800.
- [2] Lei, S., Shin, Y. C., Incroper, F. P., Thermo-mechanical modeling of orthogonal machining process by finite element analysis, *Tribology International* 39 (5) (1999) 731–750.

Experimental and numerical research of the structure made of geopolymer composite

A. Hrouda^a, L. Paur^a

^a Faculty of Mechanical Engineering, Technical University of Liberec, Studentská 2, 461 17 Liberec, Czech Republic

The composite materials with geopolymer matrix are materials, which are claimed to composite materials with very good material properties, such as low weight, high stiffness, strength and also temperature resistance [2, 4]. Geopolymers are a class of amorphous aluminosilicate materials composed of cross-linked AlO_4 and SiO_2 which form polysialates with alkali metal ions. Subject of our research was to investigate some of these properties and later to use them for the experiment with the loading of the circular plate. Two types of geopolymer matrix were used in our research with working title B3P1 and FC4. For the reinforcement phase, basalt fabrics was used.

For the purpose of research of the geopolymer composite material, the samples in the form of plates with rectangular cross section were prepared. This has been done by hand lay-up process in laboratory conditions, where basalt fabrics were laid up upon each other and saturated with geopolymer matrix. After that the samples stayed compressed in plastic bags for one month. Firstly has been done a tensile test for the standalone basalt fabric to estimate its influence on the whole geopolymer material. This has shown, that the ultimate strenght of the fabric decreaseas after the termal treatment (500 °C for the time span 30 minutes), that means the temperature influences geopolymer properties. These tests were also made firstly under ambient temperature (23 °C) and than after the thermal treatment (500 °C for the time span 30 minutes). Tensile test was made on the tensile testing machine and the deformation speed was set on the velocity of 5 mm/min. Three point bending test was done on the tensile testing machine (Fig. 1) and the deformation speed was also 5 mm/min. The sample had rectangular shape and rectangular cross section and the supports distance was 150 mm. Shear test was made also on the tensile testing machine. The shear test was made just under ambient temperature and was made according to the Arcans model [1]. These tests have shown differencies between both matrices and also the influence of the thermal treatment as shown in Fig. 2.

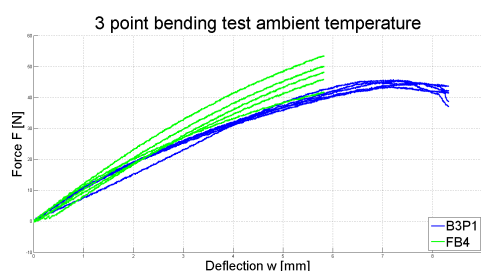


Fig. 1. Bending test matrix B3P1 and FC4

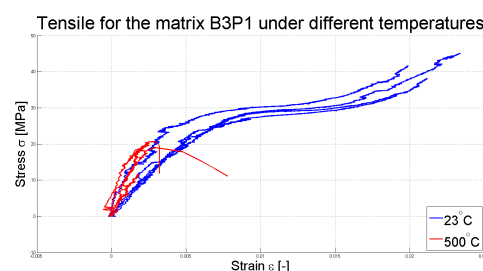


Fig. 2. Tensile test for the matrix B3P1

The last phase of the research was focused on the experiment with circular plate. This plate was cut out of the geopolymer matrix FC4 and was built-in during the experiment on its outer edge by a flange and series of bolts. The plate was loaded in its center by a spherical shaped indenter. The experiment also took place on the testing machine and was controlled by displacement and the force was measured. The experimental setting is shown in the Fig. 3. This experiment was then simulated by two different numerical approaches. The first one was the Ritz Method based on variational principle [3]. This method was programmed in the Matlab software. The second approach was the finite element method, which should simulate the real experiment. For the indenter, the displacement was defined as the result was solved the reaction force between plate and indenter. For the purpose, a chart was made for the comparison of these two methods which shows, how well these two methods correlate with the measured experimental data, as shown in Fig. 4. The conclusion was made, then the two models correlate pretty well for the smaller deformations, for the bigger deformations the Ritz correlates better with the experimental data.

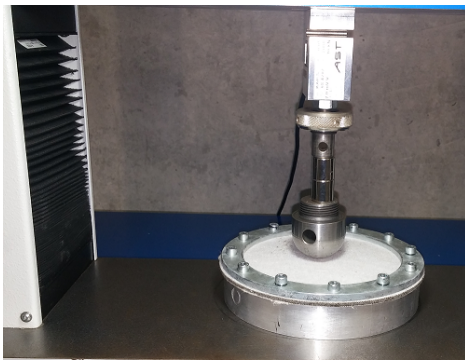


Fig. 3. Experimental set-up

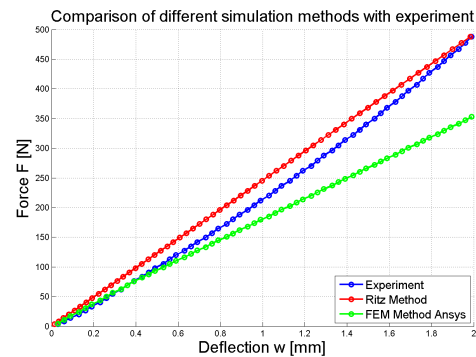


Fig. 4. Comparison of the results

Acknowledgements

This article was written at the Technical University of Liberec, Faculty of Mechanical Engineering with the support of the Institutional Endowment for the Long Term Conceptual Development of Research Institutes, as provided by the Ministry of Education, Youth and Sports of the Czech Republic in the year 2017.

References

- [1] Arcan, M., Hashin, Z., Voloshin, A., A method to produce uniform plane-stress states with applications to fiber-reinforced materials, *Experimental Mechanics* 18 (4) (1978) 141–146.
- [2] Krystek, J., Laš, V., Pompe, V., Hájková, P., Influence of temperature on selected mechanical properties of geopolymer composites, *Proceedings of the 55th Conference on Experimental Stress Analysis – EAN2017*, Nový Smokovec, Slovakia, 2017.
- [3] Lekhnitskii, S. G., *Anisotropic plates*, New York: Gordon and Breach, 1968.
- [4] Petříková, I., Marvalová, B., Hrouda, A., Paur, L., Properties of composites with geopolymer matrix reinforced by basalt fabric, *Proceedings of the 55th Conference on Experimental Stress Analysis – EAN2017*, Nový Smokovec, Slovakia, 2017.

Akaike information criterion and cartilage models

B. Hučko^a, M. Bényi^a, R. Jančo^a, M. Musil^a

^a Faculty of Mechanical Engineering, Slovak University of Technology in Bratislava, Nám. Slobody 17, 81321 Bratislava, Slovakia

Until now many different biomechanical models of cartilage have been developed from hyperelastic, poroelastic models to biphasic models [3]. They differ from each other by the number of parameters that affect the efficiency and quality of the calculations. To achieve the optimal ratio between the efficiency and the quality we can apply information criteria. We have applied Akaike information criterion (AIC) in our study for the cartilage model [1]. The numerical cartilage model was based on the multi-parametric Mooney-Rivlin model. Using experimental results and AIC the optimal number of parameters for the cartilage model has been determined.

The experimental method of dynamic biomechanical properties testing employs an approach, based on drop-weight impact sample deformation examination [4]. A pendulum-like apparatus setup enables tracking of material response to single impact. Rapid increase of acting force should resemble physiological joint cartilage loading. Sample deformation is read simultaneously by piezoelectric accelerometer and Laser Doppler Vibrometer LDV, see Fig 1.

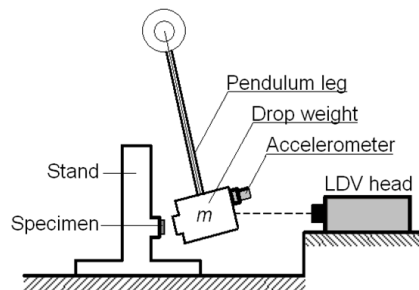


Fig. 1. Experimental setup

The experimental results are represented by experimental stress- strains curve, see Fig. 2.

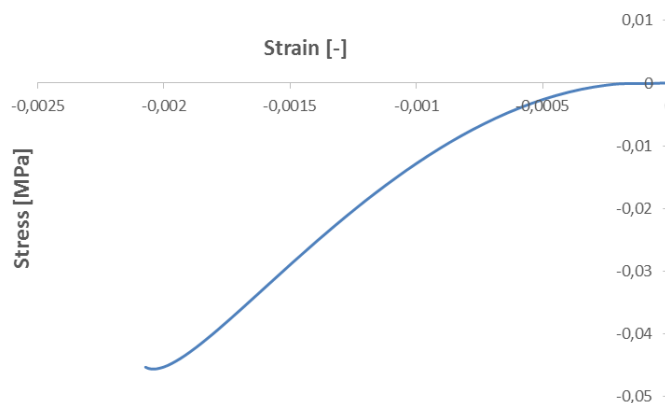


Fig. 2. Experimental stress-strain curve

The next step is using curve fitting for experimental curves to determine the corresponding parameters. This approach has been applied for the multi-parametric Mooney-Rivlin model. The models with 2, 3, 5 and 9 parameters have been tested.

To assess the quality of each model we tried to build numerical models in ANSYS Workbench [2]. The numerical models reflect the experimental tests, Fig. 3.

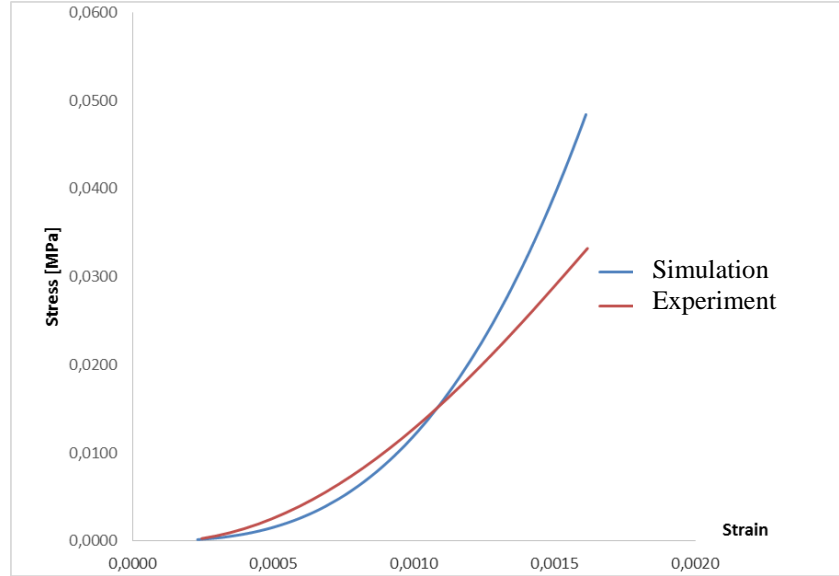


Fig. 3. Comparison stress – strain curves for 5-parametric model

Then we applied AIC in the form as follows

$$AIC = n \cdot \ln(\hat{\sigma}^2) + 2(k + 1),$$

where

$$\hat{\sigma}^2 = \sum_{i=1}^n (y_{cal} - y_{exp})^2 / n$$

and n is number of testing points, k is number of model parameters. The smallest AIC represents the best model. The smallest value of $AIC = -372$ has been reached for 3-parametric Mooney-Rivlin model.

Acknowledgements

This work has been supported by the grant project KEGA 060STU-4/2016. The authors greatly appreciate this support.

References

- [1] Akaike, H., Akaike's information criterion, International Encyclopedia of Statistical Science, Springer, 2014.
- [2] ANSYS Workbench, Version 14.
- [3] Mow, V. C., Kuei, S. C., Lai, W. M., Armstrong, C. G., Biphasic creep and stress relaxation of articular cartilage in compression: Theory and experiments, Journal of Biomechanical Engineering 102 (1980) 73-84.
- [4] Varga, F., Drzík, M., Handl, M., Chlpík, J., Kos, P., Filová, E., Rampichová, M., Necas, A., Trc, T., Amler, E., Biomechanical characterization of cartilages by a novel approach of blunt impact testing, Physiological Research 56 (S1) (2007) S61-S68.

Motorcyclist barrier impact: A comparative study

L. Hynčík ^a, T. Bońkowski ^a, J. Vychytil ^b, J. Špička ^c

^a Faculty of Applied Sciences, University of West Bohemia, Univerzitní 8, 306 14 Plzeň, Czech Republic

^b New Technologies – Research Centre, University of West Bohemia, Univerzitní 8, 306 14 Plzeň, Czech Republic

Road traffic accidents cause one of the highest numbers of severe injuries. Virtual human body models play an important role to assess injuries during impact loading especially for scenarios, where complex dynamical loading is taken into account. It concerns mainly vulnerable road users, where motorcyclists are also addressed. The presented work shows exploitation of virtual human body model in barrier impact analysis.

Currently, there are several national standards and test protocols related to the assessment of the protection provided by barriers to motorcyclists coexisting in Europe [4]. There are small differences for testing in France, Germany, Italy and Spain. The impact tests defined by the protocols run usually with an anthropomorphic test device (ATD) or crash test dummy lying on its back and impacting the barrier by the angle 30 degrees and the velocity 60 km/h. The ATD used in the protocol is dressed up with motorcyclist protective clothing and helmet and head and neck performance is monitored. As the approach towards harmonization, CEN [1] developed The European Technical Specification (TS) CEN TS 1317 – 8, which defines full-scale impact test consisting of launching a dummy at a given speed against a barrier as shown in Fig. 1. TS1317-8 also considers two severity levels I and II.

Since the barrier impact testing concerns complex motion of the human body at high velocities addressing also personal protective equipment, virtual simulations appear to be a suitable tool for assessing such impact and designing safe barriers. For running the barrier impact, the Virthuman model, which was previously developed and tested for complex impact scenarios [5], is coupled to helmet [2, 3]. At the current stage, there is no any special protective clothing and the contact between the Virthuman model and the protective clothing is given only by the contact friction. The protective clothing considerably influences the ROM of particular joints, however, for the present situation, the influence is negligible due to the fact that the extremities stay along the body.

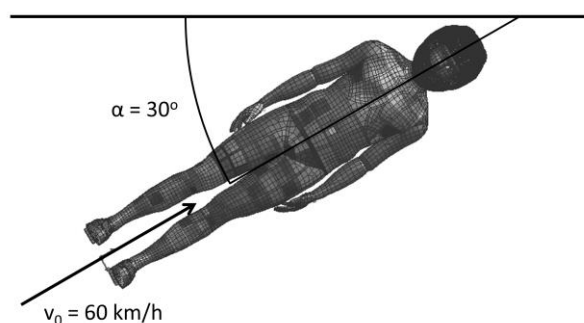


Fig. 1. CEN TS 1317 – 8 barrier test setup

The Virthuman model is positioned according to the experimental test setup and impact is run by the initial velocity equal to 60 km/h against the barrier at the angle equal to 30 degrees (see Fig. 1). The work does not address any particular barrier used in the current infrastructure, a fictitious barrier is considered as a continuous system [4] made by simple iron plate ($E = 210$ GPa, $\nu = 0.3$, $\gamma = 200$ MPa) just in order to show the performance of the model and its exploitation for such kind of test.

Table 1 shows the performance of the virtual human body model. The resulting numbers lie usually above the limits, but as was stated above, the considered barrier is developed just for exploiting the existing human body in the barrier impact scenario.

Table 1. CEN TS 1317 – 8 critical values

Body region	Parameter	Severity level	Limit	Simulation
Head	HIC ₁₆	I	650	2420
		II	1000	
Neck	Lateral flexion	I	134 Nm	254 Nm
		II	134 Nm	
	Extension	I	42 Nm	180 Nm
		II	57 Nm	
	Flexion	I	190 Nm	191 Nm
		II	190 Nm	

The work shows the exploitation of the existing human body model Virthuman in the safety barrier assessment. The fictitious barriers were used, where the human body model was positioned according to CEN TS 1317 – 8. After running the impact at velocity 60 km/h, particular output was correlated to CEN TS 1317 – 8. The work shows the potential of virtual human body models for developing and designing safe infrastructure.

Acknowledgements

The work has been supported by the research project LTC17001 “Exploitation of virtual human model for reducing injury risk of PTW riders” as the national link to the COST Action TU1407 “Scientific and technical innovations for safer Powered Two Wheelers (PTW)” and the internal grant project SGS-2016-059 “Computer modelling and monitoring of human body used for medicine”.

References

- [1] European Committee for Standardization, <https://www.cen.eu>.
- [2] Ghajari, M., Galvanetto, U., Iannucci, L., Wilinger, R., Influence of the body on the response of the helmeted head during impact, *International Journal of Crashworthiness* 16 (3) (2011) 285-295.
- [3] Ghajari, M., Peldschus, S., Galvanetto, U., Iannuccia, L., Effects of the presence of the body in helmet oblique impacts, *Accident Analysis and Prevention* 50 (2013) 263–271.
- [4] Lopez-Valdes, F. J., Vaa, T., Ferrer, A., Molinero, A., Hernando, A., Road barriers: State of the art, Deliverable no. 3.1a, COST Action TU1407, 2017.
- [5] Vychytil, J., Mañas, J., Čechová, H., Špirk, Hynčík, L., Kovář, L., Scalable multi-purpose virtual human model for future safety assessment, *SAE Technical Paper* 2014-01-0534, 2014, doi:10.4271/2014-01-0534.

Experimental and numerical solution of friction stir welding

R. Jančo ^a, P. Élesztős ^a, L. Écsi ^a

^a Institute of Applied Mechanics and Mechatronics, Faculty of Mechanical Engineering, Slovak University of Technology in Bratislava, Nám. slobody 17, 812 31 Bratislava, Slovak Republic

Friction stir welding (FSW) is a relatively new joining technology which was developed and patented in 1991 by The Welding Institute (TWI), United Kingdom [1]. This is a solid state welding process providing good quality of butt and lap joints. The FSW process has been proved to be ideal for creating high quality welds in a number of materials, including those which are extremely difficult to weld by conventional fusion welding. A schematic of the friction stir welding process is illustrated in Fig. 1.

The welding zone is completely isolated from the atmosphere during the welding process. The advantages of this type of welding are minimized formation of voids in the welding zone, so that welding defects and large distortions commonly associated with fusion welding are minimized or avoided. This welding technique is extensively applied in the aerospace, automobile and shipbuilding industries [2–5].

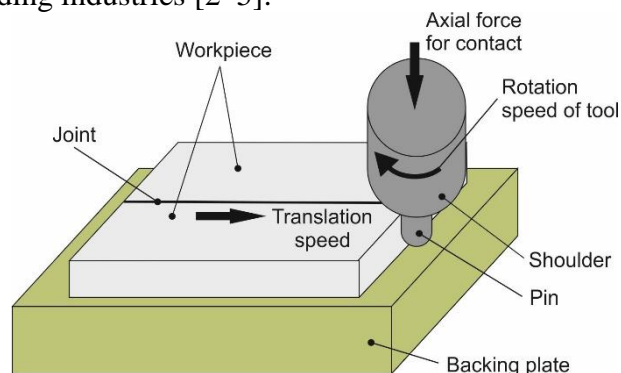


Fig. 1. Schematic diagram of FSW

The aim of this paper is to describe the thermal-fluid-mechanical simulation of FSW using the finite element method and by controlling the temperature at given points. The numerical solved points are compared by experimental data measured.

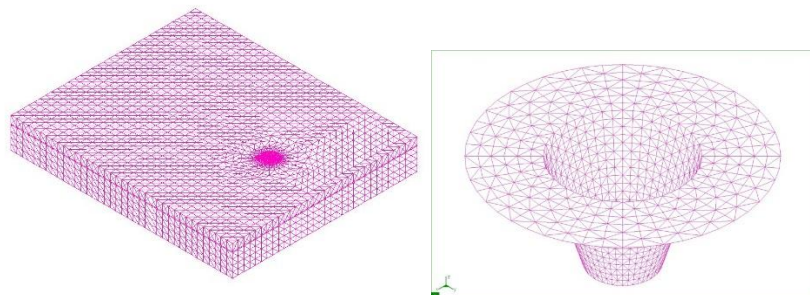


Fig. 2. FEM model of the sheet and backing plate and the FEM model of the tool

In Fig. 2, a finite element model of the sheet and backing plate and the finite element model of tool are presented. The SYSWELD® solution results are presented in Fig. 3.

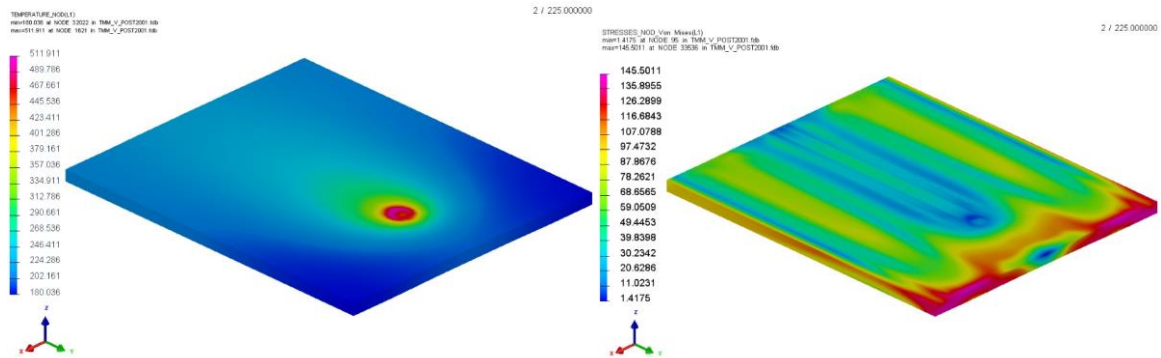


Fig. 3. Temperature field (°C) and Von Mises stress field (MPa) at time 225 s

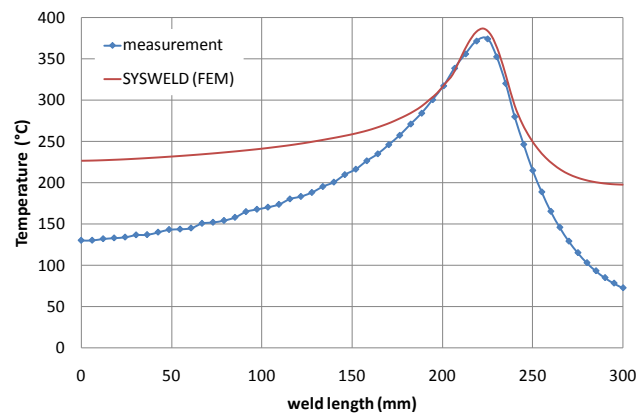


Fig. 4. Comparison of temperature measurements with a numerical solution

The computer modelling and measurements of the temperature and stress evolution in the FSW of AlMg4.5Mn0.7 Al alloy is conducted, and the experimental values validate the efficiency of the proposed model, see Fig. 4.

Acknowledgements

This publication is the result of the project implementation: Research of friction stir welding (FSW) application as an alternative to melting welding methods no. 26240220031 supported by the Research & Development Operational Programme funded by the ERDF. The paper was supported by the grant from Grant Agency of VEGA no. 1/0740/16 titled "Mathematical model proposal for numerical simulation of creep behavior of TiAl intermetallic alloys".

References

- [1] Chen, C. M., Kovacevic, R., Finite element modeling of friction stir welding – thermal and thermomechanical analysis, *International Journal of Machine Tools & Manufacture* 43 (2003) 1319-1326.
- [2] Frigaard, Ø., Grong, Ø., Midling, O. T., A process model for friction stir welding of age hardening aluminium alloys, *Metallurgical and Materials Transactions A* 32A (2001) 1189-1200.
- [3] Feulvarch, E., Robin, V., Boitout, F., Bergheau, J. M., 3D modelling of thermofluid flow in friction stir welding including metallurgical and mechanical consequences, *Mathematical Modelling of Weld Phenomena* 8 (2007) 1-24
- [4] Jančo, R., Écsi, L., Élesztős, P., FSW numerical simulation of aluminium plate by Sysweld – Part I., *Journal of Mechanical Engineering – Strojnický časopis* 66 (1) (2016) 47-52.
- [5] Jančo, R., Écsi, L., Élesztős, P., FSW numerical simulation of aluminium plate by Sysweld – Part II., *Journal of Mechanical Engineering – Strojnický časopis* 66 (2) (2016) 29-36.

Sensitivity analysis of laser drawing process of Mg tubes

E. Janouchová^a, M. Lepš^a

^a*Faculty of Civil Engineering, Czech Technical University in Prague, Thákurova 7, 166 29 Praha 6, Czech Republic*

Although magnesium alloys are widely used in the industry they suffer from low ductility at room temperature which causes technological difficulties. New production processes need to be developed mainly for small elements like tubes of small dimensions. This contribution aims to a novel production technology based on laser dieless drawing process in which tubes (AZ31 alloy) are produced from previously extruded tubes of a larger diameter. The technological process involves local laser heating of a tube with concurrent drawing and rotation of a sample. However, the process is relatively sensitive and the setting of material parameters as well as the varying control parameters like drawing speed on tube ends, laser power or torque play a substantial role. In this contribution, the sensitivity of material models' parameters are evaluated and their influence on the resulting output from FEM analysis is evaluated.

First, the sensitivity and inverse analyses have been conducted to properly identify material parameters from available experimental data. The core of the material model consists of a flow stress model and a fracture criterion. The flow stress model for magnesium alloy is described with Hansel-Spittel equation [1]:

$$\sigma = A \exp(-m_1 t) \varepsilon^{m_2} \xi^{m_3} \exp\left(\frac{m_4}{\varepsilon}\right) (1 + \varepsilon)^{m_5 t} \exp(m_7 \varepsilon) \xi^{m_8 t} t^{m_9}, \quad (1)$$

where σ , ε , ξ , t are effective stress, effective strain, effective strain rate and temperature, respectively. The parameters A and m_1, \dots, m_9 should be specific for particular material and are usually sought by an inverse analysis procedure. Sensitivity analysis reveals that only four parameters play significant role, namely parameters A , m_1 , m_4 and m_9 . Next, Bayesian inference [2] was used to estimate these parameters from eight experimental curves obtained for different speed of loading and changing operational temperature. Obtained samples from Markov chains confirm sensitivity analysis results except that the parameter m_4 cannot be reliably identified from the experimental data. Mean values of input parameters are also in agreement with their optimal setting found out by optimization procedure [3].

The fracture criterion is based on the value of a critical strain. As long as a strain is smaller than a critical strain the material can be deformed without cracking

$$D = \frac{\varepsilon}{\varepsilon_p(k_\sigma, t, \xi)} < 1, \quad (2)$$

where D is a ductility function, ε_p a critical deformation function and k_σ is a triaxiality factor. The critical strain is calculated from the following equation depending on values of the triaxiality factor, temperature and strain rate

$$\varepsilon_p(k_\sigma, t, \xi) = d_1 \exp(-d_2 k_\sigma) \exp(d_3 t) \xi^{d_4}, \quad (3)$$

where d_1, \dots, d_4 are again phenomenological parameters. Although the sensitivity analysis predicts low influence of the d_2 parameter, Bayesian inference shows relatively narrow bounds for all parameters, see Fig. 1, and therefore, their importance is high. Moreover all the parameters except d_1 can be reliably obtained from the experimental data.

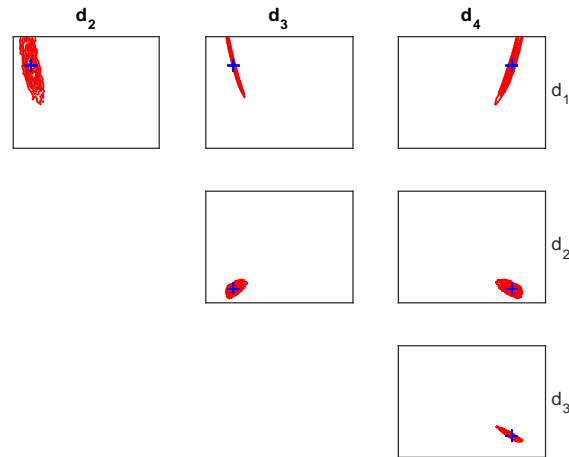


Fig. 1. Joint probability distributions of Markov chains for the ductility function; blue crosses are optimal values from direct identification [3]

Finally, a previously developed FEM model [3] is used for the evaluation of the numerical sensitivities of the process parameters. Almost half of the settings leads to a rupture of the specimen and only a very limited number of combinations of control parameters leads to a uniformly shaped tubes. As a next stage, an optimization procedure will be applied to obtain more uniformly formed samples.

Acknowledgement

Financial support of the Ministry of Education, Youth and Sports of the Czech Republic (Project No. 8F15004) (Project title: Multi scale model of the laser dieless drawing process of tubes from hardly deformable magnesium alloys, Project acronym: MgTubeDieLess, Visegrad Group (V4)-Japan Joint Research Program on Advanced Materials) is gratefully acknowledged.

References

- [1] Hansel, A., Spittel, T., Power and work requirements for plastic shaping methods, VEB Deutscher Verlag für Grundstoffindustrie, Lipsk, 1979. (in German)
- [2] Janouchová, E., Kučerová, A., Sýkora, J., Vorel, J., Wendner, R., Bayesian calibration of lattice discrete particle model for concrete, Proceedings of the conference REC 2016, Bochum, Germany, 2016, pp. 399–410.
- [3] Milenin, A., Kustra, P., Byrska-Wójcik, D., Plonka, B., Petráňová, V., Hrbek, V., Němeček, J., Numerical optimization and practical implementation of the tube extrusion process of Mg alloys with micromechanical analysis of the final product, Key Engineering Materials 716 (2016) 55–62.

Active vibration suppression using collocated pair of piezo-patches

J. Karlíček ^a, Z. Šika ^a, J. Volech ^a

^a Faculty of Mechanical Engineering, Czech Technical University in Prague, Technická 4, 16607 Prague, Czech Republic

In recent years elevated attention has been devoted to the field of active vibration control and smart structures. These structures often have multiphysical nature. In this paper simple steel cantilever beam with two piezoelectric actuators on top and one collocated piezoelectric sensor on bottom surface is considered. Some approaches of modeling piezoelectric components are presented in [3, 4]. In this paper finite element method via Ansys software is used. In addition, to solve this type of problems suitable control strategy needs to be chosen. There are described approaches based on LQR, LQG, H₂ and other regulators. In this work fixed order H-infinity regulator is used.

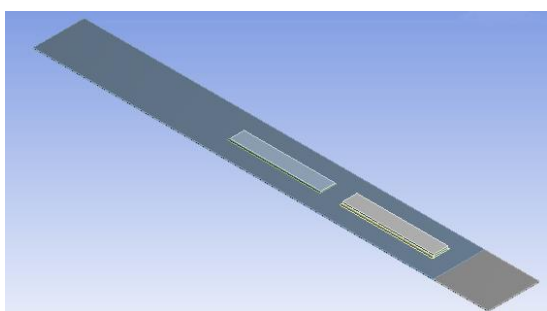


Fig. 1. FE model of clamped beam

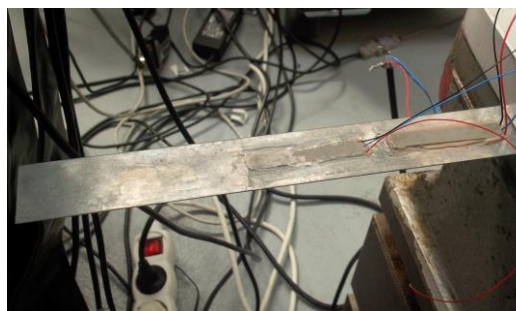


Fig. 2. Cantilever beam, view from top

The structure of steel clamped beam with dimensions 250x28x0.55 mm is chosen. To find out its basic behavior and especially its eigenfrequencies numerical model (Fig. 1) using Ansys Workbench and extension Piezo And MEMS was created. Modal analysis was performed and three first eigenfrequencies were acquired. Their values are apparent in 2nd row of Table 1.

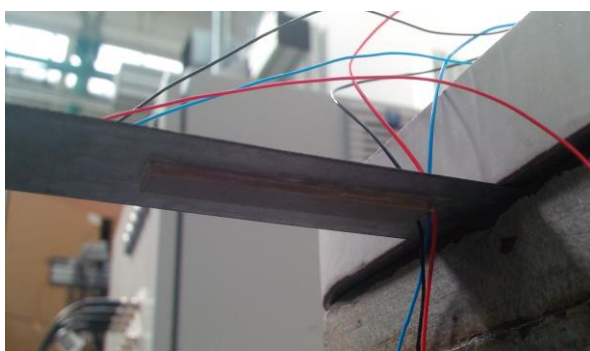


Fig. 3. Cantilever beam, view from bottom

Table 1. Comparison of eigenfrequencies of models

Eigenfrequency	1	2	3
FE model [Hz]	12.1	54.5	151.3
Identified model [Hz]	13.4	62.7	175.9

Experimental form of modeled structure is presented on Fig. 2 and Fig. 3. Near clamped end there is a pair of collocated piezo patches. Patch on the top (Act1) is used to suppress the vibration generated by 2nd patch (Act2) on the top surface further from clamped end. Bottom patch is used as a sensor, generating voltage, when the beam is deformed. Based on measured data discrete model of 14th order in state-space form was identified. Simulated and measured sensor voltage is illustrated on Fig. 4. Eigenfrequencies of identified model compared to the FE model are in Table 1.

Based on identified model H-infinity regulator of 5th order was designed using the HIFOO package [1, 2] for Matlab. Performance of this regulator was studied by simulation and experiment. Sinusoidal voltage with frequency 80 Hz was chosen for Act2 to generate vibration of the beam in experiment. Fig. 5 describes response of sensor to this excitation.

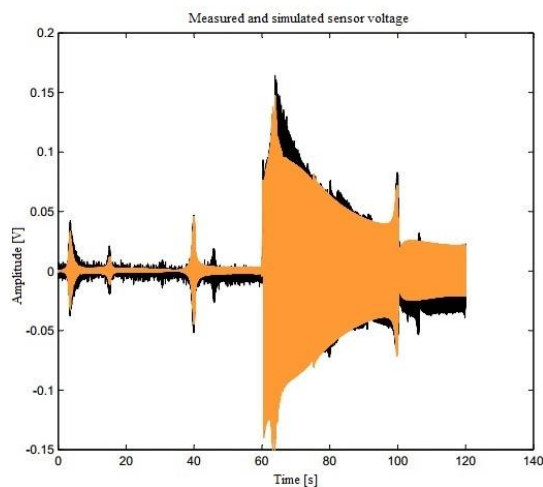


Fig. 4. Sensor voltage during excitation with CHIRP signal from Act2 in first 60 sec and from Act1 in last 60 sec. Simulated (orange) and measured (black)

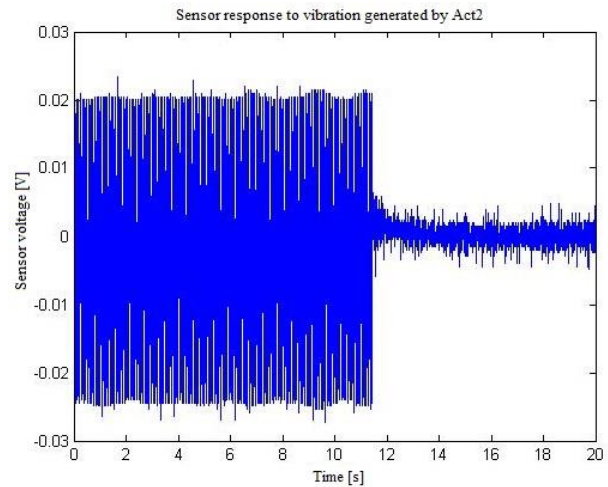


Fig. 5. Response voltage of sensor to vibration generated by Act2 without control (until 11.5 sec) and with control (after 11.5 sec) in experiment

On Fig. 5 approximately 80% reduction of sensor voltage is noticeable when regulator is turned on. Further development in this field could lead to more complex structures with many piezoelectric components and more efficient control strategies.

Acknowledgement

The presented research has been supported by the Czech Science Foundation under the project Mechatronic structures with heavily distributed actuators and sensors, No. 16-21961S.

References

- [1] Arzelier, D., Deaconu, G., Gumussoy, S., Henrion, D., H2 for HIFOO, Proceedings of the International Conference on Control and Optimization with Industrial Applications, Bilkent University, Ankara, Turkey, 2011.
- [2] Gumussoy, S., Henrion, D., Millstone, M., Overton, M., Multiobjective robust control with HIFOO 2.0, Proceedings of the IFAC Symposium on Robust Control Design, Haifa, 2009.
- [3] Preumont, A., Mechatronics - dynamics of electromechanical and piezoelectric systems, Springer, Dordrecht, 2006.
- [4] Preumont, A., Vibration control of active structures, Springer, Dordrecht, 2011.

Pressure relationship in the area of hemodialysis access when determining the blood flow rate through the vein using the dilution method

M. Kašpárek ^a, L. Nováková ^a, J. Adamec ^a

^a Faculty of Mechanical engineering, Czech Technical University in Prague, Technická 4, 166 07 Prague, Czech Republic

Monitoring sufficient volume flow rate through the supply vein during hemodialysis is one of the important operations used to diagnosing the correct functioning of the vascular access. Commonly, volume flow rate through the vascular access is measured by the dilution method [2]. The principle of this method is to introduce a contrast medium into the patient's body using hemodialysis needles. During this procedure the needles are inserted in the opposite configuration than at the hemodialysis. This paper deals with the change in the pressure relationship in the hemodialysis access using a dilution method for blood volume flow rate measurement in hemodialysis access.

Two needles are inserted into the vascular access during hemodialysis. Needles are inserted into the vein in two different settings, either in the retrograde setting (Fig. 1a) or anterograde setting (Fig. 1b).

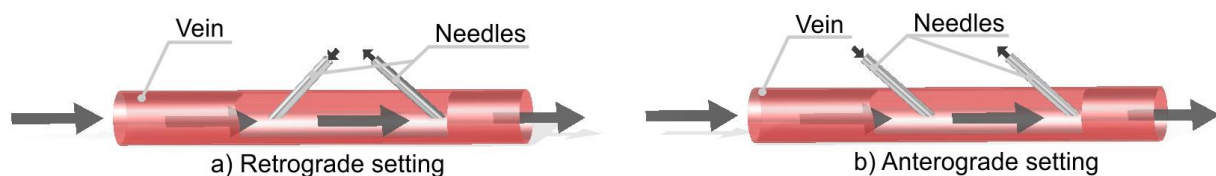


Fig.1. Types of insertion of needles to vascular access

Experimental model of an arm with a hemodialysis access and a hemodialysis circuit is described in this paper. In the experiment, arm (11 970 Pa) and periphery of arm (5 320 Pa) pressure drop were set for volume flow rate 150 ml/min [1]. Two flexible models of venous access with anterograde and retrograde setting of insertion of needles have been examined. The solution of distillate water and glycerin in weight ratio (distilled water: glycerin) 55:45 was used as working fluid [3]. This solution has the similar viscosity to the blood - $4.2 \cdot 10^{-3}$ Pa.s [4]. Pressure measurements were performed for the volume flow rate 400, 500, 600, 700 and 800 ml/min in the vein, and volume flow rate in circuit of blood filtering 0, 185, 235 and 255 ml/min.

The experimental results are shown in Figs. 2 and 3. The graph on Fig. 2 shows the dependence of the pressure drop on venous flow rate at constant flow rate through the hemodialysis circuit. It can be seen from the graphs that the pressure drop increases with the increasing volume flow rate through the vein. Graphs show that the pressure drop for retrograde setting of needles is greater than the pressure drop for anterograde settings of needles. This behavior is in accordance with the expectations.

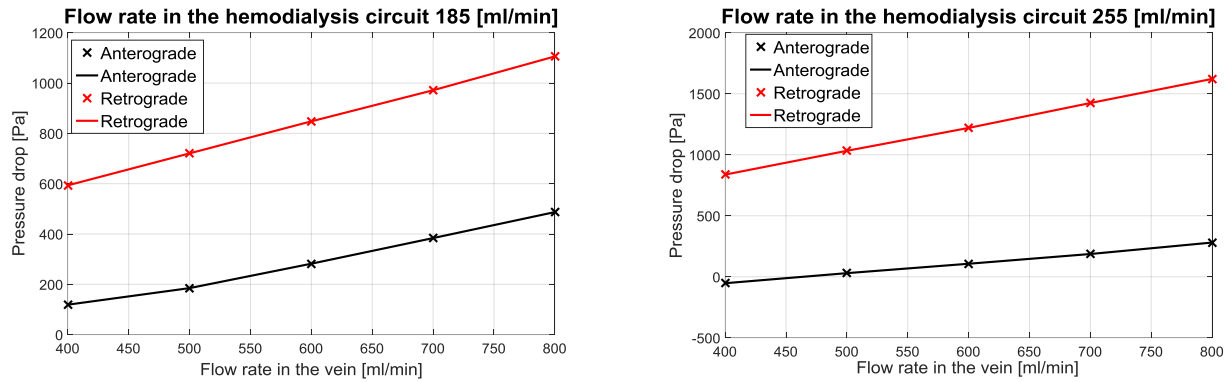


Fig. 2. Dependence of the pressure drop on venous flow rate

The graph on Fig. 3 shows the dependence of pressure drop on flow rate of hemodialysis circuit at constant venous flow rate. It can be seen from the graphs the different behavior of pressure drop for the both types of needle insertion settings. For the retrograde settings of needles, the pressure drop increases with the increasing volume flow rate through the hemodialysis circuit, but for the anterograde settings of needles, the pressure drop has the opposite tendency.

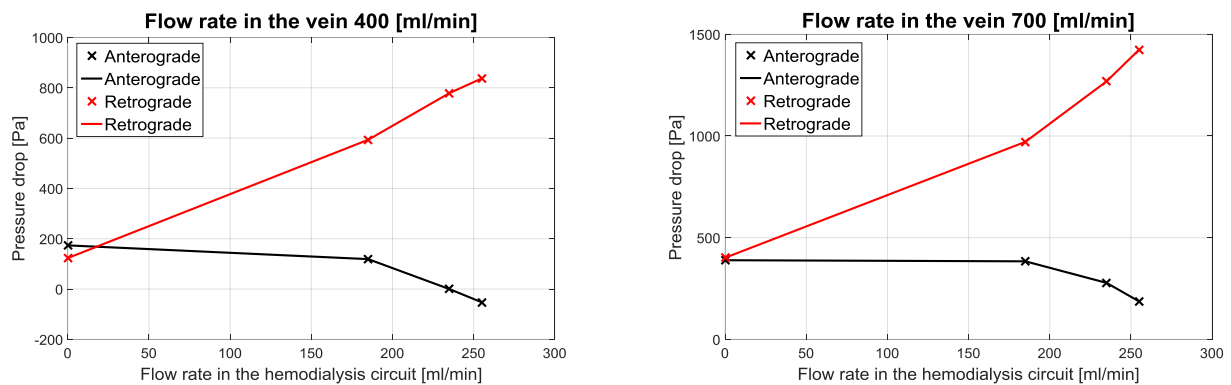


Fig. 3. Dependence of the pressure drop on flow rate of hemodialysis circuit

Experimental results show that the settings of insertion of needles greatly influence pressure drop. Retrograde setting has more significant pressure drop than anterograde setting. Our measurement shows that anterograde setting causes the decrease in pressure drop at increasing flow rate of hemodialysis circuit.

Acknowledgement

The work has been supported by the grant project SGS17/073/OHK2/1T/12.

References

- [1] Guyton, A. C., Hall, J. E., Textbook of medical physiology, Elsevier Saunders, Philadelphia, Pennsylvania, 2015.
- [2] Lopot, F., Influence of the arterial needle direction on access flow measurement, Proceedings of the 43rd ESAO Congress, Warsaw, 2016.
- [3] Segur, J. B., Oberstar, H. E., Viscosity of glycerol and its aqueous solutions, Industrial and Engineering Chemistry 43 (9) (1951) 2117-2120.
- [4] Yousif, M. Y., Holdsworth, D. W., Poepping, T. L., Deriving a blood-mimicking fluid for particle image velocimetry in Sylgard-184 vascular models, In: Engineering in Medicine and Biology Society, Proceedings of the EMBC 2009, Annual International Conference of the IEEE, 2009 Minneapolis, USA, IEEE, 2009, pp. 1412-1415.

Method for the preliminary design of the fan propulsion system

J. Klesa^a, Š. Piksa^a

^aFaculty of Mechanical Engineering, Czech Technical University, Karlovo náměstí 13, 121 35 Praha 2, Czech Republic

UL-39 ultralight aircraft has been developed at the Department of Aerospace Engineering, Czech Technical University in Prague. This aircraft is powered by unique propulsion system, which consists of a fan driven by piston engine. Design and optimization methods for single components are available in various textbooks, papers and reference works. However, unknown input parameters are required for the design of any of these components. Experience from the turbofan engines cannot be directly used due to the different characteristics of piston engine. This paper presents method for the computation of these input parameters. It is shown that almost constant fan power consumption at constant engine RPM can be reached for the speed range from 0 to maximum flight velocity, which means optimal usage of engine power.

Experience with the design of the fan propulsion system for the UL-39 aircraft (see Fig. 1) is described in [1, 3, 5]. The aircraft was developed from scratch at the Department of Aerospace Engineering. The combination of a fan powered by a piston engine was used so that the aircraft follows the requirements for the ultralight category (UL2 regulation).



Fig. 1. The first prototype of UL-39 aircraft during flight

Several methods for the preliminary design of the propulsion system were developed during past years. Energetic methods were used in these attempts [4]. However, the results were not satisfactory due to considerable difference between theoretical and experimental results. Thus the novel method for the preliminary design was developed. This contains simplified description of the fan characteristics according to [2] and includes also viscous losses in the flow duct and the flow acceleration in the nozzle. Unknown parameters of the propulsion system are the relative rotor outflow angle β'_1 (see Fig. 2) and nozzle velocity ratio k . The system of equations is solved numerically so that the fan has required power consumption P_{ref} for both flight velocity equals to 0 and maximum design velocity v_D .

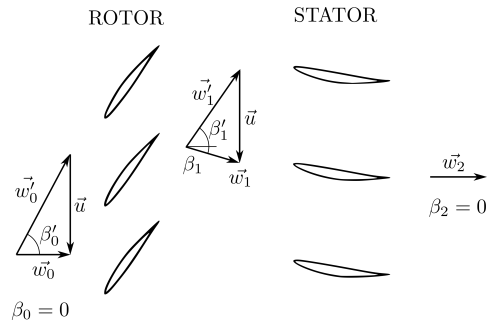


Fig. 2. Fan geometry at the reference radius

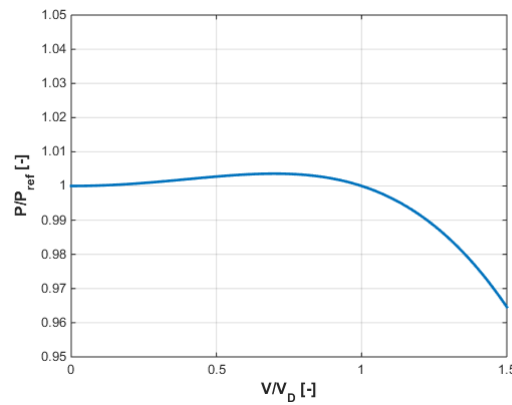


Fig. 3. Dependence of the fan power on the flight velocity

Result of the design procedure is presented in Fig. 3. The difference between required power P_{ref} and actual power P is less than 0.5% for the flight velocity in the range from 0 to v_D . This means that the requires almost constant power at constant engine speed for any flight velocity which means that engine power is optimally used during all phases of flight. This is reached by the means of the fixed geometry (i.e. no variable guide vanes or regulated nozzle is used) so that simplicity, low price and high efficiency can be reached simultaneously. This method is used for the design of the propulsion system for the second prototype of the UL-39 aircraft.

Acknowledgment

This work was supported by the Grant Agency of the Czech Technical University in Prague, grant No. SGS17/079/OHK2/1T/12.

References

- [1] Brabec, J., Helmich, M., Development of an ultralight with a ducted fan, Acta Polytechnica 52 (5) (2012) 138–143.
- [2] Cumpsty, N. A., Compressor aerodynamics, Longman, 1989.
- [3] Helmich, M., Static tests of unconventional propulsion units for ultralight airplane, Acta Polytechnica 54 (3) (2014) 183–190.
- [4] Jerie, J., Engine theory: Propulsion theory and internal aerodynamics of turbine engines, ČVUT, Praha, 1981. (in Czech)
- [5] Klesa, J., Helmich, M., Sommer, T., Comparison of various fan conceptions for light sport aircraft, Proceedings of the 7th EASN Conference, Warszawa, Poland, 2017.

Identification of material parameters of cork-rubber composite based on uniaxial and biaxial experiments

J. Kocáb^a, R. Kottner^a, J. Krystek^a

^a Faculty of Applied Sciences, University of West Bohemia, Univerzitní 8, 306 14 Plzeň, Czech Republic

Cork-rubber composites from a group of composition cork are modern materials with a wide variety of uses. They are used as a dumping and insulating layers in hybrid composite structures. Composition cork materials are made from cork particles bonded together using different adhesive agents. This work is focused on cork-rubber composites, where the adhesive agents are rubbers. A behaviour of cork-rubber composites cannot be described using simple engineering methods compared to metals or CFRP composites. The Behaviour of the material is very complex, time and rate depended, which makes the procedure of material parameter identification very complicated. Based on earlier research was proved that the response of the material is viscoelastic with high dependence on strain rate [3].

Material parameters identification of investigated material was based on comparing results of experiments and results of finite element simulations. Force-time curves or force-displacement curves were compared using objective function. Material parameters were searched using numerical optimization methods implemented in OptiSlang software.

Stress relaxation experiments were performed to identify the behaviour of the material. Samples of the material were loaded up to 30% of engineering strain and 3 different strain rates were investigated. There were chosen uniaxial and biaxial tension experiments and shear experiments with an arcan sample. Experiments were done using planar biaxial test system TestResources 574LE and a servohydraulic dynamic test system Instron 8850. Fig. 1 shows performed experiments and the Fig. 2 shows the results of a uniaxial tension experiment.

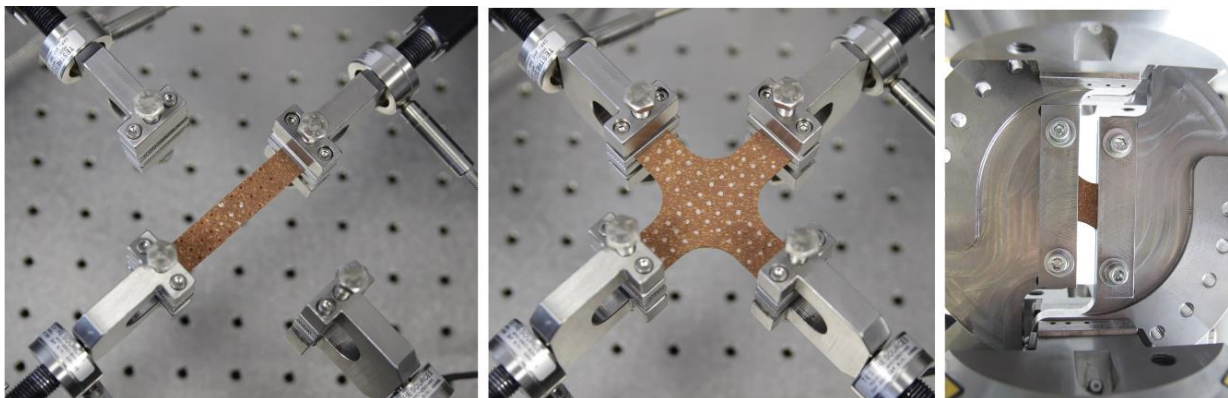


Fig. 1. Performed experiments: uniaxial tension, biaxial tension, shear of an arcan sample

Finite elements models were created using an Abaqus software and they correspond to performed experiments. All models are parametric and they can be modified using a text file. Load history of FE simulations is taken from experimental data, which makes simulations very

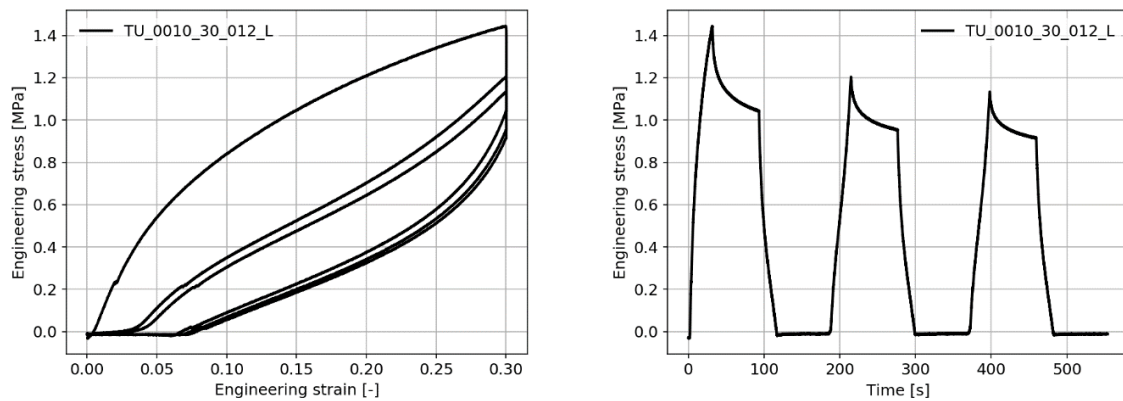


Fig. 2. Results of a uniaxial tension experiment

versatile and easily editable. This approach also makes experiments and simulations synchronised.

The Parallel network model is one of the most advanced material model suitable for modelling of rubber-like materials. The model is capable to describe the behaviour of non-linear viscoelastic or viscoplastic materials [1,2]. The model allows to combine several material models in one framework. Non-linear viscoelasticity, plasticity, Mullins effect, permanent set and many other models are available in the framework. In this work was used Parallel network model represented by 3 viscoelastic networks and one pure elastic network as shown in Fig. 3.

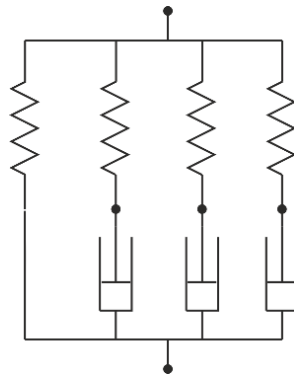


Fig. 3. Parallel network model scheme

Acknowledgement

The work has been supported by the grant project SGS-2016-038.

References

- [1] Dalrymple, T., Hurtado, J. A., Lapczyk, I., Ahmadi, H. R., Parallel rheological framework to model the amplitude dependence of the dynamic stiffness in carbon-black filled rubber, *Constitutive Models for Rubbers IX*, 2015.
- [2] Hurtado, J. A., Lapczyk, I., Parallel rheological framework to model non-linear viscoelasticity, permanent set, and Mullins effect in elastomers, *Constitutive Models for Rubber VIII*, 2013.
- [3] Kocáb, J., Material parameters identification of rheological model of rubber matrix composite, *Master Thesis*, University of West Bohemia, Pilsen, 2016.

Computational model of plastic shoulder protector

R. Kottner^a, V. Hrdlička^a, J. Krystek^a, S. Kaňáková^a

^aFaculty of Applied Sciences, University of West Bohemia, Technická 8, 301 00 Pilsen, Czech Republic

Only helmet is the personal protective equipment (PPE) required by law when a motorcycle is ridden. However, also protective clothing reduce the vulnerability of motorcyclists to injury [4]. To improve PPE and to demonstrate importance of protective clothing including various protectors, the computational model of a clothed motorcyclist is being created. Previous work dealt with leather of motorcycle garments [1]. Different foams used e.g. as a hinge or a backbone protectors were tested in [5]. This work is focused on a shoulder protector shown in Fig. 1. A plastic shell with honeycomb and a viscoelastic foam are basic parts of the protector which absorb energy.

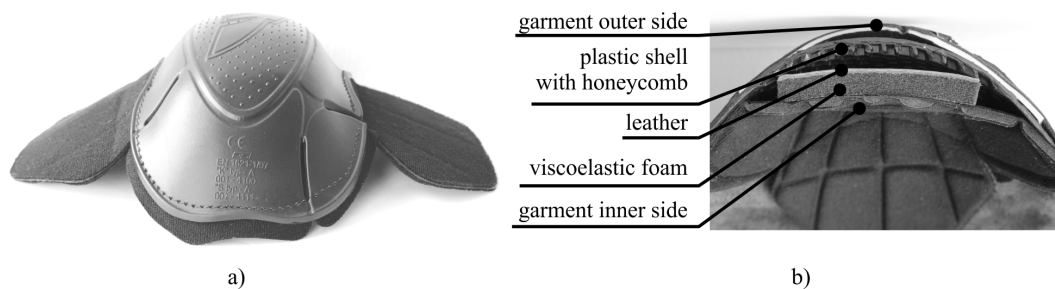


Fig. 1. Shoulder protector: a) overall view, b) cross-section

Tensile and compressive tests of samples cut directly from the plastic shell were performed. Samples of the viscoelastic foam were tested only in compression. These experiments were simulated using the finite element method (FEM). Elastic-plastic material model with hardening was used for the plastic shell description. Prony series were used to model the viscoelastic foam. Based on the comparison of the experimental and the numerical data, material parameters of both materials were identified. A sample from plastic shell after the compressive test and its numerical simulation (only one fourth of the sample was modeled) is shown in Fig. 2.

Lather was modeled as a hyperelastic material. Material parameters of the Ogden model identified in [1] were used.

The computational model of the shoulder protector was created in the FEM software Abaqus. A standard test according to [3] was simulated (see Fig. 3). The influence of the thicknesses of the leather and the viscoelastic foam on the transmitted force during the impact was investigated. Possible modifications of the protector which would lead to approval of the protector according to safer grade of the standard test [3] were introduced [2].

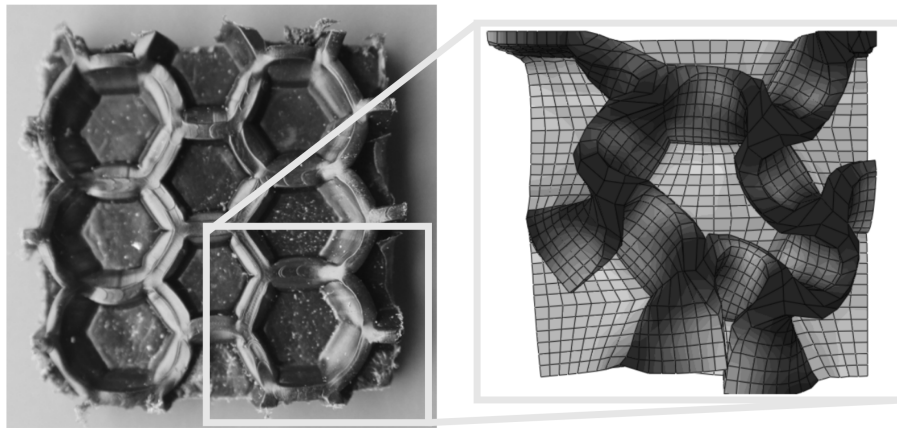


Fig. 2. Plastic shell sample after compressive test (*left*) and its numerical simulation (*right*)

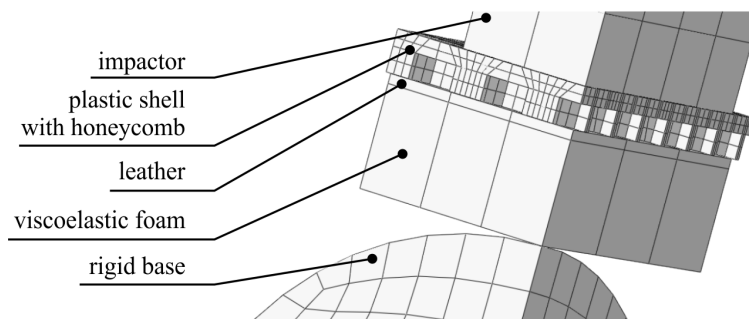


Fig. 3. Numerical simulation of standard test

Acknowledgements

This work was supported by the internal grant project SGS-2016-059 "Computer modelling and monitoring of human body used for medicine". The authors would like to thank PSÍ HUBÍK for providing shoulder protectors.

References

- [1] Bońkowski, T., Kottner, R., Krystek, J., Hubík, L., Görner, T., Hynčík, L., Tensile test of motorcycle garment leather, Proceedings of the 54th International Conference on Experimental Stress Analysis, Srní, University of West Bohemia, 2016, pp. 1–7.
- [2] Hrdlička, V., Design of motorcyclist shoulder protector, Master thesis, University of West Bohemia, 2017.
- [3] Motorcyclists' protective clothing against mechanical impact - Part 1: Motorcyclists' limb joint impact protectors - Requirements and test methods, EN 1621-1, 2012.
- [4] de Rome, L., Ivers, R., Fitzharris, M., Du, W., Haworth, N., Heritier, S., Richardson, D., Motorcycle protective clothing: Protection from injury or just the weather?, Accident Analysis and Prevention 43 (6) (2011) 1983–1990.
- [5] Šoltés, L., Bońkowski, T., Kottner, R., Hynčík, L., Drop test of foams used in motorbike protectors, Proceedings of the 55th International Conference on Experimental Stress Analysis, Nový Smokovec, Technical University of Kosice, 2017, pp. 1–4.

Numerical simulation of thermomechanical phenomena and fluid flow inside a small chamber

J. Kouba^a, T. Radnic^{a,b}, J. Novotný^a

^a Department of Fluid Dynamics and Thermodynamics, Faculty of Mechanical Engineering, Czech Technical University in Prague, Technická 4, 16607 Praha 6, Czech Republic

^b Institute of Thermomechanics, The Czech Academy of Sciences, Dolejškova 1402/5, 18200 Praha 8, Czech Republic

This paper deals with numerical simulation of fluid flow and thermodynamic phenomena inside of a 75 x 75 x 120 mm stainless steel square pipe with wall thickness of 4 mm (Fig. 1). The pipe has two orthogonally placed round visor with diameter of 40 mm. The chamber is then closed by two copper plates with Peltier tiles that are being used for cooling. The chamber is used for calibration of LIF method in gasses and therefore must meet calibration criteria of homogenous temperature field in the area illuminated by the laser sheet. The temperature span of the calibration is -50 to 20°C and absolute pressure span is 50 kPa to 100 kPa. For fulfillment of the homogenous temperature criteria the extreme conditions were deemed critical. The numerical simulation was conducted for the temperature of -50°C and atmospheric pressure. The outside temperature of the chamber is 25°C, which creates rather large temperature difference that can induce significant flow speed in the chamber, despite its dimensions. Maximal speed is anticipated in the centre of the chamber.

The solver used was the Ansys CFX. A structured mesh of 6.5 milion elements was used. The Peltier tiles were simulated by an isothermal boudary condition of the top and the bottom of the closing copper plates. The temperature was set to 223 K. The sidewalls of the chambre were modeled by stanless steel with heat transfer coefficient of $14.63 \text{ W}\cdot\text{m}^{-1}\cdot\text{K}^{-1}$. The chambre was equipped with an insulation of constatn thickness layer, which heat transfer coefficient was used as a parameter for modeling different insulators and thickneses. The outside temperature was set to 298 K.

The modeled fluid was air, with constant thermal expansivity. The flow regime was set to laminar both inside and outside of the chambre. The heat transfer coefficient was calculated based on the wall temperature and wall adjacent temperature. The convergence of the system was assured by increasing the gravity in the simulation in steps. For the calculation, four different types of insulation were used. The Table 1 contains values of the thermal conductivity λ and the recalculated thermal conductivity λ_r for insulation of 4 mm width.

The simulation was carried out on a simple structured mesh. The viscous model was used for natural convection simulation. Results of numerical simulation are shown in temperature and velocity line chart (Fig. 2). This numerical simulation allowed the overview of usable insulations for calibration chamber.

Acknowledgements

This work was supported by the Grant Agency of the Czech Technical University in Prague, grant No. SGS17/074/OHK2/1T/12.

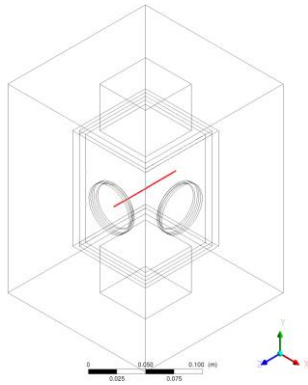


Table 1. List of used insulations with values of the thermal conductivities

Insulation	λ [$\text{W}\cdot\text{m}^{-1}\cdot\text{K}^{-1}$]	λ_r [$\text{W}\cdot\text{m}^{-1}\cdot\text{K}^{-1}$]
Polystyren 10mm	0.04	0.016
Aerogel 10mm	0.02	0.008
Aerogel 20mm	0.013	0.0026
Vacuum insulated panel 10mm	0.008	0.0032

Fig. 1. CFD model with red marked line (axis of round visor) for data collection

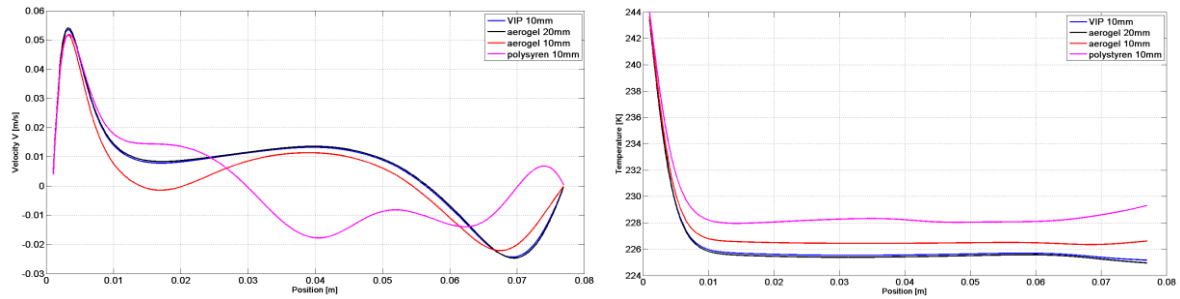


Fig. 2. Line chart with velocity in vertical direction (left) and gas temperature (right) dependent on line length coordinate

References

- [1] Incropera, F. P., DeWitt, D. P., Fundamentals of heat and mass transfer, 4th edition, New York: John Wiley, 1996.
- [2] Michejev, M. A., The basics of heat sharing, Průmyslové vydavatelství, Knihovnice energetického průmyslu, Praha, 1952. (in Czech)
- [3] Versteeg, H. K., Malalasekera, W., An introduction to computational fluid dynamics: The finite volume method, 2nd edition, Pearson Education Ltd., New York, 2007.

Flutter analysis of 28m wingspan sailplane

A. Kratochvíl^a, T. Sommer^a, S. Slavík^a,

^a Department of Aerospace Engineering, Faculty of Mechanical Engineering, Czech Technical University in Prague, Technická 4, 166 07, Prague, Czech Republic

The flutter is self-excited vibration, which leads to destruction of an airplane. It occurs without warning, and is so fast that a pilot has no chance to react. The flutter is defined by critical velocity V_{FL} by flutter analysis. Paper deals with flutter analysis of extreme wingspan sailplane EB29DR of 28.3m see Fig. 1, it is the same as Boeing 737-100. Maximal design speed is $V_D = 325\text{km/h}$ and the sailplane has to be flutter free up to $1.2 \cdot V_D = 390\text{km/h}$.



Fig. 1. Ground vibration test of EB29DR

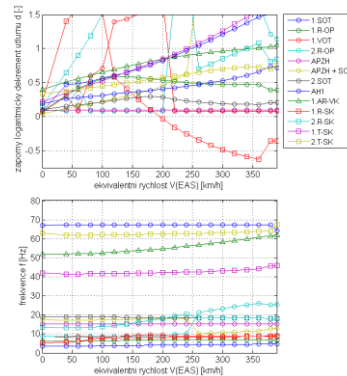


Fig. 2. Damping and frequency plots

An input data for flutter analysis are modal parameters and mass characteristics. The modal parameters were determined by ground vibration test [2]. The test is based at excitation of structure by electrodynamic shakers and sensing the response by accelerometers and force meters. The analyzed configurations were minimal and maximal take-off weight, free and blocked control. The determination of a mass characteristic such as mass, static moment and moment of inertia for each lifting surface and each control surface were determined experimentally by mass weighing and swinging. The influence of a control was simulated by add moment of inertia [4] based on mass of a rods and a levers moment of inertia.

The flutter analysis is an analytical calculation process of damping and frequencies over velocity. A mathematical model [3] is p-k type, based on Lagrange differential equations in modal coordinates with unsteady aerodynamic forces of ideal non-compressible flow developed by Theodorsen [5]. The mathematical model was developed at CTU in Prague, is processed in Matlab environment and has been used for 23 sports airplanes since 2010.

The results from flutter analysis of EB29DR shows that airplane is flutter free in blocked control configuration, but there is the flutter occurrence for free control at velocity 195km/h and frequency 7.8 Hz see Fig. 2. The flutter is caused by coupling eigen-modes 1st Rudder rotation and 1st Rotation of Tail-plane (Fuselage torsion).

There were carried out a flight tests based on flutter analysis. The tests were done by pilot impulse to control for inducing the flutter. Those tests did not proof any flutter occurrence. The test were done up to velocity 325km/h . [1] The current family of EB29 sailplane counts 40pcs with several modification but tail-plane structure is the same for all of them. Since first

flight of EB29 sailplane in 2009 no one reported a flutter occurrence. This problem with low frequency rudder flutter with tail-plane rotation for free control according the flutter analysis, which have not been demonstrated by flight tests exist since 1980. It concerns a sailplane ASW-22, ETA and now EB29DR, possibly others.

The main scope of paper is investigation the difference in results between flutter analysis and flight test. There has been performed an analytical study. The purpose is to consider measurement errors, verify the flutter case, find the possible solutions for flutter suppression or find a reason of inconsistencies in the results. For analytical study summary of see Table 1.

Table 1. Summary of analytical study. SOT: Side fuselage bending; R-OP: Fuselage torsion; VOT: Vertical fuselage bending; R-SK: Rudder rotation

Variation of	Description	Results
Static moment of rudder	Control surface mass balancing	Increasing V_{FL} max. about 15km/h
Moment of inertia of rudder	-50% ÷ +50%	$V_{FL} = 126 \div 242$ km/h
Vertical fin mass characteristic	-30% ÷ +30%	$V_{FL} = 189 \div 198$ km/h
Add moment of inertia for rudder	Weight of pilot's legs 0 ÷ 40 kg	$V_{FL} = 195 \div 383$ km/h
Structural damping	Simulation of control surface damper	Increasing V_{FL} about 10km/h
Removing selected eigen-modes	Post-processing error, verify the flutter case	Without 1.SOT: $V_{FL} = 168$ km/h Without 1.R-OP: $V_{FL} = 198$ km/h Without 1.VOT: $V_{FL} = 192$ km/h Without 2.R-OP: $V_{FL} = 195$ km/h Without 1.R-SK: $V_{FL} =$ N/A Without 1.R-OP & 2.R-OP: 199 km/h
Selected modes frequency variation	Measurement error and/or influence of changes sailplane structure stiffness. $\Delta f = \pm 1.7$ Hz	1.SOT $f=3.5$ Hz; $V_{FL} = 190 \div 204$ km/h 1.R-SK $f=5.2$ Hz; $V_{FL} = 182 \div 211$ km/h 1.R-OP $f=6.2$ Hz; $V_{FL} = 191 \div 196$ km/h 2.R-OP $f=8.7$ Hz; $V_{FL} = 194 \div 203$ km/h

The analytical study shows that common used flutter suppression method – control surface balancing has almost no influence at flutter velocity. Also possible measurement error or artificial increasing of structural damping has not significant influence. It is show that flutter case is not caused by coupling of previously mentioned modes but by couplings more modes together or by coupling different mode than removed one. It is clear that rudder mode is causing the flutter and removing one (such as post-processing error) can make the sailplane free from flutter. Most influence to flutter has inclusion the weight of pilot to control.

Based on analytical study a second vibration test was preform for measuring rudder modes with pilot and to verify tail-plane and free rudder modes. The second test showed correctness of previously measured modals parameters. Result of additional flutter analysis with pilot control configurations was that flutter would not occur for this configuration.

The correctness of the input data to flutter analysis was verified. The reason of free control flutter and inconsistency with flight test can be in systematic error during evaluation of mode 1st Rudder rotation. Eventually by inappropriately executed flight test with pilot induced impulse to control. There will be an attempting to repeat the flight test with more appropriate way to induce rudder oscillation without influence of pilot. It can't be clearly determined which mode is coupling with rudder rotation to cause the flutter, more investigation have to be done.

References

- [1] Binder, W., Flutter flight test, Binder Motorenbau GmbH, Ostheim v .d. Rhön, HB DE.21G.0138.
- [2] Kratochvíl, A., Slavík, S., Flutter analysis of EB-29DR double seater sailplane. ČVUT v Praze. Technical Report TZP/ULT/29/2016, 2017.
- [3] Slavík, S., Weigl, K., Flutter calculation model with isolated modal characteristics of control surfaces for small sport airplanes, Czech Aerospace Proceedings 2 (2008).
- [4] Stender, W., Kiessling, F., Aeroelastic flutter prevention in gliders and small aircraft, DLR-Mitteilung 91-03, 1991.
- [5] Theodorsen, T., Garrick, I. E. J., Nonstationary flow a Wing-AileronTab combination including aerodynamic balance, Report No. 736, NACA, 1943.

Optimization of a dynamic vibration absorber with multiple degrees of freedom

K. Kraus^a, V. Hlaváček^a, P. Beneš^a, Z. Šika^a

^a Faculty of Mechanical Engineering, CTU in Prague, Technická 4, 160 00 Praha 6, Czech Republic

The concept of tuned dynamic absorber joined to the primary structure has been published and patented more than hundred years ago [3]. It turned out as a highly effective solution for vibration reduction of machines, buildings, ships etc. using such a simple mechanism as a single mass with spring and damper is. The biggest advantage of passive absorber is that no energy is needed – just the opposite – the energy is dissipated. The only disadvantage is quite narrow frequency band of usability. In order to improve such a mechanism, convenient dumping can be tuned, or – after all – active control used [1]. Another approach could be a group of absorbers, which is able to reduce more than one of the structure eigenfrequencies [2], or can even be used for reduction vibration in different directions. However, this paper deals with reduction of multiple directions (MDOF) vibrations at once, using only single mass properly attached to the primary structure, and optimization of such a mechanism for specific case.

The whole design and optimization process was performed on the mathematical model of 2D structure attached to ground using 4 damped springs (Fig. 1). The absorber was then represented by a single mass attached to the primary structure by 3 springs.

The complexity of problem grows with DOF, but one of the significant reasons is inseparability of mass in different directions. For example – in 3D, three moments of inertia can be determined for three different axes of rotation, but there is only one mass for 3D based translation motion, and even a position of mass center matters significantly. In 2D – there is only one moment of inertia easily separated from mass and its translation motion, but the mass itself stands for 2D translation motion. Therefore, this paper deals with the optimization approach of such a problem for specific situation.

The given structure is a platform attached by springs to ground in various random directions with applied force in specific direction (Fig. 1, dashed line). The point of interest, which vibration of is supposed to be reduced, is usually the same spot, where the load is applied (e.g. working machines), and where the center of mass is not located at the same time. Therefore, even the mathematical model has two different points (Fig. 1). Clearly, the stiffness of springs joining absorber to the primary structure, the absorber mass and moment of inertia all belong to the optimization parameters set, but more significantly – the position of attachment of such springs to the absorber and primary structure has the biggest influence on the results. In addition, applied force direction and frequency band of interest must be set. The

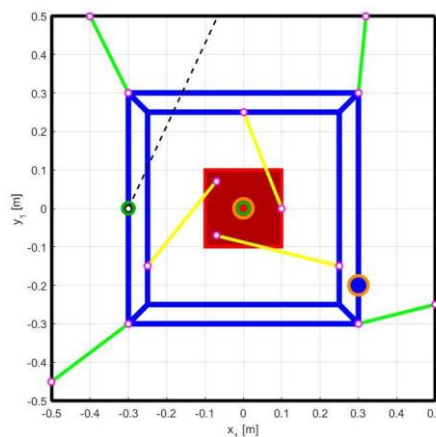


Fig. 1. Model

cost function then represents reduction of maximum velocities of primary structure during harmonic load.

The optimization itself is then performed using time simulation. The harmonic force applied to the point of interest is represented by a chirp signal in given frequency interval – in this case e.g. from 130 to 170 rad/s – and direction (since e.g. working machines are more likely to vary load frequencies than force direction). In order to make the structure robust to working position change, the cost function sums up multiple cases of simulation in different initial positions of the primary structure in space into one value. Finding the fact, that some of the first successful results were quite robust to various force directions, it was not included into optimizing parameters. In order to speed up the optimization process, all cases, that contain any of the eigenfrequencies (using linearized model) in the desired frequency band, have immediate cost function handicap in form of high number. The primary structure itself has three eigenfrequencies [160.6, 263.6 561.6] rad/s. Designed absorber is supposed to squeeze the first frequency out of the given freq. interval, but at the same time brings three new eigenfrequencies into the whole system, which are also supposed to be out of the freq. interval.

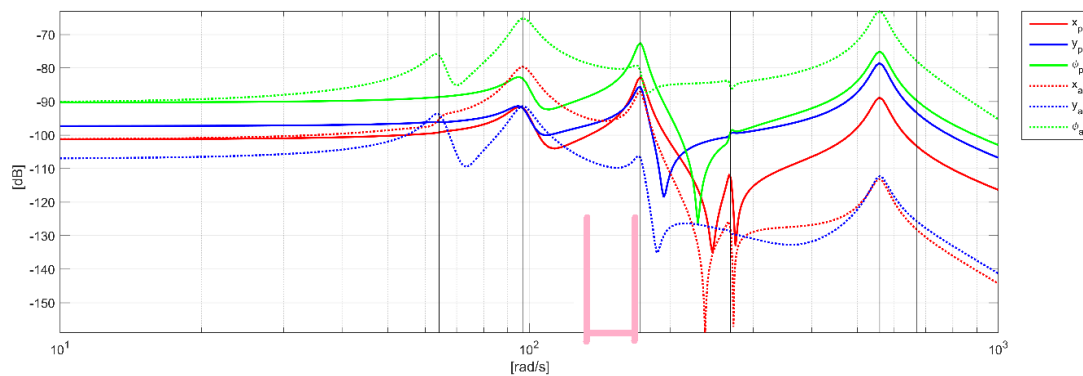


Fig. 2. Bode diagram of optimized structure and given frequency band (pink)

The results of such a optimization varied with respect to used optimization method properties, such as global genetic algorithm has, and with respect to parameter limits defined for whole process. However, all final results have certain similarity in the geometry of absorber attachment. For desired frequency interval it has succeeded to squeeze all eigenfrequencies (even those brought by absorber) out of such an interval (Fig. 2).

Acknowledgement

The work has been supported by the Czech Science Foundation project GA17-20943S – Active multidimensional vibration absorbers for complex mechanical structures based on delayed resonator method

References

- [1] Lin, G. L., Lin, C. C., Chen, B. C, Soong, T. T., Vibration control performance of tuned mass dampers with resettable variable stiffness, *Engineering Structures* 83 (2015) 187-197.
- [2] Rice, H. J., Design of multiple vibration absorber systems using modal data, *Journal of Sound and Vibrations* 160 (1993) 378-385.
- [3] Vyhlidal, T., Olgac, N., Kucera, V., Delayed resonator with acceleration feedback – Complete stability analysis by spectral methods and vibration absorber design, *Journal of Sound and Vibration* 333 (25) (2014) 6781-6795.

Myosin motor movement controlled by a potential barrier

M. Krejčová^a, M. Holeček^a

^a*Faculty of Applied Sciences, University of West Bohemia, Univerzitní 8, 306 14 Plzeň, Czech Republic*

Myosin molecular motors have a key role in a muscle contraction. Their movement is controlled by a concentration of calcium (Ca^{2+}) and by adenosine triphosphate (ATP) molecules. The calcium cations concentration increase leads to interaction between myosin and actin filaments [2]. The ATP serves as a fuel for myosins. One molecule of ATP is enough to provide sufficient energy per multiple steps of myosin motor [1]. These steps are in the presented work denote as unbound, weakly bound and post-power-stroke. However, myosins work continuously so this is just one of possible approximations of the movement to discrete states.

The briefly described the principle of myosin motors contraction is possible to well represent a mathematical point of view by a Fokker-Planck equation system. This approach comes out from a statistical prediction of a behaviour of a Brownian particle, where belong also myosin (characteristic size is a few nanometers). The Fokker-Planck equation has a form of partial differential equation. Thus,

$$\frac{\partial \rho_i}{\partial t} = D \frac{\partial}{\partial x} \left[\frac{1}{k_B T} (V_i(x) + F_{Load}) \rho_i \right] + D \frac{\partial^2 \rho_i}{\partial x^2} + \sum_{j=1}^N k_{ij} \rho_j - \sum_{j=1}^N k_{ji} \rho_i. \quad (1)$$

In Eq. (1), ρ_i is probability density distribution of i -state, t and x are time and spatial variables, respectively. D is diffusion coefficient, which represents random walk here, which corresponds to the Brownian motion. $V(x)$ is a potential given by calcium cations and F_{Load} determines loading force on the motor. The parameter $k_B T$ is the characteristic size of the fluctuations in the microworld. It is composed of a product of k_B , which is Boltzmann constant, and thermodynamic temperature T . The last parameters, k_{ij} and k_{ji} , denote transition rates between myosin states, from state i to state j and vice versa, respectively [3]. These rates are dependent on the concentration of ATP molecules.

For needs of a numerical simulation, it is essential to make proper discretization. In the literature [3], as a suitable algorithm for biomolecular transport is presented the WPE algorithm for spatial discretization. It is based on modifying a partial differential equation (here Fokker-Planck equation) to an ordinary differential equation through probability fluxes. These fluxes are between each node in spatial dimension l and are called simply forward F and backward B flux, respectively. To do so, it requires an assumption of small changes at a time, precisely local steady-state solution. The keeping detail balance (condition on fluxes) is a consequence [3]. It leads to the master equation in a form of

$$\frac{dp_i^l}{dt} = F_i^{l-1/2} p_i^{l-1} - (B_i^{l-1/2} + F_i^{l+1/2}) p_i^l + B_i^{l+1/2} p_i^{l+1}. \quad (2)$$

The variable p is probability, which is connected with probability density ρ by a simple approximation $p \approx \rho \Delta x$, where Δx is a distance between two nodes.

The fluxes are related to Eq. (1) by simple relationships

$$F = \frac{D}{\Delta x} \frac{(V - xF_{Load})/k_B T}{\exp[(V - xF_{Load})/k_B T] - 1}, \quad (3)$$

$$B = - \frac{D}{\Delta x} \frac{(V - xF_{Load})/k_B T}{\exp[(V - xF_{Load})/k_B T] - 1}. \quad (4)$$

In a muscular cell can happen a change in the concentration of calcium cations. The change will have an influence on the potential V_i , so it blocks myosin movement along the actin filament. From a mathematical point of view, it temporarily breaks the evolution of the system due to the pure transitions between states and begins to deform probability density distribution. The deformation is quite fast and in a wrong time scale, it is like instantaneous.

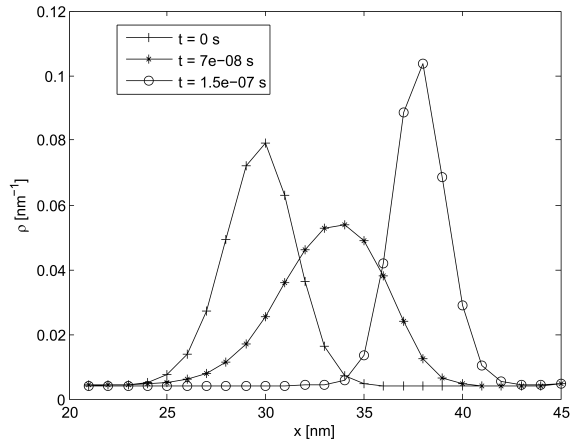


Fig. 1. Probability density distribution of post-power-stroke state in different times: initial condition, after the change of potential and its next evolution on a limited spatial dimension

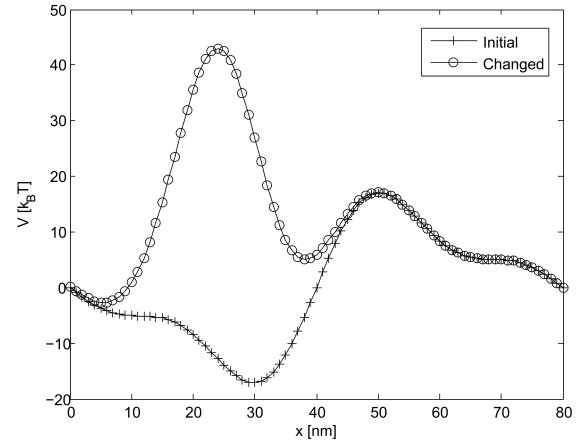


Fig. 2. An original potential and a new potential after the change of calcium concentration on a full spatial dimension

For the presented results on Figs. 1 and 2, the diffusion coefficient was set to $D = 5.47 \cdot 10^7 \text{ nm}^2\text{s}^{-1}$. The probability density distribution final state corresponding to the new local minimum of potential. The transition state is clearly very influenced by diffusion because it has gaussian shape and direction of the movement harmonises with direction to the new local minimum.

Acknowledgements

M. Krejčová was supported by SGS-2016-038 and SGS-2016-059. She also wishes to express her big thanks to Mr Rosenberg for his valuable advice.

References

- [1] Kitamura, K., Tokunaga, M., Esaki, S., Iwane, A. H., Yanagida, T., Mechanism of muscle contraction based on stochastic properties of single actomyosin motors observed in vitro, *Biophysics* 1 (2005) 1–19.
- [2] Rosenberg, J., Liška, V., *Experimental surgery – New technologies in medicine, Volume 2: Biomechanics*, Charles University in Prague, Faculty of Medicine in Pilsen, Pilsen, 2013. (in Czech)
- [3] Wang, H., Several issues in modeling molecular motors, *Journal of Computation and Theoretical Nanoscience* 5 (2008) 1–35.

Full dispersion analysis of the Newmark family in finite element method in elastodynamics

A. Kruisová^a, R. Kolman^a, M. Mračko^a

^a*Institute of Thermomechanics of the Czech Academy of Sciences, Dolejškova 5, 182 00 Praha 8, Czech Republic*

Both the spatial and the temporal discretization used in finite element method introduces the dispersion errors in numerical analysis of the stress wave propagation. The dispersion is studied on the example of the plane strain linear and the biquadratic serendipity finite elements.

In previous works [1] and [2] the dispersion analysis of these elements for the central difference method was presented. In this contribution this work was extended for the Newmark time integration method.

Generally, the finite element solution is polluted by dispersion errors as an effect of spatial finite element discretization and by the period elongation errors and numerical damping of the direct time integration [1]. The dispersion errors are caused by the difference of numerical wave speeds from the wave speeds in continuum and are dependent on the frequency of the propagation wave and its orientation in the finite element grid.

There are several methods available to compute the dispersion but all of them suppose the periodicity of solution in space and time and their common basis is provided by the Fourier method. This means that they are based on assuming the harmonic solution propagating through the periodic structure. The nodal displacements in time $t = s\Delta t$ of a plane wave problem, see Fig. 1(a), corresponding to the wave solution in discrete form, are

$$\begin{aligned} u_{m,n}^h &= U_{0m,n} e^{i(k^h x_m p_x + k^h y_m p_y - \omega s \Delta t)}, \\ v_{m,n}^h &= V_{0m,n} e^{i(k^h x_m p_x + k^h y_m p_y - \omega s \Delta t)}, \end{aligned} \quad (1)$$

where $u_{m,n}^h$ and $v_{m,n}^h$ are the displacements in x and y direction in nodes (m, n) with the coordinates x_m and y_m , see Fig. 1(b), $U_{0m,n}$ and $V_{0m,n}$ are unknown amplitudes, ω marks the angular velocity, k^h is the numerical wave number and p_x and p_y are components of the unit normal vector expressed as $p_x = \cos \theta$ and $p_y = \sin \theta$.

The most widely used group of one-step methods for direct time integration is the Newmark family where the approximation of the displacement and velocity vector with two parameters β and γ . If $\gamma < 1/2$ and $\gamma > 1/2$ a negative and positive damping is introduced by the algorithm, respectively. For this reason, the further analysis is restricted only to $\gamma = 1/2$. Then this general group includes several well-known cases, such as the average acceleration method with $\beta = 1/4$, the linear acceleration method with $\beta = 1/6$ and the Fox-Goodwin method with $\beta = 1/12$. The explicit central difference method can be incorporated with $\beta = 0$.

Using the relations for the velocity and the acceleration approximations of the Newmark method in the matrix form of equation of motion, we obtain the final system of equation for the periodic part of the problem. Then the dispersion relation can be obtained from the eigenfrequency analysis of that system. The angular velocities ω_i of the propagated waves expressed in

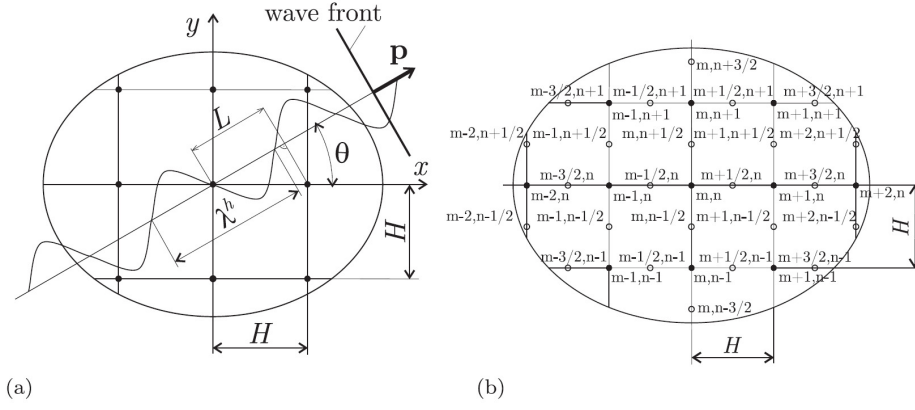


Fig. 1. (a) Two-dimensional infinite bilinear regular finite element mesh and plane wave inclined by angle θ and (b) two-dimensional infinite serendipity regular finite element mesh

terms of β for $\gamma = 1/2$ are

$$\omega_i = \frac{2}{\Delta t} \arcsin \sqrt{\frac{\Lambda_i E \Delta t^2}{4\beta \Lambda_i E \Delta t^2 + 4H^2 \rho}}, \quad i = 1, 2, \dots, N_c, \quad (2)$$

where E is the Young modulus, ρ is the density of the material and H is the size of the element. The eigenvalues Λ_i are obtained from the generalized eigenvalue problem of one periodic cell containing one corner node for bilinear element and one corner and one midside node for the biquadratic serendipity element.

This dispersion relation can be transformed in dimensionless form by setting $\bar{\omega}_i = \omega_i H / c_1$ for dimensionless angular velocity (c_1 is the velocity of the longitudinal wave propagating in isotropic elastic domain, $c_1 = \sqrt{(\Lambda + 2G)/\rho}$), by denoting the Courant number $Co = \Delta t c_1 / H$ and denoting $c_0 = \sqrt{E/\rho}$

$$\bar{\omega}_i = \frac{2}{Co} \arcsin \sqrt{\frac{\Lambda_i Co^2 c_0^2}{4\beta \Lambda_i Co^2 c_0^2 + 4c_1^2}}, \quad i = 1, 2, \dots, N_c. \quad (3)$$

Such relation serves for setting the time step and element size for required accuracy.

Acknowledgement

The work was supported by the grant project 17-22615S of the Czech Grant Agency within the institutional support RVO: 61388998.

References

- [1] Kolman, R., Plešek, J., Červ, J., Okrouhlík, M., Pařík, P., Temporal-spatial dispersion and stability analysis of finite element method in explicit elastodynamics, *International Journal for Numerical Methods in Engineering* 106 (2) (2016) 113–128.
- [2] Kolman, R., Plešek, J., Okrouhlík, M., Gabriel, D., Grid dispersion analysis of plane square bi-quadratic serendipity finite elements in transient elastodynamics, *International Journal for Numerical Methods in Engineering* 96 (1) (2013) 1–28.

Biomechanics in clinical practice

J. Křen^a, L. Lobovský^a, M. Jansová^a, J. Hartlová^b, M. Salášek^c

^a*NTIS – New Technologies for the Information Society, Faculty of Applied Sciences, University of West Bohemia, Univerzitní 8, 306 14 Plzeň, Czech Republic*

^b*Department of Mechanics, Faculty of Applied Sciences, University of West Bohemia, Univerzitní 8, 306 14 Plzeň, Czech Republic*

^c*Clinic for Orthopaedics and Traumatology of Locomotive Organs, University Hospital in Pilsen, alej Svobody 80, 304 60 Plzeň, Czech Republic*

In the following, selected biomechanical studies on bone mechanics that resulted from cooperation between the New Technologies for the Information Society (NTIS) research center of the University of West Bohemia and the Clinic for Orthopaedics and Traumatology of Locomotive Organs (COTLO) of the University Hospital in Pilsen are presented. An attention is paid to experimental and computational modelling of pelvic ring injuries [4], computational models of proximal femur osteosynthesis [2], total knee arthroplasty (focused on patelofemoral and tibiofemoral joint coupling while respecting the surrounding synovial fluid) [3] and distal femur periprosthetic fractures [1].

Mathematical models based on the theory of continuum mechanics are used to solve biomechanical problems outlined above. The related computational (numerical) models utilise the finite element (FE) method while material parameters of human tissues are mostly based on data published in literature. Experimental studies are focused mainly on mechanical testing of orthopaedic models of human bone structures and analysis of structural deformations by methods of photogrammetry and digital image correlation (DIC). In general, the applied biomechanical models (either experimental or computational) target on assessment of applicability and efficiency of various fixation techniques in clinical osteosynthesis. In order to assess the quality of the selected fixation technique, several criteria are studied such as dislocation of the treated bone parts in loading, structural stiffness, von Mises stress in both the treated bone and the fixator etc. Some of the studied computational models are displayed in Fig. 1.

The cooperation with COTLO started with analysis of proximal femoral nail (PFN) fixator which was used for osteosynthesis of proximal femur fractures (perthrochanteric fractures, femoral neck fractures). The major clinically observed problem was a dislocation of a hip pin in femoral head. Thus an analysis of statics as well as dynamics of the bone fixation was demanded and a stress-strain analysis of the osteosynthesis was performed.

The study on PFN fixators was followed by research on total knee arthroplasty (TKA) which focused on the influence of positioning the knee implant on patelofemoral and tibiofemoral joint coupling. Improper positioning of the implant deteriorates tribological properties of the knee joint and may result in excessive after-surgery pain. The biomechanical model of TKA was based on CT scans of all knee components and reflected the mechanical effects of surrounding tissues and synovial fluid.

The study on osteosynthesis of pelvic ring bones was performed both experimentally and computationally. A special attention was paid to sacral bone fixation techniques. The experimental measurements were performed using orthopaedic plastic models with well-defined material properties. Ten surgical techniques using a combination of four orthopaedic fixators (TIFI

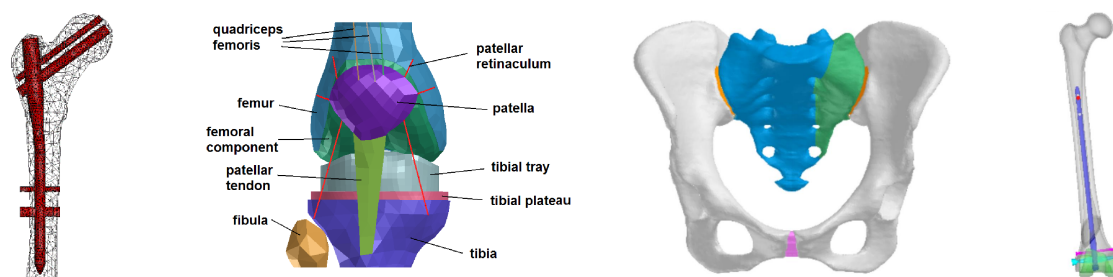


Fig. 1. *From left to right:* model of proximal femoral nail fixation, model of total knee arthroplasty, model of pelvis with unilateral transforaminal fracture, model of periprosthetic fracture of distal femur

– transiliac internal fixator, ISS – iliosacral screw, TP – transiliac plate and SB – sacral bar) were examined for the case of unilateral transforaminal fracture. Non-invasive optical measurements of pelvic ring deformations under mechanical loading were performed using the DIC technique. A biomechanical stability of the fixation was assessed as a ratio between stiffness of the pelvic structure after surgical treatment versus stiffness of the intact pelvis. The computational model was developed based on CT scans of the orthopaedic plastic models. The FE analysis of the pelvic ring deformations verified the experimental results.

Periprosthetic fractures of distal femur are the most recent field of the research conducted in cooperation with COTLO. The main goal of this research is an identification of the cause of distal femoral fractures right above TKA. Mechanical properties of selected clinically used fixators (DFN – distal femoral nail, DCS – dynamic condylar screw, ABP – angled blade plate) and a stability of bone fixation is also assessed.

The major aim of the performed studies and of the overall cooperation between NTIS and COTLO is a translation of the scientific results into clinical practice, when biomechanical models are used to provide additional information required by surgeons.

Acknowledgement

This study was supported by the project LO1506 of the Czech Ministry of Education, Youth and Sports under the program NPU I.

References

- [1] Jansová, M., Malotín, T., Křen, J., Votápek, P., Lobovský, L., Hynčík, L., FE analysis of supracondylar periprosthetic femoral fracture treatment, Proceedings of the 32nd conference Computational Mechanics, Špičák, University of West Bohemia, 2016.
- [2] Křen, J., Hynčík, L., Stability of proximal femur nail fixating per-trochanteric fracture, Proceedings of the 18th conference Computational Mechanics, Nečtiny, University of West Bohemia, 2002.
- [3] Křen, J., Jansová, M., Pokorný, J., Koudela, K. sr., Koudela, K. jr., Femoro-tibial joint in the total knee arthroplasty, Proceedings of the 28th conference Computational Mechanics, Špičák, University of West Bohemia, 2012.
- [4] Lobovský, L., Salášek, M., Jansová, M., Hartlová, J., Krystek, J., Křen, J., Comparative study on various fixations of sacral bone injuries, Proceedings of the 21st Congress of the European Society of Biomechanics, Praha, 2015.

Thermohydraulic and structural analyses of VVER 440 components

V. Kutiš^a, J. Paulech^a, G. Gálik^a, J. Murín^a

^aFaculty of Electrical Engineering and Information Technology, Slovak University of Technology, Ilkovičova 3, 812 19 Bratislava, Slovak Republic

The most important part of primary circuit of nuclear power plant (NPP) is the nuclear reactor, where fission reaction takes place. Geometry model of a Russian pressurized water reactor VVER 440 is shown in Fig. 1 (middle). Main components of the reactor are as follows: reactor pressure vessel (RPV), reactor shaft core barrel, bottom of reactor shaft core barrel, core basket, block of protecting tubes and upper block. In the core basket, which contains the reactor core, there are 312 fuel assemblies (FA) and 37 control rods (HRK).

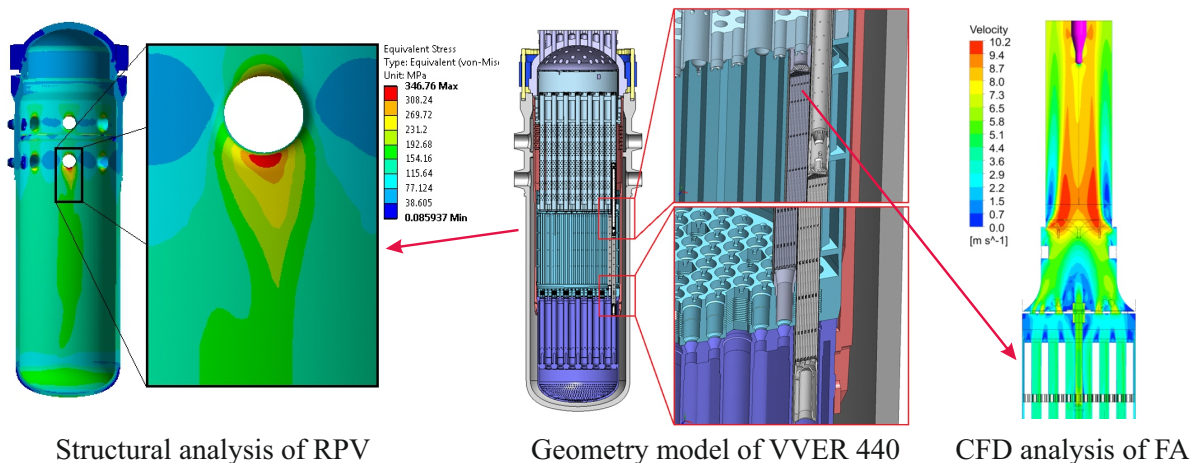


Fig. 1. *Left* – structural analysis of RPV, *middle* – geometry model of a pressurized water reactor VVER 440 with internal components, *right* – CFD analysis of coolant flow through FA

Processes that occur in the nuclear reactor, belong to different physical domains such as nuclear physics, hydromechanics, thermomechanics and mechanics. The strength of interaction between individual physical domains depends on the particular analysed problem. Basic analyses in the above mentioned physical domains are the analysis of neutron flux in reactor core, thermohydraulic analysis of coolant flow and thermal and structural analysis of individual reactor components. The interaction between the individual analyses is shown in Fig. 2.

The output of the neutron flux analysis in the reactor core is the distribution of the neutron flux as well as the generated thermal power in the fuel. Thermal power is an input parameter for thermohydraulic analysis of coolant flow, the output of this analysis is the distribution of temperature, pressure and velocity fields in the flowing coolant. These conditions directly affect the moderation properties of the coolant, which affects the backward distribution of the neutron flux. Physical conditions in the coolant represent the input for thermal analysis of individual

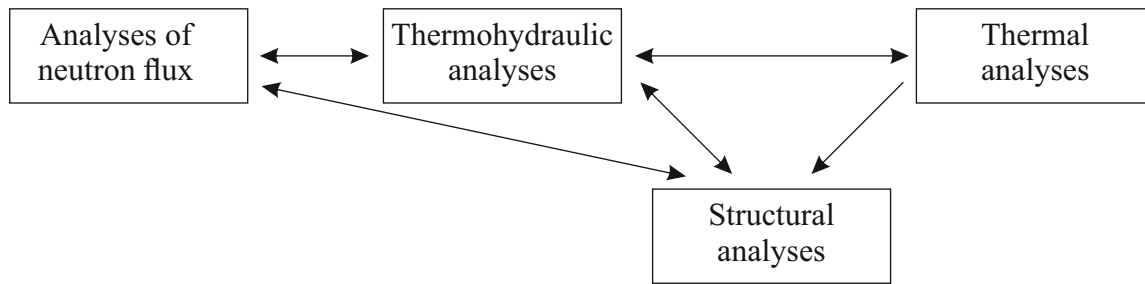


Fig. 2. Interaction between the individual analyses

components, like RPV, but also represent the input for structural analysis of these components. Deformation of the components affects both the thermohydraulic and the neutron flux conditions.

Stochastic or deterministic approach can be used to analyse a given problem. Stochastic approach is applied mainly to neutron flux analyses, while other types of analyses use a deterministic approach. To solve a problem in a deterministic way, the model can be analysed as a system model [2] or as a continuous model [3]. This contribution describes is focused on thermohydraulic analysis of FA and downcomer of reactor as well as to thermohydraulic and structural analysis of the whole reactor under the condition of small break LOCA event. All investigated models are continuous models, but the boundary conditions are derived from system model analyses.

Thermohydraulic CFD analysis of FA, Fig. 1 (right), is focused on coolant flow parametric analysis of the FA bypass effect as well as the analysis of influence of surrounding FAs. Analyses include sensitivity study of turbulent models and mesh density [1]. Thermohydraulic CFD analysis of downcomer is focused on the numerical calculation of the FA mixing factors from individual hot loops. The last part of the contribution deals with the coupled structural, Fig. 1 (left), and thermohydraulic analysis under the conditions of the small break LOCA event.

Acknowledgements

This work was supported by the Slovak Research and Development Agency under the contract No. APVV-14-0613, by Grant Agency VEGA, grant No. 1/0453/15. Authors are also grateful to the HPC Centre at the Slovak University of Technology in Bratislava, which is a part of the Slovak Infrastructure of High Performance Computing (SIVVP project, ITMS code 26230120002, funded by the European Regional Development Funds), for the computational time and resources made available.

References

- [1] Oberkampf, W. L., Trucano, T. G., Verification and validation in computational fluid dynamics, Sandia National Laboratories, 2002.
- [2] Todreas, N. E., Kazimi, M. S., Nuclear systems volume I: Thermal hydraulic fundamentals, 2nd edition, CRC Press, 2011.
- [3] Versteeg, H., Malalasekera, W., An introduction to computational fluid dynamics: The finite volume method, 2nd edition, Prentice Hall, 2007.

Acoustic modal analysis of water filled pipe

J. Kůrečka^a, V. Habán^a, D. Himr^a

^aFaculty of Mechanical Engineering, Brno University of Technology, Technická 2896/2, 616 69 Brno, Czech Republic

Result of modal analysis is eigen frequency and if damped then also damping of a system. Coupled Fluid Structure modal analysis can be used to determine frequencies and modes of submerged bodies [2]. This contribution deals with inverse problem, frequency of fluid volume bounded by structure. In case of the water filled pipe and with omission of the structural part the first eigen frequency can be calculated analytically using Eq. (1). Pressure and velocity pulsation for mode with this frequency is half wave, minimum of pressure amplitude is at the middle of a pipe and maximal amplitude on both ends (Fig. 1).

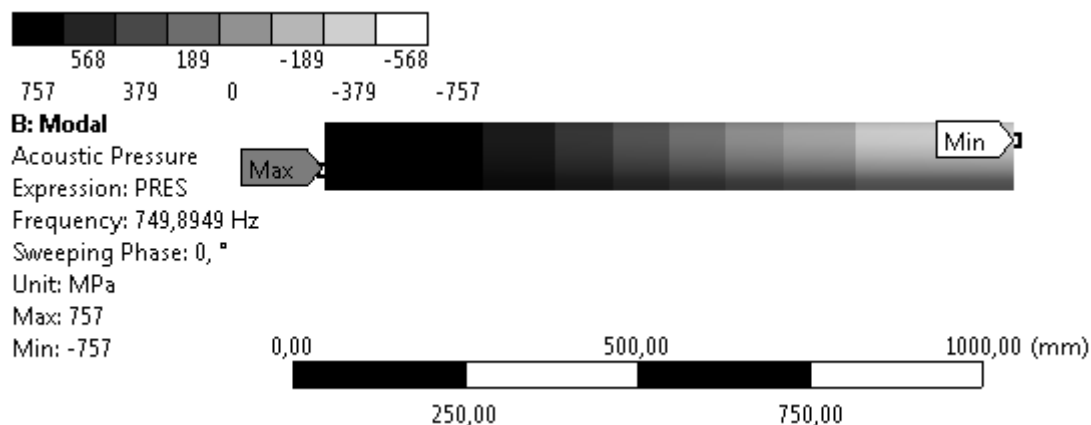


Fig. 1. Pressure pulsation amplitude computed by ANSYS Acoustical

$$f = \frac{a}{2 \cdot L}, \quad (1)$$

where f [Hz] is frequency, a [$\text{m} \cdot \text{s}^{-1}$] is speed of sound and L [m] is length. If this modal analysis example is solved using FEM software ANSYS acoustic or custom code based on TMM (transfer matrix method) the results are consistent with analytical solution. So for one-meter-long pipe and sound speed of $1\,500 \text{ m} \cdot \text{s}^{-1}$ the first eigen frequency is 750 Hz.

In this contribution this problem is extended to include pipe wall. This change produce different result of eigen frequency because the elasticity of pipe wall allows dilatation. The modal analysis in ANSYS Acoustics of fluid only domain is solved using Eq. (2) [1]

$$(-\omega^2 [\mathbf{M}_f] + j\omega [\mathbf{C}_f] + [\mathbf{K}_f]) \{p\} = 0, \quad (2)$$

where ω [$\text{rad} \cdot \text{s}^{-1}$] is angular velocity, j is imaginary number, \mathbf{M} , \mathbf{C} and \mathbf{K} are mass, damping and stiffness matrices of fluid. Eq. (3) is used to include structural part and system is solved as

fluid structure interaction problem [1]

$$\left(-\omega^2 \begin{bmatrix} \mathbf{M}_s & 0 \\ \rho_0 \mathbf{R}^T & \mathbf{M}_f \end{bmatrix} + j\omega \begin{bmatrix} \mathbf{C}_s & 0 \\ 0 & \mathbf{C}_f \end{bmatrix} + \begin{bmatrix} \mathbf{K}_s & -\mathbf{R} \\ 0 & \mathbf{K}_f \end{bmatrix} \right) \begin{Bmatrix} u \\ p \end{Bmatrix} = 0. \quad (3)$$

Subscript s denotes matrices of solid part, \mathbf{R} is fluid boundary matrix and ρ_0 is fluid mass density constant.

TMM code is solving similar system consisting of Navier-Stokes and continuity equations describing fluid behavior and equations of structural part with properties defined as Voigt-Kelvin material model. This software is solving only 1D problem, but since the pressure pulsations at dominant frequency are longitudinal (in direction along the axis of pipe), this simplification of physical model is satisfactory.

In Table 1 comparison of results is presented. Material of structural part is steel with Young modulus 225 GPa, steel density $\rho_{steel} = 7800 \text{ [kg}\cdot\text{m}^{-3}]$ and wall is 3 mm thick. Fluid properties are density $\rho = 998 \text{ [kg}\cdot\text{m}^{-3}]$ and speed of sound $a = 1500 \text{ [m}\cdot\text{s}^{-1}]$.

Table 1. First eigen frequencies of water filled pipe (length 1 m, diameter 32 mm)

	Frequency with rigid pipe wall [Hz]	Frequency with elastic pipe wall [Hz]
ANSYS	749.89	785.58
TMM code	749.66	784.54
Eq. (1)	750	–

Results show change of frequency caused by elasticity of pipe wall and frequencies obtain by FEM simulation does not differ from values acquired from running the TMM code. From their agreement we can conclude that elastic pipe wall does influence damped frequency of hydraulic systems and that both TMM 1D and FEM ANSYS Acoustic analysis can be used to solve this problem.

Acknowledgements

This work has been supported by the 2017 Science Fund of Faculty of Mechanical Engineering, identification number FV 17-25 and by NETME Centre, regional R&D centre built with the financial support from the Operational Programme Research and Development for Innovations within the project NETME Centre (New Technologies for Mechanical Engineering), Reg.no. CZ.1.05/2.1.00/ 01.0002 and, in the follow-up sustainability stage, supported through NETME CENTRE PLUS (LO1202) by financial means from the Ministry of Education, Youth and Sports under the National Sustainability Programme I.

References

- [1] ANSYS Inc., Introduction to acoustics, ANSYS Acoustics Lectures, 2016.
- [2] Graf, B., Chen, L., Correlation of acoustic fluid-structural interaction method for modal analysis with experimental results of a hydraulic prototype turbine runner in water, Proceedings of ISMA 2010 – International Conference on Noise and Vibration Engineering, including USD 2010, Katholieke Universiteit Leuven, 2010, pp. 2489–2504.

Corrected Signal to noise ratio and Mutual information for accuracy determination in PIV

I. Machovská^a, J. Novotný^a

^a Faculty of Mechanical Engineering, Czech technical university in Prague, Technická 4, 166 07 Praha, Czech Republic

In this work, we focus on an estimation of the measurement accuracy at each measured point using PIV method, a formulation of a suitable metric of the correlation plane and a definition of the dependency between specific metric and the measurement accuracy using the synthetic test so called Uniform flow test and algorithm called multi-step standard cross-correlation. The main contribution of this work is the correction of known metrics of the correlation plane called Primary peak ratio and Mutual information. The correction of these metrics involves the effect of particle displacements within the interrogation area and the effect of the size and the number of the particles on the evaluation of the metric. The result of this work is the functional dependency defining the relationship between the metric value and the accuracy of the PIV measurement.

In [3], there was described and shown suitable function for approximation of the found dependencies, which clearly shows that one equation with other coefficients may be used for all metrics without filtration. After filtration of the "out-of-layers" vectors, the use of one equation is no longer possible and other function or other method of metrics calculation has to be found. For that reason, PPR and MI metrics are used and further adjusted. Definition of PPR and MI metrics and their use in the determination of PIV measurement accuracy were discussed in [1– 3]. In [1], PPR and corrected PPR metric was discussed in detail and following equation presented

$$PPR_{\Delta,MI} = \frac{PPR - 1}{16 * \sqrt{(\Delta x^2 + \Delta y^2)} * MI^{(-0.42)} + \frac{0.08}{MI} + 0.001} + 1. \quad (1)$$

Corrected PPR metric defined by equation (1) was corrected by the measured displacement determined in the last iteration using multi-step cross-correlation method of correlation plane evaluation. Dependency of the measurement accuracy on the values of the corrected PPR metric is shown Fig. 1.

It may be assumed, based on the results above, that the use of correction of the PPR metrics is a very suitable way of improving the algorithm accuracy and is applicable in a wide range of the metrics value. Metric MI can be corrected according to the following equation

$$MI_{\Delta} = \frac{MI}{2 * (\Delta x^2 + \Delta y^2) + 0.001}. \quad (2)$$

Corrected MI metric defined by equation (2) was corrected by the measured displacement determined in the last iteration using multi-step cross-correlation method. Dependence of the measurement accuracy when using the corrected MI value is shown in Fig. 2. Analyzing the results, it is evident, compared to the uncorrected metrics, that throughout the entire range of the measured metrics the individual deviations are less than 0.01 pixel. The applicability of such modified metrics is not limited only to metrics values exceeding ten times the minimum

values of the given metrics, but they can also be used in cases in which the value of the given metrics approaches its minimum value.

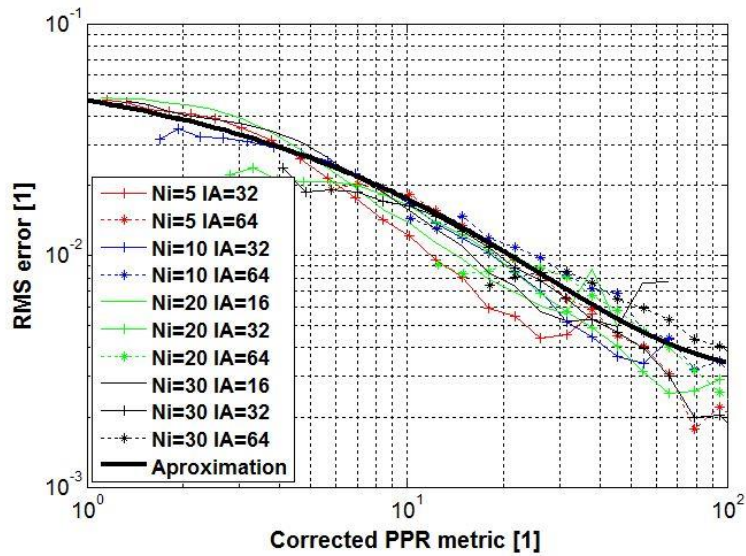


Fig. 1. Dependency of the measurement accuracy on the values of the corrected PPR metric

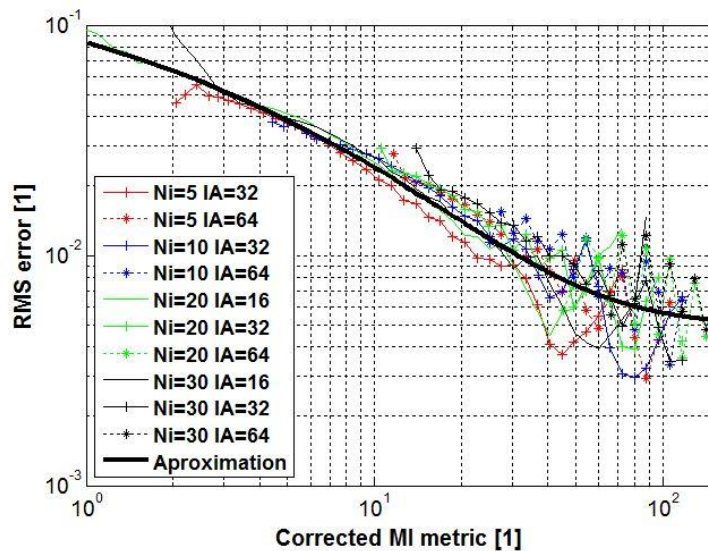


Fig. 2. Dependency of the measurement accuracy on the values of the corrected MI metric

Acknowledgement

This work was supported by the Grant Agency of the Czech Technical University in Prague, grant No. SGS17/074/OHK2/1T/12.

References

- [1] Novotný, J., Machovská, I., Corrected metric for uncertainty estimation methods in Particle Image Velocimetry, Proceedings of the 9th World Conference on Experimental Heat Transfer, Fluid Mechanics and Thermodynamics, Foz do Iguazu, 2017.
- [2] Xue, Z., Charonko, J., Vlachos, P., Particle image pattern mutual information and uncertainty estimation for particle image velocimetry, Measurement Science and Technology 26 (7) (2015) No. 074001.
- [3] Xue, Z., Charonko, J., Vlachos, P., Signal-to-noise ratio, Error and Uncertainty of PIV measurement, Proceedings of the International Symposium on Particle Image Velocimetry, Delft, 2013.

Computational study of novel valveless piston pump for macro scale

T. Machů^a, F. Pochylý^a, J. Šulc^b

^a Faculty of Mechanical Engineering, Brno University of Technology, Technická 2896/2, 616 69 Brno, Czech Republic

^b Faculty of Civil Engineering, Brno University of Technology, Veveří 331/95, 602 00 Brno, Czech Republic

Check valves are integral parts of displacement pumps which use piston or membrane for fluid transport. Valves secure proper fluid flow through pump. On the other hand, they are considered as the most unreliable parts of mentioned pumps. Valves are also sources of hydraulic losses and they can be clogged in case of fluid mixture pumping. These liabilities are reason why valveless pumping principles have been studied. Valveless pumps can be divided in two groups: micro and macro scale pumps. Micro scale pumps are commonly used in various microfluidic devices such as chemical analysis systems, microdosage systems, etc. Macro scale pumps are used only for pumping of hazardous fluids where the demands on reliability are much higher than the demands on efficiency. This work presents mathematical model of valveless piston pump (Fig. 1) and results of CFD analysis of novel valveless piston pump for macro scale pumping.

Main principle of valveless piston pumps is based on different dissipation at suction and discharge piping. Dissipation function determines energy input, which must be given to a system to cover hydraulic losses. Dissipation function is defined by density of entropy production depending on dynamic viscosity for incompressible fluid and on bulk viscosity for compressible fluid. This work assumes incompressible fluid, so influences of bulk viscosity are neglected. Newtonian fluid is assumed and dissipation function is expressed by volume integral depending on non-reversible stress tensor and strain rate tensor. Problem is solved in curvilinear coordinate system to underline physical principle of dissipation function. Especially influences of interior shape will distinguish here. Mathematical model is defined in special orthogonal curvilinear mesh, whose one of the coordinates is a streamline. New forms of Navier – Stokes equations and continuity equation are derived based on curvilinear coordinates. Shape of pump interior is designed based on qualitative analysis of dissipation function terms, so evolved swirl structures compensate role of check valves. The idea is creation of swirl structures in place of imaginary valves, which will gradually close suction and discharge piping of the pump. Based on this mathematical model is also possible to study separated flow and flow in boundary layer close to curved wall.

Pump geometry consist of two modified Venturi fluidic diodes, which are placed in piping. Diodes are also equipped with obstacles. Between diodes there is the piston cylinder perpendicularly connected. Design of the pump is based on idea, which assumed that obstacles placed in diodes, will in reverse flow direction create vortexes. That will cause higher resistance in reverse flow direction then in forward flow direction.

Transient CFD analysis was used to obtain volumetric efficiency of the pump. Simplified 2D geometry of the pump was used for the analysis. Whole geometry was meshed with hexahedral mesh, which contained about 60 000 cells. Piston motion was simulated by time-dependent velocity inlet boundary condition. Pressure outlet boundary condition was used for

discharge and suction piping. Value of pressure on both outlet boundary conditions was set 0 Pa that means outlet into atmospheric pressure. Valveless pumps are very dependent on piston motion frequency, so the pump was calculated for several frequencies and volumetric efficiency was observed.

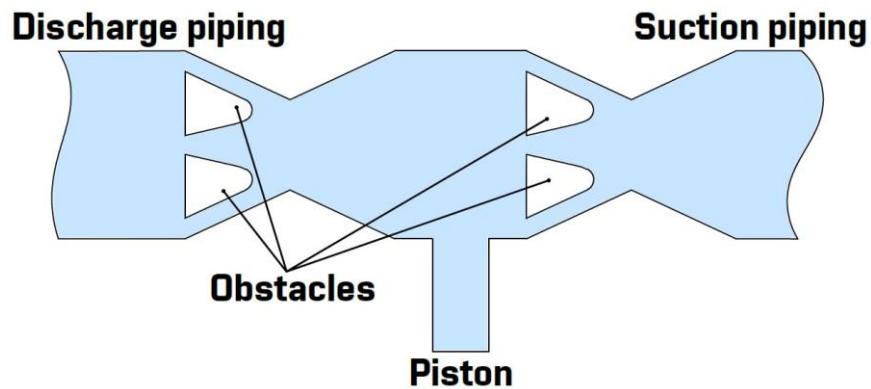


Fig. 1. Valveless pump geometry

New design of valveless piston pump for macro scale was created. Simplified transient CFD calculations of the pump was used to determine pump characteristics. Results of CFD analysis shows that pump has achieved about 13% of volumetric efficiency. Determined mathematical model based on dissipation function will be used to optimize performance of the pump.

Acknowledgements

Presented research was supported by centre of competence of Technology Agency of the Czech Republic TE02000232 “Rotary machines” and by the research project FSI-S-17-4615 “Multiphysics problems of fluid mechanics”.

References

- [1] Brdička, M., Samek, L., Sopko, B., Continuum mechanics, Academia, Praha, 2000.
- [2] Nabavi, M., Steady and unsteady flow analysis in microdiffusers and micropumps: A critical review, *Microfluidics and Nanofluidics* 7 (5) (2009) 599-619.
- [3] Tesař, V., Safe pumping of hazardous liquids – A survey of no-moving-part pump principles, *Chemical Engineering Journal* 168 (1) (2011) 23-34.

Stiffness analysis of the helmet

O. Medůna^a, P. Hisem^a

^a R&D Department of Computations and Modelling, VUTS, a. s., Svárovská 619, Liberec XI- Růžodol I, 460 01 Liberec, Czech Republic

The article deals with the stiffness analysis of the 12 versions of the helmet using FEM model. Each version of the helmet is a unique combination of these parameters: outside shell geometry, shape and thickness of inside ribs, shell material and strap stiffness. The aim of helmet parameters changes during the development process was to increase energy absorbed by shell and strap deformation at a given load to the level defined by technical standards.

The real helmet consists of the shell, the inner soft pad and the straps. The straps are attached to the helmet using the clips. The FEM model of each helmet version consists of longitudinal symmetric part of the helmet. The shell of the helmet and the clips consist of 3D tetrahedral elements. The textile straps and the inner soft pad used to stabilize the real helmet on the head are replaced with node-to-node springs (Fig. 1). Stiffness of the “straps” springs depends on the expected strap properties which has changed during development process of the helmet.

Rigid sphere vertically pushed as a punch to the top of the helmet is considered as the load of helmet model as in the real static tests. The punch is loaded with a linearly increasing force until its vertical displacement reaches δ_{\max} .

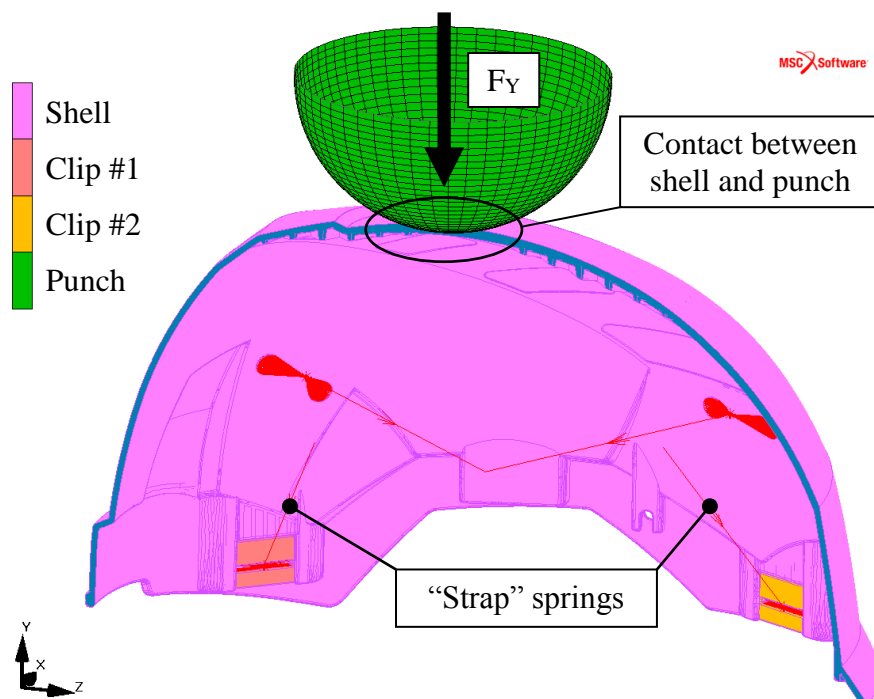


Fig. 1. FEM model of the helmet

In the simulations, an ideal elastic-plastic material models were used for the shell and clips. The parameters for this type of material model are determined based on our own tensile tests.

The evaluation of each helmet version was carried out by comparing the value of the deformation energy E [J], which is absorbed by the helmet during the load by deforming the shell and stretching the straps. This value must be greater than the minimum required energy E_{min} [J] that depends on the weight of the punch and on the height of its fall (parameters of the real dynamic test).

The second parameter we monitored is the maximum value of vertical load force F_Y [N] at maximum allowed value of vertical punch displacement δ_{max} (Fig. 2) that should be less than maximum allowed force on punch F_{Ymax} .

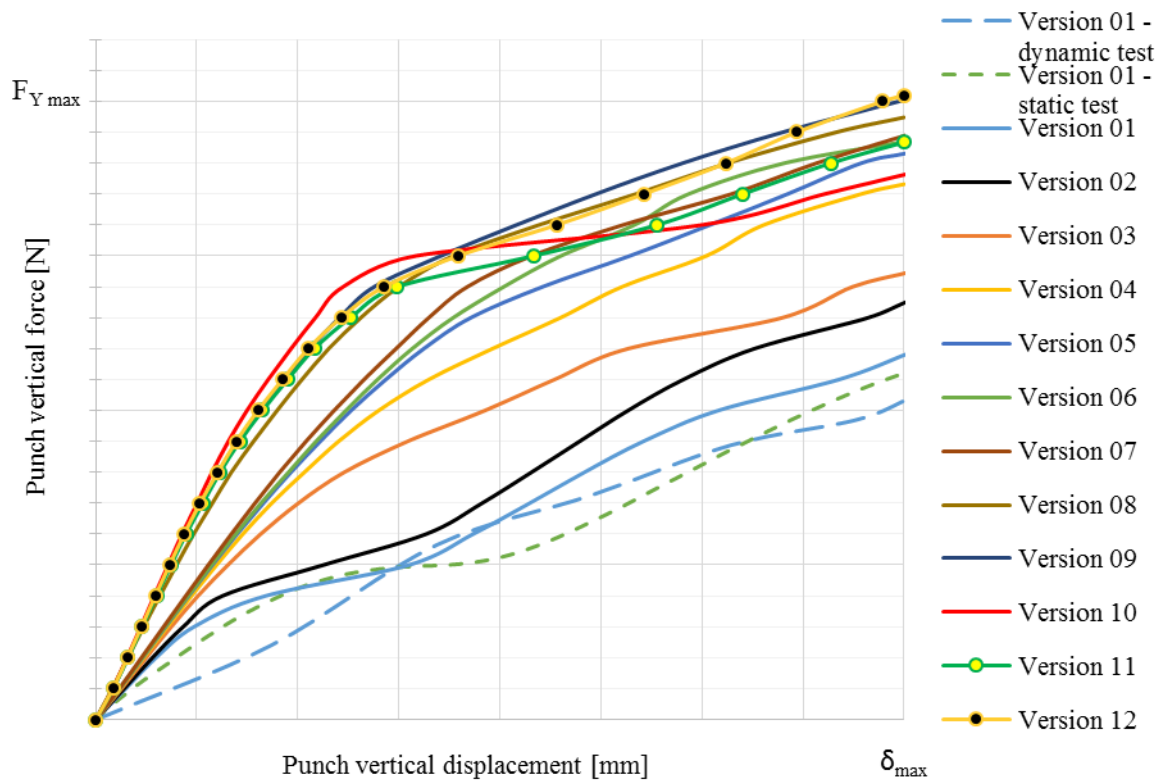


Fig. 2. Comparison of the stiffness characteristics

From the analysis results, it is clear that the stiffness of the whole helmet is primarily influenced by the stiffness of the straps at the beginning of the loading. The stiffness of the shell itself will take effect at a higher load of a helmet. Using very rigid straps will increase the stiffness of the helmet at the beginning of the load, which will significantly increase the absorbed energy E . As a result of shell geometry modifications with suitably selected straps, the value of E/E_{min} ratio increased from 59 % (version 01) to 118 % (version 12).

Modelling of effects of a locomotive three-axle bogie on track

T. Michálek^a, L. Haupt^b, J. Zelenka^a, M. Kohout^a, S. Liberová^a

^a University of Pardubice, Detached Branch of the Faculty of Transport Engineering, Nádražní 547, 560 02 Česká Třebová, Czech Republic

^b CZ LOKO, a.s., Semanínská 580, 560 02 Česká Třebová, Czech Republic

The three-axle bogie (see Fig. 1) for a diesel-electric locomotive for the track gauge 1520 mm is being developed in co-operation of the company CZ LOKO and the Faculty of Transport Engineering of the University of Pardubice in years 2015 to 2017. The development of the new bogie is supported by the Technology Agency of the Czech Republic and the main result of the project is manufacturing of a bogie prototype.

The bogie consists of a welded bogie frame and three wheelsets with axle-mounted traction motors and brake discs in wheels. The primary suspension is ensured with a couple of flexi-coil springs and a hydraulic damper per axle box; wheelset guiding is realized by means of longitudinal rods. Longitudinal force transmission between the bogie frame and locomotive body is ensured by means of a pivot, going through a hole in the main crossbeam of the bogie frame, which is situated between the second and third wheelset – i.e. closer to the centre of the locomotive. The secondary suspension consists of three flexi-coil springs with rubber-metal pads on each longitudinal beam of the bogie frame and is supplemented with vertical and lateral hydraulic dampers. The bogie can be equipped with an active element for bogie steering, situated laterally on the front beam of the bogie frame. This active element can also serve as a passive yaw damper. A more detailed description can be found in paper [1].

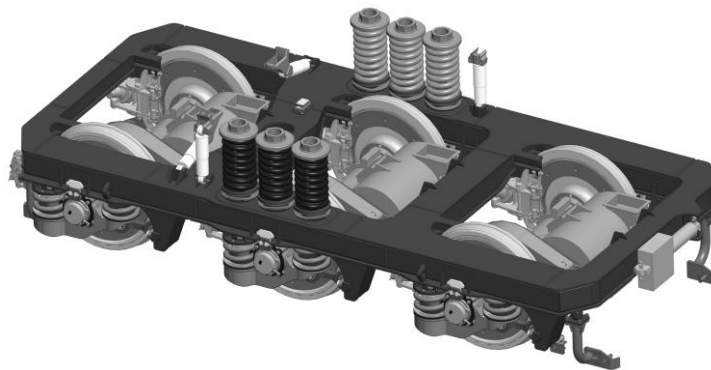


Fig. 1. Visualization of the new three-axle bogie

In framework of development of the bogie, workers of the Detached Branch of the Faculty of Transport Engineering in Česká Třebová performed multi-body simulations of running and guiding behaviour of a locomotive equipped with the bogies. For this purpose, a new version of the simulation tool SJKV was created. A computational model of the vehicle has 114 DoFs and one of the most challenging tasks to solve was modelling of the secondary suspension. The combination of the flexi-coil spring with a special rubber-metal pad leads to a strong directional dependency of the horizontal stiffness characteristic of such suspension element (see, e.g., [2]). Therefore, a mathematical description of the horizontal characteristics of the used elements is based on results of measurement of a real spring with pad performed on the dynamic test stand in laboratories of the Faculty of Transport Engineering in Pardubice.

Besides the original arrangement of the secondary suspension, a system of active elements for bogie steering was proposed in order to reduce guiding forces as well as wear of wheels and rails in bogies. In the simulations, the active system is controlled on basis of the bogie rotation relatively to the vehicle body and in small radius curves it supports radial steering of the bogies. The parameters of the active elements (i.e. the maximum force in the element and its reaction time) were discussed with their manufacturer. In Fig. 2, there are demonstrated simulation results of guiding behaviour of a six-axle locomotive with the total mass of 150 t in form of observed quasistatic values of the guiding forces acting on individual wheels at the run of the vehicle through a curve with radius of 250 m under common “GOST conditions” (defined by the unbalanced lateral acceleration and the wheel/rail contact geometry).

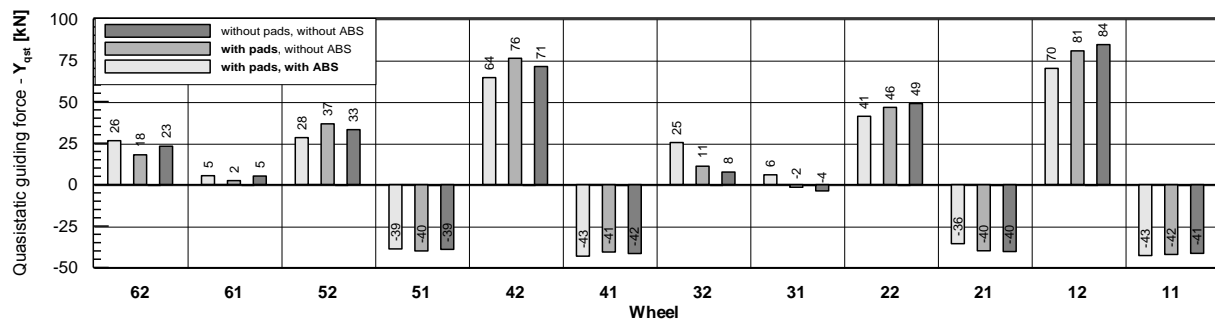


Fig. 2. Results of comparative simulations of guiding behaviour of a locomotive with the axle-load of 25 t in a R250 curve at the speed corresponding to unbalanced lateral acceleration 0.7 m.s^{-2} under the condition of dry rails (the locomotive with/without pads in secondary suspension and with/without active bogie steering)

The simulation results show that the tilting rubber-metal pads under the secondary springs help to reduce the quasistatic guiding force on the leading wheel (i.e. the wheel 12 in Fig. 2). However, the influence of the pads on the rear bogie (on the wheel 42) is reverse. This effect is related with the reduction of the bogie yaw resistance which is reached by means of using of the pads. The application of the system of active radial bogie steering in combination with the proposed arrangement of the secondary suspension (i.e. the flexi-coil springs with pads and the eccentric position of the central pivot) can lead to a significant reduction of quasistatic guiding forces on both bogies, or – more precisely – to a better (i.e. more even) distribution of the lateral forces on individual wheelsets of the vehicle and therefore to a lower level of wear of the wheels and rails in curves, as well.

It can be stated that the active element systems for radial bogie or wheelset steering can represent a very effective tool for improvement of “track-friendliness” of railway vehicles. Modes of practical support of their introduction into the regular operation are presented in [3].

Acknowledgements

The work has been supported by the project No. TH01010455 “Research and Development of a Three-axle Bogie for the Track Gauge 1520 mm” of the Technology Agency of the Czech Republic.

References

- [1] Haupt, L., Kopal, J., Michálek, T., Štěpánek, J., Benický, M., Staněk, P., Čejka, T., Liberová, S., Development of a three-axle bogie for diesel-electric locomotive, Proceedings of the 23rd Conference with international participation Current Problems in Rail Vehicles, Pardubice, University of Pardubice, 2017, pp. 141-150. (in Czech)
- [2] Michálek, T., Zelenka, J. Modelling of flexi-coil springs with rubber-metal pads in a locomotive running gear, Applied and Computational Mechanics 9 (1) (2015) 21-30.
- [3] Michálek, T., Zelenka, J., Questions of the vehicle action effects on the track related to the infrastructure charges, New Railway Technique 24 (5) (2016) 12-20. (in Czech)

Experimental and finite element analysis of composite gun barrels

D. Mochar^a, J. Trnka^a, F. Valeš^a, M. Chlada^a, J. Červ^a, J. Masák^a,
D. Gabriel^a, J. Vtípil^b

^aInstitute of Thermomechanics of the CAS, v. v. i., Dolejškova 5, 182 00 Prague, Czech Republic
^bČeská zbrojovka, a.s., Svatopluka Čecha 1283, 688 27 Uherský Brod, Czech Republic

The accuracy of gun barrels is one of the main indicator of their quality. A shot dispersion of every weapon is greatly influenced by the barrel vibration during firing process. The improvement of the accuracy can be achieved by increasing the rigidity of barrel [2] using modern materials such as composites instead of conventional steel materials [3]. In this work experimental and computational assessment of different types of composite gun barrels subjected to impact loading was performed.

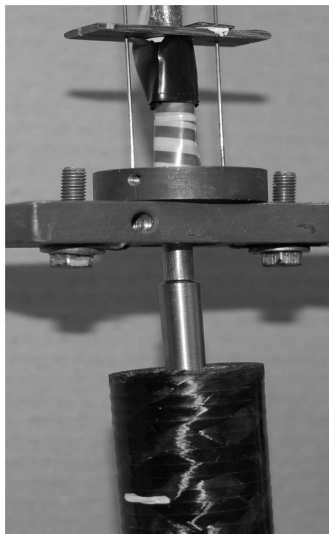


Fig. 1. Drop weight tester

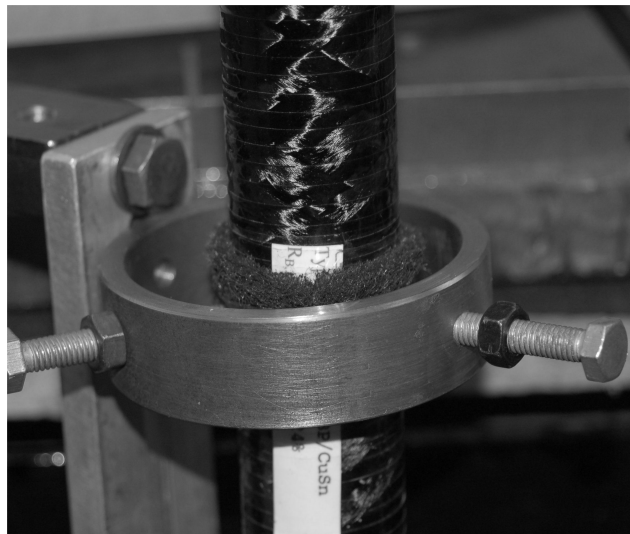


Fig. 2. Deposition of composite barrel

The experiment was done using drop weight tester (see Fig.1), which allows to measure force acting on the front of composite barrel using semiconductor strain gauges located on an impactor marked by X in Fig. 3. The second pair of semiconductor strain gauges are placed in the middle of the barrel marked by Y in Fig. 3 to capture the axial strain. Note that the composite barrel has been put in foam handles to prevent potential loss of energy (see Fig. 2). The seven different types of wound composite barrels have been tested ranging between 14 to 16 layers wound up on a steel core. The geometries of composite barrels were determined by length $L = 660$ mm, inner diameter $d_1 = 8$ mm and outer diameter, which varies from $d_2 = 29.1$ mm to $d_2 = 30.6$ mm.

For future optimisation of strength and geometric characteristics of composite gun barrels, the finite element analysis was performed in Abaqus package for one selected barrel composi-

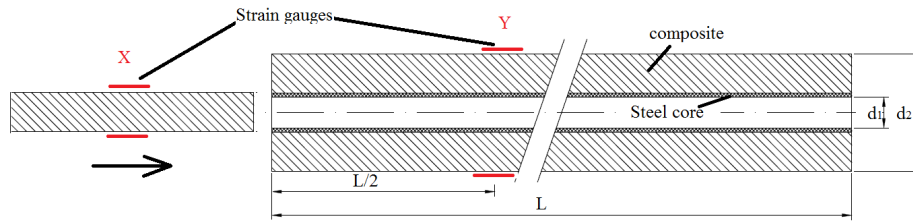


Fig. 3. Scheme of composite gun barrel

tion. The problem was treated as an axisymmetric one modelled by regular mesh containing 16500 linear S4R elements with reduced integration [1]. The mesh size was 1x1 mm. The shell composite material model was utilised based on the introduction of material properties for each anisotropic layer including its thickness and position in the finite element model of composite gun barrel. For the integration of equations of motion the central difference method with automatic length of time step was employed.

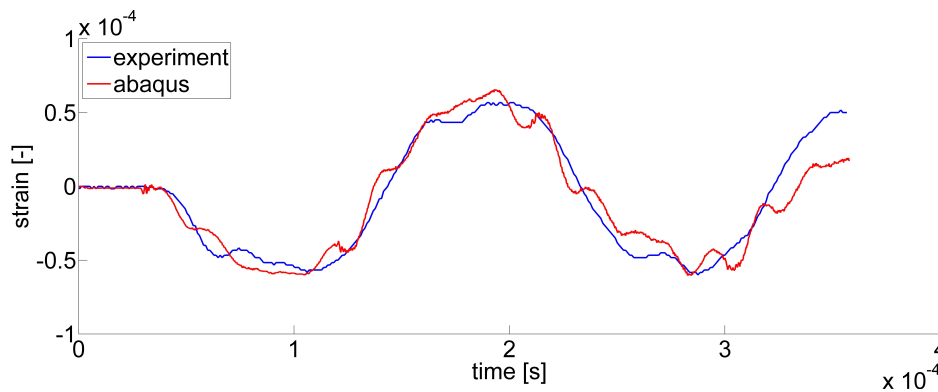


Fig. 4. Comparison of time strain distribution obtained from finite element solution and experimental measurement for one selected composite material

The comparison of time strain distribution obtained from the finite element solution and experimental data at the point 'Y' corresponding the location of strain gauges is shown in Fig. 4. Quite a good agreement between the experimental measurement and numerical results was observed. It can be concluded that the proposed finite element model can be used for finding the optimal structure of composite gun barrels.

Acknowledgements

This work was supported by the Technology Agency of the Czech Republic under grant No TH01010772 within institutional support RVO:61388998 and the European Regional Development Fund under Grant No. CZ.02.1.01/0.0/0.0/15_003/0000493 (Centre of Excellence for Nonlinear Dynamic Behaviour of Advanced Materials in Engineering).

References

- [1] Abaqus 6.14 Online Documentation, Dassault Systèmes, 2014, 23-7-2014.
- [2] Fišer, M., Construction of small-caliber firearm barrels, Military Academy, Brno, 2002. (in Czech)
- [3] Jones, R. M., Mechanics of composite materials, 2nd edition, New York & London, 1999.

Shape optimization of obstacles in incompressible viscous flow using OpenFOAM

F. Moravcová^a, V. Lukeš^a, E. Rohan^a

^aFaculty of Applied Sciences, University of West Bohemia, Univerzitní 8, 306 14 Plzeň, Czech Republic

The objective of this paper is the shape optimization of obstacles (as e.g. turbine blades) with the aim to minimize the dissipative power between the flow inlet and outlet. We consider a reference configuration Ω of the flow domain. The external boundaries (inlet, outlet and channel's boundaries) are specified by the user, while the shape of the obstacle is parameterized by n control points. An example of such geometry is shown in Figs. 1 and 2 illustrating the flow domain Ω and the obstacle shape, respectively. The obstacle shape can be modified smoothly when moving one or more control points. This induces a one-to-one mapping of Ω into a new configuration Ω' that can be described by the field $\Delta \mathbf{x} = \mathbf{x}' - \mathbf{x}$ (where $\mathbf{x} \in \Omega$ and $\mathbf{x}' \in \Omega'$). This field is proportional to the displacements U^i of each control point through the B-spline basis functions $B^i(\mathbf{x})$:

$$\Delta \mathbf{x} = \sum_{i=1}^n B^i(\mathbf{x}) U^i. \quad (1)$$



Fig. 1. Flow domain

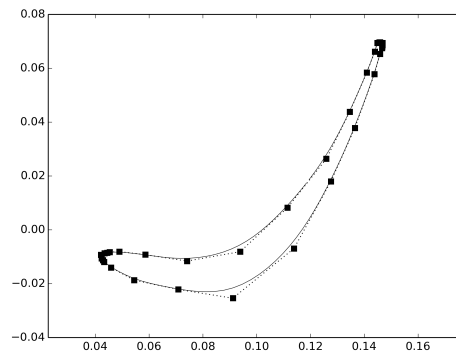


Fig. 2. Obstacle geometry (solid line) and control points (squares)

The sensitivity analysis developed in our previous paper [1] is used for computing the gradient of the dissipative power w.r.t. the position of the controls points:

$$\mathbf{s}^i \equiv \frac{\partial J}{\partial U^i} = -\nu \int_{\Gamma_{obstacle}} (\mathbf{n} \cdot \nabla) \mathbf{w} \cdot (\mathbf{n} \cdot \nabla) \mathbf{v} B^i \mathbf{n} d\Gamma, \quad (2)$$

where the dissipative power J can be described in terms of the enthalpy loss between the inlet and outlet parts

$$J = - \int_{\Gamma_{inlet} \cup \Gamma_{outlet}} \left(p + \frac{1}{2} v^2 \right) \mathbf{v} \cdot \mathbf{n} d\Gamma, \quad (3)$$

where the pressure p and the velocity \mathbf{v} are solutions of the flow problem, \mathbf{w} is the adjoint velocity, \mathbf{n} is the outward unit normal vector and ν is the fluid viscosity. This step is done with OpenFOAM. The optimization problem, read as follows:

find $\mathbf{U} \in \mathcal{C}$ such that:
 $J(\mathbf{U}, (p, \mathbf{v})) \rightarrow \min$
s.t. (p, \mathbf{v}) solves the flow problem,

is solved by the gradient-based SLSQP method implemented in ‘pyOpt’, the Python-based package. Geometric constrains are involved in the set \mathcal{C} which represents an equality constrain keeping the obstacle’s surface area constant and a set of inequality constrains preventing degenerations of the obstacle shape. Finally, as an illustration, a solution example is shown in Figs. 3 and 4. There, the obstacle shape optimization leads to the dissipative power decreasing by 6.5%.

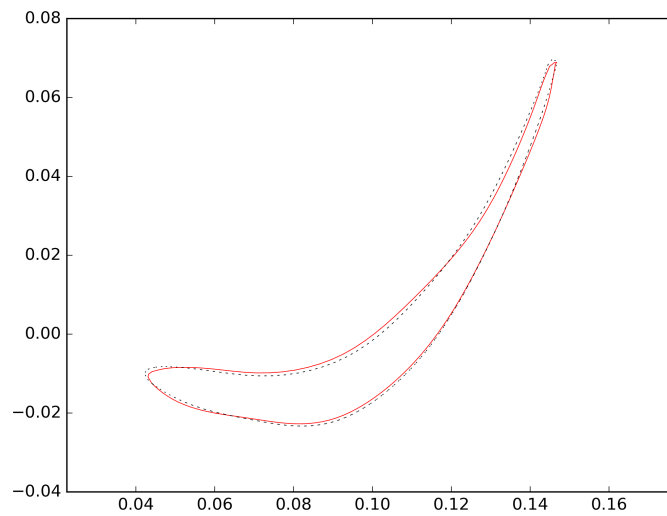


Fig. 3. Optimal (red solid line) and reference (black dashed line) obstacle geometries

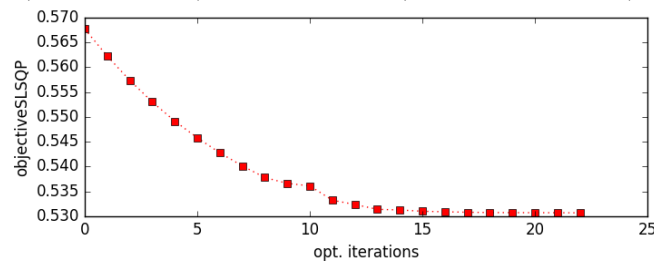


Fig. 4. Evolution of the dissipative power during the optimization process

Acknowledgment

This research is supported by project “Centre of research and experimental development of reliable energy production” TE01020068 of the Technology Agency of the Czech Republic.

References

- [1] Moravcová, F., Lukeš, V., Rohan, E., Surface sensitivities computation for turbine blades using OpenFOAM, Proceedings of the conference Computational Mechanics 2016, Špičák, University of West Bohemia, 2016.

Critical time step estimators in explicit dynamics

M. Mračko^a, A. Tkachuk^b, R. Kolman^a, J. Plešek^a, D. Gabriel^a

^a*Institute of Thermomechanics, The Czech Academy of Sciences, Dolejškova 1402/5, 182 00 Praha 8, Czech Republic*

^b*Institute for Structural Mechanics, University of Stuttgart, Pfaffenwaldring 7, 70550 Stuttgart, Germany*

Generally an explicit integration in time is only conditionally stable. To fulfill the stability condition one must determine the stable/critical time step size for the integration in time. The critical time step size of a linear system for the central difference scheme is given as $\Delta t_{\text{crit}} = 2/\omega_{\text{max}}$ [1], where ω_{max} is the maximum eigen-frequency from the generalized eigenvalue problem: $\det(\mathbf{K} - \omega^2\mathbf{M}) = 0$; \mathbf{K} is stiffness matrix and \mathbf{M} is mass matrix. This paper is devoted to estimation of these critical values in multidimensional cases. Two-dimensional 4-node quadrilateral and three-dimensional 8-node hexahedron isoparametric elements are taken into account. One-point Gauss integration and lumped mass matrix \mathbf{M} are used here, which is usual in explicit dynamic problems. Several methods for accurate computation of maximum eigenvalues exist, e.g. Power iterations method or Lanczos algorithm, but these are computationally expensive. Therefore a set of cheaper local methods was developed. Three methods are presented here: Courant-Friedrichs-Lewy (CFL) [2] condition based, Gershgorin's circle theorem [4] based and Belytschko's method [3].

CFL condition is given as $C = \Delta t \cdot c_L/l_c \leq C_{\text{max}}$, where C is a Courant number and $C_{\text{max}} = 1$, Δt is a time step size and l_c is a characteristic dimension of a finite element, given as $l_c = \text{Volume}/\text{Area}_{\text{max}}$ in 3D. This leads to a formula for the maximum eigen-frequency estimate

$$\omega_{\text{max}}^{\text{CFL}} = \frac{2c_L}{l_c},$$

where c_L is a longitudinal wave speed, which depends on material and the problem to be solved. Formulas for determination of c_L are following. For 1D uniaxial stress $c_L = \sqrt{\frac{E}{\rho}}$, for 2D plane stress $c_L = \sqrt{\frac{E}{(1-\nu^2)\rho}}$, for 2D plane strain $c_L = \sqrt{\frac{\Lambda+2G}{\rho}}$ and for 3D $c_L = \sqrt{\frac{\Lambda+2G}{\rho}}$, $\Lambda = \frac{\nu E}{(1+\nu)(1-2\nu)}$ and $G = \frac{E}{2(1+\nu)}$ are Lamé parameters. In numerical test, there were used Young's modulus $E = 2.1 \cdot 10^{11}$ Pa, density $\rho = 7850 \text{ kg} \cdot \text{m}^{-3}$ and Poisson ratio $\nu = 0.3$.

Maximum eigen-frequency estimate by method based on Gershgorin's circle theorem, proposed by Kulak [5], is given as

$$\omega_{\text{max}}^{\text{Ger}} \leq \max_i \sqrt{\frac{\sum_{j=1}^n |K_{ij}|}{M_{ii}}},$$

where K is stiffness matrix, M is lumped mass matrix and n is number of degrees of freedom of the problem of interest. This strategy can be performed both on local and global level (local or global matrices K and M).

Belytschko's method bounds maximum eigen-frequency (in 2D or 3D) with a relation [3]

$$\frac{n_N c_L^2}{n_D \Omega^2} a_{ii} \leq \omega_{\max}^2 \leq \frac{n_N c_L^2}{\Omega^2} a_{ii},$$

where n_N is a number of nodes, n_D is a dimension of a problem, c_L is a longitudinal wave speed, Ω is a volume (for 3D) or area (for 2D) of an element, a_{ii} is a trace of some matrix A based on a matrix of shape functions derivatives B [1].

A simple 3D problem is shown here: free vibrations of free beam-shaped body. The length is 10 m, cross-section is a square 1×1 m. This body is divided into 10 elements along its length, 5 different meshes are considered, presented in Table 1.

Table 1. Different meshes with corresponding element lengths [m]

Regular	1	1	1	1	1	1	1	1	1	1
Irregular 1	1	1.05	1	0.98	1	1.02	0.95	1	0.99	1.01
Irregular 2	3	2	1.45	1.05	0.8	0.6	0.45	0.3	0.2	0.15
Irregular 3	0.15	0.2	0.3	0.45	0.6	0.8	1.05	1.45	2	3
Irregular 4	0.45	1.05	2	0.2	1.45	0.15	0.6	3	0.8	0.3

All estimated values of ω are normalized with respect to accurate value as $\omega_{\text{norm}} = \omega_{\text{eig}}/\omega_{\text{est}}$, Table 2. Accurate values ω_{eig} are computed simply with "eig" command in Matlab. The least overestimated results are given by "Gershgorin's" method used on global level.

Table 2. Normalized estimations of ω_{\max} with respect to the exact value "Eig"

BCs	Mesh	Eig [Hz]	CFL	Ger _{Glob}	Ger _{Loc}	Bel
free - free	Regular	2 353	1.148	1.106	1.106	1.406
	Irregular 1	2 370	1.170	1.103	1.144	1.421
	Irregular 2	11 305	1.139	1.197	1.197	1.152
	Irregular 3	11 305	1.139	1.197	1.197	1.152
	Irregular 4	5 215	2.469	1.369	2.594	2.496

Acknowledgements

This work was supported by the Centre of Excellence for Nonlinear Dynamic Behaviour of Advanced Materials in Engineering CZ.02.1.01/0.0/0.0/15_003/0000493 (Excellent Research Teams) in the framework of Operational Programme Research, Development and Education. The work was also supported by the grant project Nos. 16-03823S and 17-22615S of the Czech Science Foundation within institutional support RVO:61388998 and by project SGS15/187/OHK2/3T/12.

References

- [1] Bathe, K.-J., Finite element procedures, Prentice Hall, 1996.
- [2] Courant, R., Friedrichs, K., Lewy, H., On the partial difference equations of mathematical physics, *Mathematische Annalen* 100 (1928) 32–74. (in German)
- [3] Flanagan, D. P., Belytschko, T., Eigenvalues and stable time steps for the uniform strain hexahedron and quadrilateral, *Journal of Applied Mechanics* 51 (1) (1984) 35–40.
- [4] Gerschgorin, S., On the restriction of eigenvalues of a matrix, *Bulletin de l'Académie des Sciences de l'URSS, Classe des sciences mathématiques et na* 6 (1931) 749–754. (in German)
- [5] Kulak, R. F., Critical time step estimation for three-dimensional explicit impact analysis, Technical Report, Argonne National Laboratory, Argonne, 1989.

Non-uniform torsional modal analysis of thin walled FGM beams

J. Murín^a, M. Aminbaghai^b, J. Hrabovský^a, V. Kutíš^a

^a Department of Applied Mechanics and Mechatronics, IAMM FEI STU in Bratislava, Ilkovičova 3, 812 19 Bratislava, Slovakia

^b Vienna University of Technology, Institute for Mechanics of Materials and Structures, Karlsplatz 13, A-1040 Vienna, Austria

The effect of non-uniform torsion must be considered in structural elastostatic and elastodynamic analysis of thin-walled beams with both open and closed cross-sections made of homogeneous material. The maximum normal stress due to the bimoment occurs at the points action of the external torques (except for a free end of the beam) and at the cross-sections of restrained warping (e.g. clamped cross-sections). Comprehensive overview of the literature dealing with the issue of a non-uniform torsion can be find in the articles [3, 5], for example. The last research results show that for non-uniform torsion of beams with closed cross-sections the impact of the Secondary Torsion Moment Deformation Effect (STMDE) is especially significant.

Beam structures are often exposed to time-dependent loads. Commercial FEM codes allow performing modal and transient dynamic analysis by 3D finite beam elements with and without consideration of the warping effects [1, 2, 4]. For torsion, very often an improved Saint-Venant theory is used and special mass matrices are proposed.

Common feature of the above cited works is that constant material properties of the beams in longitudinal direction are considered.

In this paper, the contribution [3] is extended on non-uniform modal analysis of the Functionally Graded Material (FGM) beams (Fig. 1) with longitudinal continuously varying material properties. A brief summary of the differential equations for non-uniform torsional deformations are formulated including the inertial line moments. In non-uniform torsion, the part of the bicurvature caused by the bimoment is taken into account as the warping degree of freedom, and the STMDE is also considered. A general semi-analytical solution of the differential equation is presented and the transfer matrix relation is established, from which the finite element equations of the two nodal straight beam finite element are derived. Omitting the external load the FEM equation for torsional natural free vibration are obtained. The results of numerical investigation from modal analysis of cantilever beam with open I cross-sections and rectangular hollow cross-sections are presented and compared with the ones obtained by commercial FEM codes. The effect of longitudinally varying material properties is evaluated. The final assessment of the proposed method is contained in the conclusions.

The main novelty of this contribution is original inclusion of the longitudinal variation of material properties into the differential equations for uniform and non-uniform torsion-free vibrations. The transfer relations are derived, from which the finite element equations of the two nodal straight beam finite element are derived for calculation of the torsional eigenfrequencies of straight beams including warping. The bimoment and the primary part of the bicurvature are taken to specify boundary conditions. The proposed approach is used for non-uniform torsion modal analysis of beams with open and closed cross-sections.

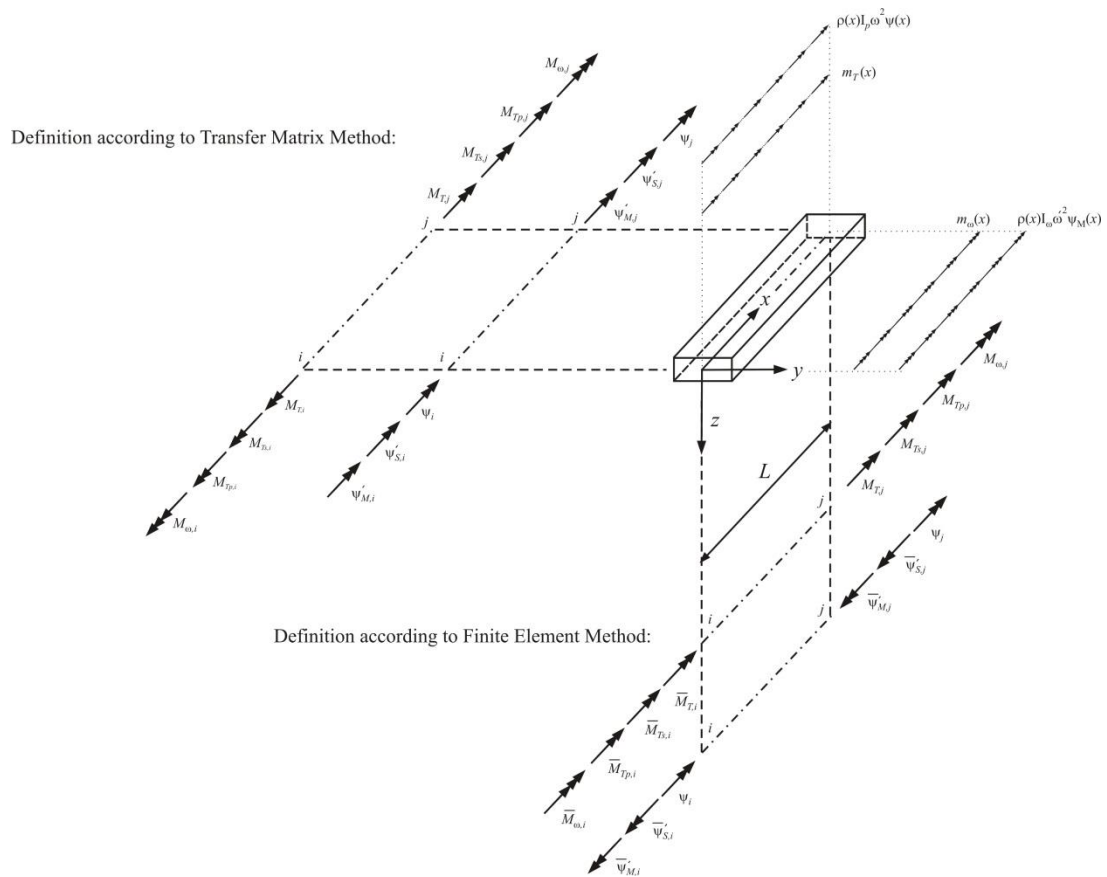


Fig. 1. Positive orientation of the moments and rotation angles at element nodes for the TMM and FEM

Acknowledgements

The authors gratefully acknowledge financial support by the Slovak Grant Agencies: VEGA No. 1/0453/15.

References

- [1] ABAQUS/CAE, Version 6.10-1, Dassault Systemes Simulia Corp. Providence, RI, USA.
- [2] ADINA R & D, Inc. Theory and Modelling Guide. Volume I: ADINA. 2013.
- [3] Aminbaghai, M, Murin, J, Hrabovsky, J, Mang, H.A., Torsional warping eigenmodes including the effect of the secondary torsion moment on the deformations, Engineering Structures 106 (2016) 299-316.
- [4] ANSYS Swanson Analysis System, Inc., 201 Johnson Road, Houston, PA 15342/1300, USA.
- [5] Dikaros, I.C., Sapountzakis, E.J., Argyridi, A.K., Generalized warping effect in the dynamic analysis of beams of arbitrary cross section, Journal of Sound and Vibration 369 (2016) 119-146.

Lifetime assessment of particulate ceramic composite with residual stresses

L. Náhlík ^{a,b}, Z. Majer ^{a,b}, K. Štegenerová ^a, P. Pokorný ^a, R. Bermejo ^c

^a Institute of Physics of Materials, Czech Academy of Sciences, Žitkova 22, 616 62 Brno, Czech Republic

^b Faculty of Mechanical Engineering, Brno University of Technology, Technická 2, 6016 69 Brno, Czech Republic

^c Institute of Structural and Functional Ceramics, Montanuniversität Leoben, Franz-Josef-Strasse 18, A-8700 Leoben, Austria

A micro-crack propagation in particulate ceramic based composite was studied using finite element method (FEM). Subcritical crack growth (SCG) was numerically simulated under complex load conditions (mechanical loading and loading by internal residual stresses). The effect of residual stresses on the crack propagation was studied. Two-dimensional and simplified 3D computational model of particulate ceramic composite was developed in finite element (FE) system ANSYS.

The contribution is devoted to the micro-crack propagation in the ceramic particulate composite under conditions of subcritical crack growth. The general assumption has been that a crack does not extend as the applied stress intensity factor is increased until the critical value is reached, at which point the crack propagates very rapidly. However, in many ceramics cracks grow slowly under values of applied stress intensity well below the critical value for rapid fracture, that is, K_{IC} [5]. The principal subcritical crack propagation mechanism in ceramics at room temperature involves stress-assisted reaction with the environment – especially reaction with water. This mechanism is known as stress corrosion cracking [5]. This mechanism and mathematical description of subcritical crack growth is a bit similar to the fatigue crack propagation in metals, however the applied load is not of cyclic nature in this case.

A crack of initial depth a_i propagates slowly until a critical load-dependent size a_c is attained at which unstable crack extension follows. Crack growth is governed only by the stress intensity factor K and for a given material and environment there is a unique relation between the crack growth rate v and K_I [3]

$$v = da/dt = v_0(K_I(a) / K_{IC}), v = \frac{da}{dt} = f(K_I), \quad (1)$$

where the parameter v_0 is critical crack growth rate. The time to failure can be expressed as

$$t_f = \int_0^{t_f} dt = \int_{a_i}^{a_c} \frac{da}{v_0 \left(\frac{K_I}{K_{IC}}\right)^n}, \quad (2)$$

where a_i is the initial crack size and a_c is the critical value at the moment of failure. Note that the initial surface defect (flaw, scratch, etc.) can be deep several micrometers, see Fig. 1.

Ceramic particulate composite with surface defect was modelled by means of FE method. 2D and 3D numerical models were developed with tens of regularly distributed particles to study crack propagation through the composite. Volume fraction of particles was 20% and their diameter was 1 μm . Material characteristics were taken from [1].

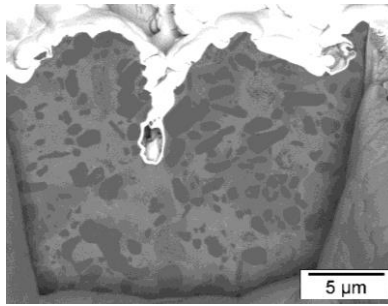


Fig. 1. Particulate composite with glass matrix and surface defect (by courtesy of Raul Bermejo, Montanuniversitaet Leoben)

The initial crack length was chosen as $a_i = 5\mu\text{m}$ according to real defect size. The crack propagation was simulated with crack increment $0.1\mu\text{m}$. Numerical models were remeshed after each computational step. Stress intensity factors for normal and shear mode (K_I and K_{II}) were determined in each step. Sih's strain energy density criterion [4, 2] was used for determination of crack propagation direction after each step. Two different models were considered. One loaded by constant tensile load with different applied stress levels (75, 100, 130 MPa) and by volume load applied by change of temperature from 850°C to 20°C . The temperature change leads to the strong internal stresses in the model (this corresponds to the cooling from the sintering temperature to the room temperature of real composite). The second model was loaded by tensile stress only. Then the time to failure was estimated using Eq. (2). By comparison of results from both models the role of residual stresses in the ceramic particulate composite can be expressed.

The results indicate that the presence of residual stresses significantly reduces values of stress intensity factor in the vicinity of composite surface and the direction of residual stresses around the particles contributes to the micro-crack deflection from the particles and to slower crack propagation through composite.

Acknowledgements

This research was supported through the grant No. GA15-09347S of the Czech Science Foundation. The research infrastructure IPMinfra (www.ipminfra.cz) was used for research activities. IPMinfra is supported through the project No. LM2015069 of Ministry of Education, Youth and Sport of the Czech Republic.

References

- [1] Bermejo, R., Supancic, P., Krautgasser, C., Morrell, R., Danzer, R., Engineering fracture mechanics 100 (2013) 108.
- [2] Majer, Z., Náhlík, L., Štegnrová, K., Hutař, P., Bermejo, R.: Study of influence of residual stresses on crack propagation in particulate ceramic composites, Solid State Phenomena 258 (2017) 178-181.
- [3] Munz, D., Fett, T., Ceramics: mechanical properties, failure behaviour, materials selection, Springer-Verlag Berlin Heidelberg, 1999.
- [4] Sih, G.C., A special theory of crack propagation: methods of analysis and solutions of crack problems, Springer Netherlands, 1973.
- [5] Wachtman, J.B., Cannon, W.R., Matthewson, M.J., Mechanical properties of ceramics, 2nd edition, John Wiley & Sons, 2009.

Stochastic stability of the generalized van der Pol system under random additive excitation

J. Náprstek^a, C. Fischer^a

^a*Institute of Theoretical and Applied Mechanics, CAS v.v.i., Prosecká 76, CZ-190 00 Praha, Czech Republic*

The paper is motivated by a series of wind tunnel experiments investigating aeroelastic SDOF and TDOF section models of various shape and aeroelastic properties. It reveals that most of them can be theoretically modeled by the van der Pol – Duffing type equations or their combination adjusting degree of individual nonlinear terms or their coefficients, see for instance [1] or [3]. It should be emphasized that this character of the system response is very stable and is obvious in linear as well as in weakly nonlinear domain when the post-critical effect emerges. Moreover, many special effects identified by an experimental way evoke properties recognized in the pure theory of differential equations.

As the first step the authors attempt to develop an authentic theoretical model characterizing response of a nonlinear SDOF system associated with the aeroelastic model, which is investigated in conditions of the homogeneous stream with the velocity slowly sweeping up and down outside the resonance domain. In this regime the random excitation component of the additive type is dominant. This regime corresponds to the super-critical state, usually characterized by a high Reynolds number and being typical for high velocities of the stream. Let us take a note, that following experimental results the exciting random process is different from the white noise and its spectral density cannot be considered as a constant. On the other hand, the process is more or less correlation stationary.

Let us consider the van der Pol equation with an extended nonlinear damping part and with random excitation of the additive type:

$$\ddot{u} - (\eta - \nu u^2 + \vartheta u^4) \cdot \dot{u} + \omega_0^2 \cdot u = h \cdot \xi(t), \quad (1)$$

where: η, ν, ϑ – parameters of the damping. Basically it holds $\nu > 0$, while η should be considered positive or negative, and ϑ varies in an interval $(-\infty, \vartheta_{max})$; ω_0 – eigen-frequency of the adjoint linear SDOF system, $\xi(t)$ – broadband weakly stationary Gaussian random process; h – multiplicative constant.

When applied in aeroelasticity of the SDOF or TDOF systems, we should be aware that coefficients η, ν, ϑ are functions of the stream velocity v_s . Regarding ν, ϑ , they vanish for $v_s = 0$, as they follow from aeroelastic processes only. Coefficient η consists of two components: (i) elastic part $\eta_e < 0$ corresponding to conventional damping ratio of a linear SDOF system and (ii) aeroelastic part $\eta_a \geq 0$, which is zero for $v_s = 0$ and rises monotonously for increasing v_s . Therefore, the total value of η crosses zero for a certain value of $v_{s,crit}$ and becomes positive. Starting this point, the trivial solution of the homogeneous equation is no more stable and nonlinear part of the damping should stabilize the response in the first limit cycle which makes an attractor, see e.g. [2]. We apply the harmonic balance solution method supposing a

slow variability of the response partial amplitudes following this expression:

$$u(t) = a_c \cdot \cos \omega t + a_s \cdot \sin \omega t, \quad \dot{u}(t) = -a_c \omega \sin \omega t + a_s \omega \cos \omega t, \quad (2)$$

where a_c, a_s are slowly time variable partial amplitudes. Stochastic averaging leads after a number of adaptations to the Ito system as follows:

$$\begin{aligned} da_c &= \frac{\pi}{\omega} \left[\eta a_c + \delta a_s - \frac{1}{4} \nu \cdot a_c (a_c^2 + a_s^2) + \frac{1}{8} \vartheta \cdot a_c (a_c^2 + a_s^2)^2 \right] dt \\ &\quad + \left(\frac{\pi}{\omega^2} \Phi_{\xi\xi}(\omega) \right)^{1/2} \cdot dB_c(t), \\ da_s &= \frac{\pi}{\omega} \left[-\delta a_c + \eta a_s - \frac{1}{4} \nu \cdot a_s (a_c^2 + a_s^2) + \frac{1}{8} \vartheta \cdot a_s (a_c^2 + a_s^2)^2 \right] dt + \frac{\pi}{\omega} P \omega dt \\ &\quad + \left(\frac{\pi}{\omega^2} \Phi_{\xi\xi}(\omega) \right)^{1/2} \cdot dB_c(t), \end{aligned} \quad (3)$$

where $B_c(t)$ is the Wiener process related with input excitation $\xi(t)$ and $\Phi_{\xi\xi}(\omega)$ is the spectral density of the process $\xi(t)$ at frequency ω . Relevant reduced Fokker-Planck Equation (FPE) for the stationary cross Probability Density Function (PDF) $p(a_c, a_s)$ can be written in the form:

$$\begin{aligned} \frac{\partial}{\partial a_c} \left[\eta a_c + \delta a_s - \frac{1}{4} \nu \cdot a_c (a_c^2 + a_s^2) + \frac{1}{8} \vartheta \cdot a_c (a_c^2 + a_s^2)^2 \right] p - \frac{1}{\omega} \Phi_{\xi\xi}(\omega) \frac{\partial^2 p}{\partial a_c^2} \\ + \frac{\partial}{\partial a_s} \left[-\delta a_c + \eta a_s - \frac{1}{4} \nu \cdot a_s (a_c^2 + a_s^2) + \frac{1}{8} \vartheta \cdot a_s (a_c^2 + a_s^2)^2 \right] p - \frac{1}{\omega} \Phi_{\xi\xi}(\omega) \frac{\partial^2 p}{\partial a_s^2} = 0. \end{aligned} \quad (4)$$

Its general solution has the form:

$$p(A) = CA \exp \left(\frac{A^2}{2S} \left(\eta - \frac{1}{8} \nu A^2 + \frac{1}{24} \vartheta A^4 \right) \right), \quad \vartheta \leq 0, \quad (5)$$

where $A^2 = a_c^2 + a_s^2$. The formula (5) is independent on the phase shift $\varphi = a_s/a_c$.

Let us take a note that only negative ϑ is considered in this study. If $\vartheta > 0$, the stationary or asymptotically stable solution of FPE (4) does not exist any more. It means that the operation of the stochastic averaging which leads to the system of Eqs. (3) is no more applicable. The PDF is not integrable with respect to amplitude A and the normalization constant does not exist. Therefore, if the excitation process admits infinite values, the solution cannot be considered as a PDF either constant (independent on time) or variable with respect to the slow time. It is obvious that the PDF of excitation noise $\xi(t)$ has a crucial character. Basically, the excitation PDF could be defined with limited values preventing that the response never reach the outer limit cycle. Therefore, the task becomes a character of the problem of the first excursion beyond a defined limit. Such a concept requires a different approach and the authors will pay attention to this task in the next paper.

Acknowledgements

The kind support of the Czech Scientific Foundation No. 15-01035S and of the RVO 68378297 institutional support are gratefully acknowledged.

References

- [1] Náprstek, J., Fischer, C., Analysis of the quasi-periodic response of a generalized Van der Pol non-linear system in the resonance zone, *Computers and Structures* 112 (2017) 1–28.
- [2] Náprstek, J., Fischer, C., Stability of limit cycles in autonomous nonlinear systems, *Meccanica* 49(8) (2014) 1929–1943.
- [3] Nayfeh, A.H., Char-Ming, C., Non-linear interactions in a parametrically excited system with widely spaced frequencies, *Nonlinear Dynamics* 7 (1995) 195–216.

Static and fatigue testing of composite external fixator

Z. Padovec^a, R. Sedláček^a, P. Růžička^a, M. Růžička^a

^aCzech Technical University in Prague, Faculty of Mechanical Engineering, Department of Mechanics, Biomechanics and Mechatronics, Technická 4, Prague, 166 07, Czech Republic

Our work focused on the design of the body of an external fixator for the treatment of long bone fractures to be manufactured from consolidated randomly-oriented C/PPS pellets (see e.g. [3]). The ProSpon UNI-FIX external fixator was chosen as a model (see Fig. 1). This fixator is currently manufactured from duralumin. The design of the body structure has to take into account the different material properties and the different manufacturing technology when the C/PPS composite with pellets is applied. The supporting tube was manufactured from a composite material with continuous fiber by the filament winding technology. The tube will not be telescopic. The structure is supplemented with sleeves of a spherical joint made from Ti alloy. Between the body of the fixator and the tube, and also between body of the fixator and the sleeve, a bonded joint has been designed with the use of LOCTITE EA 9394 AERO.

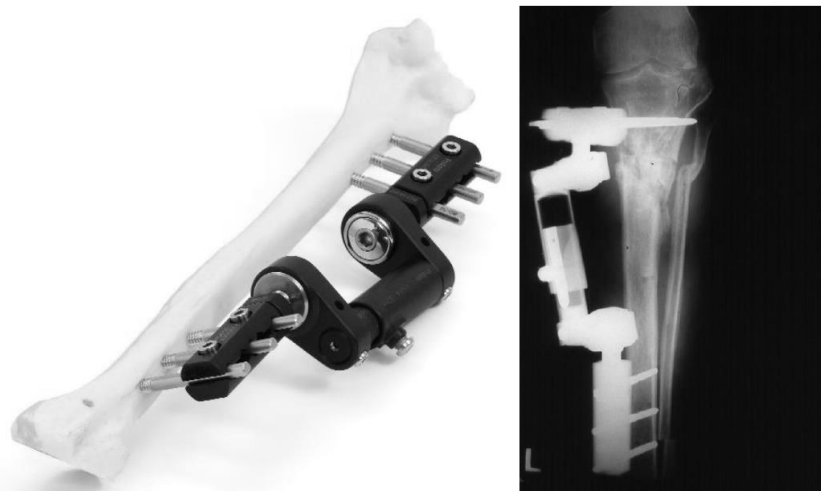


Fig. 1. The ProSpon UNI-FIX unilateral fixator, and a radiograph of a broken tibia with the fixator applied

The tests on the external fixator are performed as quasi-static loading until the axial load reaches 1 300 N. The fixator is attached in special jaws, and its supporting tube should be at a distance of 100 mm from the axial loading force. The displacement of the loading part is 40.0 mm.min⁻¹. After the prescribed load has been reached, there is a 30 s stay on that load. If the structure has not been destroyed, the assembly is unloaded again at a constant speed of 40.0 mm.min⁻¹. If the fixator reaches the described load without being destroyed, it is considered to be static verified.

The cyclic testing is based on [2]. The fixator should withstand a pulsating force of 220 N over 10 000 cycles. The methodology for cyclic loading developed in our lab required a greater number of cycles – 100 000. This requirement is based on the demands placed on the mechanical properties of a femoral or tibial splint, having in mind that the fixator is used primarily in the treatment of long bones. The loading frequency is 5 Hz. Both ends of the

bone substitutes (beechwood rods) are fixed in the jaws (without gripping). The parameters monitored during the tests include the displacement amplitude of the loading part. The outcome of the test is a statement that the fixator has withstood the prescribed number of cycles without being destroyed and without malfunctioning.

Two versions of the specimens were prepared for the tests. In version A, conical screws 6 mm in diameter, 100/30 mm in length and with a 6/5 mm thread (PROSPON PN S0010002) were used for anchoring the fixator to the bone substitutes. The distance between the axis of the supporting tube and the loading axis was 100 mm (in accordance with the methodology developed at CTU in Prague). In version B, conical screws 6 mm in diameter, 120/40 mm in length and with a 4.5/3.5 mm thread (PROSPON PN S0010107) were used for anchoring the fixator to the bone substitutes. The distance between the bone substitute and the nearest part of the head of the fixator was 50 mm [1]. Version A is clearly stiffer, because the screws are thicker and there is a shorter distance between the axis of the supporting tube and the loading axis. The relationship between loading force and displacement is shown in Fig 2.

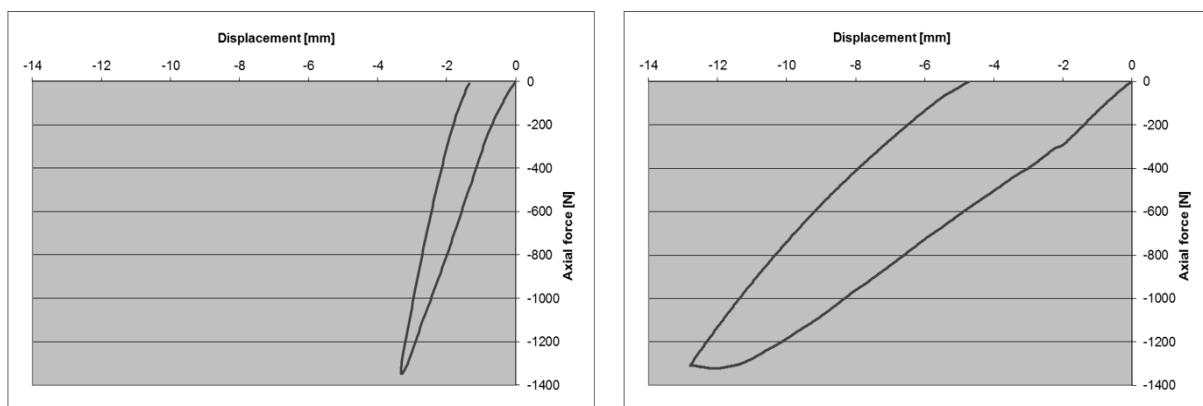


Fig. 2 Relationship between loading force and displacement – version A on the left, version B on the right

Experiments have been carried out to test the strength of a prototype of an external fixator. Two versions of the fixators were assembled for the tests (screws with different threads and of different lengths). The evaluation showed that the external fixator made of composite materials (randomly oriented C/PPS pellets for the body and wound supporting tube) fulfilled the requirements for the static experiments and also for the cyclic experiments. The carbon composite fixator structure remained intact and functional after the experiments, and was reusable for further tests. The concept and the design of the external fracture fixation device made from composite materials has been successfully tested, and it can be further developed for use in clinical practice.

Acknowledgements

This work has been supported by project TA03010209 of the Technological Agency of the Czech Republic and by the Grant Agency of the Czech Technical University in Prague, under grant No. SGS15/188/OHK2/3T/12.

References

- [1] ASTM F1541-02 (2015) - Standard specification and test methods for external skeletal fixation devices.
- [2] Gardner, T. N., Evans, M., Kenwright, J., A biomechanical study on five unilateral external fracture fixation devices, *Clinical Biomechanics* 12 (2) (1997) 87-96.
- [3] Padovec, Z., Růžička, M., Sedláček, R., Král, M., Růžička, P., Comparison of the thermoelastic properties of a randomly reinforced composite computed by the classic lamination theory and Monte Carlo simulation, *Mechanics of Composite Materials* 53 (1) (2017) 149-158.

Validation of a fluid-structure interaction code based on the discontinuous Galerkin method

A. Pecka^a, O. Bublík^a, J. Vimr^a

^a*NTIS – New Technologies for the Information Society, Faculty of Applied Sciences, University of West Bohemia,
Univerzita 8, 306 14 Plzeň, Czech Republic*

The target of this contribution is to validate the fluid-structure interaction (FSI) code developed for the purpose of aeroelastic flutter analysis as a part of FlowPro software. FlowPro [2] is a multipurpose numerical software developed by the authors of this contribution.

The underlying mathematical model of Navier-Stokes equations in the arbitrary Lagrangian and Euler (ALE) form [1] can be written as follows

$$\frac{D^A \mathbf{w}}{D^A t} - V^j \frac{\partial \mathbf{w}}{\partial x^j} + \frac{\partial \mathbf{f}^j}{\partial x^j}(\mathbf{w}) = \frac{\partial \mathbf{f}_v^j}{\partial x^j}(\mathbf{w}, \nabla \mathbf{w}),$$

where \mathbf{w} is the fluid state vector and \mathbf{f}^j and \mathbf{f}_v^j are components of given inviscid and viscous fluxes, respectively. Note that the summation over $j = 1, \dots, d$ is implied. By $\frac{D^A \mathbf{w}}{D^A t} = \frac{\partial \mathbf{w}}{\partial t} + V^j \frac{\partial \mathbf{w}}{\partial x^j}$ we denote the ALE derivative, which is the time derivative with respect to a moving observer, whose velocity components with respect to the chosen frame of reference are V_j .

The developed algorithm is based on the discretisation of the system of Navier-Stokes equations by the discontinuous Galerkin method with the Lax-Friedrichs numerical flux. Furthermore, the time integration is performed by the second order backward difference formula (BDF2), which is an unconditionally stable implicit method. In its general form, it also allows as to adaptively change the size of time steps.

In this contribution, we present only one benchmark for the developed FSI software but the most important one and that is the flutter boundary prediction. The flutter boundary is a curve in \mathbb{R}^2 which determines the threshold for the occurrence of the instability of type flutter depending on two variables, namely the Mach number M and speed index U_F . Here, we study the flutter boundary for a wing with the NACA 64A0010 aerofoil cross section, while considering the wing model of Isogai [4] shown in Fig. 1. The dynamics of the wing is determined by the following system of two differential equations

$$\begin{aligned} m\ddot{y} + S_\alpha \ddot{\alpha} + K_y y &= L, \\ S_\alpha \ddot{y} + I_\alpha \ddot{\alpha} + K_\alpha \alpha &= M_A, \end{aligned}$$

where L is the lift and M_A is the moment on the aerofoil both due to the aerodynamic forces. The rest of the coefficient can be calculated using following relations

$$m = \mu \pi \varrho_\infty b^2, \quad S_\alpha = m b x_a, \quad I_\alpha = m r_a^2, \quad K_y = m \omega_y^2, \quad K_\alpha = I_\alpha \omega_\alpha^2,$$

where

$$\omega_\alpha = \frac{U_\infty}{U_F b \sqrt{\mu}}, \quad \varrho_\infty = \left(1 + \frac{\kappa - 1}{2} M^2\right)^{\frac{1}{\kappa - 1}}, \quad U_\infty = M \sqrt{\frac{\kappa p_\infty}{\varrho_\infty}}, \quad p_\infty = \left(1 + \frac{\kappa - 1}{2} M^2\right)^{\frac{\kappa - 1}{\kappa}}$$

and the structural parameters are $x_a = 1.8$, $r_a^2 = 3.48$, $\mu = 60$ and the heat capacity ratio is $\kappa = 1.4$. In order to solve the second order ordinary differential equation, we first rewrite it as a first order ordinary differential equation and consequently apply the two-step Adams-Bashforth scheme.

We solve the FSI problem as a whole by solving the flow field and the rigid body dynamics in turns. The fluid flow influences the rigid body through the lift L and moment M_A . Conversely, the rigid body influences the fluid flow by changing its own position given by the displacement y and angle α . Hence, the mesh vertices must be recalculated at each time step, which we achieve by the blending function approach [1].

The flutter boundary is established using an iterative process in which aeroelastic simulations are performed for many combinations of values of the Mach number M and speed index U_F . If the resulting motion grows in an unbounded fashion with time, the system is considered unstable and prone to aeroelastic flutter. If the disturbances are damped with time, the system is stable and flutter does not occur. If the system continues to oscillate with constant amplitude, the system is neutrally stable and the flutter boundary is established. The flutter boundary determined by the developed FSI software in comparison with the flutter boundary established by Kirshmann [5] and Hall [3] is plotted in Fig. 2, from which a sensible agreement is apparent.

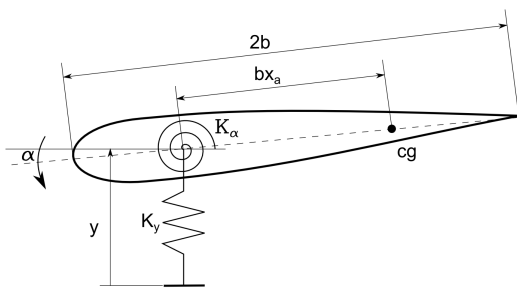


Fig. 1. Isogai wing model

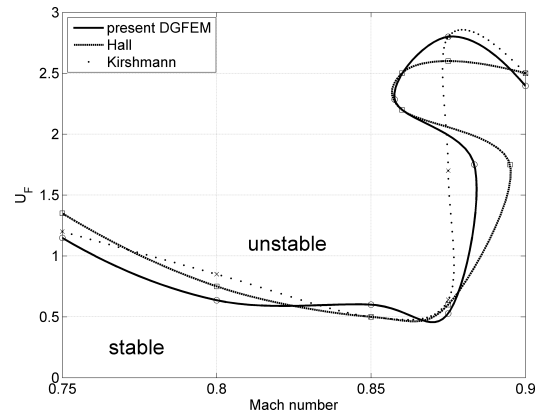


Fig. 2. Flutter boundary

Acknowledgement

The authors appreciate the kind support by the grant GA 16-04546S "Aero-elastic couplings and dynamic behaviour of rotational periodic bodies" of the Czech Science Foundation.

References

- [1] Bublík, O., Vimmr, J., Jonášová, A., Comparison of discontinuous Galerkin time integration schemes for the solution of flow problems with deformable domains, *Applied Mathematics and Computation* 267 (2015) 329–340.
- [2] Bublík, O., Vimmr, J., Pecka, A., FlowPro - multipurpose CFD software written in Java, *Extended abstracts of the 33th conference with international participation Computational Mechanics 2017*, University of West Bohemia, Plzeň, 2017, pp. 2.
- [3] Hall, K. C., Jeffrey, T. P., Dowell, E. H., Proper orthogonal decomposition technique for transonic unsteady aerodynamic flows, *AIAA Journal* 38 (10) (2000) 1853–1862.
- [4] Isogai, K., On the transonic-dip mechanism of flutter of a sweptback wing, *AIAA Journal* 17 (6) (1979) 793–795.
- [5] Kirshman, D. J., Liu, F., Flutter prediction by an Euler method on non-moving Cartesian grids with gridless boundary conditions, *Computers and Fluids* 35 (6) (2006) 571–586.

Experimental verification of the friction and fretting wear coefficients for strong adhesion of two unlubricated surfaces

L. Pecinka^a, J. Svoboda^b

^a UJV REZ, Hlavní 130, Řez, 250 68 Husinec, Czech Republic

^b CV REZ, Hlavní 130, Řez, 250 68 Husinec, Czech Republic

It is well known that friction between unlubricated metals is due to shearing of junctions formed by adhesion between minute asperities of the sliding surfaces. The type of interaction between unlubricated metal surfaces is crucially dependent on the nature of their surface films and can conveniently be divided following mechanical categories:

- seizure (complete or intermittent) or very high friction. In this case friction remains very high, $f=3-10$,
- strong adhesion, the surface films reduce f to about 1 but the adhesion between asperities may still be strong enough,
- weak adhesion and interlocking. Adhesion is often seriously weakened by surface films.

The disassembling experiences from the operation of VVER 440/213 and VVER 1000/320 reactors shown that at take out of the reactors internals from the reactors pressure vessel the crane force at the first lift up this one is higher than the related dead weight. From the design of the reactor is possible to suppose that this effect is generated by the friction between interconnected surfaces. To verify this hypothesis the set of experiments has been performed.

The friction coefficient has been evaluated using relation

$$f = \frac{F_{exp}}{F_N} + \frac{mX\omega^2}{F_N} - \frac{2f_p r_p}{l}$$

where denote f_p coefficient of the pin friction, r_p radii of the pin, l vertical distance between pins, m accelerated mass, X amplitude of the movement, ω angular frequency of the movement. List of performed experiments is to be seen in Table 1.

Table 1. Performed experiments

N° of the experiment	1	2	3	4	5	6	7	8
Frequency Hz	16.6			25			16.6	
Pushing force kN	1	2	3	1	2	3	3	3

Strong adhesion has been observed in the experiments N° 3, 7 and 8 meanwhile for the experiments N° 1 and 4 the weak adhesion was typical. Friction and fretting wear coefficients are plotted in Tables 2 and 3. The mean values of the friction force as the function of the time in the experiment N° 8 are illustrated in Fig. 1.

Table 2. Friction coefficient f

Pushing force P_m kN	Friction force T_{mean} kN			Friction coefficient f		
	N° of experiment			N° of experiment		
	3/5.91	7/4.664	8/4.79	3/1.78	7/1.39	8/1.436

Table 3. Fretting wear coefficient μ (Sign - denote loss of the mass, Sign + denote increment of the mass)

Fretting wear coefficient [g/J]					
3		7		8	
Key	groove	key	groove	key	groove
-1.266E-7	-8.7E-7	-1.926E-6	+6.37E-7	-1.19E-6	+2.7266E-7

Conclusions: Performed experiments proved

- difference of the crane force and dead weight of the core barrel during the first lift of is given by the friction between keys and grooves
- seisure depend on the value of the pushing force
- if F reach of the value 3 kN it result in so called "forget welding"
- from the point of view of the friction physic this phenomenon represent strong adhesion
- in this case the friction coefficient is every higher than 1.

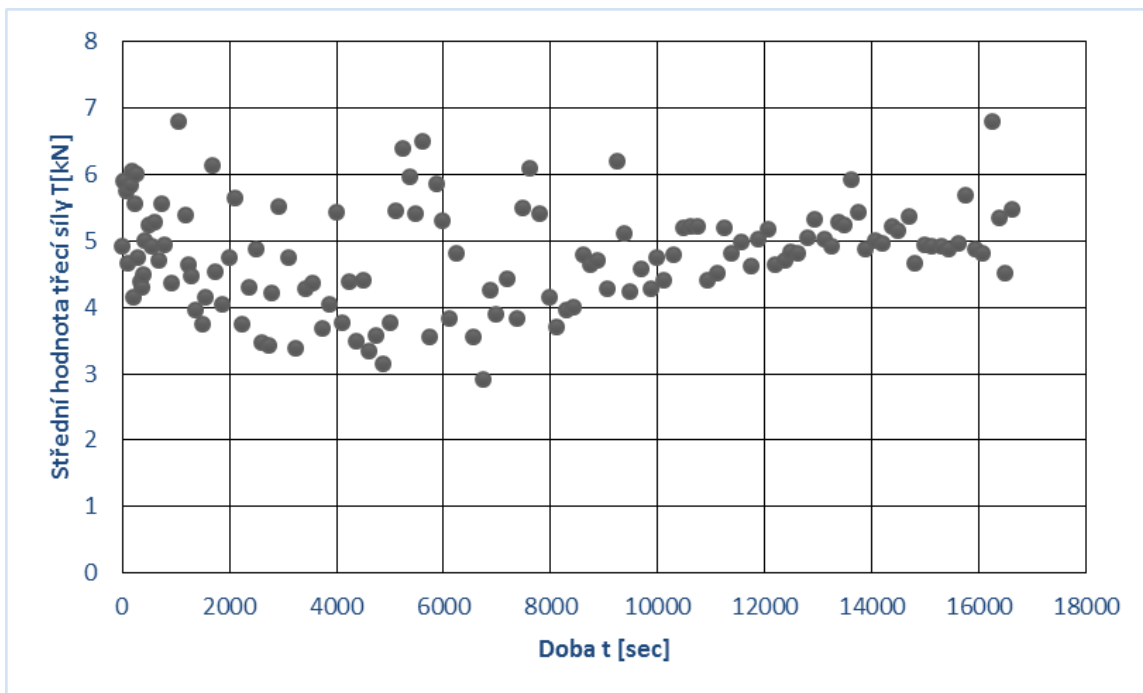


Fig. 1. Mean value of the friction force as a function of time

Experimental research and modelling of the response of magnetorheological elastomers to cyclic load

I. Petříková^a, B. Marvalová^a

^a Faculty of Mechanical Engineering, Technical University of Liberec, Studentská 2, 461 17 Liberec, Czech Republic

Magnetorheological elastomers (MREs) belong to the new group of functional materials called “smart”. MREs are a class of materials with rheological properties rapidly varied by the application of a magnetic field. The MREs consist of micron sized, magnetically permeable particles, dispersed in non-magnetic matrix. The MR effect is increased by choosing the material of the particles with high permeability.

The magnetorheological elastomer composites were prepared using room temperature vulcanization silicone rubber as the matrix material and globular carbonyl iron micro-particles have been used as the filler. Carbonyl iron micro-particles of 27 vol% were mixed into the silicone rubber mixture of ZA 22 base and RZA 22 curative at a ratio of 1:1. Polymerization was carried out without the presence of a magnetic field, MRE samples are therefore isotropic.

Dynamic viscoelastic measurements were carried out on an Instron Electropuls 3kN, [3]. Double lap shear specimens were loaded in cyclic shear under displacement control. The amplitude of the cyclic shear strain was 0.1 and the frequency was changed in steps from 1 to 10 Hz. The samples were cyclically loaded under the magnetic field with the magnetic flux density increasing from 0.1 to 0.8 T. The samples were tested without and with the magnetic field to obtain the basic dynamic MRE properties, namely storage and loss moduli and the loss angle. Dynamic moduli and the loss angle were determined as the function of the magnetic field intensity and of the frequency and amplitude of cyclic deformation in shear. The dynamic stiffness of MRE depends on magnetic flux density and increases with increasing testing frequency. The loss factor of MRE samples is tunable by the magnetic flux density and it also depends on the testing frequency and amplitude.

The behaviour of viscoelastic materials under uniaxial loading may be represented by means of conceptual rheological models composed of elastic and viscous elements. Rheological Zener model is a particular case of the generalized Maxwell model composed of a Maxwell branch in parallel with a spring. Such a model of three parameters is not sufficient for the quantitative representation of the behaviour of the MRE. In order to improve the representation the number of parameters need to be increased. This is done by combining a number of springs and dashpots - to create a so called ladder model.

The dependency of dynamic moduli can be represented with a minimum of material constants using the fractional calculus. The fractional Zener model is an adequate uniaxial model for small strains [1, 2]. It corresponds to a linear spring with a elastic modulus in parallel with a fractional Maxwell element. The fractional differential equation is fairly similar to the 1st order differential equation of the classic Zener element. The model has 4 parameters (elastic part of the viscoelastic branch of the model G_e , the stiffness of the spring in elastic branch G_m , the relaxation time τ and the fractional parameter α) which should be fitted to the experimental data.

The shift from the time domain to the frequency domain is realized by the Fourier Transform. Storage and loss moduli are obtained by separating the real and imaginary part of the dynamic modulus.

The loss tangent values evaluated from experiments were fitted to the fractional Zener model. We obtained an exceptionally good agreement even for a different intensity of the magnetic field (ranging from 0 to 0.6 Tesla) as can be seen in Fig. 1. But the values of storage and loss modulus functions calculated using the fitted parameters were not so impressive.

The hysteresis loop record carries all the information we can harvest from a dynamic experiment. It is therefore appropriate to fit the model parameters directly to the recorded raw data of strain and stress. The fitting was carried out in Matlab by nonlinear least squares. The dynamic moduli G' , G'' and loss tangent were determined on the basis of the fitted parameters of the fractional model. The comparison of experimental and fitted data for storage modulus is in Fig. 2.

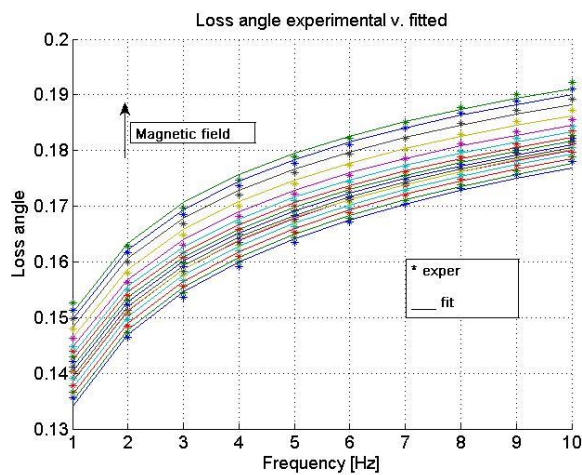


Fig. 1. Fitting the loss angle alone to the experimental data

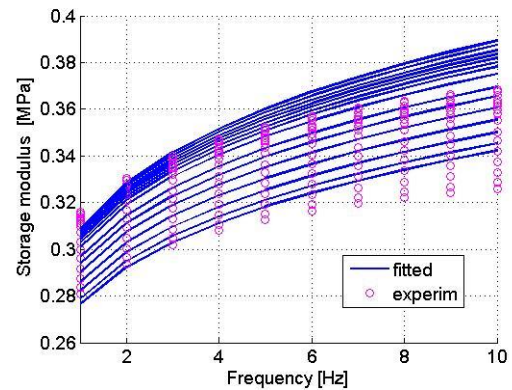


Fig. 2. Fitting the fractional model to hysteresis loops – storage modulus

In this contribution, we presented a study of the mechanical behaviour of magneto-sensitive elastomers with isotropic distribution of the magnetic particles in an external magnetic field and we presented the phenomenological model of the dynamic response based on fractional derivative rheological element. The fitted parameter alpha of the fractional order derivative decreases slightly with the rising magnetic field intensity. This indicates that with the increasing intensity of the magnetic field, the stiffness of the MRE sample increases.

Acknowledgements

This work was supported by the Ministry of Education, Youth and Sports of the Czech Republic within the Institutional Endowment.

References

- [1] Agirre-Olabide, I., Lion, A., Elejabarrieta, M. J., A new three-dimensional magneto-viscoelastic model for isotropic magnetorheological elastomers, *Smart Materials and Structures* 26 (3) (2017) No. 035021.
- [2] Lion, A., Thermomechanically consistent formulations of the standard linear solid using fractional derivatives. *Archives of Mechanics* 53 (2001) 253-273.
- [3] Petrikova, I., Marvalova, B., Experimental research and numerical simulation of the damping properties of magnetorheological elastomers, *Proceedings of the 10th European Conference on Constitutive Models for Rubber*, Munich, Taylor & Francis Group, London, 2017, pp. 11-18.

Asymmetry in CRB specimen and its influence on test results

J. Poduška^{a,b}, P. Hutař^b, J. Kučera^c, F. Arbeiter^d, A. Frank^d, L. Náhlík^b

^a Faculty of Mechanical Engineering, Brno University of Technology, Technická 2869/2, 616 69 Brno, Czech Republic

^b Institute of Physics of Materials, Czech Academy of Sciences, Žitkova 22, 616 62 Brno, Czech Republic

^c Polymer Institute Brno, Tkalcovská 36/2, 602 00 Brno, Czech Republic

^d Polymer Competence Center Leoben, Roseggerstrasse 12, A-8700 Leoben, Austria

Testing performance of modern polymer pipe materials in terms of lifetime and crack growth resistance can be tricky, because these materials were designed to make pipes that withstand even more than 100 years in operation [2]. Usually, the performance of pipes is presented in the form of the results of a certain accelerated test, during which a notched specimen of a specified shape is loaded and time to fracture is measured (or number of cycles to failure, if cyclic loading is applied).

One of the most effective and least time-consuming methods of accelerated testing is the CRB (cracked round bar) test. The CRB test is carried out on cylindrical specimen with a sharp notch in the middle. A cyclic tensile force is used to load the specimen, which increases the speed of crack growth process, but does not change the desired mechanism of fracture, which is the so called “slow crack growth”. This is a typical and most frequent mechanism of failure of polymer pipes in actual operation. [1,3]

The CRB test provides an easy way to evaluate the basic performance of polymer pipe materials based on the number of cycles to failure that were needed for the given material at a certain load. Apart from that, the CRB specimen also offers the possibility to evaluate the crack growth rate for the given material. This is done by measuring the COD by extensometers at three different spots positioned on the edge of the notch around the specimen (120° apart from each other) – see Fig.1. The crack length is then calculated from the measured COD using previously measured compliance of the material. The crack growth rate is measured at different R-ratios (eg. 0.1, 0.5 and 0.7) and the crack kinetics for R=1 (i.e. static loading) is then obtained via extrapolation. Crack growth rate (or crack kinetics) parameters are then considered material constants. These parameters can be used in a calculation of residual lifetime estimation for an actual polymer pipe. [3,4]

In some cases, an asymmetrical crack growth occurs in the CRB specimen (see Fig. 1). The crack propagates faster on one side of the specimen than on the opposite side. This asymmetry is most likely caused by residual stress that can remain in those specimen that were manufactured directly from the actual pipe wall. It is quite a well-known issue, that polymer pipes contain a certain level of residual stress as a result of uneven cooling during manufacture [5]. The crack growth in these CRB specimen was modelled by FEM to prove that the presence of residual stress can cause a similar asymmetry. The comparison of the actual crack surface and to the calculated crack propagation can be seen in Fig. 2.

Another simulation of the crack growth in the CRB specimen was then carried out considering asymmetrically growing crack. A certain crack growth rate was assumed. The COD was calculated and the evaluation of the crack growth rate was done from these results. This was done to see, if there is a significant difference between the evaluated crack growth rate and the originally assumed crack growth rate. It turned out that the difference is not large

and that means it is safe to evaluate the crack growth rate even from the asymmetrically fractured CRB specimens.



Fig. 1. CRB specimen with extensometers [3]

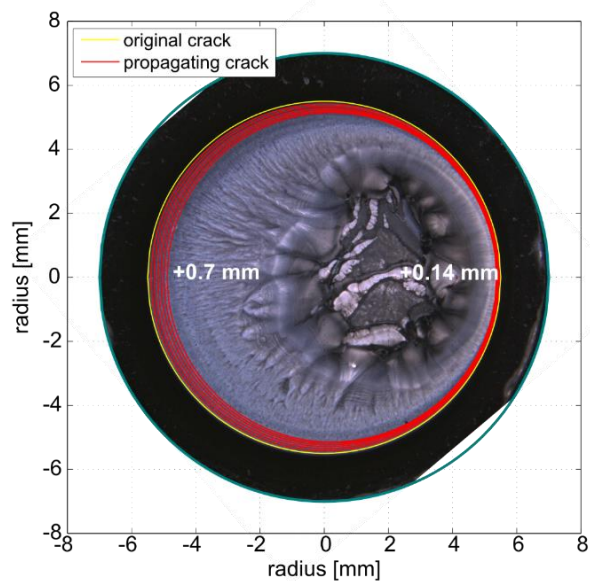


Fig. 2. Comparison of calculated crack propagation with the actual fracture surface of a CRB specimen

FEM simulation was used to assess the actual influence of an asymmetrically growing crack in a CRB specimen on the results of the whole CRB test. The crack growth rate calculated from the COD measured on the asymmetrically fractured specimen does not differ from the actual crack growth rate by more than 10%.

Acknowledgements

The research has been supported by the specific research project FSI-S-14-2311 provided to Brno University of Technology, Faculty of Mechanical Engineering.

References

- [1] Arbeiter, F., Schritteser, B., Frank, A., Berer, M., Pinter, G., Cyclic tests on cracked round bars as a quick tool to assess the long term behaviour of thermoplastics and elastomers, *Polymer Testing* 45 (2015) 83–92.
- [2] Brömstrup, H., PE 100 pipe systems, 3rd ed., Vulkan-Verlag, Essen, 2009.
- [3] Frank, A., Freimann, W., Pinter, G., Lang, R.W., A fracture mechanics concept for the accelerated characterization of creep crack growth in PE-HD pipe grades, *Engineering Fracture Mechanics* 76 (2009) 2780–2787.
- [4] Hutař, P., Ševčík, M., Náhlík, L., Pinter, G., Frank, A., Mitev, I., A numerical methodology for lifetime estimation of HDPE pressure pipes, *Engineering Fracture Mechanics* 78 (2011) 3049–3058.
- [5] Poduška, J., Hutař, P., Kučera, J., Frank, A., Sadílek, J., Pinter G., Náhlík, L., Residual stress in polyethylene pipes, *Polymer Testing* 54 (2016) 288–295.

Computational and experimental investigation of rotor dynamics with fluid film instabilities

P. Polach^a, L. Smolík^a, M. Hartl^b, M. Omasta^b, P. Šperka^b, M. Hajžman^a

^a *New Technologies for the Information Society, European Centre of Excellence, Faculty of Applied Sciences, University of West Bohemia, Univerzitní 8, 306 14 Plzeň, Czech Republic*

^b *Institute of Machine and Industrial Design, Faculty of Mechanical Engineering, Brno University of Technology, Technická 2896/2, 616 69 Brno, Czech Republic*

Dynamics of rotating systems deals with behaviour and diagnostics of rotating structures. When hydrodynamic journal bearings are used to support a rotor, a rotor-bearing system becomes a complex dynamic system, which may exhibit fluid-induced instabilities. Understanding of behaviour of the journal bearing closely before, during and after the rotor instability origin and growth is the main motivation for the complex research of local and global dynamics of the rotor-bearing system. Deep knowledge of relations between local fluid film dynamics and dynamic response of rotating systems during instabilities can help to improve design of many modern rotating machines.

During last few years many local aspects regarding fluid film instabilities were introduced (e.g. [1]). To meet these challenges successfully more attention should be paid to physical characteristics of the fluid film itself. A typical rotor dynamic test rig usually utilizes a set of proximity transducers and accelerometers, which provide orbits of the lateral motion of the shaft centerline. Nevertheless, this configuration does not allow a deeper investigation of local phenomena. With respect to successful applications in other fluid film systems optical methods offer an insight into the fluid film instabilities with the emphasis on local effects.

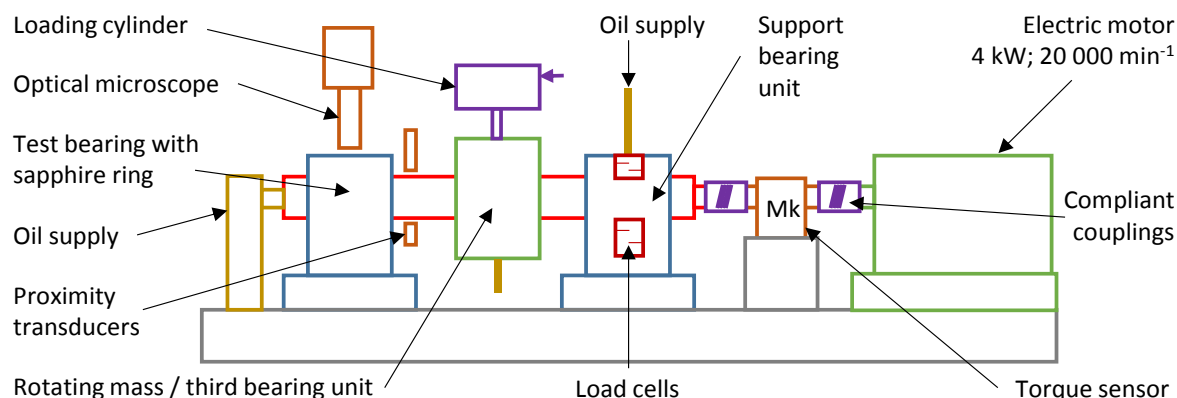


Fig. 1. Scheme of the developed rotor-bearing test rig

Further development of high-speed rotation systems with fluid-film bearings and their reliable operation requires both prediction of a wider range of parameters and deeper understanding of basic fluid-induced effects. Better knowledge is essential for a development of condition monitoring techniques and systems and active oil whirl/whip control mechanisms. The motivation for dealing with this problem is the development of unique experimental (see Fig. 1 and Fig. 2) and numerical methods and their application into the

research of fluid-induced instabilities on a local level related to nonlinear unstable behaviour on a global level. This approach helps to clarify the phenomena occurring mainly in the transitions between instabilities and at a risk of rotor-stator contacts due to the instabilities. The local view of these issues considering roughness effects and fluid rheology still lacks.

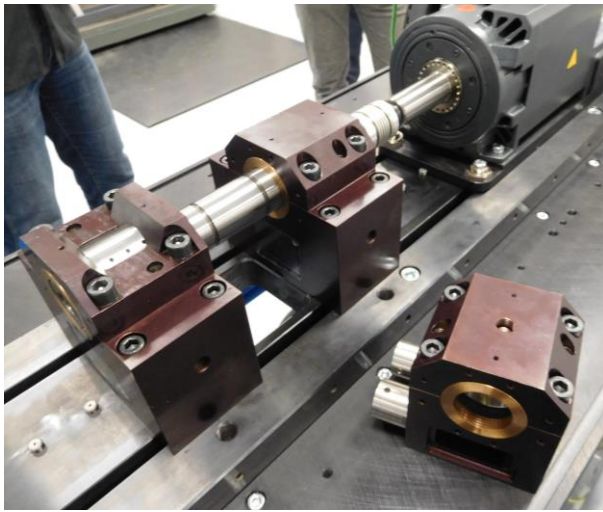


Fig. 2. The current state of the rotor-bearing test rig

is a pressure distribution in the oil film. It has to be solved in each time integration step and the resultant pressure distribution is transformed into dynamical forces that are subsequently included into the global rotor dynamical model. The local nonlinear phenomena that possibly occur in the bearing (the Reynolds equation solution) can be compared with the global rotor dynamic behaviour of the system and the experimental results obtained using optical methods.

The rotor dynamic characteristics as well as the fluid film behaviour will be investigated experimentally using the rotor-bearing test rig (see Fig. 1 and Fig. 2). According to the scheme in Fig. 1, the shaft is supported by two fluid film journal bearings of the same dimensions – the first one is test, the second one is supporting. Lubricating oil is supplied by a lubrication unit with a controllable flow, pressure and temperature. The shaft can be loaded with an unbalanced rotating mass or with a pneumatic cylinder through the third bearing unit. Rotational movement of the shaft is provided by 4 kW, 20 000 RPM electric motor with a frequency converter, which offers sufficient capacity for a wide range of contact conditions.

Optical investigation is made possible through a sapphire ring as a part of the test bearing. In this case, oil supply is ensured through a hollow shaft. In addition to optical parts the test rig includes proximity transducers for the shaft orbit investigation, load cells measuring reaction forces on the second bearing and a friction torque sensor.

The developed versatile experimental and computational infrastructures facilitate current as well as future research tasks.

Acknowledgement

The paper has originated in the framework of solving No. 17-15915S project of the Czech Science Foundation entitled “Nonlinear dynamics of rotating systems considering fluid film instabilities with the emphasis on local effects”.

References

- [1] Polach, P., Hajžman, M., Byrtus, M., Dyk, Š., Smolík, L., Mathematical modelling of rotor systems with journal bearings in limit cases, Proceedings of the 23rd International Conference Engineering Mechanics 2017, Svratka, Brno University of Technology, 2017, pp. 794-797.

Aero-elastic vibration of bladed turbine wheel

L. Půst^a, L. Pešek^a, M. Byrtus^b

^a *Institute of Thermomechanics, Czech Academy of Sciences, Veleslavínova 11, 301 14 Plzeň, Czech Republic*
^b *Faculty of Applied Sciences, University of West Bohemia, Univerzitní 8, 306 14 Plzeň, Czech Republic*

Dynamic properties of blades cascades in gas or steam turbines have been intensively investigated during the several last decades. During the many experimental investigations, the flutter running waves have been observed. The presented contribution brings a simple analysis of influence of numbers of blades in stationary and rotating turbine wheels on the origin and on properties of forced and aero-elastic running waves in blade cascade.

In order to obtain at least basic information about the dynamic behaviour of real turbine blade cascade, the studied system is simplified on the rotating wheel with $l_r = 12$ blades, each modelled as the 1 DOF dynamic system (mass m [kg], stiffness k [kg s⁻²], damping coefficient b [kg s⁻¹]). If we limit our study on the narrow frequency range, this restriction is possible. The model of rotating turbine wheel with twelve blades is shown in Fig. 1, where also the stationary wheel with eleven blades cascade is added.

The dynamic interaction between neighbouring blades through the common fixing into viscous-elastic turbine disk is modelled by Voigt-Kelvin element with parallel connected spring (stiffness k_1 [kg s⁻²]) and damping element with coefficient b_1 [kg s⁻¹]. External forces acting on the blades are produced by the aerodynamic forces of the flowing steam from stationary cascade with l_s blades. Usually numbers of blades on rotating and on stationary wheel are different, $l_s \neq l_r$ which can produce running waves in the rotating blade cascade. The acting aerodynamic forces are of different type:

a) The wakes of steam-flow from stationary cascade excites the i -th rotating blade by a periodic force, which can be simplified on the first harmonic component $F_{0i} \cos(\omega t - (i-1)\Delta\phi)$. The phase delay $\Delta\phi$ depends on the ration l_s / l_r of rotor and stator blades: $\Delta\phi = 2\pi(1 - l_s / l_r)$.

b) The flowing gas can cause also instability and increase of self-excited oscillations. The Van der Pol model applied in the first approximation for describing self-excited forces G_i acting on i -th blade is

$$G_i = -\mu(1 - (x_i / r)^2)\dot{x}_i \quad (1)$$

where x_i, \dot{x}_i [m, m/s] are displacement and velocity of i blade, r [m] is the displacement at which the negative aerodynamic force changes into positive one, μ [Ns/m] is a scalar parameter indicating the intensity of this non-linear damping.

c) There are also further aero-dynamic forces. They depend on the actual distance of neighbouring blades and on theirs velocities. Corresponding mathematical model is

$$Q_{i,i+1} = -\mu_1(1 - (x_i - x_{i+1})^2 / r_1^2)(\dot{x}_i - \dot{x}_{i+1}) \quad (2)$$

where $Q_{i,i+1} = -Q_{i+1,i}$.

Motion equations of the closed 12-blade cascade with the 1 DOF blades excited by the delayed harmonic forces: $F_i(t) = F_0 \cos(\omega t - (i-1)\Delta\phi)$ from the steam flowing through stationary blade cascade with 10 blades are

$$m\ddot{x}_i + b\dot{x}_i + kx_i + g_i - g_{i-1} + G_i - G_{i-1} = F_{0i} \cos(\omega t - (i-1)\Delta\phi), \quad i = 1, \dots, 12 \quad (3)$$

Amplitude of wake forces are $F_{0i} = 1$ N and the other parameters are selected according to the similar bladed disk, measured in laboratory of IT ASCR, [1]. The ratio of blades' numbers $l_s/l_r = 10/12$ gives $\Delta\phi = \pi/3$. If only wakes of flowing steam excited rotating blades ($G_i=0$), all blades vibrate with this phase shift, which results into running wave shown in the left half of Fig. 1. This small forced vibrations initiate much larger aero-elastic oscillations (flutter, Eq. (1), $\mu = 3$) shown in the right half of Fig. 1. This flutter running waves have the same velocity and the same direction as the forced vibrations determined by the ratio l_s/l_r . Modes of both these vibrations are drawn in Fig. 2.

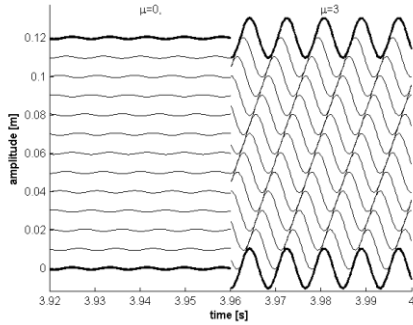


Fig. 1. Running waves at $\mu=0$ and $\mu=3$

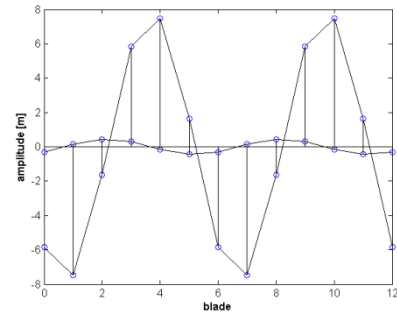


Fig. 2. Modes of vibrations

Another kind of running flutter vibrations is produced by mutual aerodynamic forces $Q_{i,i+1}$ between neighbouring blades – see Eq. (2). Result of solution similar to the previous case is shown in Fig. 3 and Fig. 4. Mutual flutter forces cause that neighbouring blades oscillate with opposite phase with the mode quite different from the mode corresponding to the wakes excitation and shown before.

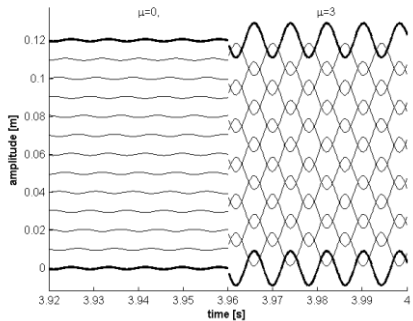


Fig. 3. Running waves at $\mu=0$ and $\mu=3$

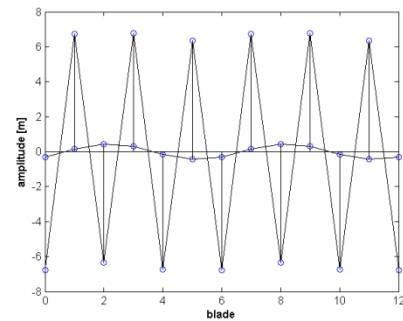


Fig. 4. Modes of vibrations

It is shown that the problem of flutter running waves in blade cascade is complicated and the dynamic behaviour of flutter running waves depends on many parameters, especially on the type of aero-elastic forces. More examples will be shown at presentation.

Acknowledgment

This contribution has been supported by the grant project of CSF No. 16-04546S.

References

- [1] Pust, L., Pesek, L., Running waves in turbine 12 blades cascade, Applied and Computational Mechanics 2017. (Under review)

Suspension design and tire modelling of Formula SAE

J. Rendl^a, M. Hajžman^a, E. Menclová^a

^a*Faculty of Applied Sciences, University of West Bohemia, Technická 8, 306 14 Plzeň, Czech Republic*

The Formula SAE (FSAE) is the international competition between universities. Students have to design and build the car according to rules and prepare it for defined races. The races are compound of static (cost plan, design presentation and safe test) and dynamic disciplines (acceleration, skidpad, autocross and endurance). The Formula SAE has to be lightweight, powerful, reliable, safe and mainly very good controllable. Mainly the driving properties affect the final competition results. For this reason it is necessary to be focused on the creation and simulation of the formula computational model as much properly as is possible. This paper deals with the methodology for the optimal suspension kinematic design and with the creation of full vehicle computational model with identified tire parameters.

Formula handling properties are mainly influenced by the design of suspensions and steering. The FSAE cars usually use double-wishbone suspensions, which are lightweight, adjustable and easy structured. The behaviour of suspensions is described by kinematic variables [3], which are typical for vehicle mechanics (roll centre, camber angle, toe angle, etc.). The motion of the suspension during the ride is possible to divide into three simple tests – jouncing, rolling and steering. Based on these basic kinematic tests and the requirement of minimal change around the desired values, it is possible to define suitable objective function characterizing certain optimal design. Mounting positions of arms are further found via optimization procedures. The kinematic calculations and the whole optimization procedure were performed by the in-house software created in MATLAB. The objective function can be generally formulated in the form

$$\psi(\bar{\mathbf{p}}) = \sum_i w_i \left(1 - \frac{P_i(\bar{\mathbf{p}})}{P_i^{req}} \right)^2, \quad (1)$$

where w_i are the weights for the specific kinematic variables, $P_i(\bar{\mathbf{p}})$ are current values or current differences of important kinematic variables and P_i^{req} are their corresponding target (required) values. Dimensionless relative parameters representing arm mounting positions and concentrated in vector $\bar{\mathbf{p}}$ are used during the whole optimization process for better numerical conditionality.

Very important part of the computational model of each vehicle is the modelling of tires. The exact and correct mathematical model allows to transfer forces and torque from the tire through suspensions to the chassis as well as in reality. Thus the second part of this paper aimed at the methodology of the parameter identification for realistic tire modelling. The tire mathematical model can be described by so called Pacejka Magic Formula [2] in sine (2) and cosine (3) forms

$$y(x) = D \sin \left[C \arctan \left(Bx - E (Bx - \arctan Bx) \right) \right], \quad (2)$$

$$y(x) = D \cos \left[C \arctan \left(Bx - E (Bx - \arctan Bx) \right) \right], \quad (3)$$

where the sine form is used for the longitudinal and lateral forces and the cosine form for the aligning torque. Unknown parameters (factors) B , C , D , E have different effects on Magic Formula characteristics and depend on a particular type of tires, independent variable x is the longitudinal slip for the longitudinal force or the slip angle for the lateral force and the aligning torque. Magic Formula expressions are kind of semi-empiric equations. The goal of the identification is to find the unknown Magic Formula parameters in order to obtain mathematical model, whose force and torque characteristics correspond to measured curves.

Specific tires for Formula SAE are tested and investigated by *The FSAE Test Tire Consortium*. Since UWB Racing team Pilsen is a member of this consortium, the experimental results were available for employed tires. The tire force calculation using Pacejka Magic Formula was parametrized and implemented as an in-house computational software in MATLAB and the whole optimization procedure was also performed in MATLAB. Huge set of measured curves, which were modified and interpolated, were used for the definition of the objective function in an analogous form as in (1). This leads to the finding of suitable parameters of the tire computational model for handling analysis. The comparison of experimentally measured curves and results of the force calculation after the optimization of unknown parameters is shown in Fig. 1.

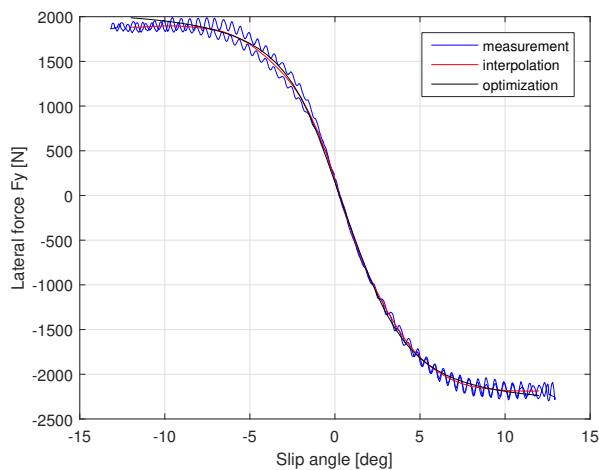


Fig. 1. Lateral force

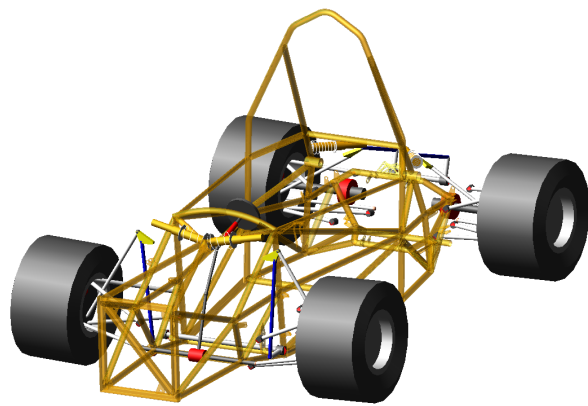


Fig. 2. Formula – multibody model

The proposed suspension design and identified tire model parameters were used for the creation of the complex multibody model of the whole Formula SAE (see Fig. 2) in MSC.ADAMS Car software [1]. The accuracy of basic kinematic tests and efficiency of kinematic characteristics were successfully verified. The proposed kinematic optimization helped to speed up the design process and to find more complex solutions than manual design. The whole formula multibody model was used in various numerical simulations of handling in order to test its controllability and maneuverability.

Acknowledgements

Authors would like to thank UWB Racing Team Pilsen, The FSAE Tire Test Consortium and Calspan company. The presented work was supported by the project SGS-2016-038.

References

- [1] MSC.ADAMS Car, MSC.Software, 2017.
- [2] Pacejka, H. B., Tire and vehicle dynamics, Butterworth-Heinemann, Amsterdam, 2006.
- [3] Trzesniowski, M., Race car technology, Graz, Springer, 2012. (in German)

The numerical studies of symmetric and non-symmetric strain gradient theory of elasticity

M. Repka ^a, V. Sládek ^a, J. Sládek ^a

^a *Institute of Construction and Architecture, Slovak Academy of Sciences, Dúbravská cesta 9, 845 03 Bratislava 45, Slovakia*

Due to the recent advances in material science and engineering the sophisticated small scale structures started to play important role. It has been observed via nano-indenters and atomic force microscopes that if the size of the specimen is in micro or nano-scales the size dependent behavior becomes dominant. The conventional strain based elastic theory does not capture size dependent behavior due to the absence of internal length parameter in constitutive equations as well as this theory cannot treat singularities arises in crack tip or point loads. Therefore it is necessary to consider a contribution of strain gradients. During the last decades many authors have contributed to enrichment of strain gradient theories of elasticity like [3], [2] however many of the theories are limited for practical purpose because they require a lot of material coefficients to quantify. The simplified strain gradient theory with one constitutive constant has been proposed by [1]. In literature, the strain gradient theory of elasticity often contains strain gradient which is non-symmetric 3rd rank tensor. It is the aim of this paper to apply symmetrized form of strain gradient elastic theory and compare with non-symmetric strain gradient theory of elasticity.

The comparison of the related boundary value problems (e.g., Fig. 1) of both theories has been done numerically via the finite element method. The weak form of the governing equations has been derived and implemented in to the commercial software Comsol .The Argyris type of finite element with C^1 continuity has been used to discretize the domain. The obtained results have shown the differences between the symmetric and non-symmetric strain gradient theories.

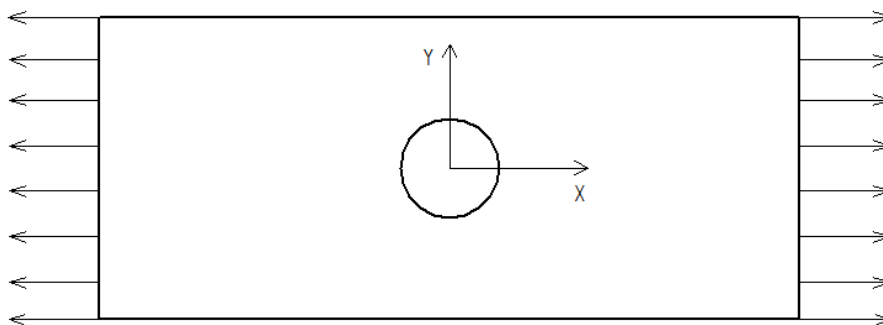


Fig. 1. The plate with hole subjected to tensile load

Acknowledgement

The financial support by APVV-14-0440 (Slovak Research and Development Agency) is greatly acknowledged.

References

- [1] Aifantis, E., On the role of gradients in the localization of deformation and fracture, *International Journal of Engineering Science* 30 (10) (1992) 1279-1299.
- [2] Eringen, A., On differential equations of nonlocal elasticity and solution of screw dislocations and surface waves, *Journal of Applied Physics* 54 (9) (1983) 4703-4710.
- [3] Mindlin, R., Micro-structure in linear elasticity, *Archive for Rational Mechanics and Analysis* 16 (1) (1964) 52-78.

The computational homogenization for modelling of large deforming fluid saturated porous media

E. Rohan^a, V. Lukeš^a

^a*NTIS – New Technologies for the Information Society, Faculty of Applied Sciences, University of West Bohemia, Univerzitní 8, 306 14 Plzeň, Czech Republic*

We have developed a model of fluid saturated porous media (FSPM) subject to large deformation. The mechanical model describes FSPM with hyperelastic skeleton and compressible viscous fluid. The dynamic behaviour is confined to an approximation of the inertia effects associated with the relative fluid-solid motion so that the model is convenient for describing quasistatic loading of large-deforming porous structures.

The computational algorithm is based upon a consistent incremental formulation in the Eulerian framework [4], such that the incremental formulation uses the updated Lagrangian approach. The formulation is based on a quasistatic perturbation of the medium described by the Biot model which is constituted by poroelastic coefficients and the permeability governing the Darcy flow. The equilibrium equation and the mass conservation are expressed in the spatial, deformed configuration. Using the material derivative with respect to a convection velocity field, a rate formulation is derived which allows to approximate the residuum function associated with the unknown configuration using the last known configuration.

Residual formulation. The state of the two-phase continuum is described by the solid material displacement \mathbf{u} , the fluid velocity \mathbf{w} and the fluid pressure p . In the following residual formulation, $\Omega(t)$ is the actual configuration decomposed into the solid and fluid parts, Ω_s and Ω_f , respectively, whereby the kinematic condition of the non-slip flow yields $\mathbf{w} = \dot{\mathbf{u}}$ on the interface. By virtue of the fluid reference configuration $\tilde{\Omega}_f$, one may introduce the relative flow field $\tilde{\mathbf{w}} = \mathbf{w} - \tilde{\mathbf{u}}$, where $\tilde{\mathbf{u}}$ is an extension of the solid displacements from Ω_s to the whole domain Ω . Find $(\mathbf{u}, \mathbf{w}, p) \in V(t) \times W(t) \times Q(t)$ such that (we disregard volume forces)

$$\Phi_t((\mathbf{u}, \mathbf{w}, p); (\mathbf{v}, \mathbf{z}, q)) = 0 \quad \forall (\mathbf{v}, \mathbf{z}, q) \in V_0(t) \times W_0(t) \times Q_0(t), \quad (1)$$

where the residual function is:

$$\begin{aligned} \Phi_t((\mathbf{u}, \mathbf{w}, p); (\mathbf{v}, \mathbf{z}, q)) = & \int_{\Omega_s(t)} \boldsymbol{\sigma}^s(\mathbf{u}) : \nabla \mathbf{v} - \int_{\Gamma(t)} \boldsymbol{\sigma}^f : \mathbf{n}^s \otimes \mathbf{v} - \int_{\partial_\sigma \Omega(t)} \mathbf{h} \cdot \mathbf{v} \\ & + \int_{\tilde{\Omega}_f(t)} (\boldsymbol{\sigma}^f(\mathbf{w}, p) : \nabla \mathbf{z} + \rho \dot{\tilde{\mathbf{w}}} \cdot \mathbf{z}) + \int_{\tilde{\Omega}_f(t)} q \nabla \cdot \mathbf{w}. \end{aligned} \quad (2)$$

In the above formulation, the virtual velocity field $\mathbf{z} = 0$ on $\Gamma(t)$. By dot $\dot{\cdot}$ we denote the material rate; in the fluid part, the convective field is relative to the moving configuration $\tilde{\Omega}_f$ associated with $\tilde{\mathbf{u}}$. By $\partial_\sigma \Omega(t)$ we denote the solid phase surface, where traction stress is prescribed; for simplicity, we assume closed fluid pores on $\partial\Omega$.

Effective properties of the upscaled medium. Using the residual formulation, the differentiation yields linearized model equations to which the homogenization can be applied. The

proposed upscaling approach allows us to establish the effective medium properties involved in the incremental formulation using the homogenization of the microstructure with locally periodic structure. In this way, modified poroelastic coefficients can be computed for given updated configurations, see [4], where the linear continua with hierarchical structures are treated. By virtue of the homogenization based on the linearized model, the fluid flow upscaling yields the Darcy-type flow. The sensitivity of the homogenized coefficients is computed using the sensitivity analysis w.r.t. the microstructure deformation and the pressure perturbation, cf. [3]. The resulting model is consistent with the updated-Lagrangian computational incremental scheme based on the Eulerian formulation, [2].

Acknowledgments

This research is supported by project GACR 16-03823S and in part by project LO1506 of the Czech Ministry of Education, Youth and Sports.

References

- [1] Rohan, E., Modelling large-deformation-induced microflow in soft biological tissues, *Theoretical and Computational Fluid Dynamics* 20 (4) (2006) 251–276.
- [2] Rohan, E., Lukeš, V., Modelling large-deforming fluid-saturated porous media using an Eulerian incremental formulation, *Advances in Engineering Software* 113 (2017) 84–95.
- [3] Rohan, E., Lukeš, V., Modeling nonlinear phenomena in deforming fluid-saturated porous media using homogenization and sensitivity analysis concepts, *Applied Mathematics and Computation* 267 (2015) 583–595.
- [4] Rohan, E., Naili, S., Lemaire, T., Double porosity in fluid-saturated elastic media: Deriving effective parameters by hierarchical homogenization of static problem, *Continuum Mechanics and Thermodynamics* 28 (5) (2016) 1263–1293.

Towards smart porous piezoelectric materials

E. Rohan^a, V. Lukeš^a

^a*NTIS – New Technologies for the Information Society, Faculty of Applied Sciences, University of West Bohemia, Univerzitní 8, 306 14 Plzeň, Czech Republic*

We consider porous media constituted by piezoelectric porous skeleton with pores saturated by viscous fluid. Such materials are generated as periodic structures using a representative volume element containing the piezoelectric solid part (the matrix) and the fluid saturated pore (the channels). Both the matrix and the channels form connected subdomains. In this work we consider electrically neutral fluid. The macroscopic model is obtained by the homogenization of the microscopic model which involves the quasi-static equilibrium equation governing the solid piezoelectric skeleton, the Stokes model of the viscous fluid flow in the channels and the coupling interface conditions on the transmission interface. Also conductive fibers can be considered which allow for local controlling of the structures by the electric field. In Fig. 1, the periodic structure is depicted; the representative periodic cell $Y = Y_m \cup Y_c \cup Y_* \cup \Gamma_Y$ consists of the piezoelectric matrix Y_m , conductive parts Y_* , and the fluid saturating the channels Y_c ; by Γ_Y we mean the union of all interfaces.

Using the unfolding method of homogenization [2], cf. [1], we obtain equations of the macroscopic model involving the displacements \mathbf{u} , the pore fluid pressure p , and the electric potential φ . The following constitutive equations for the macroscopic stress $\boldsymbol{\sigma}^H$ and electric displacements \vec{D} are derived

$$\begin{aligned}
 \boldsymbol{\sigma}^H &= \mathbb{A}^H \mathbf{e}(\mathbf{u}) - (\underline{\mathbf{G}}^H)^T \nabla \varphi - p \hat{\mathbf{B}}, \\
 \vec{D} &= \underline{\mathbf{G}}^H \mathbf{e}(\mathbf{u}) + \mathbf{D}^H \nabla \varphi - \underline{F} p, \\
 -p &= \frac{1}{\hat{M}} \left(\hat{\mathbf{B}} : \mathbf{e}(\mathbf{u}) - \underline{F} \cdot \nabla \varphi + j \right),
 \end{aligned} \tag{1}$$

where $\mathbf{e}(\mathbf{u})$ is the strain tensor and $j = J/|\Omega|$ is the local fluid volume production in the porous material per volume; for non-stationary problems, in (1)₃, we consider the pressure rate \dot{p} and the strain rate $\mathbf{e}(\dot{\mathbf{u}})$, whereby $j = \nabla \cdot \mathbf{w}$, with \mathbf{w} representing the seepage velocity governed by the Darcy law.

We also consider media with prescribed voltage on a finite number of conductor mutually disconnected period networks penetrating into the structure of the porous material. In this case, the electric field distribution is determined locally by the finite number of the prescribed potentials $\{\bar{\varphi}^k\}_k$, where $k = 1, \dots, \bar{k}$, such that

$$\begin{aligned}
 \boldsymbol{\sigma}^H(\mathbf{u}, p) &= \mathbb{A}^H \mathbf{e}(\mathbf{u}) - p \hat{\mathbf{B}}^H + \sum_k \mathbf{H}^k \bar{\varphi}^k, \\
 p &= \frac{1}{\hat{M}} \left(\sum_k Z^k \bar{\varphi}^k - \hat{\mathbf{B}} : \mathbf{e}(\mathbf{u}) - j \right).
 \end{aligned} \tag{2}$$

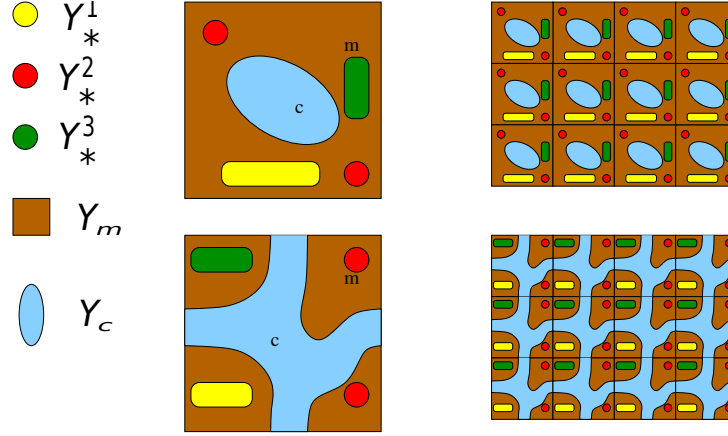


Fig. 1. Periodic structure of the piezo-porous fluid-saturated medium with conducting wires. *Left*: the representative periodic cells Y . *Right*: periodic microstructures. The skeleton always forms a connected domain, while the fluid pores can constitute a connected porosity, or can be disconnected. The conducting parts are distributed as inclusions, or constitute mutually disconnected networks associated with different potentials $\bar{\varphi}^k$

For the case of the connected fluid porosity, the fluid redistribution and the medium deformation are driven by the following system of PDEs imposed in the domain Ω ,

$$\begin{aligned}
 -\nabla \cdot \boldsymbol{\sigma}^H(\mathbf{u}, p) &= \hat{\mathbf{f}} \quad \text{in } \Omega, \\
 \hat{\mathbf{B}} : \mathbf{e}(\dot{\mathbf{u}}) + \hat{M}\dot{p} - \nabla \cdot (\bar{\eta}^{-1} \mathbf{K} \nabla p) &= \sum_k Z^k \bar{\varphi}^k.
 \end{aligned} \tag{3}$$

In the paper, we present the mathematical models and discuss some other topics related to the microstructure topology, namely connectness of the fluid pores and conductive fibers, see Fig. 1. Some illustrative numerical results were obtained using the FE method implemented in the SfePy computational software, see sfepy.org. Model (2) – (3) allows for simulation of the fluid transport due to the macroscopic volume changes and the associated pressure gradients induced by the piezoelectric effect. The future work be focused on the modelling of the transport with inertia effects and locally varying pressure at the micro-level.

Acknowledgments

This research is supported by project GACR 16-03823S and in part by project LO 1506 of the Czech Ministry of Education, Youth and Sports.

References

- [1] Miara, B., Rohan, E., Zidi, M., Labat, B., Piezomaterials for bone regeneration design – homogenization approach, *Journal of the Mechanics and Physics of Solids* 53 (2005) 2529–2556.
- [2] Rohan, E., Lukeš, V., Homogenization of the fluid-saturated piezoelectric porous metamaterials, *Proceedings of the conference Coupled Problems in Science and Engineering VII*, Rhodes Island, Greece, M. Papadrakakis, E. Onate, and B. Schrefler (Eds.), 2017.

Time-reversibly thermostatic oscillators in the modelling of dynein

J. Rosenberg ^a, M. Byrtus ^b

^a Research Centre New Technologies, University of West Bohemia in Pilsen, Univerzitní 8, 306 14 Plzeň, Czech Republic
^b NTIS – New Technologies for the Information Society, Faculty of Applied Sciences, University of West Bohemia in Pilsen, Univerzitní 8, 306 14 Plzeň, Czech Republic

In the modelling of the molecular motor, it is necessary to model the Brownian motion of the stalk with the binding site. In [3], there is mentioned the possibility to reproduce this motion as a solution of the dynamical system consisting of special type of oscillators - time-reversibly thermostatic oscillators (TRTO). In this contribution, the properties of these oscillators are analyzed using entropy-complexity causality plane, forbidden/missing patterns and ergodicity testing which constitute novel tools to analyze the chaotic or stochastic nature of dynamical systems. It will allow to compare these systems with another stochastic models of the Brownian motion.

In [4], three dynamical systems describing the TRTO are recommended. Here a compact form of the notation is used

$$\begin{aligned} \dot{x} &= p - PB \xi \cdot x, \\ \dot{p} &= 0.1(-p\zeta - x - HH \cdot \xi p^3 - 0.5), \\ \dot{\xi} &= (p^4 - 3p^2)HH + MKT(\zeta^2 - 1) + PB(x^2 - 1), \\ \dot{\zeta} &= (p^2 - 1) \alpha - MKT \xi \zeta. \end{aligned}$$

If PB=1 and HH=MKT=0, one obtains the equation for Patra-Bhattacharya oscillator (PB) and similarly if HH=1, the Hoover-Holian oscillator (HH) and and if MKT=1, the Martyna-Klein- Tuckerman oscillator (MKT). Parameter α is usually equal one.

All these oscillators have the chaotic attractors. To use them for the simulation of the Brownian motion it is necessary to study more deeply the properties of their attractors. The suitable instruments could be Lyapunov exponents, Poincare mapping, entropy, complexity and the ergodicity testing. The last three terms need at least very short explanation.

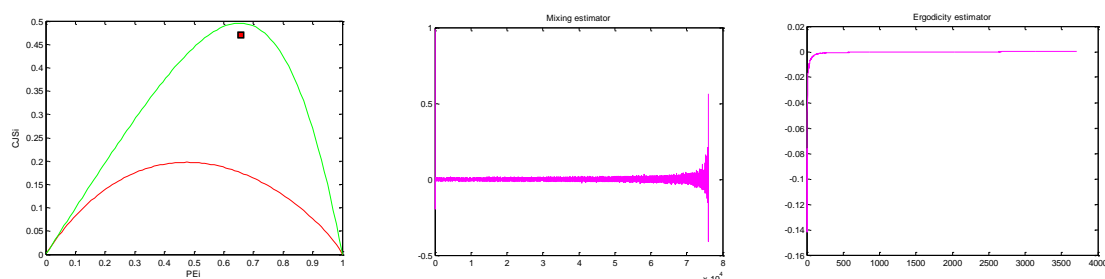


Fig. 1. The position in the entropy-complexity plane and the mixing and ergodicity criterion

As an entropy we will use the permutational entropy introduced by Bandt and Pompe in [1]. The statistical complexity (e.g. [7]) enables to define more precisely the properties if the normalized entropy is inside the interval between 0 and 1. It's the product of entropy and the Jensen-Shannon disequilibrium. The best algorithms are published in [5].

To analyse all the above mentioned criteria, an in-house software has been developed. As an example the results for Hoover-Holian oscillator are shown on Fig. 1. The red and green curves on the Fig. 1 left are the minimum and maximum complexity. Maximum complexity corresponds with the maximum disequilibrium. The number of the missing patterns is 584 (from $6!=46656$ – for the pure noise is this parameter zero). The position in the entropy-complexity plane depends strongly on the sampling period. According [6], it is necessary to find the period leading to the maximum complexity - in our case 105 s (other possibilities -e.g. Poincare section [2] - will be also discussed). This approach allows to compare the different dynamical systems with each other. On the left hand side of Fig. 2 (overtaken from [2]), it is possible to see the position of the fractional Brownian motion (fBM) with different Hurst parameters. This is used as a standard for the stochastic modelling of the Brownian motion. This parameter governs the roughness of its time series. Similar result can be seen on Fig. 2b for HH where the sampling period is 50, 100, 200, 400, 800s.

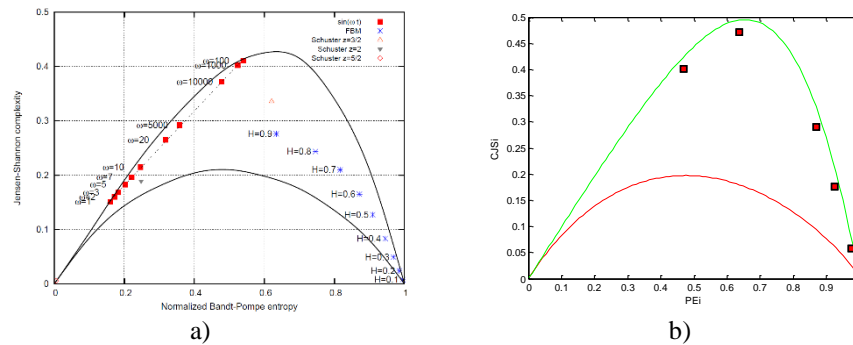


Fig. 2. Position of the fBM in the entropy-complexity plane (a) and of the HH oscillator for the different sampling periods

Similar analysis has been done for all three above mentioned oscillators. The HH oscillator seems to be good suited to simulate the Brownian motion in the dynein computational model.

Acknowledgements

The work has been supported by the grant project LO1402 Centem+ and by the project PUNTIS (LO1506) of the Ministry of Education, Youth and Sports of the Czech Republic.

References

- [1] Bandt, C., Pompe, B., Permutation entropy: A natural complexity measure for time series, *Physical Review Letters* 88 (17) (2002) No. 174102.
- [2] Chrisment, M. C., Firpo, M.-C., Entropy-complexity analysis in some globally-coupled systems. *Physica A: Statistical Mechanics and its Applications* 460 (2016) 162-173.
- [3] Hoover, W. G., Aoki, K., Hoover, C. G., De Groot, S. V., Time-reversible deterministic thermostats, *Physica D: Nonlinear Phenomena* 187 (1-4) (2004) 253–267.
- [4] Hoover, W. G., Hoover, C. G., Ergodicity of a time-reversibly thermostated harmonic oscillator and the 2014 Ian Snook prize, Ruby Valley Research Institute, 2014.
- [5] Lanoiselee ,Y., Grebenkov, D. S., Revealing nonergodic dynamics in living cells from a single particle trajectory, *Physical Review E* 93 (5) (2016) No. 052146.
- [6] De Micco, L., Fernández, J. G., Larrondo, H. A., Plastino, A., Rosso, O. A., Sampling period, statistical complexity, and chaotic attractors, *Physica A: Statistical Mechanics and its Applications* 391 (8) (2012) 2564-2575.
- [7] Rosso, O. A., Larrondo, H. A., Martin, M. T., Plastino, A., Fuentes, M. A., Distinguishing noise from chaos, *Physical Review Letters* 99 (2007) No. 154102.

Transient analysis of thin FGM plates with multi-gradation coupling effects

L. Sator^a, V. Sladek^a, J. Sladek^a

^a *Institute of Construction and Architecture, Slovak Academy of Sciences, Dúbravská cesta 9, 845 03 Bratislava, Slovak Republic*

Plates are three dimensional structural elements whose thickness is significantly smaller than the other dimensions. Due to the small aspect ratio of thickness to in-plane dimensions, in the plate theories the 3-D formulation of elastic problem is assumed in semi-integral form across the plate thickness, and due to this assumption the original problem is simplified to a 2-D problem. One of the best known plate bending theories is the Kirchhoff-Love theory (KLT), in which the shear deformations are omitted and the deflections can be calculated separately from the in-plane deformations in homogeneous plates.

The FGM composites [5] have significant utilization in design of structural elements not only because of superior properties of micro-constituents but also for elimination of interface discontinuities occurring in laminated composite structures, where the stress distributions are smooth. Although FGMs are microscopically inhomogeneous, the phenomenological theories are applicable to various effect described in continuous media including FGMs in which the material coefficients vary continuously and smoothly within their bulk according to gradual change of composition over volume. Ergo, the FGMs are composites in which material properties are determined by the values of material coefficients and continuously variable volume fractions of particular constituents. In recent decades, several approaches have been developed for modelling FGMs, such as the Mori–Tanaka scheme [2], a composite cylindrical assemblage model [3] etc. Nowadays, an emphasized attention has been paid to composite plates with functionally graded material properties using various computational methods for numerical analyses.

Note that a thorough derivation of the equations of motions is required in the KLT for deformations of FGM thin elastic plates. There are interesting phenomena associated with functional gradation of material coefficients of plates. The transversal gradation of Young's modulus and/or mass density by power-law functions yields coupling between the bending and in-plane deformation modes. Let us consider FGM plates with unspecified in-plane gradation of material coefficients and the power-law gradation in the transversal direction as

$$E(\mathbf{x}, z) = E_0 E_H(\mathbf{x}) E_V(z), \quad E_V(z) = 1 + \zeta \left(\frac{1}{2} \pm z \right)^P, \quad (1)$$

$$\rho(\mathbf{x}, z) = \rho_0 \rho_H(\mathbf{x}) \rho_V(z), \quad \rho_V(z) = 1 + \eta \left(\frac{1}{2} \pm z \right)^q. \quad (2)$$

The gradation of these material properties across the plate thickness gives rise to the coupling between the plate deflection and the in-plane deformations even in the case of pure transversal loading of the plate [4]. The correctly derived governing equations for FGM plates with variable thickness reveal another type of coupling effect, so called multi-gradation coupling effects, arising in FGM plates with transversal gradation of material properties and

an additional in-plane gradation of material properties and/or plate thickness. The investigation of such phenomena in the case of pure in-plane loading main purpose of this paper.

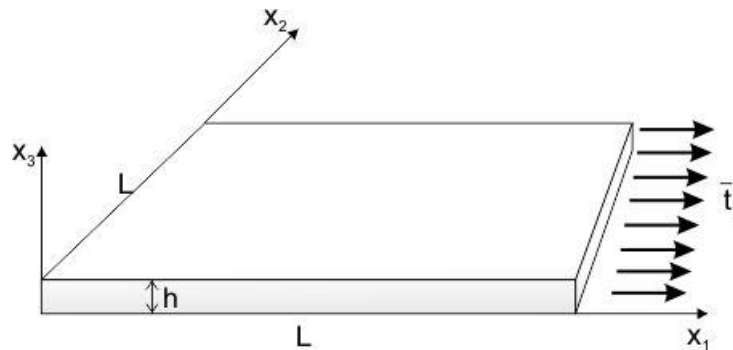


Fig. 1. Square FGM plate loaded by pure in-plane loading

The equations of motion are much more complicated because it becomes the PDE with variable coefficients in contrast to the PDE with constant coefficients. The equations of motion in the KLT are the PDE of the 4th order either with variable or constant coefficients.

Recall that the high order derivatives are inappropriate from the point of view of numerical methods because of increasing inaccuracy with increasing the order of derivatives. The computational efficiency suffers also from the evaluation of high-order derivatives especially in case of meshless approximations. The decomposed formulation is proposed with introducing 2 new field variables in addition to the deflection and in-plane displacement fields. Then, the equations are coupled 2nd order PDE.

To facilitate the numerical solution of the boundary value problems for rather complex governing equations, we propose the strong formulation combined with meshless approximations [1] for field variables. The Moving Least Square (MLS) approximation technique is employed for approximation of field variables. Several numerical examples are presented to investigate the response of the FGM plates. The coupling effects are studied for FGM plates with variable plate thickness under external tension load on the plate's boundary edge (Fig.1).

Acknowledgements

The financial support of the Slovak Research and Development Agency under the contract No. APVV-14-0440 is greatly acknowledged.

References

- [1] Atluri, S. N., The meshless method (MLPG) for domain & BIE discretizations, Tech Science Press, Forsyth, 2004.
- [2] Benveniste, Y., A new approach to the application of Mori–Tanaka's theory in composite materials, *Mechanics of Materials* 6 (2) (1987) 147–157.
- [3] Hashin, Z., Analysis of properties of fiber composites with anisotropic constituents, *ASME Journal of Applied Mechanics* 46 (3) (1979) 543-550.
- [4] Sator, L., Sladek, V., Sladek, J., Coupling effects in elastic analysis of FGM composite plates by mesh-free methods, *Composite Structures* 115 (2014) 100-110.
- [5] Suresh, S., Mortensen, A., *Fundamentals of functionally graded materials*, Institute of Materials, London, 1998.

Mutual interaction of multiple cracks growing in the particulate composite with brittle matrix under conditions of sub-critical crack growth

O. Slávik^a, Z. Majer^b

^a Institute of Physics of Materials, Academy of Sciences of Czech Republic, Žižkova 22, 616 62 Brno, Czech Republic

^b Dept. of Fracture Mechanics and Mesomechanics of Materials, Faculty of Mechanical Engineering, Brno University of Technology, Technická 2896/2, 616 69 Brno, Czech Republic

Composite materials are one of the most popular group of materials nowadays. They consist of two or more substances, each of which has different material properties. The result is a composite material with specific material properties, so that required function can be fulfilled. Such an example of composite materials are the so called LTCC (low temperature co-fired ceramics) materials. LTCC are particulate composites with brittle matrix, used as substrates for semiconductor boards. They are also known for their residual stresses, which are formed around particles during the manufacture.

It is assumed in linear elastic fracture mechanics that crack is stable until the stress intensity factor (SIF) is higher than fracture toughness [1]. However, LTCC materials may be used for operating in aggressive environment with higher humidity. In such environment a special type of crack extension can occur, called subcritical crack growth, which is a time-dependent phenomenon, where crack is growing at constant load even below the fracture toughness [3].

There are multiple articles showing numerical analyses of crack propagation in ceramics [4]. However, it is known that materials with brittle matrix such as ceramics are containing multiple cracks. These are caused by manufacturing, treatment or transportation of the material. And even though these multiple microcracks usually develop into a magistral crack, there are always many interesting mutual interactions between them to study.

In order to study these mutual interactions a parametrical FEM numerical model needs to be created, so that by simple manipulation of an input data it is possible to create many different crack configurations, where these interactions will show up. In this particular case, only two cracks were considered. The goal of the numerical model was to simulate

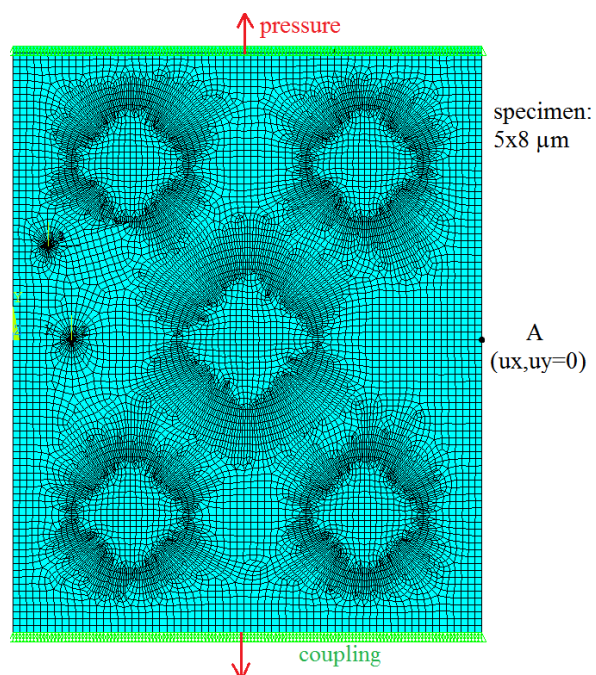


Fig. 1. 2D FEM numerical model of the specimen

a simple tensile test, where upper and bottom edges are stretched away from each other by tensile force and their nodes are coupled which means that each node of a specific edge will have the same displacement (Fig. 1). Also, to create the residual stresses around particles the specimen needs to be cooled from a certain reference temperature. The principle of the FEM model was based on calculating SIF K_I and K_{II} at the end of each step using the *kcalc* command [2]. In the next step, the crack with higher value of SIF K_I was extended. To calculate the angle of rotation of the crack tip the maximum tangential stress criterion (MTS) was used.

In a usual case of crack extension, it can be said, that the longer the crack, the higher is the SIF at its tip. That is not necessary the case in particulate composites, where the residual stresses around the particles take their parts. There was a configuration where crack A was propagating until it reached close distance from a particle surface, where the SIF K_I decreased due to the effect of residual stress. As the value of SIF K_I in crack A decreased under the current value of SIF K_I in crack B, the crack B started to propagate.

In some cases, the crack closure was also observed (Fig. 2). The reason for that was probably size of the specimen, where mutual distance of these cracks was rather small. Problem with this phenomenon was that software is able to calculate SIF even in closed crack what is of course a mistake. Therefore, it needed to be treated using another condition about the displacement of nodes in the crack tip.

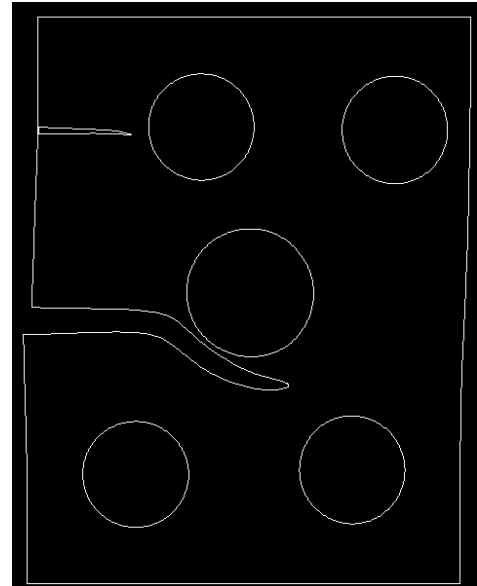


Fig. 2. Crack closure

Parametrical FEM numerical model was used to study mutual interactions between two cracks in particulate composites. Results showed some interesting interactions between them, however we were limited by computer attributes so only a small specimen with lower number of particles and cracks could be observed.

References

- [1] Anderson, T. L., Fracture mechanics: Fundamentals and applications, 3rd edition, Boca Raton, Taylor & Francis, 2005.
- [2] ANSYS – KCALC, *ANSYS help 15.0*, SAS IP, Inc. [access 2017-05-10].
- [3] Bermejo, R., Supancic, P., Krautgasser, C., Morrell, R., Danzer, R., Subcritical crack growth in Low Temperature Co-fired Ceramics under biaxial loading, *Engineering Fracture Mechanics* 100 (2013) 108-121.
- [4] Majer, Z., Pletz, M., Krautgasser, C., Náhlík, L., Hutaf, P., Bermejo, R., Numerical analysis of sub-critical crack growth in particulate ceramic composites, *Procedia Materials Science* 3 (2014) 2071-2076.


Modal testing as a tool for composite damage detection?

P. Steinbauer^a, J. Němec^a

^aFaculty of Mechanical Engineering, Czech Technical University in Prague, Technická 4, 16000 Praha 6, Czech Republic

The modal testing provides global information about the investigated structure. Thus modal parameters should be good indicator of structure state – health. However, published papers contain contradicting information about usage and results for various types of structures ranging from bridges to machines (see [2-4, 6]). On the other hand, accuracy of modal testing is still quite dependent on many parameters, modal test boundary conditions, used measurement technology etc. It was shown (see [1]) that same simple structure measured by different labs and teams was evaluated with quite different results (eigen frequency differences up to 4%, but modal damping up to 30%).

The composites receive increasing attention in every field of engineering design, because it is possible to design composite properties with specific eigen modes and directly influence damping of selected modes. So the deterioration of the composite may have more severe impacts. Therefore the paper investigates whether controlled impact damage of the composite can be effectively detected by modal testing methods. Two composite samples, carbon fiber tube and glass fiber plate were used. The accuracy and repeatability of modal tests were compared to impact damage influence on modal parameters. The composite sample was measured in “free boundary” setup using soft rubber straps.



Experiment number	Experiment characteristics
1-8	Repeated reference measurement
9-12	Impact 100mm
13-16	Impact 200mm
17-20	Impact 500mm
21	Repeated measurement
22	Impact 750mm
23	Impact 800mm ball hammer
24	Repeated measurement
25	Impact 500mm, no support
26	Impact 800mm 3x, no support
27	Impact 800mm 5x, no support
28	Impact 800mm 3x, no support, ball hammer
29	Impact 800mm 5x, no support, ball hammer

Fig. 1. Experiment setup and strategy

The scanning laser Doppler vibrometer was used to measure response (no contact with measured sample - Fig. 1), the excitation was introduced by electromechanical shaker. The actual acting force was measured by force transducer. The sample was repeatedly measured in initial state and then destroyed by controlled hammer impact (see the list in the Fig. 1). The data postprocessing was based on in-house implementation of EMA regression algorithm (Fig. 2) to ensure complete calculation repeatability.

The results are summarized in the Fig. 3. The fluctuation of both eigen frequencies and modal damping was comparable for cases of only repeated measurements and lightly damaged sample. Only for higher eigen frequencies with more spatially complex eigen modes it was possible to determine substantial change of both modal damping and eigen frequency for serious damage.

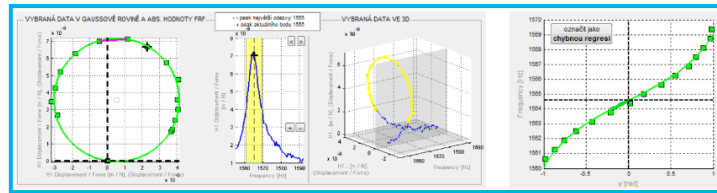


Fig. 2. In house implementation of the EMA regression algorithm

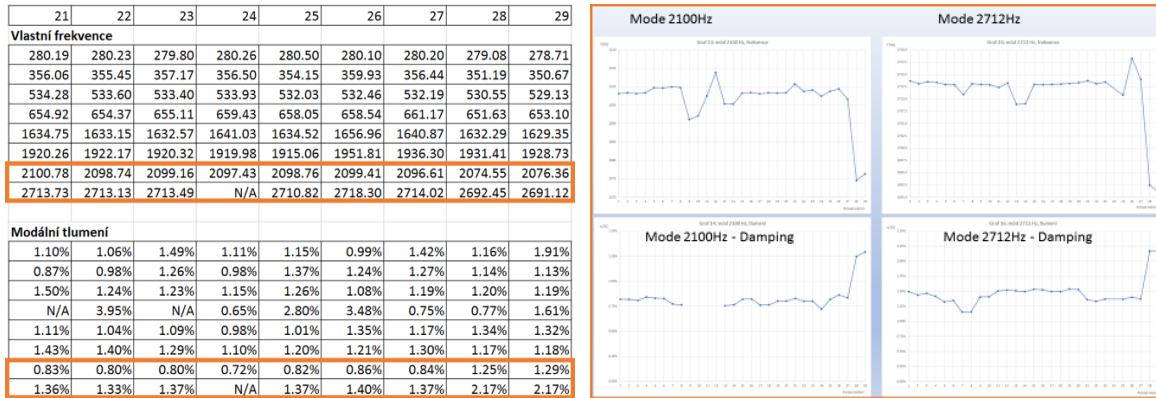


Fig. 3. Measurement results and evaluation

The experimental results may provide sufficient information to detect serious damage of the composite sample. However, not all modes are sufficiently sensitive to impact damage and higher modes seems to be more sensitive. Some modes are not affected at all. These conclusions are in line with previous research concerning lighting pole corrosion damage ([5]). Accuracy and repeatability of sample fitting (realization of “free boundary”) has great influence on experiment results. More complex (higher) modes are often more sensitive, complex motion increases probability that deformation occurs in the vicinity of the damage. But the responses of complex modes must be measured in very detailed mesh.

Acknowledgements

This research has been realized using the support of EU Regional Development Fund in OP R&D for Innovations (OP VaVpI) and The Ministry of Education, Youth and Sports, Czech Republic, project # CZ.1.05/2.1.00/03.0125 Acquisition of Technology for Vehicle Center of Sustainable Mobility and The Ministry of Education, Youth and Sports program NPU I (LO), project # LO1311 Development of Vehicle Centre of Sustainable Mobility. This support is gratefully acknowledged.

References

- [1] Balmes, E., Wright, J. R., GARTEUR group on Ground Vibration Testing, Results from the test of a single structure by 12 laboratories in Europe, OFFICE NATIONAL D ETUDES ET DE RECHERCHES AEROSPATIALES ONERA-PUBLICATIONS-TP, 1997.
- [2] Doebling, S. W., Damage identification and health monitoring of structural and mechanical systems from changes in their vibration characteristics: A literature review, Los Alamos National Laboratory, University of California, 1996.
- [3] Frantík, P., Lehký, D., Influence of eigenfrequencies for damage localization of cantilever beam, Proceedings of the conference Pravděpodobnost porušování konstrukcí, Brno, 2006, pp. 307-312. (in Czech)
- [4] Salawu, O. S., Detection of structural damage through changes in frequency: A review, Engineering structures 19 (9) (1997) 718-723.
- [5] Steinbauer, P., Valášek, M., Mechatronic lighting pole testing device, Recent Advances in Mechatronics (2010) 127-132.
- [6] Tang, J.-P., Leu, K.-M., Vibration tests and damage detection of P/C bridges, Journal of the Chinese Institute of Engineers 14 (5) (1991) 531-536.

Advanced control systems in vehicle flow simulations

R. Stojan^a, Z. Šika^a, P. Steinbauer^a

^aDepartment of Mechanics, Biomechanics and Mechatronics, Faculty of Mechanical Engineering,
Czech Technical University in Prague, Technická 4, Praha 6, Czech Republic

In recent years the amount of traffic on the roads has increased significantly. The roads were not designed for so many vehicles and it results in many traffic complications, such as two problems addressed in this paper, the reduction of traffic fluency and the increase of fuel/energy consumption. Two of the possible solutions are building new roads or higher utilization of the existing roads. It is really expensive and not always possible to build new roads or add lanes to existing ones, e.g. in the centre of city.

On the other side the advanced control systems allow increasing the capacity utilization even on the existing roads and enable better route and driving strategy planning. These control system solutions also require investments to traffic infrastructures and new equipment of vehicles, but it should be cheaper, faster (deployment) and more efficient and comfortable solution. The advanced control systems can be upgraded and used even for the autonomous driving in the future.

The hybrid and electric vehicles are spreading into traffic. Together with the rising price of the fuel/power and the limited electro-powered range of the hybrid and electric vehicles, the consumption is another important subject to explore.

This study is focused on simulations of the driving with different vehicle types (and their penetration) and cruise control systems (human, PID, MPC) in the vehicle flow. The simulations are performed in two environments, the MathWorks Matlab Simulink and SUMO (Simulation of Urban Mobility, [1]).

The vehicle flow consists of two main vehicle classes, the leading vehicle (leader) and the following vehicles. The *leader* vehicle follows prescribed velocity profile for the route (legally allowed, energy optimized, etc.). The *following* vehicles follow the leader's velocity profile and keep the safe gap (set e.g. as distance travelled in 2 seconds) between vehicles/from a preceding vehicle.

The study was also motivated by the development of the system capable to optimize vehicle driving in terms of power consumption [2]. The main interest is the impact on the surrounding traffic. In general it can be expected, that in terms of power/fuel consumption, the optimization will lead to the vehicle speed and accelerations reduction.

The current version of (under development) driving optimization system was modified and integrated with other systems such as SUMO [1] or the agent system developed by Ricardo. Integration into the SUMO environment builds on [3], where a predictive controller for a car-following model was integrated and further extends the capabilities of the system for our researching purposes. The optimization system has been developed in the MathWorks Matlab environment. For the first version of the optimizer integration, the dynamic DLL library form (that MATLAB can generate) was chosen.

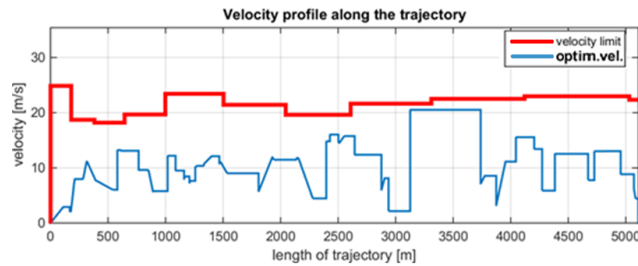


Fig. 1. Example of optimized velocity profile

The influence of the optimization system on surrounding traffic has been studied, see for example Fig. 1. The results suggest that quite significant reduction of power consumption (up to 25% with current version, depending on route) can be achieved for a single “optimized” vehicle, but this vehicle can lead to lower efficiency of the surrounding traffic (e.g. unexpected slowdowns for human drivers leading to “shockwaves”, such as in Fig. 2) on public roads.

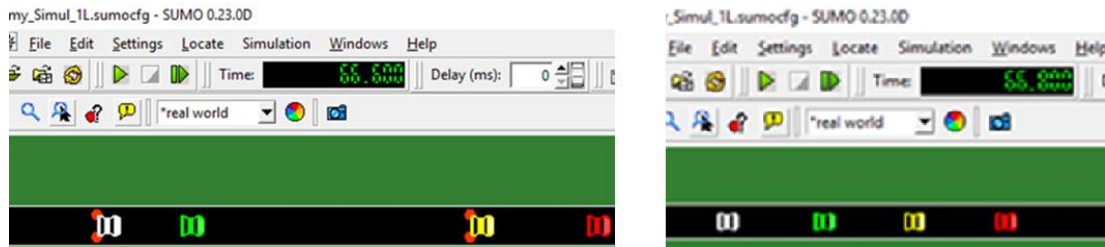


Fig. 2. Driving according to optimised profile using predictive MPC control (on the right) compared to disorderly human drivers (on the left)

The future development should also involve the impact on the surrounding traffic and use the enhancements enabled by V2X communication and modern control systems.

Acknowledgements

This research has been realized using the support of the grant SGS16/208/OHK2/3T/12 of CTU in Prague, "Mechatronics and adaptronics", the support of The Ministry of Education, Youth and Sports program NPU I (LO), project # LO1311 Development of Vehicle Centre of Sustainable Mobility and the support of Technological Agency, Czech Republic, programme Centres of Competence, project # TE01020020 Josef Božek Competence Centre for Automotive Industry. This support is gratefully acknowledged.

References

- [1] Denk, P., Steinbauer, P., Šika, Z., Macek, J., Morkus, J., Route segmentation designed for optimization of the vehicle behaviour and control by the adaptive cruise control, Proceedings of the 21st Workshop of Applied Mechanics, Czech Technical University in Prague, 2016, pp. 9-12.
- [2] Krajzewicz, D., Erdmann, J., Behrisch, M., Bieker, L., Recent development and applications of SUMO - Simulation of Urban Mobility, International Journal On Advances in Systems and Measurements 5 (3, 4) (2012) 128-138.
- [3] Stojan, R., Steinbauer, P., Šika, Z., Simulation study of mechatronic systems influence in vehicle flow control, Proceedings of the 19th Workshop of Applied Mechanics, Czech Technical University in Prague, 2015, pp. 46-49.

On boundary conditions in problem of flow induced vibrations of human vocal folds model

P. Sváček

*Department of Technical Mathematics, Faculty of Mechanical Engineering, Czech Technical University in Prague,
Karlovo nám. 13, 12135 Praha, 2, Czech Republic*

The mathematical modelling of human creation is a complex difficult task, which requires many obstacles to be overcome. The primary source of human voice is created in the glottis - the narrow part of the channel between the two vocal folds. The vocal folds vibration leads to periodical (almost or complete) closure of the channel, which is the main source of the generated sound. In order to describe such a behaviour with a mathematical model, one of the most important is the choice of suitable inlet boundary conditions allowing the physical behaviour of the flow model within the context of closing channel.

The choice of suitable boundary conditions at the inlet or outlet part of the channel is difficult particularly also for the problems of inner aero-hydroelasticity, i.e. when some part of the channel walls is deformable. Such a situation can lead to the critical velocity to be very sensitive both on the choice of the inlet/outlet boundary conditions as well as on the lengths of the channel downstream or upstream of the vibrating part. For instance in the paper [3] the flutter velocity of an aeroelastic system was substantially dependent on the type of prescribed boundary conditions at the inlet.

In this paper a simplified model of vibrating airfoil is used, see e.g. [2]. These simple mass-spring models are coupled with a quasi-1D airflow and they were proved to be very useful in estimation e.g. of the vocal folds loading by impact stress during collisions. The main advantage of these models is the ability to perform nearly real-time simulations. Here, this simplified model is coupled by the incompressible Navier-Stokes equations model of fluid flow and the main attention is paid to the almost complete closing of the channel. Particularly, the choice of the proper inlet/outlet boundary condition is discussed.

The flow of an incompressible viscous fluid in the domain Ω_t^f is described by the system of the Navier-Stokes equations written in the ALE form

$$\rho \frac{D^A \mathbf{v}}{Dt} + \rho((\mathbf{v} - \mathbf{w}_D) \cdot \nabla) \mathbf{v} = \operatorname{div} \boldsymbol{\tau}^f, \quad \nabla \cdot \mathbf{v} = 0, \quad (1)$$

where \mathbf{v} is the fluid velocity vector, ρ is the constant fluid density, and $\boldsymbol{\tau}^f$ is the fluid stress tensor given by $\boldsymbol{\tau}^f = -p\mathbb{I} + 2\mu\mathbb{D}(\mathbf{v})$. Here, p is the pressure, $\mu > 0$ is the constant fluid viscosity and $\mathbb{D}(\mathbf{v}) = \frac{1}{2}(\nabla \mathbf{v} + (\nabla \mathbf{v})^T)$. In order to allow the complete closure of the channel, the inlet boundary condition at Γ_I is realized with the aid of the penalization approach, which means that at the inlet Γ_I a modified boundary condition is prescribed

$$-\mathbf{n} \cdot \boldsymbol{\tau}^f + \frac{1}{2}\rho(\mathbf{v} \cdot \mathbf{n})^- \mathbf{v} = p_I \mathbf{n} + \frac{1}{\varepsilon}(\mathbf{v} - \mathbf{v}_I), \quad (2)$$

where $\varepsilon \in (0, +\infty)$ is a suitable penalization parameter. Formally by taking $\varepsilon = +\infty$ the boundary conditions (2) yields the modification of the do-nothing boundary condition, whereas for $\varepsilon \rightarrow 0_+$ we obtain the Dirichlet boundary condition.

The vibrations of the vocal folds usually exhibit two dominant eigenfrequencies. This behaviour can be described with the aid of a simplified three-mass aeroelastic model with two degrees of freedom. The motion of Γ_{Wt} is governed by the displacements $\theta_1(t)$ and $\theta_2(t)$ of the two masses m_1 and m_2 , respectively. The displacement vector $\boldsymbol{\theta} = (\theta_1, \theta_2)^T$ is obtained by the solution of the following equations

$$\mathbb{M}\ddot{\boldsymbol{\theta}} + \mathbb{B}\dot{\boldsymbol{\theta}} + \mathbb{K}\boldsymbol{\theta} = -\mathbf{F}, \quad (3)$$

where \mathbb{M} is the mass matrix, \mathbb{K} is the diagonal stiffness matrix with spring constants c_1, c_2 on its diagonal and \mathbb{B} is the matrix of the proportional structural damping.

The numerical results shows that using the proposed penalization boundary condition it is possible to treat the almost complete closure of the channel and it is possible to address the flow induced vibrations also in the post-critical regime.

Acknowledgment

This work was supported by the *Czech Science Foundation* under the *Grant No. 16 - 01246S*.

References

- [1] Bruneau, C.-H., Fabrie, P., Effective downstream boundary conditions for incompressible Navier-Stokes equations, *International Journal for Numerical Methods in Fluids* 19 (8) (1994) 693–705.
- [2] Horáček, J., Švec, J. G., Aeroelastic model of vocal-fold-shaped vibrating element for studying the phonation threshold, *Journal of Fluids and Structures* 16 (7) (2002) 931–955.
- [3] Sváček, P., Horáček, J., Numerical simulation of glottal flow in interaction with self oscillating vocal folds: Comparison of finite element approximation with a simplified model, *Communications in Computational Physics* 12 (3) (2012) 789–806.

Random heterogeneous materials: Wang tile size vs circular particle packing

D. Šedlbauer

Department of Mechanics, Faculty of Civil Engineering, CTU in Prague, Thákurova 7/2077, 166 29 Prague, Czech Republic

Within last years the Wang tiling [4] approach has been successfully integrated into the family of concepts for modelling of random heterogeneous materials. The main advantage of Wang tiling is ability to compose large or even infinite aperiodic random heterogeneous material domains with a relative small set of building blocks – Wang tiles. There exist several ways how to generate Wang tiles. It is worth to mention inter alia image quilting or algorithms using molecular dynamics. The last mentioned method is suitable for materials with circular or ellipsoidal non-overlapped hard particles randomly placed within a matrix on which this paper aims at. There is an effort on one hand to create large basic tiles in order to have the greatest match with reference material characteristics, on the other hand such an assumption brings great computer demands. In this contribution we will focus on Wang tile size in terms of circular packing, possibilities of particle arrangement and degree of heterogeneity via set of simplified simulations.

The investigated Wang tile set consists of eight tiles in accordance with stochastic CSHD algorithm [1] based on two different codes (colours) for both vertical and horizontal tile edges. The generation of Wang tiles is utilized through molecular dynamics algorithm with adaptive boundaries [3]. In the beginning of the algorithm centres of particles are randomly thrown into tile set. In the same time particles are assigned with random velocity vector. During time steps particles move, rebound of the walls and collide with each other until stopping criterion is reached. The crucial goal in the very beginning of the algorithm seems to be to define number of particles for every tile with respect to the required particle fraction.

In Fig. 1 there are shown two tilings of artificial material domains with particles of equal radii. Even if these samples are both random and have the same particle fractions, arrangement in the first case is closer to the periodic structure whereas the second one exhibits higher value of degree of heterogeneity.

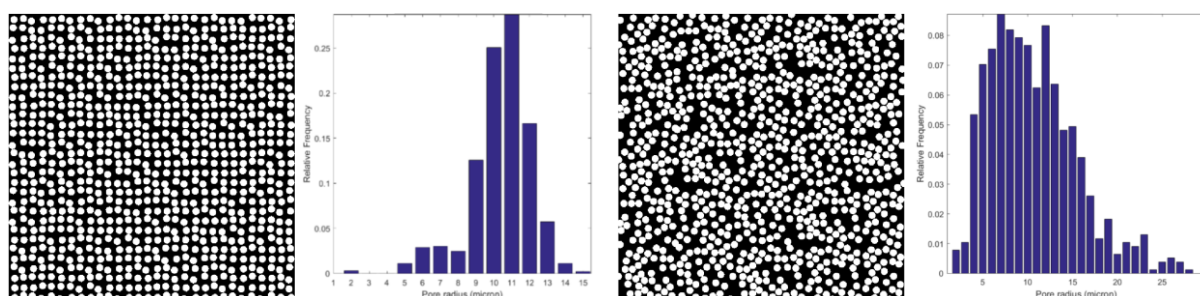


Fig. 1. Tilings with pore distribution a) 30x30 tiles; 1 particle per tile b) 5x5 tiles; 36 particles per tile

In the first two simulations each tile of Wang tile set has the same number of particles. Such an assumption is valid for materials without significant particle clusters or large pores. There is also an option to generate large tiles with great number of particles. Nevertheless these efforts lead to losing main advantage of Wang tile principles – ability to compose large domain with small set of tiles preserving computer demands.

Another possibility is to have the set of Wang tiles with different number of particles within. In Fig. 2 there are artificial material domains according to the last presumption. It has to be noted the need to modify tiling algorithm. The depicted samples were made with original stochastic CSHD tiling algorithm with equal acceptance probability for two tiles of the set which can be added into tiling grid.

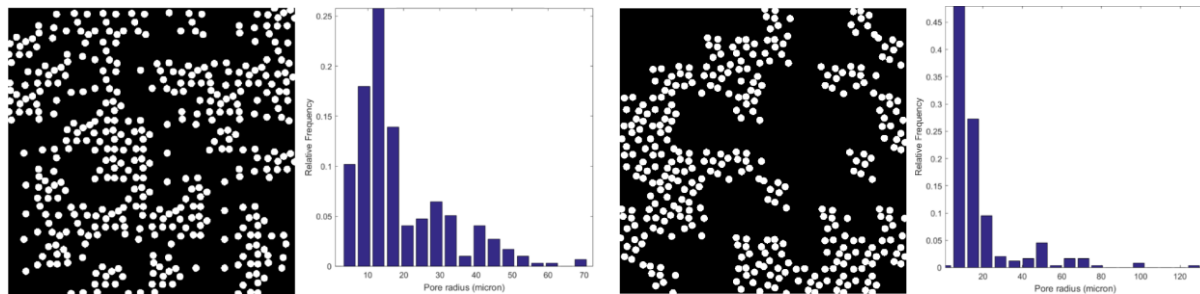


Fig. 2. Tilings with pore distribution a) 10x10 tiles; 10, 8, 6, 4, 2, 1, 1 0 particles per tile – basic set of eight tiles b) 10x10 tiles; 8, 8, 8, 8, 0, 0, 0, 0 particles per tile – basic set of eight tiles

From the comparison between Fig.1 and Fig. 2 the result might be: the more are different tiles in the set, the higher degree of heterogeneity can be achieved. Nevertheless with higher differences in tiles arises another problems. If the reconstructed material domain exhibits both higher particle fraction and clusters or pores, algorithm for tile generation has to deal with the maximal possible arrangement in the container of given shape – dense packing [2]. The higher particle fraction in tile extremely increase computer demands based on the nature of molecular dynamics with particle collisions. Finally, the determination of Wang tile size can be divided into two steps. The first investigation deals with geometrical relations between tile size and particles of reconstructed domain. On the other hand the tiling size as well as tile size varies with respect to the observed microstructural characteristics. This paper deals with the first approach, but with further works we will aim at the second approach in order to provide complete support for users and researches with reconstruction of random heterogeneous microstructures.

Acknowledgements

The financial support of the Grant Agency of the Czech Technical University in Prague, grant No. SGS17/042/OHK1/1T/11, is gratefully acknowledged.

References

- [1] Cohen, M., Shade, F. J., Hiller, S., Deussen, O., Wang tiles for image and texture generation, Proceedings of the conference SIGGRAPH'03, 2003, pp. 287-294.
- [2] Szabó, P., Packing up to 200 equal circles in a square, Models and Algorithms for Global Optimization: Optimization and Its Applications, Springer, Boston, 2007.
- [3] Šedlbauer, D., Adaptive boundaries of Wang tiles for heterogeneous material modelling, Advanced Materials Research 1144 (2017) 159-166.
- [4] Wang, H., Proving theorems by pattern recognition-II, Bell System - Technical Journal 40 (1) (1961) 76-102.

Design and optimization of additional piezo-actuated platform of cable mechanism

Z. Šika ^a, R. Bulín ^b, J. Zavřel ^a, P. Beneš ^a, J. Miletín ^c

^a Faculty of Mechanical Engineering, CTU in Prague, Technická 4, 166 07 Praha 6, Czech Republic

^b Faculty of Applied Sciences, University of West Bohemia, Univerzitní 8, 306 14 Plzeň, Czech Republic

^c BMD a.s., Modlanská 1862, Teplice, Czech Republic

The cable/fibre driven variants of parallel kinematic mechanisms (PKM) combine the concept of parallel machines with the usage of cables instead of rigid links. This solution removes many weaknesses of PKM and brings further advantages, but also an advanced control of these systems is necessary [1, 2]. Besides other mechanisms the experimental demonstrator of spherical mechanism QuadroSphere was optimized and realized [3]. It is positioned by four drives and its orientation is measured by means of incremental sensors in central joint. Concerning the control algorithms especially the combination of the antibacklash control with the removal of mutual drive fighting has been investigated and successfully implemented.

The weak point of the cable driven PKM is relatively low resultant stiffness and the narrow frequency bandwidth of their feedback motion control. To avoid these problems the concept of a multi-level mechanisms has been introduced. The term multi-level means a hierarchical structure composed from the parallel cable driven mechanism for large and slow motions and the active structure connected to the mechanism platform for the small and high frequency motions. The preliminary experiments with multi-level QuadroSphere [4] use a cubic 6 DOF architecture with 6 piezoactuators of maximum stroke 60 μm . Such extent was too small for the correction of positioning errors of the cable driven platform of demonstrator.

Consequently the further steps have been optimization, design and build of additional platform fully tailored to the primary cable driven mechanism. The spherical QuadroSphere demonstrator has 3 DOF, the planar additional mechanism with 3 DOF (Fig. 1) is sufficient for the motion control correction. The usage of 3 mechanically amplified piezoactuators (APA) with maximum stroke 300 μm has been chosen as an optimum instrumentation.

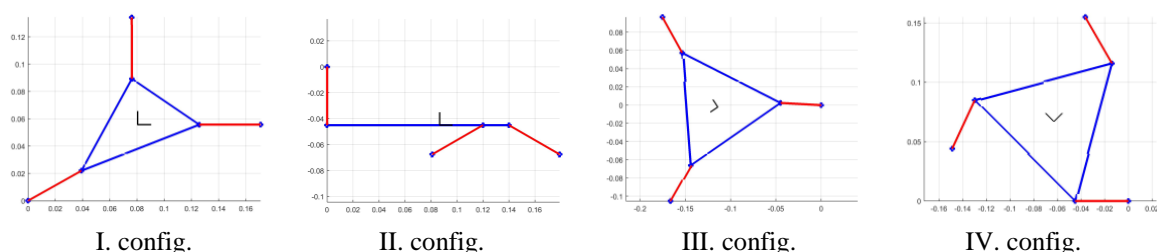


Fig. 1. Different optimized configurations of planar 3 DOF additional mechanism

The optimization of planar mechanism in the first level took into account the **dexterity**, **workspace** extension and **stiffness** in the mechanism plane. The axes of amplified motions of actuators are shown as red lines (Fig. 1). The second step of the optimization is based on the detailed 3D flexible models (Fig. 2). The particular realizations of each configuration have a significant effect on the dynamic properties of the added piezo-mechanism. Its

eigenfrequencies should be significantly higher than the 3 lowest eigenfrequencies of the primary cable driven mechanism, which are for different positions approximately between 20 and 50 Hz. Moreover the piezo-mechanism should be relatively stiff in the direction perpendicular to its motion plane.

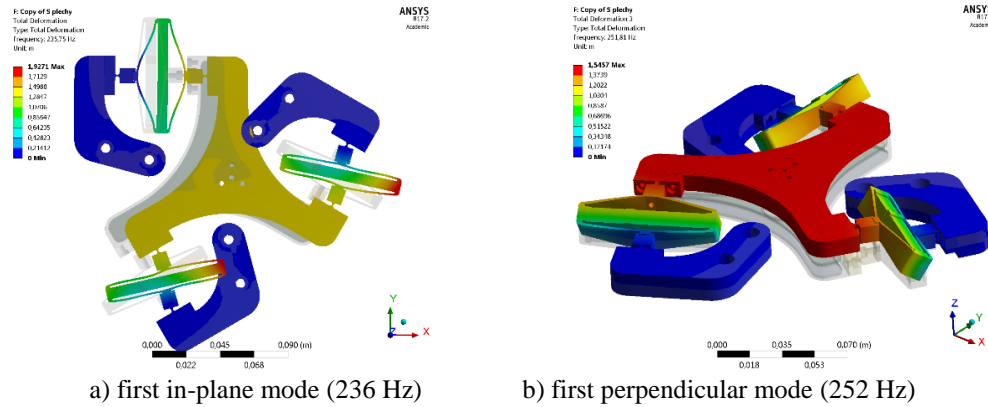


Fig. 2. In-plane and perpendicular eigenmodes with lowest eigenfrequencies

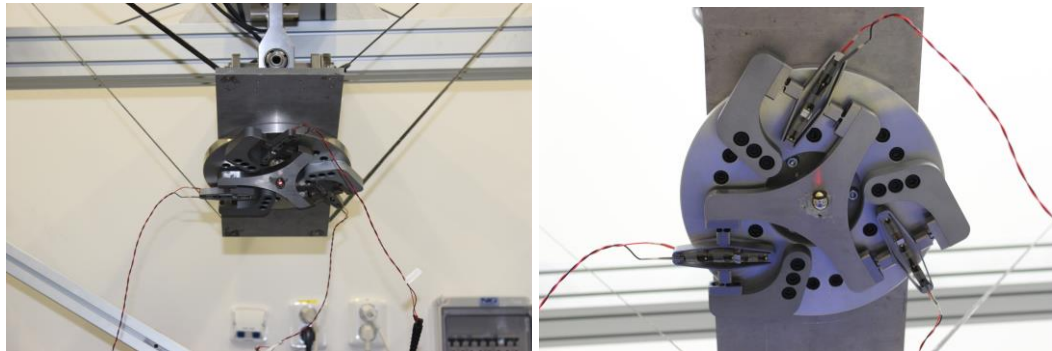


Fig. 3. Experimental 3 DOF piezo-actuated mechanism added to cable driven platform

The results of analysis of the finally chosen variant are shown in Fig. 2. The eigenfrequencies of the additional platform are above 230 Hz and thus a sufficient separation from the eigenfrequencies of the primary cable-driven mechanism has been achieved. Based on these optimizations and analysis the demonstrator of piezo-actuated mechanism has been built and mounted to the cable driven platform (Fig. 3). Currently the tuning of the motion control of the multi-level mechanism demonstrator is in progress.

Acknowledgement

The work has been supported by the Czech Science Foundation project GA15-20134S „Multi-Level Light Mechanisms with Active Structures”.

References

- [1] Kraus, W., Force control of cable-driven parallel robots, Stuttgart: Fraunhofer Verlag, Stuttgart, Ph.D. thesis, 2015.
- [2] Meunier, G., Boulet, B., Nahon, M., Control of an overactuated cable-driven parallel mechanism for a radio telescope application, IEEE Transactions on Control Systems Technology 17 (5) (2009) 1043-1054.
- [3] Svatoš, P., Optimization and control of movement of fibre driven parallel mechanisms, CTU in Prague, Ph.D. thesis, 2016.
- [4] Svatoš, P., Šika, Z., Beneš, P., Hajžman, M., Závřel, J., Cable driven mechanisms with added piezo active platform, Bulletin of Applied Mechanics 11 (38) (2015) 19-24.

Application of the neural networks for evaluation of structural steel material properties based on small punch test results

J. Špička^a, L. Kander^b

^a Research and Testing Institute Plzeň, Tylova 1581/46, 301 00, Plzeň, Czech Republic

^b Material and Metallurgical Research Co., Ltd., Pohraniční 31/639, 703 00 Ostrava-Vitkovice, Czech Republic

This paper describes results of experimental work and numerical simulations carried out within the project TE01020068 “Centre of research and experimental development of reliable energy production, work package 8: *Research and development of new testing methods for evaluation of material properties*”. The aim of this project is to develop and test a novel approach for identification of material properties of the steel. This work deals with utilization of the small punch test for evaluation of material degradation of power station in the ČEZ company. The main goal here is an improvement of empirical correlation of selected materials used in power industry for manufacturing of the critical components (rotors, steam-pipes, etc.). The effort here lays on utilization of finite element method (FEM) and neural networks (NN) for evaluation of mechanical properties (yield stress, tensile strength or fracture toughness) of the selected material at a room temperature, based on SPT results only [4].

Currently, there is an effort to maximize the service life of almost worn out operating components while maintaining the conditions for reliable and safe operation. Thus, the new test methods for evaluation of residual service life or for determination of the actual strength values and brittle fracture properties of the exploited components are developed. One of the methods used to evaluate the current state of mechanical properties is the small punch test (SPT) [1]1, 5, 6]. This method is used both for assessing the current condition of the material as well as for evaluating the so-called zero states of newly manufactured components.

The main aim of this work is to create a software, which, on the basis of already performed experiments for penetration test (SPT) and tensile test, will be able in the future, for the newly performed SPT experiments, estimate material parameters without necessity to perform the tensile test and to identify from it these parameters. The standard process of identifying yield stress, tensile strength and fracture toughness is to perform tensile test and based on this test, the material properties can be evaluated (ČSN EN ISO 9862-1, ASTM E 1820). However, tensile test requires large material specimen and it could be financially and time demanding task. The small punch test has advantage of small specimen required for the test and relatively cheap cost, but it does not allow us to directly evaluate such material properties. To ensure the safe operation of the component, it is necessary to test the actual values of the material parameters. With the advantage of this work, one would avoid the necessity to perform a costly tensile test. It would be sufficient to perform just a penetration test and using a suitable mathematical apparatus identified such mechanical parameters. This newly developed approach could facilitate identification of the actual material parameters of steel in a timely and economical manner.

A neural network (NN) was chosen as a suitable mathematical tool [2]2, 7]. The neural network is a computational system originally inspired by nature and the human brain. Dr. Robert Hecht-Nielsen defined the neural network as follows: "...a computing system made up

of a number of simple, highly interconnected processing elements, which process information by their dynamic state response to external inputs." [2]. The neural network would have the input data from the penetration test and material parameters as an output, see Fig. 1.



Fig. 1. Diagram of the program, where E = Young's modulus of elasticity, R_{p02} = yield strength, R_m = strength limit and Nu = Poisson number

The FEM model was created in the ANSYS software for simulation of the tensile test. The Gurson-Tvergaard-Needleman material model [3] was used in order to take into account material failures. This model is characterized by 11 constants (including yield strength, strength limit, Young's modulus of elasticity and the Poisson constant). Numerical optimization in the MATLAB software was used for identification of these constants and runs the tensile test with the use of the ANSYS software. The aim was to achieve that response of the numerical simulation (MATLAB + ANSYS) matched most closely possible the curve of the tensile test experiment. In this way, the material characteristics were identified for all the supplied test specimens.

The next step is the creation and training of the NN. The input was the penetration test curve (Force vs. Strain) and optimized material parameters (E , R_{p02} and R_m) were the output. The curve here was taken from zero to its maximum and it was cut here and sampled for a given number of points. Furtherly, it would be advisable to consider the curve also beyond its maximum. The neural network must not only be trained, it is always necessary to test it with the use of some known pair input-output, which was not used in training. The largest number of available samples - 18 was for the material P91. Thus, 17 pairs were taken for the network training and left one pair for testing. This was done gradually with all 18 values. To obtain the experimental data, together 3 material were tested under tensile test and SPT. The particular materials were steel 15 128 (14MoV6-3), the steels of type P91 (X10CrMoVNb9-1) containing 9% Cr, and 1% Mo, and steel P92, in which it was attempted to replace the expensive molybdenum by tungsten. In order to make this new approach applicable, it would be necessary to build the database of large number of experiments to successfully train the neural networks.

Acknowledgement

This work financially supported with the TAČR project 'TE01020068 Centre of Research and Experimental Development of Reliable Power Engineering' funded by the Czech Technology Agency.

References

- [1] Catherine-Sainte, C., Messier, J., Poussard, C., Rosinski, S., Foulds, J., Small punch test: EPRI-CEA finite element simulation benchmark and inverse method for the estimation of elastic plastic behaviour. In: Small Specimen Test Techniques: Fourth Volume, ASTM International, 2002.
- [2] Caudill, M., Neural network primer: Part I, AI Expert, 1989.
- [3] Fesich, T. M., Mohan, P., Marzougui, D., Kan, C. D., A study of the Gurson damage model and numerical simulation of ductile failure in LS-DYNA, LS-DYNA Anwenderforum, Bamberg, 2008.
- [4] Kander, L., Špička, J., Utilization of neural networks for evaluation of material properties of structural steels based on SPT results, Hutnické listy 4 (2017). (in press)
- [5] Li, Y., Hurst, R., Matocha, K., Cizek, P., Blagoeva, D., New approach to determine fracture toughness from the small punch test, Metallurgical Journal vol. LXIII, p. 94-102.
- [6] Small punch test method for metallic materials, CEN WORKSHOP AGREEMENT CWA 15627, 2007.
- [7] https://www.tutorialspoint.com/artificial_intelligence/artificial_intelligence_neural_networks.htm

Simulations of explosions for improvements of passive safety

S. Špirk^a

^a Faculty of Mechanical Engineering, University of West Bohemia in Pilsen, Univerzitní 8, 306 14 Plzeň, Czech Republic

This paper presents a knowledge for numerical simulations, testing and design of devices with significant risk of explosion. The main point of this work is to get the knowledge for safe design with controlled rupture (not heavy explosion-proof device). In chemical industry, transportation or electrical industry exist real risk of injuries caused by explosions (eg. during overload). The accident situations are usually connected with large deformations and uncontrolled structure collapse of large box with thin wall (eg. the box size 2 x 1 x 0,5 m and thickness 1 mm). For simulations is used the FEM (Finite element method) and SPH (smoothed particle hydrodynamics) methodology with experimental verification.

Firstly the effect of the detonation is estimated by Hopkinson-Cranz scale parameter (Z) in combination with Friedlander equation for wave shape. In SW excel is computed the peak pressure and wave shape in time at known distance for known initial mass of TNT explosive. With this tool is possible to estimate the amount of explosives for box rupture. The maximum overpressure can be calculated by:

$$p_0 = p_a \frac{808 \left(1 + \left(\frac{Z}{4.5} \right)^2 \right)}{\sqrt{1 + \left(\frac{Z}{0.0048} \right)^2} \sqrt{1 + \left(\frac{Z}{0.32} \right)^2} \sqrt{1 + \left(\frac{Z}{1.35} \right)^2}}, \quad (1)$$

where p_a is ambient pressure and Z is scale parameter (dependent on explosives weight, distance from charge and ratio of air density at the point of interest). The construction in SW. Matlab is clearly described in [4].

The next step is the simulations of detonation. The movement of detonation wave in explosive material is described by the Chapman-Jouguet theory. The TNT explosive charge is modeled with JWL (Jones–Wilkins–Lee) equation of state for detonation products.

$$P = A \left(1 - \frac{\omega}{R_1 V} \right) e^{-R_1 V} + B \left(1 - \frac{\omega}{R_2 V} \right) e^{-R_2 V} + \frac{\omega E_0}{V}, \quad (2)$$

where A, B, R1, R2, ω are material constants, V is the relative volume of the gas products and E_0 is the energy per unit volume. The parameters of more explosive materials can be found in [2]. The best source of experimental data is the paper [3]. With this source is possible to verified the behavior for ball source of TNT with detonation point in ball center (Fig. 1). The results can be significantly influenced by higher artificial viscosity. The three type of materials (S235JRN, S355J2N, FORA 400) are modeled with Johnson-Cook model [5]. The simulations results is compared with experimental data (Fig. 2) where the 200g of TNT at distance 20 mm is placed under flat 200x200x5 mm and the 75g of TNT at more distances in range 30-70 mm is placed under the flat with diameter 110 mm.

Unfortunately the simulations and experimental results shows than the studied process is not influenced by detonation but only with pressure increase. The significant criterion is the velocity of the process compared to the velocity of the sound. During the simulation the device is also ruptured by the local load of explosives, what is not in agreement with real explosion. The explicit simulations of pressure increase in the short time (10-100 ms) is possible. The pressure load can be applied as nodal boundary condition. The interesting challenge is the experimental part, because the fast pressure increase can be exert only with powerful pressure source (power close to 2 MW) without the convention explosives (TNT, C4, semtex etc). The pressure can be generated by propellant during the experiment. The pressure in time is based on amount of burned propellant and the burning rate is dependent on pressure. This real process can be solved numerically with Euler's Method [1]. The basic approach (simulation in Pam-Crash and Matlab) verificated by experiment can provide the tool for box design with acceptable accuracy.

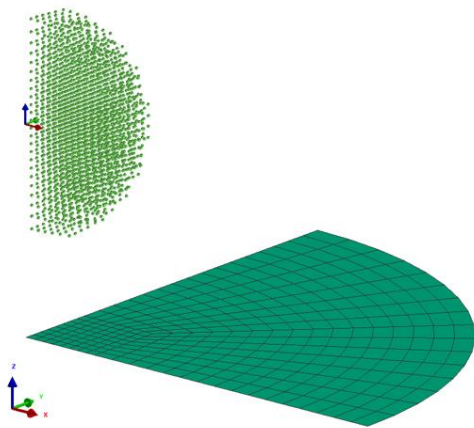


Fig. 1. The SPH simulation of detonation with ball source of TNT



Fig. 2. The comparison of simulation and experiment with flat 200x200 mm 200g of TNT

Acknowledgements

The present contribution was prepared under project POSTDOC supported by University of West Bohemia in Pilsen (Czech Republic).

References

- [1] Johnson, G.R., Cook, W.H., A constitutive model and data for metals subjected to large strains high strain rates and high temperatures, Proceedings 7th International Symposium on Ballistics, The Hague, 1983, pp. 541-547.
- [2] Lee, E., Finger, M., Collins, W., JWL equation of state coefficients for high explosives, Rept-UCID-16189, Lawrence Livermore National Laboratory, 1973.
- [3] Neuberger, A., Peles, S., Rittel, D., Scaling the response of circular plates subjected to large and close-range spherical explosions, Part I: Air-blast loading, In International Journal of Impact Engineering 34 (5) (2007) 859-873.
- [4] Plihal, B., Inner ballistics - collection of examples and tasks, Department of Weapon Systems, Brno, 1991. (in Czech)
- [5] Wilcox, C.L., Stadler, G., Burstedde, C., Ghattas, O., A high-order discontinuous Galerkin method for wave propagation through coupled elastic-acoustic media, Journal of Computational Physics 229 (24) (2010) 9373-9396.

Numerical simulation of the human vocal folds vibration – reconstruction of videokymography records

J. Štorkán^a, T. Vampola^a

^a Department of Mechanics, Biomechanics and Mechatronic, Faculty of mechanical engineering, CTU in Prague, Czech Republic

Voice problems are common especially in professional voice users like teachers, actors, and singers. The main reason may be a fatigue because of mechanical loading of the vocal fold tissue during voice production [5]. Design of a model of the human vocal folds, which would enable to model some pathological situations and voice disorders, is becoming an important part of the voice research. The loading of the vocal fold is caused by combination of the aerodynamic, inertial and impact forces. Excessive stresses during the impact may be responsible for a tissue damage. In this contribution, the reconstructed video-kymographic records [4] from the numerical simulation of the vocal fold vibration are used for evaluation of the character of vibration of the damaged vocal fold.

To estimate vocal fold tissue damage from the changes of its vibration regimes a complex three-dimensional (3D) parametric finite element (FE) model of the larynx and the vocal tract was developed (Fig. 1). The model respects the phonation position of the vocal folds and enables easily to vary their geometrical configuration.

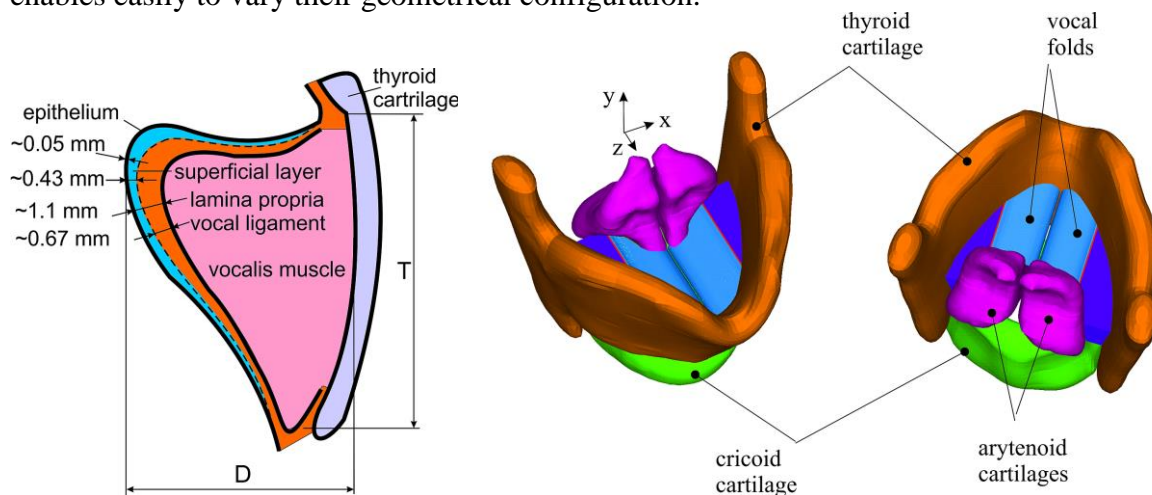


Fig.1. Schema of the vocal fold with three layers and FE model of the human larynx with the vocal folds between the arytenoids and thyroid cartilages

We concentrate here on the study of vibration of the three-layered vocal fold tissue consisted of the epithelium, ligament, and muscle [2]. The material properties of the tissue were modelled by the transversely isotropic elasticity, which is characterized by a plane isotropy at every point of the material [1]. The material nonlinearities caused by pre-stressing the vocal fold tissue in the longitudinal direction are respected as well.

The results of numerical simulation of the vocal folds oscillations excited by a prescribed aerodynamic pressure loading the surface of the tissue of focal fold were computed. The

aerodynamic pressure resulted from the simplified aero-elastic model of the vocal folds self-oscillations [3] was used for the vocal folds excitation.

A very complicated motion of the human vocal folds is evident. The mucous Rayleigh type waves are propagating near the vocal fold surface, especially in the upper part of the vocal fold. The maximum value of the peak to peak displacement in the medial (x) direction and inferior-superior (y) direction is about 1.1 mm. The medial displacement is limited by the vocal fold collisions. The anterior-posterior vibration amplitude in the z -direction is negligible. The maximum vibration amplitudes are on the vocal fold surface, the vibration amplitudes are decreasing in the deeper tissue layers. These deformations can be used for reconstruction of the video-kymograph records of the human vocal fold vibration – see Fig. 2.

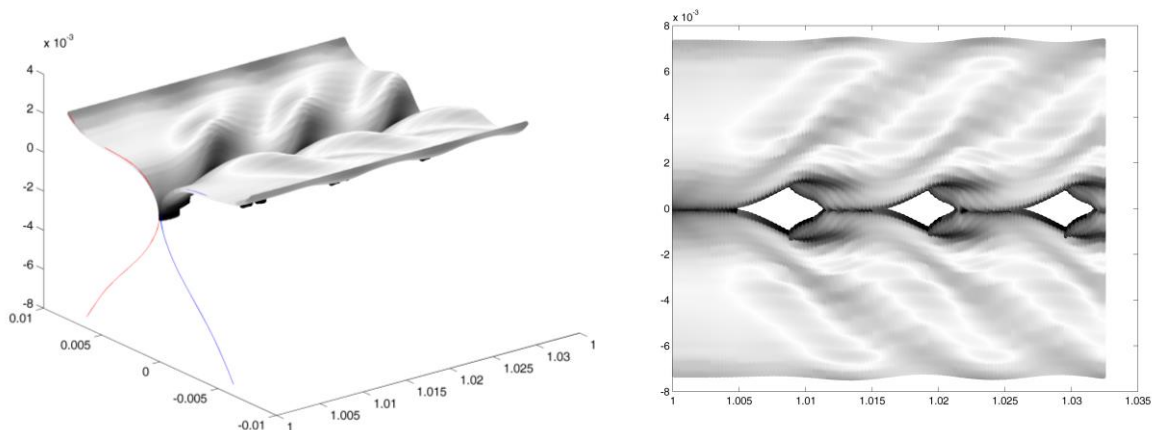


Fig. 2. Videokymographic record reconstructed from the computed dynamic response of the vocal folds

The geometry of the developed parametric FE model of the vocal folds as a part of the complex larynx model enables to modify the model easily and to apply tuning and optimisation procedures for finding proper model parameters related to the vocal folds vibration characteristics. The preliminary results are promising a determination of the injury type of the vocal fold from the character of vibration and to predict approximate stresses in the vocal fold tissue due to the vibration of the vocal folds in normal phonation regimes with collisions. The reconstructed videokymographic records are sensitive enough to the changes of the material parameters and geometric reconfigurations of the vocal fold and can be used for prediction of various vocal fold damages.

Acknowledgement

The research is supported by the Grant Agency of the Czech Republic by project No 16 01246S “Computational and experimental modelling of self-induced vibrations of vocal folds and influence of their impairments on human voice”.

References

- [1] Alipour, F., Berry, D. A., Titze I. R., A finite-element model of vocal fold vibration, *Journal of Acoustical Society of America* 108 (6) (2000) 3003-3012.
- [2] Hirano, M., Phonosurgery, basic and clinical investigations, *Proceedings of the 76th Annular Convention of the Oto-Rhino-Laryngological Society of Japan*, 1975.
- [3] Horáček, J., Laukkanen, A .M., Šidlof, P., Estimation of impact stress using an aeroelastic model of voice production, *Logopedics Phoniatics Vocology* 37 (2007) 185-192.
- [4] Švec, J. G., Schutte, H. K., Videokymography: High-speed line scanning of vocal fold vibration, *Journal of Voice* 10 (1996) 201-205.
- [5] Titze, I. R., Mechanical stress in phonation, *Journal of Voice* 8 (2) (1994) 99-105.

Analysis of processing vibration signal

P. Šulka^a, A. Sapietová^a, M. Sapieta^a

^a Faculty of Mechanical Engineering, University of Žilina in Žilina, Univerzitná 8215/1, 010 26 Žilina

Presented topic relates to the principal mathematical methods in environment of vibration research using calculation software. Analysis of oscillation and treatment vibration signals by start-up (non-stationary mode) of mechanical facility with goal to investigate and find out vibration amplitude, effect of resonance and excitation of self-excited oscillations carried out. In this article, there are introduced the description and the appropriate approach used to process vibration signals. The core of this topic consists of data obtained from real measurements, data processing by computing software, compilation of computational algorithms to acquire results for further analysis and investigation. Measurement, processing and analysis of the mechanical vibrations are principal part of the diagnostic system to monitor operating conditions of machinery in all industrial environments. The purpose of machine diagnostics is to detect the occurrence and cause of vibrations and to eliminate the possibility of their occurrence in order to ensure life expectancy and to maximize reliability of machines in operation and service [3].

The investigated machinery is rolling mill, which consists of reinforced ground, supporting steel structure, electric motor, and gearbox and rolling cartridge.

Fourier transform and its applications along with relying on wavelet transformations of various types are effective methods for processing various signals. Methods provide relevant information and results of the measurement data by applying appropriate mathematical algorithms of these methods using computer software. The results are graphic representations of the vibration signals in the time or frequency domain values with a possible detection of vibrations [2].

Short-time Fourier transform (STFT) is a tool for time-frequency analysis of non-stationary signals. The transformation provides information of the signal $f(t)$ and its spectrum $F(\omega)$ in the time-frequency window. The principle of this method is that, by multiplying the signal $f(t)$ to be analyzed with a certain type of symmetry of a window function (i.e. Window) $\omega * (t - \tau)$ of constant length, and the computation of the Fourier transform of the sections to the signal $f(t)$.

Wavelet transformation consists of unfolding and folding the input signals via the function called wavelet. Wavelet is time-localized wave i.e. wave packet. Wavelet transform has all the features created from a single parent prototype basic wavelet $\psi(t)$ by means of two basic operations scaling and offset in time contour. Wavelet transform of function $f(t) \in L^2(r)$, $R = (-\infty, \infty)$ is defined as representation $L^2(R) \rightarrow L^2(R^2)$ [1]. $L^2(a, b)$ is space, where squares of functions exist, are integral and finite.

By the measurement process of rolling mill 6,228,215 data representing acceleration values was acquired. Sensor sampling rate was set to 25,600 kHz, corresponding to a time step $t=1/f=3.90625e-005$ s. Time dependent values of acceleration and the corresponding values of rotation speed (RPM) for about 243 s. From investigation is clear to detect that the start-up (non-stationary mode) of the machinery is performed at a time interval $< 0.75s >$, increasing the speed from 100 to approximately 1,500 revolutions per minute.

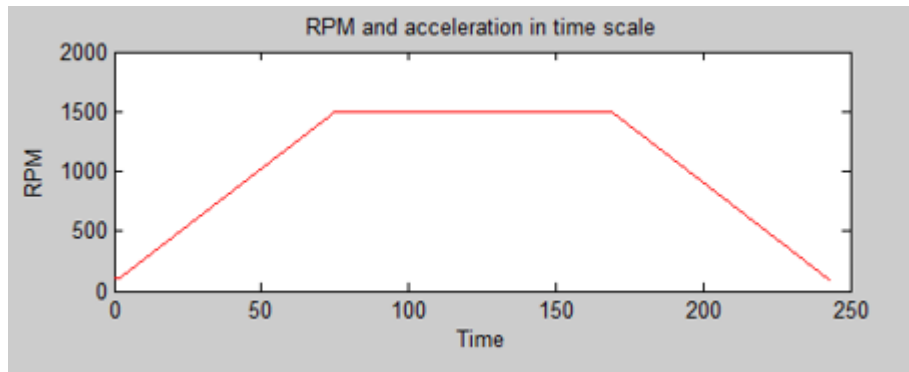


Fig. 1. Graphical contour of RPM investigated machine

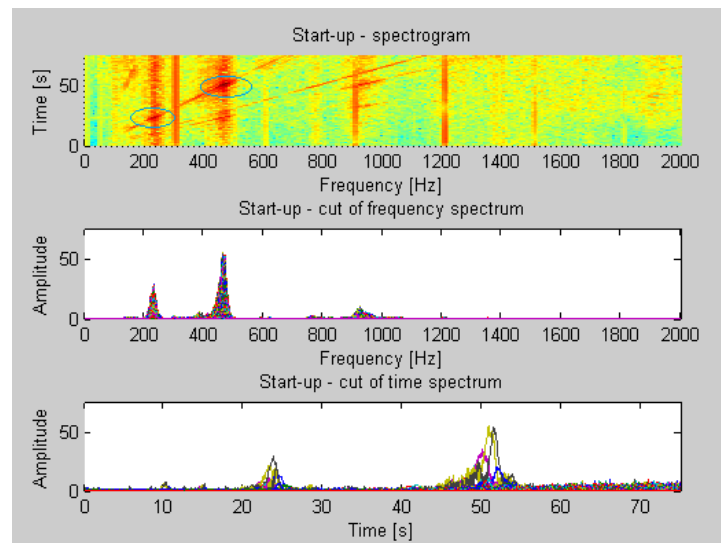


Fig. 2. Detection of resonance and self-exciting frequency by means of STFT

Displayed graphical contours investigated natural frequency and frequency aggregation that show appearance of resonance effect. From Fig. 2, we are able to investigate following parameters and their occurrence at specific frequency, time and RPM.

$$\begin{aligned}
 t = 23 \text{ s} &\rightarrow 230 \text{ Hz} \rightarrow 517.8 \text{ RPM} \rightarrow 9.22 \text{ order} \\
 t = 51 \text{ s} &\rightarrow 470 \text{ Hz} \rightarrow 1031 \text{ Hz} \rightarrow 18.43 \text{ order}
 \end{aligned}$$

Acknowledgements

The work has been supported by the grant project KEGA K-17-013-00.

References

- [1] Handrík, M., Vaško, M., Kopas, P., Mozer, V, The linear and nonlinear stability loss of structures due to thermal load, Proceedings of the 20th International Conference Machine and Simulations, MMS 2015, Terchová, 2016.
- [2] Samajova, H., Ftorek, B., Spanikova, E., Asymptotic character of non-oscillatory of functional differential systems, Electronic Journal of Qualitative Theory of Differential Equations, Szeged, 2015.
- [3] Sága, M., Žmindák, M., Dekýš, V., Sapietová A., Selected methods of analysis and synthesis of mechanical systems, UNIZA – Žilinská Univerzita v Žiline, Žilina, 2009. (in Slovak)

Identification of vibration modes in high frequency of a piezo-device with electromechanical impedance technique

H. A. Tinoco^{a,b}, C. I. Cardona^a, F. M. Peña^a, J. P. Gomez^c, S. I. Roldan-Restrepo^d

^aExperimental and Computational Mechanics Laboratory, Universidad Autónoma de Manizales, edificio Sacatín C.P. 170001, Manizales-Caldas, Colombia.

^bInstitute of Physics of Materials, Academy of Sciences of Czech Republic, Brno, Czech Republic

^cDepartment of Health, Universidad Autónoma de Manizales, Edificio Sacatín C.P. 170001, Manizales-Caldas, Colombia.

^dCentro de Innovación Roldan, Medellín-Antioquia, Colombia

In structural dynamics, vibrations modes associated to natural frequencies are observed to detect changes in mechanical systems, such as stiffness variations, Young modulus and changes in mass. Commonly, the determination of vibration modes are carried out by operational modal analysis which requires a rigorous experimental setup in monitoring conditions. Since two types of measurements are necessary, output/response and input/excitation. Because of this, it is not very useful in structural monitoring applications. This paper reports the development and dynamic characterization in high frequency (1-5kHz, 10-20kHz) of a piezo-device (vibratory system) which can be used for the structural monitoring purposes applying electromechanical impedance technique. Electromechanical impedance method was used in order to identify the vibration modes in the piezo-device which were compared with traditional kinematic (velocity) measurements in frequency. This is possible due to electromechanical coupling of piezoelectric transducers with its host structure, since mechanical resonances can be visible in the electric impedance spectrum of these transducers. However, it is necessary to identify mechanical resonances in the electrical spectrum to monitor it with the electrical impedance. Experimental results show that some resonances in the electrical spectrum correspond to mechanical vibration modes in the velocity spectrum which in turn were verified by finite element analysis.

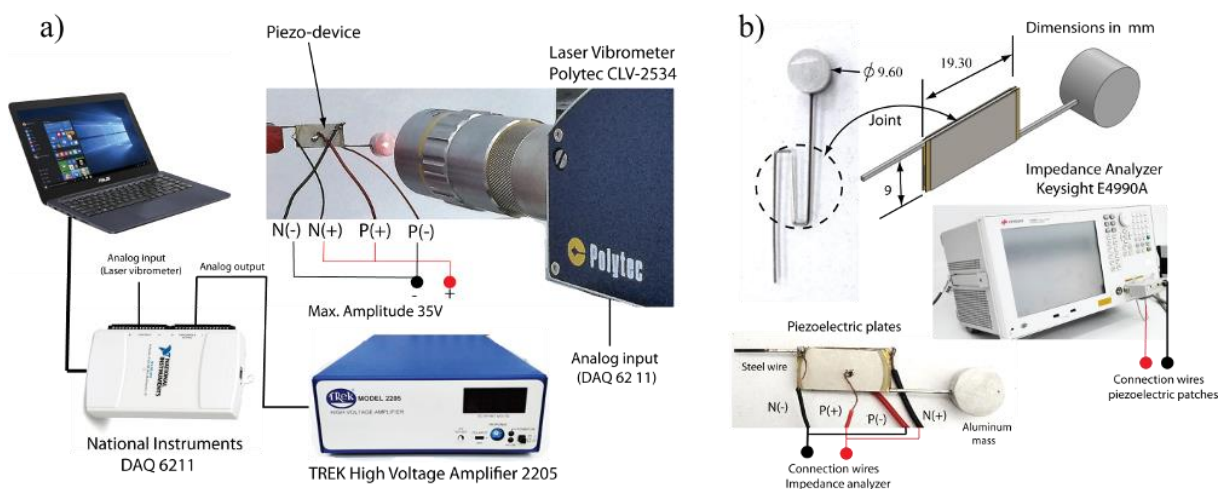


Fig. 1. a) First experimental setup; b) Second experimental setup, piezo-device and dimensions

A schematic drawing of the first experimental setup is shown in Fig. 1a, which consists of a piezo-device, a laser vibrometer (CLV 2534 POLYTEC), a high voltage amplifier (TREK 2205) and a data acquisition system (NI 6211). The piezoelectric patches are used as actuators to excite the piezo-device in bandwidths 1-5kHz and 10-20kHz. The laser vibrometer captures (frequency sample 100kHz) motions in the central point of the mass to estimate the velocity spectrum. A second experimental setup was carried out to measure the electrical impedance (Impedance Analyzer KEYSIGHT E4990A) in the piezoelectric patch with the aim to compute the electrical resistance. The electromechanical impedance technique is very sensitive in high frequencies due to the electromechanical coupling of the piezo-transducers [1].

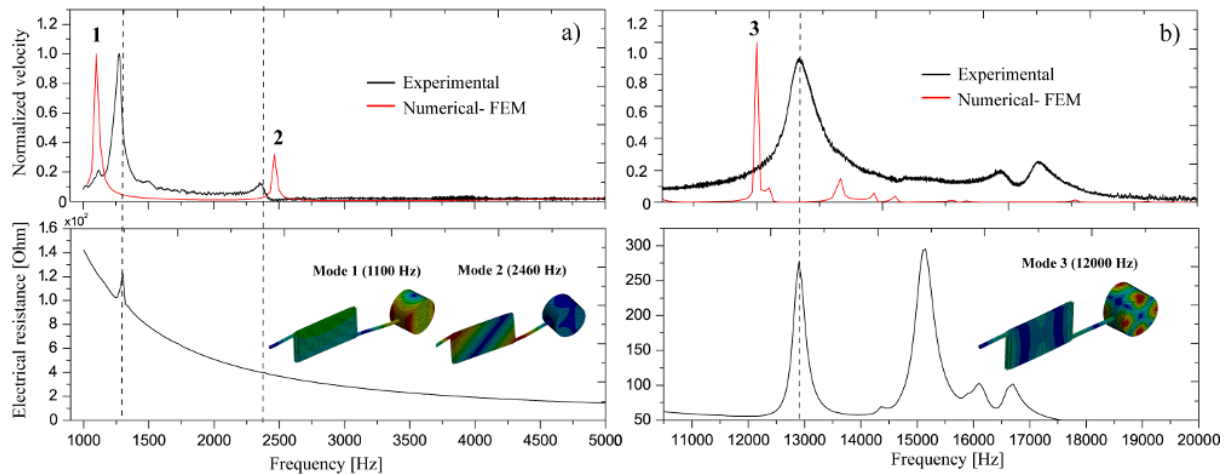


Fig. 2. Comparisons between normalized velocity and electrical resistance. a) 1-5 kHz b) 10-20kHz

In this study a frequency analysis is performed with three methods (two experimental and one numerical), which are applied and compared to identify vibration modes with the electrical impedance obtained from piezo-device. Velocity measurements in the central point of the mass (see Fig. 1a), velocity values computed by finite element analysis and electrical resistance were determined and compared as shown in Fig.2. For the analysis, two frequency windows were explored, 1-5kHz (Fig. 2a) and 10-20kHz (Fig. 2b). In the studied spectra, it was analysed that two peaks of frequency correspond with peaks determined in the electrical spectrum, which are related with vibration modes identified by means of a harmonic finite element analysis. For monitoring purposes, the values of these peaks can be evaluated through electrical impedance of the piezo-device since it is well known in structural health monitoring field that changes in resonances are associated with structural changes, such as variations in the mechanical properties.

Acknowledgements

Authors want to thank for the financial support, since this work was supported by grant from Departamento Administrativo de Ciencia Tecnología e Innovación (COLCIENCIAS) (Grant code 121974455599) legalized contract 739-2016 and obtained in the announcement 744, year 2016. Furthermore, acknowledgments to Universidad Autónoma de Manizales (UAM) and Centro de Innovación Roldan (CIR) for additional financial and technical support.

References

- [1] Annamdas, V.G.M., Soh, C.K., Application of electromechanical impedance technique for engineering structures: review and future issues, *Journal of Intelligent material systems and structures* 21 (1) (2010) 41-59.

FEM model of pneumatic spring supported by a steel plate

T. Tran Xuan^a, D. Cirkl^a

^aDepartment of Applied Mechanics, Faculty of Mechanical Engineering, Technical University of Liberec, Liberec, Czech Republic

This paper focuses on FEM simulation model of pneumatic spring supported by a steel plate. This substructure is implemented in to the cushioning of a car seat and in combination with electronic feedback control of internal pressure provides the capability to adjust pressure distribution in contact zone between the seat and the passenger. The system is designed in compliance with patent [1]. This spring is made up from latex and foam parts and from the tape. The mechanical properties of individual parts of pneumatic spring were experimentally investigated. After that suitable material models were selected in MSC.Marc software and identified by a fitting procedure based on experimental data as it was published in [4]. In real arrangement the pneumatic spring is supported by steel plate in accordance with Fig. 1. When the pneumatic spring is supplied with compressed air the latex tube stretches and bulge at both free ends and comes in to contact with sloped parts of steel plate. The simulation model of this case was created in FEM software MSC.Marc. For this purpose the friction coefficient between latex material of the spring and steel was experimentally investigated.

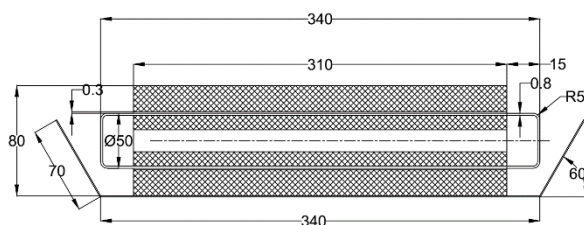


Fig. 1. Scheme of pneumatic spring

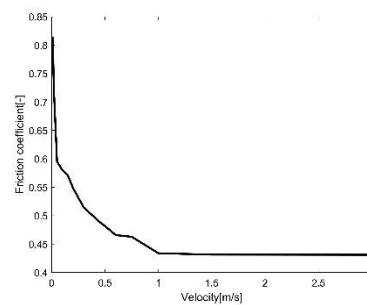
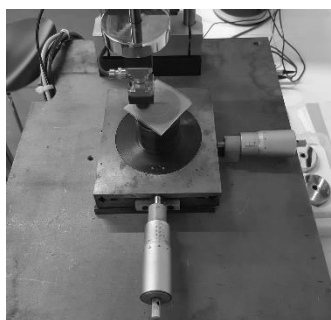
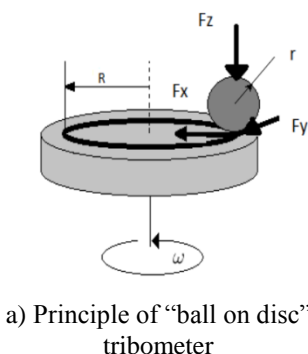


Fig. 2. Determination of friction coefficient between steel and latex

According to [3] this experiment was carried out by means of tribometer machine based on "ball on disc" principle as it is showed in Fig. 2a) and Fig. 2b). The experiment was performed with a load $m = 0.5$ kg and such combinations of the angular velocity of the disk ω and the radius R which ensures the range of tangential velocity from 0.01 m/s to 3 m/s. The

radius of steel ball was $r = 3$ mm. Measured values of friction coefficient are presented in Fig. 2c) and show obvious dependency on velocity up to 1 m/s. For higher velocity the friction coefficient keeps approximately constant value 0.43. For the purpose of this simulation the deformation speed of latex membrane is considered very low so chosen value of friction coefficient between the latex tube and steel plate is 0.8.

The feature of real system is to keep constant pressure value inside pneumatic spring by means of feedback control as it is described in more detail in [2]. Therefore the simulations were carried out for cases of internal pressure set to constant value 5 kPa, 10 kPa, 15 kPa and 20 kPa respectively. In every case also loading by external force is considered. This is performed by indenter acting on the spring assembly vertically from the top from zero up to maximum deformation 20 mm. The indenter is located in the middle position with respect to longitudinal direction of the spring. Course of displacement in dependence on time has triangular shape with rate of deformation 2 mm/s. One simulation case consists of loading and unloading phase.

As a result of simulation in Fig. 3a) there is presented deformed shape of pneumatic spring for one of the load cases. The course of loading force for every individual simulation case was obtained (Fig. 3b). In future it is necessary to focus on damping description and verify this model experimentally. The course of force obtained from simulation will be compared with experimental results from qualitative and quantitative point of view.

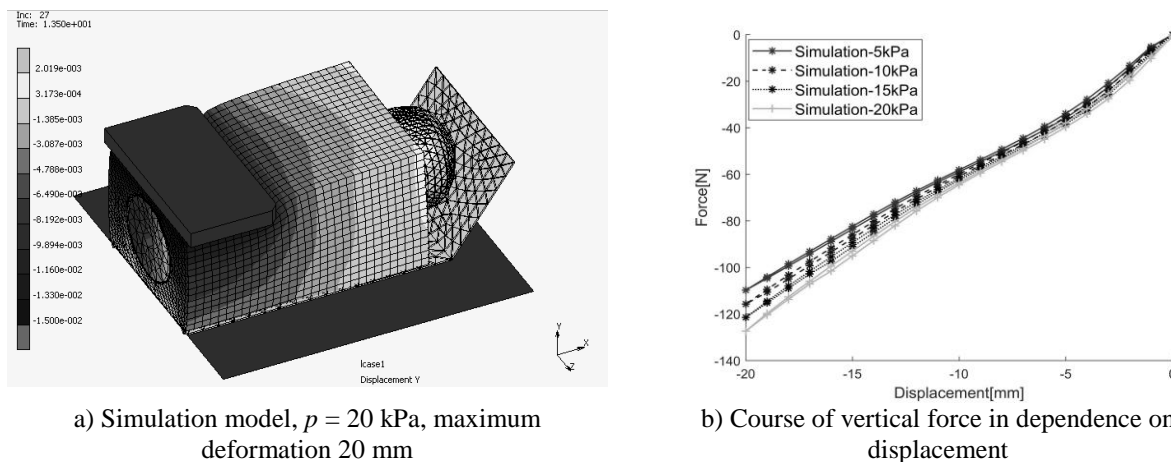


Fig. 3. Simulation of loading of pneumatic spring assembly

Acknowledgements

This article was written at the Technical University of Liberec, Faculty of Mechanical Engineering with the support of the Institutional Endowment for the Long Term Conceptual Development of Research Institutes, as provided by the Ministry of Education, Youth and Sports of the Czech Republic in the year 2017.

References

- [1] Cirkl, D., Seat, Patent No. 303163, 2012.
- [2] Cirkl, D., Tran Xuan, T., Simulation model of seat with implemented pneumatic spring, *Vibroengineering PROCEDIA* 7 (2016) 154-159.
- [3] Mázik, L., Research on tribological behaviour of rubber in dependency on its viscoelastic properties, Diploma thesis, Technical University of Liberec, Liberec 2010, pp. 32-41.
- [4] Tran Xuan, T., Cirkl, D., FEM model of pneumatic spring assembly, *Vibroengineering PROCEDIA* 13 (2017) 199-204.

Quasi-static model of ionic transport through deformable porous media

J. Turjanicová^a, E. Rohan^a, V. Lukeš^a

^a*NTIS - New Technologies for the Information Society, Faculty of Applied Mechanics, University of West Bohemia, Univerzitní 8, 306 14 Plzeň, Czech Republic*

The ionic transport in the charged porous media is widely studied problem, often in context of geoscience, the research of fuel cells or modeling of biological tissues. The latest serves as motivation to this paper, especially in the context of modeling cortical bone porous tissue. On the macroscopic scale, the cortical bone consists of the solid bone tissue perforated by network of small interconnected channels saturated by bone fluid. The physical properties of both phases in context to the ionic transport modeling are discussed below.

As usual, the fluid phase is assumed to be an electrolyte solution of two ionic species (further indexed by $i = 1, 2$) with different valencies $z_1 = -1, z_2 = 1$. By assuming solid-phase of porous medium to be deformable, it is possible to connect ionic transport not only with electrochemical phenomena, occurring due to the electric double layer formed by interaction between charged solid-fluid interface and ionized solution, but also with mechanical behavior.

The porous body occupy domain Ω with characteristic length L_c and consist of fluid phase Ω_f and solid phase Ω_s . On solid fluid interface $\Gamma = \Omega \setminus \Omega_f$, there manifests a small surface charge Σ , leading to formation of so-called electrical double layer (EDL) in the fluid. The thickness of EDL is given by Debye length parameter λ_D .

Porous body is considered to be deformable, with usual assumptions of linear elasticity, small displacement \mathbf{u} and small deformation. As the pores are saturated by electrolyte solution, the continuity of stresses in both the phases on solid-fluid interface has to be ensured. Also, considering the extension of the displacement into the fluid phase, the deformation velocity is equal to hydrodynamic velocity \mathbf{v} on the interface.

The ionic transport can be characterized by ionic species distribution in the fluid, i.e. their concentration c_i , which is governed by Eulerian mass conservation law for each species, while assuming zero ionic exchanges between the phases. Three processes influencing ionic transport are distinguished. The first is the convective movement of the solvent which is usually described by convective velocity \mathbf{w} . Let us note that in the rigid porous medium the convective velocity is equal to the hydrodynamic velocity \mathbf{v} but in the deformable porous medium applies $\mathbf{w} = \mathbf{v} - \partial_t \mathbf{u}$. The second is diffusion of the i -th ionic species in the solvent. And finally, the third is the effect on the movement of electrically charged particles in the electrical field.

As the ions can be view as small point charge, the distribution of electrical potential Ψ occurring due to EDL also influence their movement. Potential distribution is given by Poisson-Boltzmann electrokinetic equation, respecting surface charge Σ on its boundary.

To complete the system of equation describing the model, the Stokes equation modified by adding electrical driving force and compressibility condition are used to find hydrodynamic velocity \mathbf{v} and pressure p . Such model can be found through the literature, for example in [1, 2].

The system of dimensional nonlinear equations describing ionic transport is transformed into its dimensionless form by the suitable choice of space and time scaling. Following [3], it can be linearized by assuming, that its solution is only slightly perturbed from equilibrium. Also, so-called ionic potentials Ψ_i and global pressure P are introduced.

Considering porous body with periodic microstructure represented by the unit cell Y with similar decomposition as domain Ω , the problem can be treated by means of unfolding homogenization methods. This method use the known properties of so-called unfolding operator to ensure convergences of the derived homogenized model.

The homogenization procedure result into finding the effective tensors. The tensors relevant to the ionic transport are tensor of permeability \mathbf{K} , migration-diffusion tensors \mathbf{J}_i , Onsager tensors \mathbf{L}_i , diffusivity tensors \mathbf{D}_{ij} and two new tensors \mathbf{U} and \mathbf{M} which ensure the stronger coupling between electrokinetic system and elasticity. Further, it gives tensors related to the modified Biot's poroelasticity as elasticity tensor \mathbb{A}^H , Biot's tensor \mathbf{B}^H , and ionic potential tensor \mathbf{C}^H . Then, the dimensionless macroscopic homogenized system of equations, where all external forces are omitted, reads

$$\int_{\Omega} \mathbf{K} \nabla_x P^0 \nabla_x q \, dV - \sum_{j=1}^{N=2} \int_{\Omega} \mathbf{J}_j \nabla_x \Phi^0 \nabla_x q \, dV + \int_{\Omega} \mathbf{U} \delta \mathbf{u}^0 \nabla_x q \, dV = 0, \quad (1)$$

$$\frac{|Y_f|}{|Y|} \int_{\Omega} \frac{\partial c_i^{\text{eq}}}{\partial t} + \int_{\Omega} \mathbf{L}_i \nabla_x P^0 \nabla_x s \, dV - \sum_{j=1}^{N=2} \int_{\Omega} \mathbf{D}_{ij} \nabla_x \Phi^0 \nabla_x s \, dV + \int_{\Omega} \mathbf{M}_i \delta \mathbf{u}^0 \nabla_x s \, dV = 0, \quad (2)$$

$$\int_{\Omega} \mathbb{A}^H e_x(\delta \mathbf{u}^0) : e_x(\mathbf{r}) \, dV + \int_{\Omega} \hat{\mathbf{B}}^H P^0 : e_x(\mathbf{r}) \, dV - \sum_{j=1}^{N=2} \int_{\Omega} \mathbf{C}_j^H \Phi^0 : e_x(\mathbf{r}) \, dV = 0 \quad (3)$$

for any test functions $q \in L^2(\Omega)$, $s \in L^2(\Omega)$ and $\mathbf{r} \in H^1(\Omega)^d$ and where $\hat{\mathbf{B}}^H = |Y_f| \mathbf{I} - \mathbf{B}^H$.

The numerical implementation of the homogenization procedure and the homogenized model completed by suitable choice of initial and boundary conditions was made in python based FEM software *SfePy*. It can be shown, that changes in the microstructure or in the model parameters (for example change of ration between pore size l and thickness of EDL represented by λ_D) influences the resulting effective coefficients. The implemented model can be used not only for studying processes in the cortical bone, but also for wide range of other applications due to derivation of equations in general dimensionless form.

Acknowledgements

The research was supported in part by project LO1506 of the Czech Ministry of Education, Youth and Sports. Jana Turjanicová is grateful for the support by project SGS-2016-059.

References

- [1] Allaire, G., Bernard, O., Dufrêche, J.-F., Mikelić, A., Ion transport through deformable porous media: derivation of the macroscopic equations using upscaling, *Computational and Applied Mathematics* 36 (3) (2017) 1431–1462.
- [2] Allaire, G., Brizzi, R., Dufrêche, J.-F., Mikelić, A., Piatnitski, A., Ion transport in porous media: derivation of the macroscopic equations using upscaling and properties of the effective coefficients, *Computational Geosciences* 17 (3) (2013) 479–495.
- [3] O'Brien, R. W., White, L. R., Electrophoretic mobility of a spherical colloidal particle, *Journal of the Chemical Society, Faraday Transactions 2: Molecular and Chemical Physics* 74 (1978) 1607–1626.

Reduced order model of laminar Kármán vortex street

O. Urban^a, P. Rudolf^a

^a V. Kaplan Department of Fluid Engineering, Faculty of Mechanical Engineering, Brno University of Technology, Technická 2896/2, 616 69 Brno, Czech Republic

Continuous emphasis on improvement of performance in aviation, automotive transport, turbomachinery and other fields related to fluid mechanics will only be possible with incorporation of active flow control. In fact first steps have already been done, but vast expansion into real commercial applications is still expected. Active flow control strategies can be divided into two categories based on how the control law is determined. Model-based control relies on some mathematical model, which relates inputs to outputs. The development of these strategies has been driven by continuous performance improvement of computational resources, although it is still far from accurate real-time computations as direct numerical simulations of the governing equations require fine spatial and temporal discretization. This drawback led to the development of model-free control strategies, e.g. machine learning, which has become increasingly popular. However, in suitable cases, it is possible to reduce the full, so-called white-box, description of the dynamics into much simpler, so-called gray-box, model describing only the most important part of the flow in some defined sense [4]. These reduced order models are the crucial enabler for model-based flow control.

A very popular technique of model reduction is based on a decomposition of the flow into a sum of modes. The number of modes is usually very high, as it is equal to the degrees of freedom of the system. The goal is to design this decomposition so that the flow can be reconstructed as accurately as possible using as few modes as possible. If the quantity of interest is kinetic energy, proper orthogonal decomposition (POD) gives the optimal solution [1]. The governing equation is then projected onto the most dominant POD modes, which yields a system of ordinary differential equations describing the mode dynamics. Present paper illustrates the development of such reduced order model. A canonical test case is selected, namely Karman vortex street in laminar flow regime.

Model development: The spatial domain characteristics were chosen the same as in experiment by Lyn [2]. It consists of a square in a rectangular area. The inflow velocity was selected so that the Reynolds number equals to 200. On the outflow the constant pressure condition is prescribed. A numerical simulation of this setup was carried out, from which a data set covering one vortex shedding period was obtained. These data were decomposed into ensemble average and fluctuation. The proper orthogonal decomposition of fluctuation velocity field revealed that more than 95 % of fluctuation kinetic energy is contained only in the first two modes and six modes is enough to recover more than 99 % of the overall kinetic energy budget.

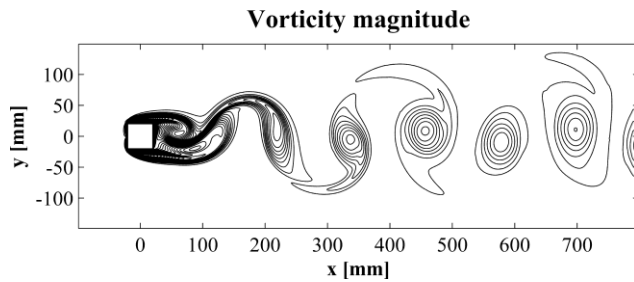


Fig. 1. Snapshot of vorticity magnitude isocontours

reduced order model gives accurate results for the initial short time period. As it can be seen from the detail, the more modes were retained, the better are the results. However, it is well

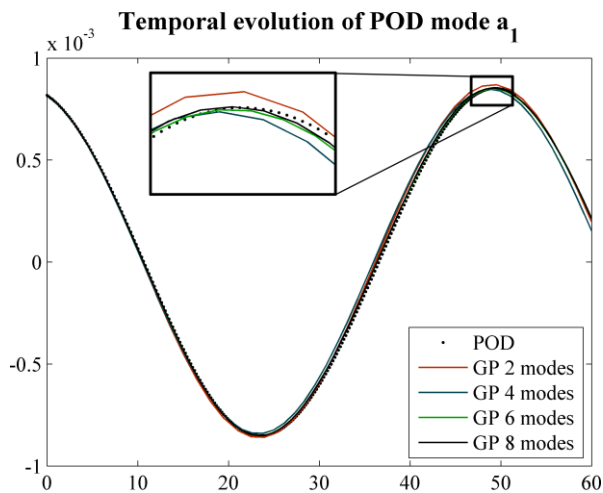


Fig. 2. Time evolution of the most dominant POD mode compared to the ROM solution

known, that POD Galerkin models suffer from structural instability, which can result in a rapid transition to an incorrect attractor or the solution can even blow up to infinity [3]. Another disadvantage of these models is narrow range of validity. It is given by the retained POD modes – the condition is that the flow has to be reconstructible by those modes. This is obviously valid for the training state, i.e. $Re = 200$ by means of the Reynolds number, but as the deviation grows, the vortex street shape is more and more different and so the solution error grows as well.

Acknowledgement

This work has been supported by the Czech Science Foundation project GA17-01088S “3D instability of a shear layer in adverse pressure gradient”.

References

- [1] Lumley, J.L., Atmospheric turbulence and radio wave propagation, Moscow: Nauka, Moscow, 1967.
- [2] Lyn, D, Rodi, W., The flapping shear layer formed by flow separation from the forward corner of a square cylinder, *Journal of Fluid Mechanics* 267 (1994) 353-376.
- [3] Noack, B.R., Afanasiev, K., Morzyński, M., Tadmor, G., Thiele, F., A hierarchy of low-dimensional models for the transient and post-transient cylinder wake, *Journal of Fluid Mechanics* 497 (2003) 335-363.
- [4] Wiener, N., Cybernetics or control and communication in the animal and the machine, MIT Press, Boston, 1948.

The reduced order model was obtained by means of Galerkin projection of Navier-Stokes equation onto selected number of spatial POD modes, which yields a system of ordinary differential equations in time. The initial condition was chosen to be the same as the initial values of temporal POD modes. This means that the solution of the differential equations should be the same as these modes. Fig.2 reveals that the reduced order model gives accurate results for the initial short time period. As it can be seen from the detail, the more modes were retained, the better are the results. However, it is well known, that POD Galerkin models suffer from structural instability, which can result in a rapid transition to an incorrect attractor or the solution can even blow up to infinity [3]. Another disadvantage of these models is narrow range of validity. It is given by the retained POD modes – the condition is that the flow has to be reconstructible by those modes. This is obviously valid for the training state, i.e. $Re = 200$ by means of the Reynolds number, but as the deviation grows, the vortex street shape is more and more different and so the solution error grows as well.

It was shown that the complicated fluid flow dynamics can be reducible to a small number of modes, which gives an opportunity to develop computationally tractable reduced

H-inf control of additional piezo-actuated platform of cable mechanism

J. Volech ^a, Z. Šika ^a, K. Kraus ^a, P. Beneš ^a

^a Faculty of Mechanical Engineering, Czech Technical University in Prague, Technická 4, 166 07 Prague 6, Czech Republic

The goal of the paper is to enhance the accuracy of the position of cable driven platform Fig. 1.

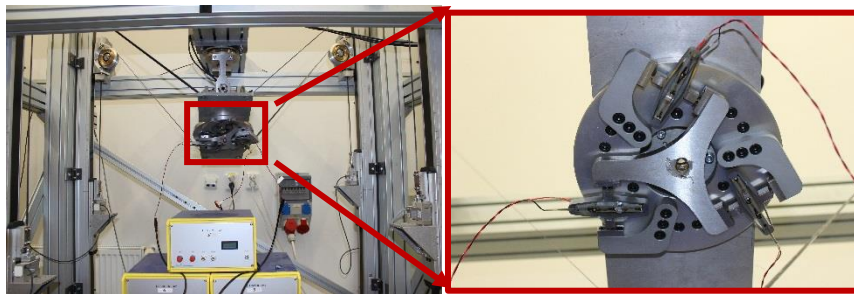


Fig. 1. Cable driven platform with piezo platform

This platform has problems in higher motion frequencies. Therefore the solution of this problem is proposed as the added platform driven by the piezoelectric elements (APA- Amplified piezoelectric Actuator), which operates on high frequencies. Firstly the mathematical model of the planar piezoelectric platform [3] with three degrees of freedom is assembled (Fig. 1) in order to develop and test the designed control theory. This model is developed based on real data from the constructed platform and is modeled with full dynamical properties. Then is tested that has the same frequency range as real platform. The coefficient of the APA is basically imported from datasheet of the manufacturer. But the damping had to be computed from experimental data measurement Fig. 2.

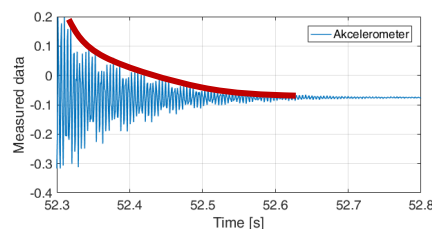


Fig. 2. Experimental measurement of the damping coefficient

The damping was calculated using logarithmic decrement with n representing the number of cycles and T represents the period of oscillation

$$\delta = \frac{1}{n} \log\left(\frac{x(t)}{x(t+nT)}\right), \zeta = \frac{1}{\sqrt{1+(2\pi/\delta)^2}}$$

Using this, the nondimensional damping coefficient was calculated as $\zeta = 0.6610$.

When the model was developed the 4th order controller K was proposed using H_{inf} [1], [2] (Fig. 3) theory with the three outputs U_{1-3} =Desired voltages to each APA separately and 6 inputs Y .

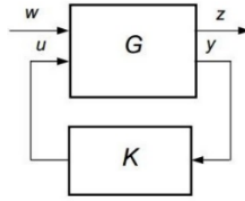


Fig. 3. HIFOO

The reference signal W in the augmented plant P as the three desired coordinates of the center of the platform and the disturbance output Z from augmented plant P as the deviation of the system from reference signal. The optimization function is then the transfer function $G=G_{wz}$ in the form of

$$\|G\|_{\infty} = \max_{\omega} \sigma_{max}(G(\omega)).$$

Due to the technical difficulties with the measurement hardware, the controller is proposed separately from the controller of the cable driven platform. Firstly was tested, that the motion of the piezo platform has negligible influence on the motion of the cable platform due to its significantly lower mass. Therefore it is possible to continue with this control theory. Then the first three inputs of Y are position of the cable driven platform acquired from three incremental sensors that measure the cable platform rotation. And three signals of Y from Laser Tracker, which measure the absolute position of the piezo platform in his coordinate system.

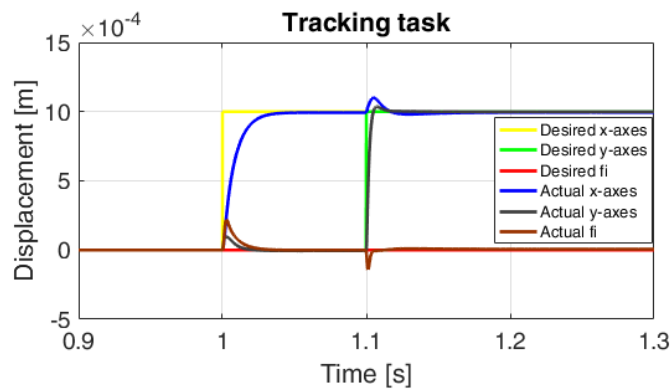


Fig. 4. Tracking task

The tested trajectory is the step signal in the x-axes and then in y-axes. The results shown Fig. 4, that the controller works fine and have potential, but still need some tuning. In the corners the overshoot of desired trajectory is undesirable and the slow reaction in step signal in x-axes is also. This can be neglected by further tuning of the designed filter on the transfer function G . Now the experimental results will be furthermore tuned and tested on the real experimental stand.

Acknowledgements

The authors appreciate the kind support by the grant SGS16/208/OHK2/3T/12 Mechatronics and adaptronics 2016 of CTU in Prague and the grant GA15-20134S „Multi-Level Light Mechanisms with Active Structures” of the Czech Science Foundation.

References

- [1] Aryelier, D., Deaconu, G., Gumussoz, S., Henrion, D., H2 for HIFOO, Proceedings of International Conference on Control and Optimization with Industrial Applications, Ankara, Turkey, 2011.
- [2] Gumussoy, S., Henrion, D., Millstone, M., Overton, M.L., Multiobjective Robust Control with HIFOO 2.0, Proceedings of the IFAC Symposium on Robust Control Design, Haifa, 2009.
- [3] Valášek, M., Design and Control of Under-Actuated and Over-actuated Mechatronical Systems - Challenges of Mechanics and Mechatronics, Vehicle System Dynamics 37 (40) (2004) 37-50.

Influence of initial imperfections of changing amplitude on the laterally loaded cylindrical shell

O. Voltr^a, P. Jilek^a

^a Faculty of Transport Engineering, University of Pardubice, Studentská 95, 532 10 Pardubice, Czech Republic

The assessed structure is considered as a part of the simplified case of cylindrical shell (part of road tank) located on two saddle supports. The initial imperfections of the shape can lower carrying capacity of the structure. In this case shape imperfections are created by pushing the saddle support into the shell. So the new deformed shape of the shell is used as an imperfect shell in the following nonlinear analysis. Current part of the research is devoted to the influence of initial imperfections of changing amplitude Δw on the carrying capacity of the laterally loaded cylindrical shell. The influence of initial imperfections on the carrying capacity of the shell is expressed by so called reduction factor α .

Numerical model (Fig. 1) is represented by the thin-walled cylindrical shell with firmly connected stiff punch in shape of saddle support in the middle span of the shell [2]. Parameters shown below (Fig. 2) are almost same as in previous work [2]. Only one different parameter is amplitude of depth of initial imperfection Δw . Amplitude Δw is no longer considered as constant, but with regard to shell thickness as dimensionless parameter $\Delta w/t$.

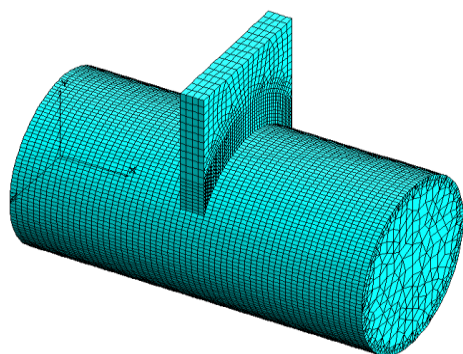


Fig. 1. Initial undeformed model
 ($2\theta=120^\circ$)

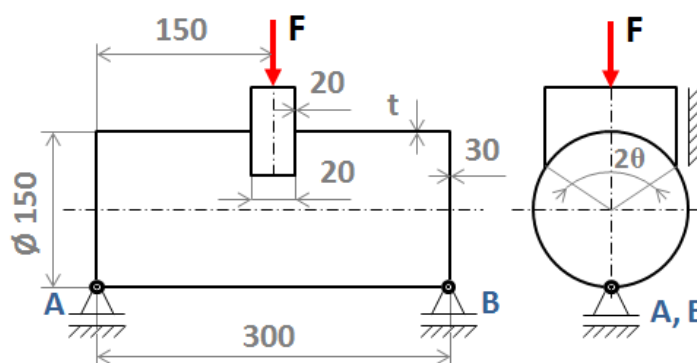


Fig. 2. Geometric parameters of the computational model

The most important parameters of the numerical model:

- embracing angle of the saddle support 2θ (60° , 90° and 120°),
- dimensionless thickness parameter R/t , varies in range of ratio $R/t \in \langle 68; 250 \rangle$,
- dimensionless parameter of depth amplitude of initial imperfection $\Delta w/t$, varies in ratios 0,1; 0,5; 1,0; 1,5; 2,0; 3,0.

Numerical analyses are carried out by means of a computer program COSMOS/M [1] based on the finite element method (FEM). Dependence of reduction factor α and parameter $\Delta w/t$ (Fig. 3) shows nine curves of R/t parameter. Throughout whole range of parameter R/t are all curves very close to each other. Maximum difference makes approximately 6%.

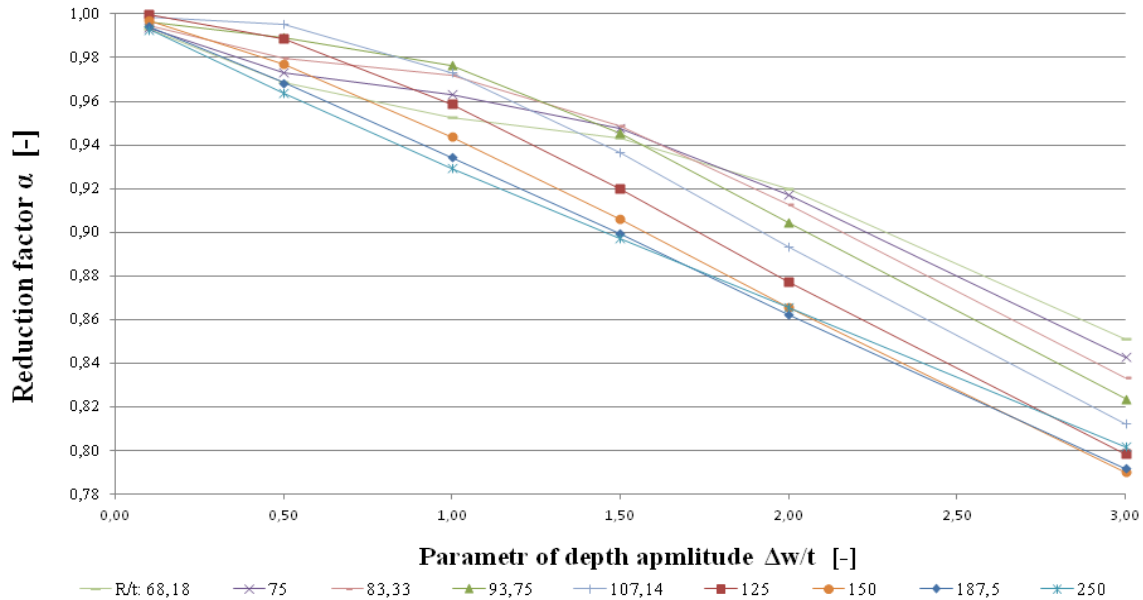


Fig. 3. Results for models with embracing angle $2\theta=120^\circ$

Also can be said that results of numerical analyses for another two embracing angles ($2\theta=90^\circ$ and $2\theta=60^\circ$) are rather similar and reached values of reduction factor α differs only slightly, too. Influence of depth amplitude of initial imperfection on the carrying capacity of the assessed shell seems lower than was expected.

The main objective of the analysis is to find the reduction factor α depending on the change of geometric parameters of the numerical model (embracing angle of saddle support 2θ , wall thickness of the shell t) and on the change of amplitude of initial imperfections (with regard to shell thickness $\Delta w/t$).

Acknowledgements

This work was supported by the University of Pardubice within the project No. SGS_2017_009.

References

- [1] FEM Computer program COSMOS/M, version 2.95, 2010.
- [2] Voltr, O., Paščenko, P., Initial imperfections of horizontal cylindrical shells on saddle supports, Proceedings of the 30th International Colloquium on Advanced Manufacturing and Repair Technologies in Vehicle Industry, Visegrád, Hungary, 2013, pp. 77-82.

Interaction of incompressible fluid flow and a vibrating airfoil

O. Winter, P. Sváček

Department of Technical Mathematics, Faculty of Mechanical Engineering, Czech Technical University, Czech Republic

In this contribution we focus on numerical simulations of aeroelastic problem of two dimensional viscous incompressible air flow. The airfoil motion is modelled by equations of motion for two degrees of freedom. The airfoil which can rotate around the elastic axis and oscillate in vertical direction is considered similarly as in [2]. The mathematical model is represented by the system of the incompressible Navier-Stokes equations and the system of ordinary differential equations. The problem is then numerically approximated by the finite volume method. The OpenFOAM, which is modified in order to solve the coupled model, is used to obtain numerical solutions.

Let us denote the computational domain $\Omega_t \subset \mathbb{R}^2$ occupied by the fluid at time instant $t \in \langle 0, T \rangle$. We assume that Ω_t is a polygonal domain for any t with the boundary $\partial\Omega_t = \Gamma_I \cup \Gamma_O \cup \Gamma_{W_t}$, where Γ_I is the inlet part of the boundary $\partial\Omega_t$, Γ_O is the outlet part of the boundary $\partial\Omega_t$ and Γ_{W_t} is the moving surface of the airfoil. In order to treat the motion of the domain Ω_t , the Arbitrary-Lagrangian-Eulerian (ALE) method is used. The incompressible fluid flow in Ω_t is described by the system of the incompressible Navier-Stokes equations in the ALE conservative form, i.e.,

$$\begin{aligned} \frac{1}{J} \frac{D^A(J\mathbf{u})}{Dt} + \nabla \cdot [\mathbf{u} \otimes (\mathbf{u} - \mathbf{w})] &= -\nabla p + \nu \Delta \mathbf{u}, \\ \nabla \cdot \mathbf{u} &= 0, \end{aligned} \quad (1)$$

where the symbol \mathbf{u} denotes the fluid flow velocity, by the symbol p is denoted the kinematic pressure, by the symbol ν is denoted the kinematic viscosity of the fluid, \mathbf{w} is the ALE domain velocity, the symbol $D^A f/Dt$ denotes the ALE derivative and J is the Jacobian of the ALE mapping, for details on ALE method, see e.g. [2], [3]. The system (1) is equipped with the boundary conditions:

$$(a) \quad \mathbf{u} = \mathbf{u}_\infty \quad \text{on } \Gamma_I, \quad (b) \quad \mathbf{u} = \mathbf{w} \quad \text{on } \Gamma_{W_t}, \quad (c) \quad p = 0 \quad \text{on } \Gamma_O, \quad (2)$$

where \mathbf{u}_∞ is the free-stream velocity, \mathbf{w} denotes the velocity of the boundary Γ_{W_t} . The equations of motion for a flexibly supported body with two degrees of freedom, see [2], reads

$$\begin{aligned} m\ddot{h} + S_\alpha \cos \alpha \ddot{\alpha} + k_h h &= -L(t), \\ S_\alpha \cos \alpha \ddot{h} + I_\alpha \ddot{\alpha} + k_\alpha \alpha &= M(t). \end{aligned} \quad (3)$$

The following notation is used: $L(t)$ (downward positive) and $M(t)$ (clockwise positive) denote the aerodynamical lift force and the torsional moment, respectively. The symbol m denotes the mass of the airfoil, I_α and S_α denote the inertia and the static moments of the airfoil around the elastic axis EA, respectively, k_h and k_α are the stiffness coefficients of the bending

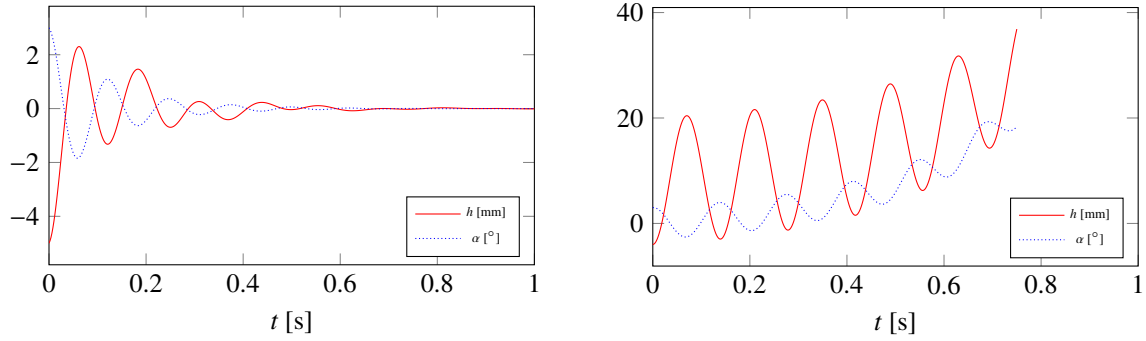


Fig. 1. Flow induced airfoil vibrations $U_\infty = 20$ m/s (left) and $U_\infty = 40$ m/s (right)

and the torsional springs, respectively, α denotes the rotational displacement around the elastic axis EA (clockwise positive) and h denotes the vertical displacement of the elastic axis EA (downward positive). The system (3) is equipped with initial conditions prescribing the values $h(0)$, $\alpha(0)$, $\dot{h}(0)$, $\dot{\alpha}(0)$.

The system of equations (1) is solved by the merged PISO-SIMPLE algorithm for the incompressible fluid flow implemented in OpenFOAM. The convective term is discretized by the upwind method with the second degree reconstruction, the viscous term by the central scheme and the ALE time derivative is discretized by the second order backward difference formula. The structure model is solved with the aid of the classical 4rd order Runge-Kutta method. The coupling of the fluid-structure problem is realized by a loosely coupled algorithm.

The numerical method for the simulation of the interaction of viscous incompressible fluid flow and a vibrating airfoil was realized within open-source code OpenFOAM. The model coefficients were used as in [3]. The results of the simulation of the airfoil motion due to the fluid-structure interaction are shown in Fig. 1 for the free-stream velocities $U_\infty = 20$ and 40 m/s. At $U_\infty \approx 40$ m/s the system is clearly unstable by the flutter combined with the divergence, which agrees well with [1].

Acknowledgements

This contribution was funded by the Grant No. *CZ.02.1.01/0.0/0.0/16_019/0000826*. Access to computing and storage facilities owned by parties and projects contributing to the National Grid Infrastructure MetaCentrum provided under the programme "Projects of Large Research, Development, and Innovations Infrastructures" (CESNET LM2015042), is greatly appreciated.

References

- [1] Dubcová, L., Feistauer, M., Horáček, J., Sváček, P., Numerical simulation of interaction between turbulent flow and a vibrating airfoil, *Computing and Visualization in Science* 12 (2009) 207–225.
- [2] Sváček, P., Numerical simulation of fluid-structure interactions with stabilized finite element method, *EPJ Web of Conferences* 114 (2016) 1–5, doi: 10.1051/epjconf/201611402118.
- [3] Sváček, P., Feistauer, M., Horáček, J., Numerical simulation of flow induced airfoil vibrations with large amplitudes, *Journal of Fluids and Structures* 23 (2007) 391–411.

Reducing energy losses in supports of rotating machines by application of smart materials

J. Zapoměl ^{a,b}, P. Ferfecki ^{b,c}, J. Kozánek ^a, M. Jirsa ^d

^a Institute of Thermomechanics, Czech Academy of Sciences, 182 00 Praha, Dolejškova 5, Czech Republic

^b Faculty of Mechanical Engineering, VŠB-Technical university of Ostrava, 17. Listopadu 15, 708 33 Ostrava, Czech Republic

^c IT4Innovations National Supercomputing Center, VŠB-Technical university of Ostrava, 17. Listopadu 15, 708 33 Ostrava, Czech Republic

^d Institute of Physics, Czech Academy of Sciences, Na Slovance 2, 182 21 Prague, Czech Republic

The energy losses in the bearings of rotating machines are approximately proportional to the transmitted load. The coefficient of proportionality is the resistance coefficient. The loss power can be reduced by minimizing

- the time varying component of the load transmitted through the bearings,
- the stationary component of the load transmitted through the bearings,
- the resistance coefficient.

A frequently used technological solution for reducing time varying forces transmitted between the rotor and its frame consists in placing damping devices in the rotor supports. To achieve their optimum performance, their damping effect must be controllable. This is offered by magnetorheological squeeze film dampers. Their applicability for reducing the energy losses is evident from the following study.

The investigated rotor (Fig.1) turns at constant angular speed and is loaded by the disc unbalance. In the developed model [3] the magnetorheological oil is represented by a bilinear material. As resistance against the flow of magnetorheological oils depends on magnetic induction, the change of the current generating magnetic flux changes the damping force.

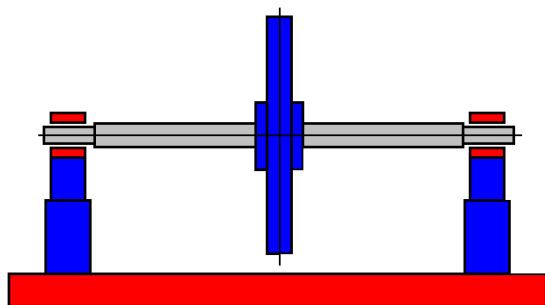


Fig. 1. Investigated rotor

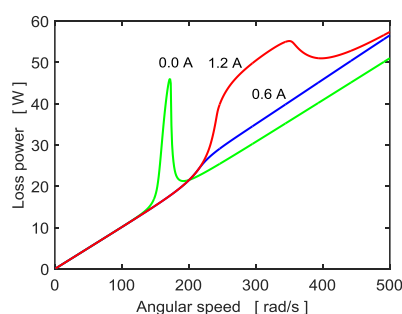


Fig. 2. Energy losses as a function of angular speed

The efficiency of reducing the energy losses by means of control of the applied current in different ranges of operating speeds is evident from Fig.2.

The stationary component of the load transmitted through the bearings is caused mostly by the rotor weight. A possible technological solution consists in lifting the rotor by permanent magnets.

The efficiency of this design arrangement is confirmed by the results of the investigation of an unbalanced vertical rotor (Fig. 3) of mass of 139 kg turning at constant angular speed of 1000 rad/s. At both its ends the rotor is coupled with the frame by rolling element bearings

and squeeze film dampers. The application of two permanent magnetic rings (one attached to the frame, the other to the disc) lifts the rotor and thus reduces the force transmitted through the bearings in the axial direction.

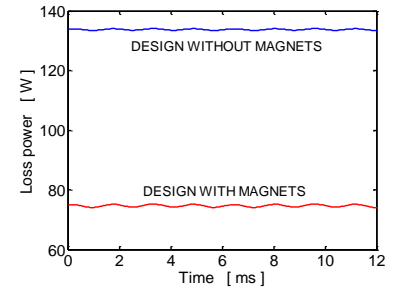
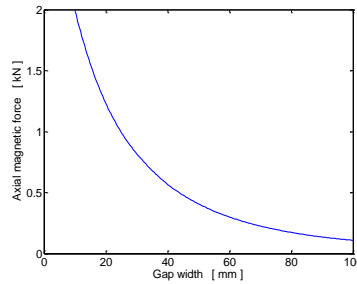
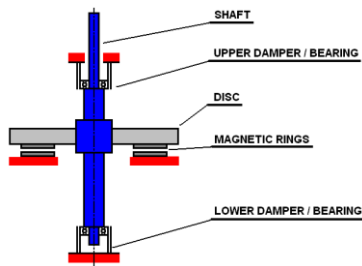


Fig. 3. Unbalanced vertical rotor

Fig. 4. Axial force/gap width graph

Fig. 5. Energy loss in two designs

To determine the repelling magnetic force the magnetic rings are discretized into small elements and each element is considered to be a small magnetic dipole [2]. The resulting force and moment action between the rings is given by their mutual interaction. The axial position of the magnetic rings was adjusted to 18 mm making use of the relationship between the axial force and the width of the gap between the rings (Fig. 4). The decrease of the loss power in the upper rotor support if the magnetic rings are installed is evident from Fig. 5.

The advanced technological solution, which makes it possible to reduce the resistance coefficient, consists in supporting the rotors by high-temperature superconducting bearings [1]. These bearings are composed of superconducting rings or bulks of a cylindrical shape and permanent magnets. The high-temperature superconductors are metal-ceramic materials that exhibit superconducting properties if they are cooled below the critical temperature (about 90 K). As they react to a change of external magnetic field in any direction by producing opposite magnetic force, they are able to stabilize the rotor both axially and radially. The high-temperature superconducting bearings show almost no resistance against the rotor rotation because of which the energy losses generated in the rotor supports are very little. A small experimental vertical rotor supported by high temperature superconducting bearings can be seen in Fig. 6.

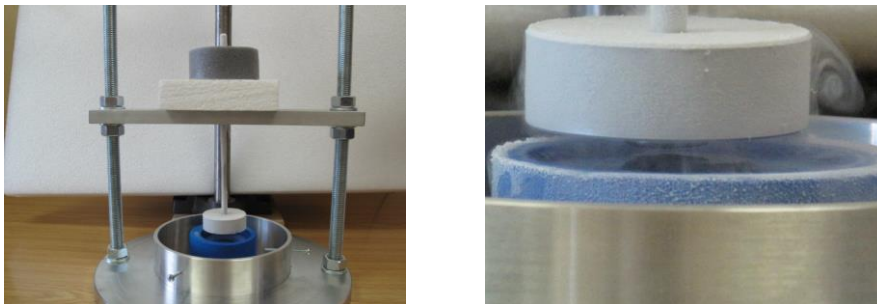


Fig. 6. Experimental vertical rotor

The performed analysis supported by results of computational simulations confirms that application of smart and advanced materials in supports of rotors and shafts makes it possible to reduce the energy losses generated in the bearings during operation of rotating machines.

References

- [1] Fujita, S., Godoy, S., Theory of high temperature superconductivity, Kluwer Academic Publishers, New York, Boston, Dordrecht, London, Moscow, 2001.
- [2] Knoepfel, H. E., Magnetic fields: A comprehensive theoretical treatise for practical use, John Wiley & Sons, Inc., New York, 2000.
- [3] Zapoměl, J., Ferfecki, P., Kozánek, J., Modelling of magnetorheological squeeze film dampers for vibration suppression of rigid rotors, International Journal of Mechanical Sciences 127 (2017) 191-197.

Modelling of the ball gel

J. Zavřel^a, T. Vampola^a, M. Dušková-Smrčková^b, V. Pawlik^a

^a Faculty of Mechanical Engineering, Czech Technical University in Prague 6, Technická 4, 166 07 Praha, Czech Republic

^b Institute of Macromolecular Chemistry AS CR, v.v.i., Heyrovského nám. 2, 162 06 Prague 6, Czech Republic

The morphology knowledge of the macroporous hydrogels is significant for modeling the deformation behavior. The morphology is given by results of complex processes in the formation of macromolecule chains and also the technique used for gel formation is essential. The article deals with the analysis of the quantity of individual gel particles - interconnected microparticles like gel beads and filling crystals. Filling the space with the gel phase forms a continuous structure. The microparticles provide through interconnection a large number of pathways passing through the gel structure. The molecular structure of the gel consists of polymer chains. These chains consist of monomer units. Some chain units are connected together and they are connected in nodes (cross-links). The structure is formed into a three-dimensional macromolecular network that can have various defects. An important parameter is the number of nodes and the number of chains between nodes as well as the cross-link density. It is necessary to include quantitative relations between the structure of the macromolecular net and its deformation behaviour [1]. The characteristic morphological parameters of the microstructure of the gel are overlapping rules, grid layout and other properties obtained from the spatial representation of the structure. Such characteristics can be obtained by using a confocal microscopy (Fig. 1) and subsequent reconstruction of the 3D gel structure.

The real sample is defined by its dimensions (borders) and the infill-density of the hydrogel or infill crystals. There are two cases of the ball-gel simulations. The first case is a simulation of connecting ball gel parts into chains (monomers form to polymers). The number of chains and cross-links defines the final cross-link density of the hydrogel [2]. The result is reliance the number of the ball microparticles on the number established chains between opposite borders of the sample.

The second case models the hydrogel filled by salt crystals. This infill is defined by size of crystals, their orientation and density. The size varies in the defined range. In the final stage are crystals dissolved by the dissolving agent. After the crystals dissolve, they create free paths through the hydrogel. The rating criterion is the number of paths between different bounds depending on the crystal quantity.

Modelling of the path growth is based on the graph theory. In the first step it is the random mesh of the crystals generated. Crystals are modelled as squares with varying sizes and orientations in the defined span. The path is than composed of the overlapping objects. The object overlapping is solved for the neighboring crystals. There are solved equations for the intersection of sides of squares. In case of overlapping they are built into paths (Fig. 2).

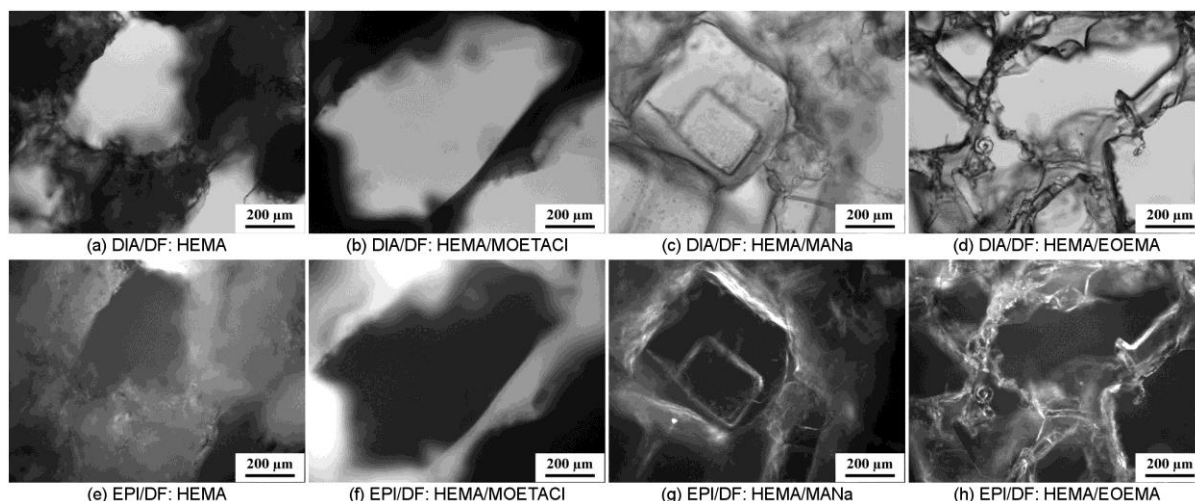


Fig. 1. Light micrographs of hydrogels of varying chemical composition with average pore dimensions 400 μm (upper row: DIA/BF -transmitted light, bright field imaging; lower row: EPI/DF -reflected light, dark field imaging; the pores appear bright/dark in DIA/BF and EPI/DF micrographs, respectively). Courtesy of Dana Kubies and Miroslav Šlouf, Institute of Macromolecular Chemistry

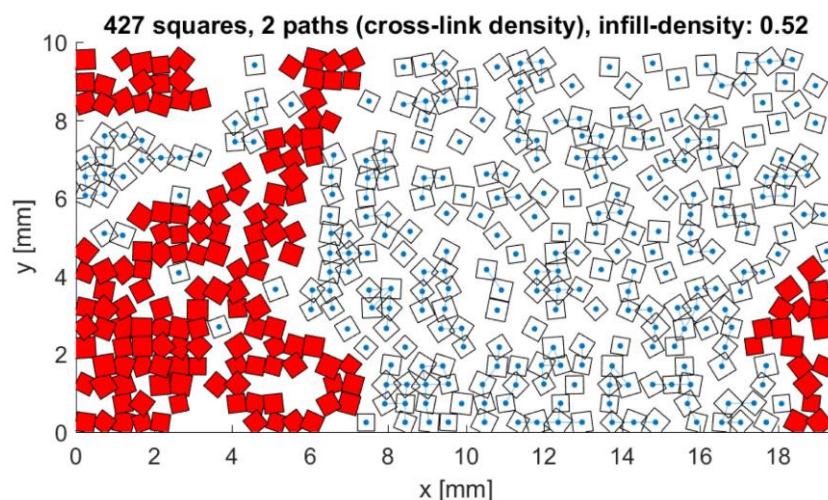


Fig. 2. Final result of path construction. The squares represent crystals in the ball-gel. The red one denote paths can be found in the case of connected borders

The aim of modelling ball gel is to find a consistency with experiments. In the future, it should be possible to predict mechanical properties based on a simulation and mathematical model.

Acknowledgements

The research is supported by the Grant Agency of the Czech Republic by project No GA17-08531S – “Computational design of hydrogel cell scaffolds“.

References

- [1] Engler, A.J., Shamik, S., Lee Sweeney, H., Discher, D.E., Matrix Elasticity Directs Stem Cell Lineage Specification, Cell 4, 2006, Vol. 126, pp. 677-689.
- [2] Příkladný, M., Dušková-Smrčková, M., Dušek, K., Janoušková, O., Sadakbayeva, Z., Šlouf, M., Michálek, J., Macroporous 2-hydroxyethyl methacrylate hydrogels of dual porosity for cell cultivation: morphology, swelling, permeability, and mechanical behaviour, Journal of Polymer Research 21 (2014) pp.579.

Modelling of the nuclear fuel assembly with impact interactions

V. Zeman^a, Z. Hlaváč^a, Š. Dyk^a

^aNTIS – New Technologies for the Information Society, Faculty of Applied Sciences, University of West Bohemia, Univerzitní 8, 306 14 Plzeň, Czech Republic

The nuclear fuel assembly (FA) is a very complicated system consisting of beam-type components. The linearized FA model was originally derived under conditions of full (backlash-free) and frictionless interaction of all FA components [2, 3]. This paper deals with modelling of nonlinear vibration of hexagonal-type FA (Fig. 1) applied in VVER 1000 type reactor.

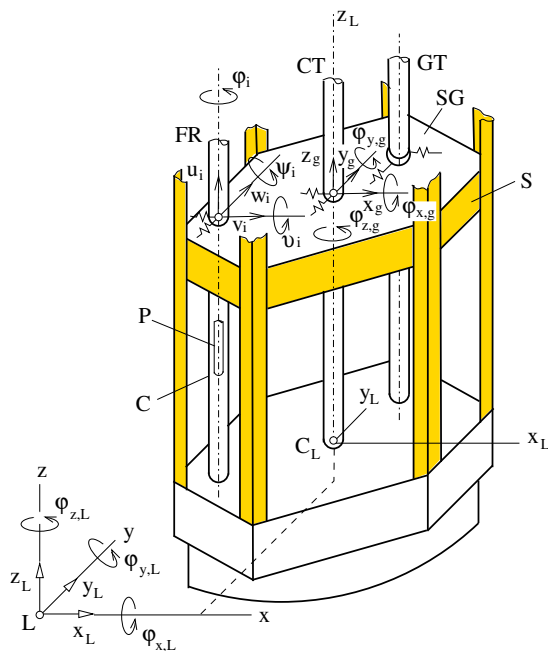


Fig. 1. Components of FA

The FA model includes 312 fuel rods (FR), 18 guide thimbles (GTs) and one central tube (CT) inserted in 8 spacer grids (SGs) placed regularly over the FA length. Each FR consists of the FR cladding in the form of the Zr thin-walled tube filled with the uranium fuel pellets stack with the radial clearance between pellets (P) and the cladding (C). Relatively rigid SGs are spot-welded with load-bearing skeleton (S) consisting of six angle pieces coupled by divided grid rim at all levels of SGs. In bottom end, each angle piece is clamped in support plate in reactor core by means of lower piece. For many reasons, it is important to estimate the vibration of the FA components excited by the pressure pulsations of the coolant [1].

Considering that all FR components of the same kind (C, P, GTs) vibrate in phase, the FA mathematical model can be derived in the configuration space

$$\mathbf{q} = [\mathbf{q}_S^T, \mathbf{q}_C^T, \mathbf{q}_P^T, \mathbf{q}_{GT}^T, \mathbf{q}_{CT}^T]^T, \quad (1)$$

where subscripts correspond to FA components-skeleton, FR cladding, FR pellets, guide thimbles and central tube, respectively. The vector of generalized coordinates $\mathbf{q}_S \in R^{48}$ of the free (kinematically not excited) plate bodies of the skeleton, including SGs, has the form

$$\mathbf{q}_S = [\dots, x_g, y_g, z_g, \varphi_{x,g}, \varphi_{y,g}, \varphi_{z,g}, \dots]^T, \quad g = 1, \dots, 8, \quad (2)$$

where x_g, y_g, z_g are displacements and $\varphi_{x,g}, \varphi_{y,g}, \varphi_{z,g}$ are torsional and bending angles of the plate body at the level of SG g . Using the FEM for 1D Euler-Bernoulli continua, the vectors of generalized coordinates of the beam-type components are defined in the form

$$\mathbf{q}_X = [\dots, u_i^X, v_i^X, w_i^X, \varphi_i^X, \vartheta_i^X, \psi_i^X, \dots]^T, \quad X = C, P, GT, CT,$$

where u_i^X, v_i^X, w_i^X are axial (vertical) and mutually perpendicular lateral displacements and $\varphi_i^X, \vartheta_i^X, \psi_i^X$ are torsional and bending angles, respectively, in the free nodal points of the component X.

The mathematical model of the FA can be written in the form

$$M\ddot{\mathbf{q}} + B\dot{\mathbf{q}} + (\mathbf{K} + \mathbf{K}_{S,CT})\mathbf{q} = \mathbf{f}_{KE}(t) + \mathbf{f}_C(\mathbf{q}, \dot{\mathbf{q}}), \quad (3)$$

where mass, damping and stiffness matrices M, B, K have the block diagonal form corresponding to uncoupled FA subsystems in block sequence defined by (1) and $K_{S,CT}$ is coupling stiffness matrix between skeleton and central tube. At the right-hand side, vector $\mathbf{f}_{KE}(t)$ represents the kinematic excitation of FA components by the FA support plates motion in the reactor core [2, 3]. The vector $\mathbf{f}_C(\mathbf{q}, \dot{\mathbf{q}})$ expresses the nonlinear coupling forces between SG cells and FR cladding, impact interactions between skeleton and guide thimbles at the level of all SGs $g = 1, \dots, 8$ and impact interactions between FR cladding and fuel pellets stack at the level of all nodal points $i = 1, \dots, 15$. Contact forces between SG cells of the skeleton and FR cladding respect friction with friction coefficient in the form

$$f(c_{l,g}) = \frac{2}{\pi} \arctan(\varepsilon c_{l,g}) [f_d + (f_0 - f_d)e^{-dc_{l,g}}], \quad (4)$$

where $c_{l,g}$ is FR cladding slip velocity in contact points $l = 1, 2, 3$ with cells at the SG level $g = 1, \dots, 8$ and ε, f_0, f_d, d are shaping parameters of the friction characteristics.

Nonlinear FA model (3) is rewritten as a set of the first order equations which is solved using ordinary tools for ODE solutions in MATLAB. The change of static preloading of the SG cells and clearances between FR cladding and the fuel pellets stack during the operational cycle of the reactor can be investigated assuming changes of the relevant parameters.

FA model can be used for estimation of maximal lateral deformations of the FA components and grid-to rod fretting wear occurring in the FR cladding contact points with SG cells.

Acknowledgement

This work was supported by the project LO1506 of the Ministry of Education, Youth and Sports of the Czech Republic.

References

- [1] Dyk, Š., Zeman, V., Modelling of the nuclear fuel assembly components as a flexible 1D continua with inner and outer impact interactions, Proceedings of the ECCOMAS Thematic Conference on Multibody Dynamics, 2017, Prague, Czech Republic.
- [2] Hlaváč, Z., Zeman, V., Vibration of nuclear fuel assemblies, LAP Lambert Academic Publishing, Saarbrücken, 2013.
- [3] Zeman, V., Hlaváč, Z., Dynamic response of nuclear fuel assembly excited by pressure pulsations, Applied and Computational Mechanics 6 (2) (2012) 219–230.

Micromechanical quantities based on Wang tiles with local tilings

L. Zrůbek^a, A. Kučerová^a, M. Doškář^a

^aFaculty of Civil Engineering, Czech Technical University in Prague, Thákurova 7, 166 29 Prague, Czech Republic

The increasing pressure to the materials utmost performance leads to necessity of excellent understanding of characteristic mechanical processes taking place on a microstructural level of materials. Therefore, the material models needs to incorporate also the microscale level.

For modelling of heterogeneous materials with stochastic patterns is used the concepts of statistically equivalent periodic unit cell (SEPUC). But because the concept uses only a single cell the stochastic heterogeneous material is transformed into unwanted periodic pattern of the same cells. Therefore, to preserve the randomness of the recreated material the method utilizing the set of representative cells must be used. This method is called Wang Tiles.

The basic principle of Wang tiles method was introduced by Mr. Hao Wang [5]. The concept is similar to the game called domino but instead of double-coded rectangular domino pieces, the tiles are squares with four edge codes - e.g. colors (Fig. 1). And contrary of creating a linear series of game pieces the tiles are placed into four cardinal directions and the two-dimensional area covered with tiles is produced. The tiles cannot be rotated or mirrored through the process and are placed side-by-side according to matching edge codes. The result is called tiling and by utilization of Cohen-Shade-Hiller-Deussen (CSHD) tiling algorithm [1] the resulting tiling is valid and also stochastic.



Fig. 1. Smallest Wang tiles set called W8/2-2

The Wang tiles method can be used for in many different fields like modelling of quasi-crystals and generating naturally looking textures for computer graphic [1]. As a substitution for the unit cell concepts (SEPUC) in material modelling or to obtain the micromechanical response for enrichment functions in numerous generalized finite element methods, e.g. [3, 2].

The whole microscopic domain can of course be discretized by very fine FEM mesh and evaluated to obtain demanded micromechanical fields like stresses, strains and displacements. But according to the fineness of the mesh and size of the domain, the evaluation time is rapidly increasing. The computational requirements can be diminished with the Wang tiles method as the process of microstructure reconstruction can be applied to the micromechanical field. The microscale quantities are evaluated on individual tiles and then synthesized back according to the same tiling as the microstructure. However, as presented in the paper [4] the non-local character of mechanical quantities is causing discontinuities on tile edges and therefore the underlying grid of tiles is recognizable. That is because of the mechanical response of each tile is affected by a different combination of surrounding tiles.

Furthermore, to be able to use the finite element method (FEM) as a solver brings another difficulty. Because the domain is represented by the tiles which are mutually compatible on the edges, the finite element meshes created on the individual tiles have to fulfil the exactly same compatibility (artificially created edge-compatible finite element meshes are displayed as the third step in process shown in Fig. 2).

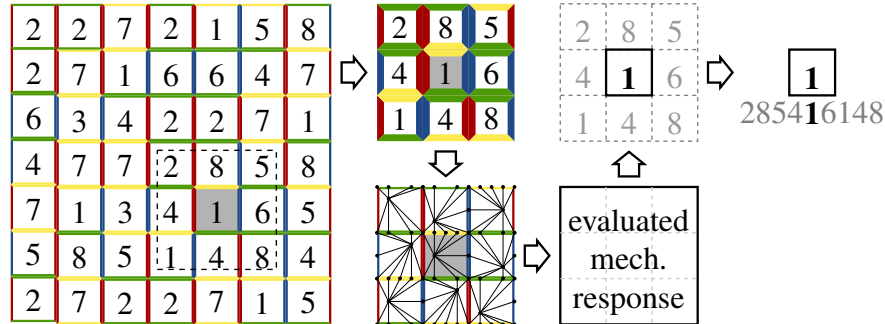


Fig. 2. Local tiling process

Our attempt to solve this problem is to include these surrounding tiles into the evaluation of the mechanical response for each tile. Therefore, for every tile T_i (grey square in the in Fig. 2) from the macro tiling we create so called *local tiling*. This local tiling is represented by the center tile T_i and the arbitrary number of surrounding layers of tiles from the macro tiling. Then the local FE mesh is synthesized and the micromechanical quantity is evaluated. Because we need only the results for the centre tile T_i we crop the results of all surrounding tiles and save the results under label $T_{285416148}$. This procedure is repeated for every tile T_i in macro-tiling. After results of all tiles are obtained, the micromechanical field of whole domain is synthesized.

The local tiling approach divides the single time-consuming evaluation of whole fluctuation field into a large number of small tasks. On top of that, each local tiling evaluation is entirely independent of others. Therefore, this approach is suitable for parallelization. Our main goal is to run sensitive analysis and determine the influence of characteristic microstructural lengths, tile size and number of necessary included layers in local tilings on the overall error of synthesized micromechanical fields.

Acknowledgement

The authors gratefully acknowledge the financial support from the Grant Agency of the Czech Technical University in Prague, the grant No. SGS17/042/OHK1/1T/11.

References

- [1] Cohen, M. F., Shade, J., Hiller, S., Deussen, O., Wang tiles for image and texture generation, *ACM Transactions on Graphics* 22 (3) (2003) 287–294.
- [2] de Freitas, J. A. T., Formulation of elastostatic hybrid-Trefftz stress elements, *Computer Methods in Applied Mechanics and Engineering* 153 (1) (1998) 127–151.
- [3] Melenk, J. M., Babuška, I., The partition of unity finite element method: Basic theory and applications, *Computer Methods in Applied Mechanics and Engineering* 139 (1) (1996) 289–314.
- [4] Novák, J., Kučerová, A., Zeman, J., Microstructural enrichment functions based on stochastic Wang tilings, *Modelling and Simulation in Materials Science and Engineering* 21 (2) (2013) 025–014.
- [5] Wang, H., Proving theorems by pattern recognition-II, *The Bell System Technical Journal* 40 (1) (1961) 1–41.